University of Alberta

The onset of superfluidity in He_N–cyanoacetylene clusters studied by Fourier transform microwave spectroscopy

by

Winifred C. Topic 

A thesis submitted to the Faculty of Graduate Studies and Research in partial fulfilment of the requirements for the degree of Doctor of Philosophy.

Department of Chemistry

Edmonton, Alberta

Fall 2006

Your file Votre référence
ISBN: 978-0-494-23119-7
Our file Notre référence
ISBN: 978-0-494-23119-7

Abstract

The weakly bound He_N–HCCCN (N = 1-17 and 26-31), He_N–DCCCN (N = 1-15), and He_N–HCCC^{15}N (N = 1-16) van der Waals clusters were observed in a free-jet expansion using a pulsed-nozzle Fourier transform microwave spectrometer in the 3-26 GHz frequency region. Nuclear quadrupole hyperfine structures due to the ^{14}N and D nuclei (both with nuclear spin quantum number I = 1) were resolved and assigned.

For the He–cyanoacetylene dimer, both *a*- and weaker *b*-type transitions were observed and the assigned transitions were fit to a distortable, asymmetric rotor model. The dimers are floppy, near T-shaped complexes. Three *ab initio* intermolecular potential energy surfaces were calculated using the coupled cluster method. The bound state rotational energy levels supported by these surfaces were determined. The quality of the potential energy surfaces were assessed by comparing the experimental and calculated transition frequencies and also the corresponding spectroscopic parameters. Simple scaling of the surfaces improved both the transition frequencies and spectroscopic constants.

Two rotational transitions were observed for each of the He_2–HCCCN, He_2–DCCCN, and He_2–HCCC^{15}N van der Waals trimers. These correspond to floppy, non-planar, asymmetric top molecules. The observed spectra of the He_N–cyanoacetylene clusters with N>2 were found to be consistent with rotational transitions within the K_a = 0 stack of prolate symmetric tops. These transitions can be adequately described with a linear rotor model. The measured rotational transition frequencies were used to fit the

rotational constant B and distortion constant D for each He_N–HCCCN, He_N–DCCCN, and He_N–$HCCC^{15}N$ cluster. The magnitude of B was found to oscillate with increasing cluster size, indicating that helium density decouples from the rotating system for $N > 9$. This is a hallmark of superfluid behaviour. Comparing the effective moments of inertia of the isotopomers allowed some information about cluster geometries to be deduced. The evolution of B with N for He_N–cyanoacetylene and He_N–N_2O clusters are compared to gauge the effect of rotor length on the onset of superfluidity as the molecules are solvated with He atoms.

Acknowledgements

Firstly, I would like to acknowledge the support, guidance, and patience of my Ph. D. Supervisor, Dr. W. Jäger. I have learned so many skills from him, and honed others under his tutelage. I also greatly appreciate the many opportunities that I have had to travel and attend conferences while conducting the research for this degree. Thank you.

Fellow researchers have provide invaluable help and insight into my work. I wish to thank Dr. Y. Xu, for teaching me the subtleties of the FTMW instrument and for sharing her expertise on He atom containing systems. The JACOBI program, which X. G. Song and P.-N. Roy generously shared with me, has been priceless. I also wish to thank N. Blinov, for many, many enlightening discussions.

I must acknowledge all the members of the Xu and Jäger groups. I have learned something from each one, past or present. My work would have been impossible if not for the instrument time chocolates, trips to Tim Horton's, insights into equations, lending of frequency generators (for weeks at a time), shoulders to cry on, and trips to the Plant. Thanks especially to J. Michaud, L. Downie, Q. Wen, Z. Su, N. Borho, and R. Lehnig who all volunteered enthusiastically to proof read this thesis. Many fewer commas are present in this work because of their dedication.

Edmonton would not have been nearly as fun or rewarding without many important people. My soccer teams, rugby team, and synchro club all provided so much more than just sport. The Shihs, H. Chavda, A. Ross, and T. Wolfe have kept me well rounded. E. Johnston was an unrelenting source of support and encouragement, and often served as my common sense.

Finally, I wish to thank my family. Specifically, my parents and sister who are inspiring examples of dedication and drive. Their belief in me has been motivating and unfaltering. And J. Wigginton, perhaps the most significant discovery I made during my graduate studies.

Table of Contents

List of Tables

List of Figures

List of Abbreviations

aug-cc-pVQZ	Augmented correlation-consistent polarized quadruple-zeta basis set
aug-cc-pVTZ	Augmented correlation-consistent polarized triple-zeta basis set
aVQZ+BF	Augmented correlation-consistent polarized quadruple-zeta basis set, supplemented with bond functions
aVTZ	Augmented correlation-consistent polarized triple-zeta basis set
aVTZ+BF	Augmented correlation-consistent polarized triple-zeta basis set, supplemented with bond functions
BF	Bond functions
CC	Coupled cluster method
CCSD	Coupled cluster method with single and double excitations
CCSD(T)	Coupled cluster method with single and double excitations and noniterative treatment of triple excitations as defined by J. D. Watts, J. Gauss, and R. J. Bartlett, J. Chem. Phys. **98**, 8718 (1993).
CCSD-T	Coupled cluster method with single and double excitations and noniterative treatment of triple excitations as defined by M. J. O. Deegan and P. J. Knowles, Chem. Phys. Letters **227**, 327 (1994).
c.m.	Centre of mass
DR	Double resonance
FTMW	Fourier transform microwave
HF	Hartree-Fock
MBPT	Many-body perturbation theory
MW	Microwave
MW-MW	Microwave-microwave
MW-MW DR	Microwave-microwave double resonance
PES	Potential energy surface
PESs	Potential energy surfaces
PIMC	Path integral Monte Carlo
POITSE	Projection operator imaginary-time spectral evolution

Ref.	Reference
Refs.	References
RQMC	Reptation quantum Monte Carlo
rms	Root-mean-squared
SAPT	Symmetry-adapted perturbation theory
VDZ	Correlation-consistent polarized double-zeta basis set
VQZ	Correlation-consistent polarized quadruple-zeta basis set
VTZ	Correlation-consistent polarized triple-zeta basis set

1

Introduction

Helium is a colourless, electrically neutral, chemically inert element that interacts only very weakly with other atoms or molecules. Under its own vapour pressure, it remains liquid at absolute zero. Early research revealed that liquid helium has many unusual properties when compared to other noble liquids. Liquid helium exists as two distinct states; a phase stable at higher temperatures, He I, behaving as an ordinary fluid and a second phase stable at low temperature, He II, that is unlike classical fluids.[1] At 2.176 K, liquid helium undergoes a phase transition. This marks the onset of very unusual behaviour,[2, 3, 4] including "frictionless flow" through narrow capillaries,[5] and abnormally high heat conduction rates.[6, 7] The observation of frictionless flow inspired the term "superfluid," in analogy to the discovery of persisting electrical current observed in

superconducting materials.[5]

The two-fluid model is a phenomenological explanation of the observed properties of liquid helium below 2.171 K. He II is assumed to consist of two simultaneously present and interpenetrating fluids, [8, 9] a superfluid Bose-Einstein condensate and a normal fluid. Atoms in a Bose-Einstein condensate simultaneously occupy the lowest energy state and are described by a single wavefunction. Thus, superfluidity can be considered a manifestation of quantum behaviour in a bulk system.

Andronikashvili directly observed normal and superfluid fraction of He II, and studied the temperature dependence of their relative concentrations.[10] By rotating a vessel containing a stack of thin plates in liquid helium, the effective moments of inertia of the vessel could be measured at various temperatures. As the temperature of the liquid helium was reduced below 2.171 K, the moment of inertia of the plates decreased. This indicated that increasing amounts of the helium density were becoming frictionless and decoupling from the rotating vessel.

In what is termed the "microscopic Andronikashvili experiment," Grebenev, Toennies, and Vilesov demonstrated that superfluidity can exist in finite ^{4}He systems.[11] Rovibrational transitions of an OCS molecule embedded within pure ^{4}He-droplets ($\sim 10^4$ atoms) were resolved, similar to the spectrum expected of an isolated, gaseous rotor. The observed moment of inertia of the OCS molecule was higher by a factor of 2.7 than that of the free molecule. The authors proposed that the superfluid fraction of the ^{4}He allowed the OCS chromophore to rotate unimpeded, while increased moment of inertia was due to normal He II density being dragged by the rotor. In this manner, they

reproduced the Andronikashvili experiment[10] on a microscopic scale. The authors of Ref. 11 suggested that a minimum of 60 ^{4}He atoms were required to form a superfluid.

By studying small clusters of He atoms, researchers are learning about what governs the onset of superfluidity. "Systematically solvating" a molecule with He atoms is one approach to investigating small He clusters.[12] This provides information about how the properties of the He_N–molecule clusters, where N is the number of He atoms, evolve as the clusters grow. By careful manipulation of both the sample and nozzle conditions, increasingly large He_N–molecule clusters (N = 2, 3..up to 72 for OCS,[12, 13, 14, 15] to 19 for N_2O,[16, 17] to 20 for CO,[18] and to 17 for CO_2[19]) have been generated using pulsed molecular beams and studied using infrared (IR) and microwave (MW) spectroscopy. For all He_N–molecule clusters studied, the effective B rotational constant initially lowers as the moment of inertia of the He_N–molecule increases with the addition of subsequent He atoms. The behaviour of the rotational constant and vibrational shifts of increasingly large clusters varies dramatically for different dopant molecules. For instance, the B rotational constant of He_N–OCS becomes smaller than the nanodroplet value[11] at N = 6.[12, 13, 14] To converge towards the B rotational constant of OCS in a nanodroplet, the B values of He_N–OCS clusters with larger N must "turn-around." As B is inversely proportional to the moment of inertia, this implies that the effective moment of inertia of the clusters must *decrease* with the addition of He atoms. Different behaviour of the B rotational constant was observed for He_N–N_2O.[16, 17] For the solvation of N_2O with He atoms, the effective B rotational constant oscillates above the nanodroplet B value with increasing N.[20] The effective moment of inertia for N up to 19

remains lower than that of N_2O in a ^{4}He nanodroplet. The observed evolution of B with N for both He_N–OCS and He_N–N_2O defies classical physics.

Spectroscopic observations have spurred on, and been supplemented by, computational simulations of He_N–molecule clusters. A number of groups are involved in using Quantum Monte Carlo (QMC) methods to study rotational and rovibrational properties of small and mid-sized He_N–molecule clusters. Recent examples include QMC studies of He_N–OCS ,[21, 22, 23] He_N–N_2O,[17, 24, 25] and He_N–CO_2.[19] The accuracy of these computational studies depends both on the choice of Monte Carlo method and potential energy surfaces describing the He–molecule and He–He interactions.

My study of He_N–cyanoacetylene clusters was motivated by both spectroscopic and computational studies of He_N–molecule systems. Specifically, I was interested in how the length of a dopant molecule influences the onset of superfluidity in He_N–molecule clusters. At 4.8 Å, cyanoacetylene is almost twice the length of any rotor studied by systematic solvation with He atoms. It is an excellent molecule for a microwave spectroscopic study, as it has a very strong permanent dipole moment giving rise to intense rotational transition signals. The synthesis of cyanoacetylene allows opportunities for isotopic substitution, thus increasing the amount of spectroscopic information available. The ^{14}N nucleus (with nuclear spin quantum number $I = 1$) of two of the studied isotopomers, HCCCN and DCCCN, gives rise to nuclear quadrupole hyperfine structures which provide a "spectroscopic signature" to aid in the assignment of rotational transitions. The rovibrational [26, 27, 28] and rotational [29] spectra of HCCCN embedded in a superfluid ^{4}He nanodroplet have been reported. The observed spectra

show a lowering of the rotational constant of HCCCN in the droplet, B = 1573.7 (7) MHz,[26] as compared to the free molecule, B = 4549.05859 (4) MHz.[30] This provides a limiting B value for very large He_N–HCCCN clusters.

Pulsed-nozzle Fourier transform microwave spectroscopy is an excellent technique for the study of He_N–molecule clusters. Clusters of atoms and molecules bound solely by van der Waals interactions or dispersion forces can be produced and stabilized in a supersonic free-jet expansion. The species initially undergo many cluster forming collisions after leaving the nozzle, but the density of the expansion drops quickly and the clusters enter a collision-free zone.[31, 32, 33, 34, 35] The expanding gas has a low translational temperature, which dramatically increases the population of low-energy rotational energy levels.[31, 33, 34, 36, 37, 38] Coupled with a Fourier transform microwave spectrometer,[39, 40] this provides a sensitive technique with which to probe van der Waals clusters free from interactions with other species.

In the following chapters, I present my spectroscopic investigation of He_N–cyanoacetylene clusters. Background information about the synthesis of cyanoacetylene and the experimental techniques used for the study of He_N–cyanoacetylene is given in Chapter 2. The systematic solvation of cyanoacetylene with He atoms begins with a detailed study of the weakly bound He–cyanoacetylene dimer, as a careful characterization of this van der Waals dimer provides the foundation for "building up" to larger He_N–cyanoacetylene clusters. The results and analysis of the rotational spectroscopic study of He–cyanoacetylene are presented in Chapter 3. Chapter 4 details the *ab initio* intermolecular potential energy surface (PES) of

He–cyanoacetylene, calculated using the coupled-cluster method. The bound rotational energy levels supported by the PES were determined, and the energy differences were compared to the measured rotational transition frequencies. This is a way to gauge how effectively current computational techniques are able to capture the interaction energies of weakly bound dimers. An introduction to the properties of bulk liquid helium, the discovery of superfluidity in finite systems and solvation of linear molecules with He atoms is provided in Chapter 5. The results of the microwave rotational study of He_N–cyanoacetylene clusters for N = 2-17 and 26-31, are given in Chapter 6. The evolution of the B rotational constant with N is analysed to provide information on cluster geometry and the onset of superfluidity in He_N–cyanoacetylene clusters. These results are compared to the B versus N behaviour of He_N–N_2O [16, 17, 24] in order to investigate the role that rotor length has on the superfluidity of small clusters. Finally, conclusions drawn from the rotational spectroscopic study of He_N–cyanoacetylene clusters are presented in Chapter 7.

1.1 References

1. W. H. Keesom and M. Wolfke, *Two Different Liquid States of Helium* in *Helium 4*, edited by Z. M. Galasiewicz (Pergamon Press, Oxford, 1971).

2. W. E. Keller, *Helium-3 and Helium-4* (Plenum Press, New York, 1969).

3. P. Nozières and D. Pines, *The Theory of Quantum Liquids: Superfluid Bose Liquids* (Addison-Wesley Publishing Company, Inc., Redwood City, CA, 1990).

4. R. J. Donnelly, *Experimental Superfluidity* (University of Chicago Press, Chicago, 1967).

5. P. Kapitza, Nature **141**, 74 (1938).

6. W. H. Keesom and A. P. Keesom, Physica **3**, 359 (1936).

7. J. F. Allen, R. Peierls, and M. Z. Uddin, Nature **140**, 62 (1937).

8. F. London, Nature **141**, 643 (1938).

9. L. Tisza, Nature **141**, 913 (1938). L. Tisza, Phys. Rev. **72**, 838 (1947).

10. E. Andronikashvili, J. Phys. (U. S. S. R.) **10**, 201 (1946).

11. S. Grebenev, J. P. Toennies, and A. F. Vilesov, Science **279**, 2083 (1998).

12. J. Tang, Y. Xu, A. R. W. McKellar, and W. Jäger, Science **297**, 2030 (2002).

13. Y. Xu and W. Jäger, Chem. Phys. Lett. **350**, 417 (2001).

14. Y. Xu and W. Jäger, J. Chem. Phys. **119**, 5457 (2003).

15. Y. Xu, W. Jäger, and A. R. W. McKellar, submitted for publication.

16. Y. Xu, W. Jäger, J. Tang, and A. R. W. McKellar, Phys. Rev. Lett. **91**, 163401-1 (2003).

17. Y. Xu, N. Blinov, W. Jäger, and P.-N. Roy, J. Chem. Phys. **124**, 081101 (2006).

18. J. Tang and A. R. W. McKellar, J. Chem. Phys. **119**, 754 (2003).

19. J. Tang, A. R. W. McKellar, F. Mezzacapo, and S. Moroni, Phys. Rev. Lett. **92**, 145503-1 (2004).

20. K. Nauta and R. E. Miller, J. Chem. Phys. **115**, 10254 (2001).

21. S. Moroni, A. Sarsa, S. Fantoni, K. E. Schmidt, and S. Boroni, Phys. Rev. Lett. **90**, 143401-1 (2003).

22. F. Paesani and K. B. Whaley, J. Chem. Phys. **121**, 4180 (2004).

23. N. Blinov, X. G. Song, and P.-N. Roy, J. Phys. Chem. **120**, 5916 (2004).

24. S. Moroni, N. Blinov, and P.-N. Roy, J. Chem. Phys. **121**, 3577 (2004).

25. F. Paesani and K.B. Whaley, J. Chem. Phys. **121**, 5293 (2004).

26. C. Callegari, I. Reinhard, K. K. Lehmann, G. Scoles, K. Nauta, and R. E. Miller, J. Chem. Phys. **113**, 4636 (2000).

27. C. Callegari, A. Conjusteau, I. Reinhard, K. K. Lehmann, and G. Scoles, J. Chem. Phys. **113**, 10535 (2000).

28. J. M. Merritt, G. E. Douberly, and R. E. Miller, J. Chem. Phys. **121**, 1309 (2004).

29. I. Reinhard, C. Callegari, A. Conjusteau, K. K. Lehmann, and G. Scoles, Phys. Rev. Lett. **82**, 5036 (1999).

30. S. Thorwirth, H. S. P. Müller, and G. Winnewisser, J. Mol. Spec. **204**, 133 (2000).

31. A. C. Legon, Ann. Rev. Phys. Chem. **34**, 275 (1983).

32. R. E. Smalley, L. Wharton, and D. H. Levy, Acc. Chem. Res. **10**, 139 (1977).

33. D. H. Levy, Ann. Phys. Chem. **31**, 197 (1980).

34. T. A. Miller, Science **223**, 545 (1984).

35. J. P. Toennies and K. Winkelmann, J. Chem. Phys. **66**, 3965 (1977).

36. C. E. Klots, J. Chem. Phys **72**, 192 (1980).

37. H. W. Liepmann and A. Roshko, *Elements of Gas Dynamics* (Wiley, New York 1957).

38. D. R. Miller, J. P. Toennies and K. Winkelmann, *9th Symposium on Rarefied Gas Dynamics Vol 2*, edited by M. Becker and M. Feibig (DFVLR Press 1974) C 9-1.

39. Y. Xu and W. Jäger, J. Chem. Phys. **106**, 7968 (1997).

40. V. N. Markov, Y. Xu, and W. Jäger, Rev. Sci. Instrum. **69**, 4061 (1998).

2

Experimental techniques and background theory

This chapter serves as a general introduction to some concepts critical to the rotational study of the solvation of cyanoacetylene with He atoms. It is divided into three main topics: the synthesis of cyanoacetylene (Section 2.1), the formation and stabilization of He_N–cyanoacetylene clusters (Section 2.2), and the measurement technique used for the study of the rotational transitions of the He_N–cyanoacetylene clusters (Section 2.3).

2.1 Synthesis of Cyanoacetylene

Cyanoacetylene is no longer commercially available in North America. It is a gas above 5 °C and polymerizes quickly at room temperature. HCCCN was synthesized in our lab according to the method of Moreau and Bongrand,[1] as modified by Miller and

Lemmon.[2] The entire process consists of two steps. First, either methyl propiolate or ethyl propiolate (Sigma-Aldrich Co.) was added to liquified ammonia to form propiolamide. The excess ammonia and alcohol side product were removed *in vacuo*. Then the propiolamide was mixed with phosphorus oxide and sand (for heat transfer), and this mixture was heated to approximately 200 °C for a minimum of two hours. The resulting cyanoacetylene was collected in a liquid N_2 cooled cold trap. The overall reaction scheme is:

$$H\text{-}C{\equiv}C\text{-}COOR \xrightarrow{liq.\ NH_3} H\text{-}C{\equiv}C\text{-}CONH_2 \xrightarrow[\Delta]{P_2O_5} H\text{-}C{\equiv}C\text{-}C{\equiv}N \qquad (2\text{-}1)$$

where *R* is either a methyl or ethyl group. An advantage of this two-step scheme is that it allows convenient opportunities for synthesizing other isotopomers of cyanoacetylene. Once trapped, cyanoacetylene can be stored under vacuum in a freezer with no observable degradation in the sample quality after more than two years.

In order to deuterate cyanoacetylene, reaction scheme 2-1 was modified slightly, in a manner similar to that reported by Mallinson and Fayt.[3] The propiolamide was dissolved in 25 mL of 99.77% D_2O (Columbia Organic Chemicals, Co., Inc.). The solution was stirred for three days, then the D_2O was pumped off. The amide was dissolved in a second aliquot of 25 mL D_2O, and stirred for a further three days. The synthesis then continued as described in Ref. 2:

$$H\text{-}C{\equiv}C\text{-}COOR \xrightarrow{liq.\ NH_3}\xrightarrow{D_2O} D\text{-}C{\equiv}C\text{-}COND_2 \xrightarrow[\Delta]{P_2O_5} D\text{-}C{\equiv}C\text{-}C{\equiv}N \qquad (2\text{-}2)$$

Vacuum distillation of the trapped product was performed to isolate highly pure DCCCN,

free of residual D_2O. Based on the relative intensities of the J'-J'' = 1-0 transition of DCCCN and HCCCN there was greater than 95% conversion.

$HCCC^{15}N$ was synthesized using the same procedure as for making HCCCN, while using isotopically enriched NH_3 (10% $^{15}NH_3$, Cambridge Isotope Laboratories, Inc.):

$$H\text{-}C{\equiv}C\text{-}COOR \xrightarrow{liq.^{15}NH_3} H\text{-}C{\equiv}C\text{-}CO^{15}NH_2 \xrightarrow[\Delta]{P_2O_5} H\text{-}C{\equiv}C\text{-}C{\equiv}^{15}N \qquad (2\text{-}3)$$

This method gives a sample of cyanoacetylene which is nominally enriched to 10% $HCCC^{15}N$.

2.2 The supersonic free-jet expansion

a) Properties of a free-jet expansion

He_N–cyanoacetylene clusters are generated and stabilized in a pulsed molecular free-jet expansion. A free-jet expansion is produced by releasing a gas sample through an orifice into a chamber maintained at low pressure. The adiabatic expansion of the gas produces a jet with characteristics that make it particularly suited for the generation and spectroscopic study of van der Waals complexes and clusters. Weakly bound clusters can be formed through three body collisions at the onset of the expansion and stabilized by the low translational temperature of the expansion. Finally, as the density of atoms in the free-jet expansion decreases, the expansion provides a collision-free environment in which to investigate the clusters, free from interference with other species.[4] The theory

of free-jet expansions and molecular beams are treated in detail elsewhere.[5, 6, 7, 8] A simplified explanation is presented here.

Atoms in a reservoir at temperature T_0 have random thermal motion, with an average velocity determined by T_0 and their mass m:

$$v_{th} = \sqrt{3kT_o/m} \tag{2-4}$$

where k is the Boltzmann constant. The distribution of this velocity was derived by J. C. Maxwell:

$$f(v) = 4\pi\left(\frac{m}{2\pi kT}\right)^{\frac{3}{2}} v^2 e^{-mv^2/2kT} \tag{2-5}$$

If this gas is expanded through a nozzle with a diameter d which is much larger than the mean free path of the atoms in the reservoir λ_o, random atomic motion in the reservoir is converted to directed mass flow. The mass flow velocity of the atomic gas, u, increases to a maximum value:

$$u_{max} = \sqrt{\frac{2\gamma}{(\gamma-1)}\frac{kT_o}{m}} \tag{2-6}$$

where γ is a constant (for monatomic gases $\gamma = 5/3$). The velocity distribution of the atoms, however, narrows and this results in a decrease in the translational temperature of the expanding gas. Figure 2.1 shows the normalized Maxwell-Boltzmann velocity distribution expected for He atoms in a reservoir at $T_0 = 300$ K and in a free-jet expansion. In an unskimmed jet, expanding atoms have components of their velocity parallel ($v_\parallel$) and perpendicular ($v_\perp$) to the direction of propagation. Following the theory developed by Toennies and Winkelmann in 1977 (Ref. 8), the velocity distribution in a

free-jet expansion is described using two Maxwell-Boltzmann equations, with different temperatures defined for velocity components parallel ($T_\parallel$) and perpendicular ($T_\perp$) to the direction of propagation:

$$f(v) = \left(\frac{m}{2kT_\parallel}\right)^{\frac{1}{2}} \left(\frac{m}{2kT_\perp}\right) e^{-\frac{m(v_\parallel - u)^2}{2kT_\parallel} - \frac{mv_\perp^2}{2kT_\perp}} \tag{2-7}$$

When $T_\parallel = T_\perp$, equation 2-7 reduces to equation 2-5. The set of moment equations which define $T_\parallel$, $T_\perp$, $v_\parallel$, and $v_\perp$ are given in Table 1 of Ref. 8. According to Hamel and Wills, $T_\perp$ continues to decrease with the square to the distance from the nozzle.[9] Binary collisions between atoms in the expansion couple $T_\perp$ with $T_\parallel$ and with internal temperatures, such as the rotational and vibrational temperatures of molecules seeded in the expansion.[10]

Introducing the Mach number M provides a standard for quantifying the extent of the expansion. The Mach number is the ratio of speed u to the local speed of sound a:

$$M = \frac{u}{a} \tag{2-8}$$

The local speed of sound, however, is defined in terms of the temperature and medium in which the soundwaves are propagating:[5]

$$a = \left(\frac{\gamma\ k\ T}{m}\right)^{\frac{1}{2}} \tag{2-9}$$

As the expansion proceeds, the Mach number increases rapidly as the local speed of sound decreases. For a given distance from the nozzle, M is defined as:[11]

$$M = b(X/d)^{\gamma-1} - \frac{\frac{\gamma-1}{\gamma+1}}{2\ b\ (X/d)^{\gamma-1}} = b(X/d)^{\frac{2}{3}} - \frac{1}{8\ b\ (X/d)^{\frac{2}{3}}} \tag{2-10}$$

where X/d is the distance from nozzle in terms of the nozzle diameter d and $b = 3.26$ for monatomic gases.[5]

In practice, dilute mixtures of dopant molecules in atomic carrier gasses are used to achieve optimal expansion conditions. Under these circumstances the behaviour of the expanding sample can be explained by considering only the properties of the atomic carrier gas.[5] An atomic gas in a reservoir has a given temperature T_o, pressure P_o, and density ρ_o. Assuming there are no shockwaves, heat sources, or heat sinks after the nozzle, the temperature T_l, pressure P, and density ρ of the expansion of a perfect gas is given by:[12]

$$\frac{T_l}{T_o} = \left(\frac{P}{P_o}\right)^{(\gamma-1)/\gamma} = \left(\frac{\rho}{\rho_o}\right)^{(\gamma-1)/\gamma} = \frac{1}{1+\frac{1}{2}(\gamma-1)M^2} \qquad (2\text{-}11)$$

Figure 2.2 is a schematic illustration of the nozzle and the free-jet expansion. The conversion of random thermal motion to directed mass flow is depicted by the conversion of arrows representing the velocity of the atoms from random lengths and orientations before the nozzle to uniform length and direction after the nozzle. The scale below the illustration shows the distance from the nozzle X in terms of diameter of the nozzle d. The Mach number, temperature (T_l) and pressure of the gas are given below the scale for the expansion of He at $T = 300$ K and $P_o = 50$ atm. For a nozzle with diameter $d = 0.8$ mm, X/d = 60 corresponds to a distance of 7.5 cm from the nozzle and an expansion temperature of 0.3 K.

As long as two-body collisions between the atoms of the expanding gas persist, T_l continues to decrease and equation 2-10 is valid. The density of the atoms decreases as

the expansion continues, reducing the frequency of binary collisions. Anderson and Fenn's model for the asymptotic approach of M to a limiting value treats the particles as hard spheres, and concludes that the terminal value of M in a monatomic gas is given by:[13]

$$M_T = 2.05\epsilon^{-(1-\gamma)/\gamma}\left(\frac{\lambda_o}{d}\right)^{(1-\gamma)/\gamma} = 133\ (P_o\ d)^{\frac{2}{5}} \qquad (2\text{-}12)$$

where ϵ is the collisional effectiveness constant, P_o is in atm, and d is in cm. Equation 2-12 reflects that cooling binary collisions continue further along in the expansion as the initial pressure in the reservoir is increased. This definition of M_T adequately describes all monatomic gases other than helium. Miller *et al.* found that the collisional cross section of helium increases rapidly as the relative energy of the colliding atoms decreases.[14] Cooling collisions continue further from the nozzle in a He atom expansion, resulting in a lower limit for the translational temperature compared to heavier monatomic gases such as Ne or Ar. Figure 2.3 is a plot of the expansion temperature achieved when M_T is reached versus reservoir pressure P_o for an expansion of He gas. In this figure, M_T was determined using equation 2-12, with the nozzle diameter $d = 0.8$ mm (used for the study of He_N–cyanoacetylene clusters). For reservoir pressures of $P_o = 6$ atm or higher the expansion has a translational temperature of < 0.1 K. Inset is a plot of the distance from the nozzle (in cm) at which M_T is reached versus reservoir pressure. The dashed horizontal line at 30 cm indicates the normal operating length of our microwave cavity. While significant additional cooling of a He free-jet expansion occurs in theory, compared to a Ne or Ar, in practice, the length of our cavity dictates that the terminal Mach value is

not reached for $P_o > \sim 23$ atm. The lowest expansion temperature for our experimental setup (~0.03 K) is higher than that dictated by a hard-sphere collision model (equation 2-12), for any $P_o > 20$ atm.

b) Rotational cooling

Collisions between carrier gas atoms and molecules seeded within the expansion lead to coupling between the translational temperature T_l of the expansion and the rotational and vibrational temperatures of the molecules (T_{rot} and T_{vib}, respectively).[4, 6, 7, 10, 12, 14] The degree of cooling of T_{rot} and T_{vib} is dependent on the efficient transfer of energy from these internal modes to the "cooling bath" of low translational temperature.[4] This mechanism is more efficient for rotational compared to vibrational degrees of freedom, and only the lowest rotational energy levels are significantly populated in a molecular beam expansion. In fact, for gentle expansion conditions, such as $P_o d = 50$ atm μm, T_{rot} is considered to equal the translational temperature ($T_l < 10$ K), while T_{vib} can range from 50 to 1000 K.[15, 16] The degree of non-equilibrium between the translational, rotational, and vibrational degrees of freedom, however, varies strongly with gas mixture and expansion conditions.[17]

While helium is a less efficient heat sink than either argon or neon, low T_{rot} values can be achieved in a He expansion from fairly moderate conditions. For example, a 0.1% mixture of benzene in 5 atm of He backing gas expanded through a nozzle of $d = 660$ μm, had a measured $T_{rot} = 0.3$ K.[18] Equations 2-12 and 2-11 give a terminal T_l of 0.2 K, while a quantum treatment would give a significantly lower T_l.[8]

The low T_{rot} of a He expansion increases the population of low rotational energy levels. For a rigid linear molecule, the relative population of a rotational energy level, J, is given by the normalized Boltzmann distribution:

$$\frac{N_J}{N} = \frac{(2J+1)}{q} e^{-\frac{hBJ(J+1)}{kT}} \tag{2-13}$$

where N_J is the population of J, N is the total population, B is the rotational constant, and q is the partition function:

$$q = \sum_J (2J+1)\, e^{-\frac{hBJ(J+1)}{kT}} \tag{2-14}$$

Figure 2.4 illustrates this by showing the relative population of the rotational energy levels of cyanoacetylene for T_{rot} = 300 K and 0.1 K. T_{rot} = 300 K corresponds to the populations expected for HCCCN in a static cell at room temperature, where as T_{rot} = 0.1 K is a conservative estimate of the rotational temperatures achieved in our free-jet expansion. Figure 2.4 was determined using B = 4549.05859 (4) MHz, the rotational constant for HCCCN.[19] For both temperatures, the peak in population occurs at $J > 0$. While the population of the individual states decreases exponentially, the degeneracy of the energy levels increases with $2J + 1$. Maximum population occurs at $J = 65$ for T_{rot} = 300 K, and at $J = 1$ for T_{rot} = 0.1 K. In the expansion, the rapid decrease in population for $J > 1$ in the expansion limits the number of observable rotational transitions but also simplifies the spectra. The observed intensity of a rotational transition investigated using a Fourier transform microwave spectrometer is proportional to the population difference between the two energy levels investigated. This will be discussed further in Section 2.3.

In the meantime, the magnitude of the population difference between J and J+1 is also plotted in Figure 2.4.

c) The formation of van der Waals clusters

The formation of van der Waals dimers in a free-jet expansion proceeds via three body collisions.[4] A sample composed of a molecule with He backing gas gives rise to three different weakly bound dimers:

$$2\ \text{He} + \text{molecule} \rightarrow \text{He–molecule} + \text{He}^* \qquad (2\text{-}15)$$

$$\text{He} + 2\ \text{molecule} \rightarrow \text{molecule–molecule} + \text{He}^* \qquad (2\text{-}16)$$

$$3\ \text{He} \rightarrow \text{He–He} + \text{He}^* \qquad (2\text{-}17)$$

where He* is the third body required to carry away the excess kinetic energy. A simple model[20] predicts that the concentration of dimers at the nozzle is proportional to $P_o d^{1/2}$. Calculations by Braun *et al.* determined that an expansion of pure He from T_o = 300 K and P_o = 500 atm contains 99.6% He monomers, 0.35% He_2, and less than 0.002% He_3.[21] With the lower He backing pressures used with our instrument (P_o < 150 atm), path 2-17 is negligible. If the concentration of the molecule is very small ([He] >> [molecule]), then path 2-15 will predominate over 2-16. The binding energy of a He–molecule van der Waals dimer (~40 to 60 cm^{-1}) is much smaller than kT if T is room temperature (~200 cm^{-1}). The low translational temperature of the free-jet expansion signifies that the relative kinetic energy of two colliding species is less than the van der Waals binding energy. Once van der Waals dimers are formed in an expansion, they are essentially

stable with respect to collisions with the surrounding gas.[6] Binary collisions between the dimer and additional He atoms leads to further cooling of the bound species.

Increasing the backing pressure P_0, lowering the reservoir temperature T_0, and decreasing the dopant concentration all lead to cluster growth by a series of three body collisions:[22]

$$2\ \mathrm{He} + \mathrm{molecule} \rightarrow \mathrm{He{-\!\!-}molecule} + \mathrm{He}^* \qquad (2\text{-}18a)$$

$$2\ \mathrm{He} + \mathrm{He{-\!\!-}molecule} \rightarrow \mathrm{He_2{-\!\!-}molecule} + \mathrm{He}^* \qquad (2\text{-}18b)$$

$$2\ \mathrm{He} + \mathrm{He_2{-\!\!-}molecule} \rightarrow \mathrm{He_3{-\!\!-}molecule} + \mathrm{He}^* \qquad (2\text{-}18c)$$

...

$$2\ \mathrm{He} + \mathrm{He_{(N\text{-}1)}{-\!\!-}molecule} \rightarrow \mathrm{He_N{-\!\!-}molecule} + \mathrm{He}^* \qquad (2\text{-}18n)$$

Increasing P_0 contributes to the formation of larger clusters in three ways: by increasing the density of colliding species at the nozzle, increasing the duration of cluster forming collisions in the expansion, and by increasing the stability of the formed clusters by decreasing the expansion temperature. Decreasing the reservoir temperature or cooling the nozzle encourages cluster formation by increasing the gas density behind the nozzle.[23] Increasing the dilution ratio promotes the growth of larger clusters by reducing the competing formation of molecule–molecule dimers. Lowering the concentration of the dopant molecule past a certain point, however, will cause weakening of the observed signal intensity.

The sample conditions used to generate He_N–cyanoacetylene clusters and study them spectroscopically were quite varied, depending on the magnitude of N. P_0 ranged

from 6 atm for the study of He–cyanoacetylene dimer to 120 atm for He_{31}–cyanoacetylene. The concentration of cyanoacetylene in He backing gas ranged from 0.03% for the largest clusters to 2% for the dimer. Nozzle cooling was found to improve the observed transition emission signal intensity for large He_N–cyanoacetylene clusters with N = 26-31. Further detail about the experimental conditions used for He_N–cyanoacetylene clusters with N = 1 and N > 1 is provided in Sections 3.1 and 6.1, respectively.

2.3 Fourier transform microwave spectroscopy

a) Theoretical background of pulsed Fourier transform rotational spectroscopy

Fourier transform microwave spectroscopy involves detecting a transient signal in the time domain. For this reason, a description of the technique necessitates the use of time-dependent Schrödinger equation. Detailed descriptions of the theory of Fourier transform microwave spectroscopy have been developed elsewhere.[24, 25, 26, 27] An overview of the theory will be presented here.

Consider, for simplicity, a molecular ensemble consisting of N two-level particles with eigenvalues of E_a and E_b and eigenfunctions of $|a\rangle$ and $|b\rangle$, respectively. The lower energy level, E_a, and the upper energy level, E_b are separated by:

$$E_a - E_b = \hbar \omega_0 \qquad (2\text{-}19)$$

where ω_0 is the angular transition frequency. The wavefunction of this two-level system is, in general, time-dependent and can be expressed as:

$$|\Psi(t)\rangle = c_a(t)|a\rangle + c_b(t)|b\rangle \tag{2-20}$$

The coefficients $c_a(t)$ and $c_b(t)$ are functions of time, $|a\rangle$ and $|b\rangle$ are the wavefunctions of the two stationary states. The density matrix of the ensemble describes the time-dependence of the coefficients:

$$\rho(t) = \begin{pmatrix} \rho_{aa}(t) & \rho_{ab}(t) \\ \rho_{ba}(t) & \rho_{bb}(t) \end{pmatrix} = \begin{pmatrix} \frac{1}{N}\sum_i^N c_{ai}(t)c_{ai}(t)^* & \frac{1}{N}\sum_i^N c_{ai}(t)c_{bi}(t)^* \\ \frac{1}{N}\sum_i^N c_{bi}(t)c_{ai}(t)^* & \frac{1}{N}\sum_i^N c_{bi}(t)c_{bi}(t)^* \end{pmatrix} \tag{2-21}$$

The diagonal elements, ρ_{aa} and ρ_{bb}, describe the population probabilities of the energy levels E_a and E_b. The off-diagonal elements ρ_{ab} and ρ_{ba} ($= \rho_{ab}^*$) are coherence terms that describe the phase relationship between $|a\rangle$ and $|b\rangle$.

The molecular ensemble interacts with an applied electromagnetic field via an electric dipole interaction. The molecules are assumed to interact with the electromagnetic field in an identical fashion but not to interact with each other. This explicitly time-dependent interaction between the electric dipole operator, $\hat{\mu}$, and the coherent electromagnetic field is treated as a perturbation:

$$\hat{H} = \hat{H}_o + \hat{H}_1 = \hat{H}_o - \hat{\mu} \cdot \epsilon_o \cos(\omega t) \tag{2-22}$$

$\hat{H}_o$ is the time-independent, unperturbed Hamiltonian, ϵ_o is the electric field strength of the microwave radiation, and ω is its frequency. The time-dependent Schrödinger equation for this system is:

$$i\hbar\frac{\partial\Psi}{\partial t} = \hat{H}\Psi = (\hat{H}_o + \hat{H}_1)\Psi \tag{2-23}$$

In quantum mechanics, an observable quantity is represented by an operator such as the

dipole operator. The matrix representation of the dipole moment operator is:

$$\mu = \begin{pmatrix} \langle a|\hat{\mu}|a\rangle & \langle a|\hat{\mu}|b\rangle \\ \langle b|\hat{\mu}|a\rangle & \langle b|\hat{\mu}|b\rangle \end{pmatrix} = \begin{pmatrix} 0 & \mu_{ab} \\ \mu_{ba} & 0 \end{pmatrix} \tag{2-24}$$

where the matrix elements μ_{ab} and μ_{ba} are equivalent. The expectation value of dipole moment operator of the two-level system is:

$$\langle \hat{\mu} \rangle = \textit{trace}\ (\rho \cdot \mu) = \mu_{ab}[\rho_{ab}(t) + \rho_{ba}(t)] \tag{2-25}$$

The observable quantity in our rotational spectroscopic measurements is the polarization, *i.e.* the macroscopic dipole moment of the entire ensemble. The expectation value of the polarization is the number density of the two-level system ${}^1N$ times the average dipole moment:

$$P(t) = {}^1N \langle \hat{\mu} \rangle = {}^1N\ \mu_{ab}[\rho_{ab}(t) + \rho_{ba}(t)] \tag{2-26}$$

It is necessary to obtain expressions for $\rho_{ab}(t)$ and $\rho_{ba}(t)$. The time evolution of the density matrix can be obtained from the density matrix formalism of the time dependent Schrödinger equation:

$$i\hbar \frac{\partial \rho(t)}{\partial t} = [H, \rho] = H\rho - \rho H$$

$$i\hbar \frac{\partial \rho(t)}{\partial t} = \begin{pmatrix} -\mu_{ab}(\rho_{ba} - \rho_{ab})\varepsilon_o \cos(\omega t) & -\rho_{ab}(E_b - E_a) - \mu_{ab}(\rho_{bb} - \rho_{aa})\varepsilon_o \cos(\omega t) \\ \rho_{ba}(E_b - E_a) - \mu_{ab}(\rho_{aa} - \rho_{bb})\varepsilon_o \cos(\omega t) & -\mu_{ab}(\rho_{ab} - \rho_{ba})\varepsilon_o \cos(\omega t) \end{pmatrix} \tag{2-27}$$

By using $\rho_{ab} = \rho_{ba}^*$, recognizing that $(E_b - E_a)/\hbar = \omega_o$, and defining the Rabi frequency as $x = (\mu_{ab}\, \epsilon_o)/\hbar$, we can simplify equation 2-27:

$$\frac{\partial \rho(t)}{\partial t} = \begin{pmatrix} ix(\rho_{ba} - \rho_{ab})\cos(\omega t) & i\rho_{ab}\omega_o + ix(\rho_{bb} - \rho_{aa})\cos(\omega t) \\ -i\rho_{ab}\omega_o - ix(\rho_{bb} - \rho_{aa})\cos(\omega t) & -ix(\rho_{ba} - \rho_{ab})\cos(\omega t) \end{pmatrix} \tag{2-28}$$

The Rabi frequency describes the strength of the interaction between the transition dipole moment of the molecular ensemble and the external radiation applied to the system. Transforming the elements of the matrix density into a rotating coordinate system gives the interaction representation that rotates with the angular frequency ω:

$$\begin{aligned} \underline{\rho_{aa}} &= \rho_{aa} \\ \underline{\rho_{ab}} &= \rho_{ab} e^{-i\omega t} \\ \underline{\rho_{ba}} &= \rho_{ba} e^{i\omega t} \\ \underline{\rho_{bb}} &= \rho_{bb} \end{aligned} \tag{2-29}$$

The following real variables are introduced:

$$\begin{aligned} u &= \underline{\rho_{ba}} + \underline{\rho_{ab}} \\ v &= i(\underline{\rho_{ba}} - \underline{\rho_{ab}}) \\ w &= (\underline{\rho_{aa}} - \underline{\rho_{bb}}) \\ s &= \underline{\rho_{aa}} + \underline{\rho_{bb}} \end{aligned} \tag{2-30}$$

Here u and v are coherence terms, proportional to the real and imaginary macroscopic polarization of the molecular ensemble, respectively. The variable w is the difference in population of E_a and E_b, while s is the sum of the population of these two energy levels. The partial derivatives of these variables with respect to time are the electric analogues to the Bloch equations of NMR spectroscopy. Using the rotating wave approximation, meaning any 2ω terms are neglected, and ignoring relaxation effects for clarity:

$$\frac{\partial u}{\partial t} = -\Delta\omega v$$
$$\frac{\partial v}{\partial t} = \Delta\omega u - xw \qquad (2\text{-}31)$$
$$\frac{\partial w}{\partial t} = xv$$
$$\frac{\partial s}{\partial t} = 0$$

where $\Delta\omega = \omega_0 - \omega$, the off-resonance of the transition frequency from that of the external microwave field. Equation 2-31 indicates that the time dependence of the population difference between E_a and E_b depends on the imaginary polarization of the ensemble. The total population of the system is constant with respect to time.

Finally, we can use equations 2-26 and 2-30 to express the macroscopic polarization after back transformation into the laboratory frame in terms of u and v:

$$P(t) = {}^1N\,\mu_{ab}[\rho_{ab}(t)e^{i\omega t} + \rho_{ba}(t)e^{-i\omega t}] = {}^1N\,\mu_{ab}[u\cos(\omega t) - v\sin(\omega t)] \qquad (2\text{-}32)$$

Before the external field is applied to the system of N particles, the coherence terms $u(0) = v(0) = 0$, reflecting that the system has yet to be polarized, and the population difference $w(0) = \Delta N_0$. When the external electromagnetic radiation is applied to the system, its amplitude is such that $x >> \Delta\omega$. Neglecting the off-resonant $\Delta\omega$ term, equation 2-31 becomes:

$$\frac{\partial u}{\partial t} = 0$$
$$\frac{\partial v}{\partial t} = -xw \qquad (2\text{-}33)$$
$$\frac{\partial w}{\partial t} = xv$$

and the solutions are:

$$\begin{aligned} u(0) &= 0 \\ v(0) &= -\Delta N_o \sin(xt) \\ w(0) &= \Delta N_o \cos(xt) \end{aligned} \tag{2-34}$$

Our detected signal is proportional to the macroscopic polarization of the system, so it is advantageous to obtain a maximum polarization. This is achieved when $\sin(xt) = 1$, according to equation 2-34. Maximum polarization occurs when the external radiation has a pulse length $t_p = \pi/2x$, $3\pi/2x$, $5\pi/2x$, *etc.* In practice, it is convenient to choose $t_p = \pi/2x$, which is commonly referred to as the "$\pi/2$ pulse." At this pulse length, the initial population difference ΔN_0 is completely converted into polarization, so $w(\pi/2x) = 0$.

Once the system has been prepared in the $\pi/2$ state, the external radiation is switched off and $x = 0$. The off-resonance term can no longer be neglected. After the application of a $\pi/2$ pulse of microwave radiation, the oscillating system has the following time dependence:

$$\begin{aligned} \frac{\partial u}{\partial t} &= -\Delta\omega \cdot v \\ \frac{\partial v}{\partial t} &= \Delta\omega \cdot u \\ \frac{\partial w}{\partial t} &= 0 \end{aligned} \tag{2-35}$$

Assuming that the system has maximum polarization, $u(\pi/2x) = 0$, $v(\pi/2x) = -\Delta N_0$, and $w(\pi/2x) = 0$, the solutions are:

$$u(t') = \Delta N_o \cos(\Delta\omega t')$$
$$v(t') = -\Delta N_o \sin(\Delta\omega t') \qquad (2\text{-}36)$$
$$w(t') = 0 \qquad (t' = t - t_p)$$

Using equations 2-32 and 2-33, we find that the macroscopic polarization during the detection period oscillates with the transition frequency, providing the molecular emission signal:

$$P(t) = {}^1N\,\mu_{ab}[u\cos(\omega t) - v\sin(\omega t)] = {}^1N\,\mu_{ab}\,\Delta N_o \sin(\omega_o t') \qquad (2\text{-}37)$$

The linear dependence of equation 2-37 on the initial population difference between E_a and E_b suggests that one method of improving the observed emission signal intensity is by increasing ΔN_o. As illustrated in Figure 2-4, a free-jet expansion results in drastically increased populations and population differences for low-lying rotational energy levels compared to a room temperature environment.

b) Microwave-microwave double resonance experiment

This gain in rotational population in an expansion quickly diminishes for higher rotational energy levels. Continuous microwave-microwave double resonance (MW-MW DR) experiments can increase the observed emission signal intensity by increasing ΔN_o. Figure 2-5 **A** shows the pumping scheme used for constructive MW-MW DR experiments. The interaction of the permanent dipole moment of the molecule with a photon with angular frequency $\omega = (E_a\text{-}E_b)/\hbar$ promotes the molecule from E_a to E_b.[28] If sufficient molecules are promoted to E_b, the population difference between E_b and E_c will

increase perceptably, and the emission signal of the transition between E_b and E_c will improve linearly. Figure 2.6 shows the signal improvement of the He_3–HCCCN $J = 2\text{-}1$ rotational transition when individual components of the nuclear quadrupole hyperfine structure of the $J = 1\text{-}0$ transition are pumped.

A second type of MW-MW DR experiment was used for the study of He_N–cyanoacetylene clusters. The pumping scheme used for the destructive DR experiments is given in Figure 2.5 **B**. A continuous source of MW radiation with $\omega = (E_b\text{-}E_c)/\hbar$ is broadcasted towards the free-jet expansion within the MW cavity. The molecular ensemble interacts with this pump frequency after it has been prepared in a superposition state of $|a\rangle$ and $|b\rangle$ by the application of a $\pi/2$ pulse. A low power DR source (~5 μW) induces splitting of the monitored $E_b\text{-}E_a$ transition, higher pumping power (≥ ~300 μW) will cause rapid decoherence of the emission signal.[29] This is illustrated in Figure 2.7 for He_8–HCCCN. The $F = 2\text{-}1$ nuclear quadrupole hyperfine component of the $F = 1\text{-}0$ transition is monitored while the pumping frequency is scanned through the $J = 2\text{-}1$ rotational transition. At moderately high power (4 mW), two sharp decreases of the $J = 1\text{-}0$ transition are observed. These correspond to the $F = 2\text{-}2$ and 3-2 components of $J = 2\text{-}1$. At high pumping power (250 mW), the emission signal intensity was reduced for all pumped frequencies and the $J = 1\text{-}0$ signal was destroyed for the entire frequency range of the $J = 2\text{-}1$ transition.

c) The pulsed-nozzle Fourier transform microwave spectrometer

The Fourier transform microwave spectrometer (FTMW) used for the study of

He_N–cyanoacetylene clusters has been described in detail elsewhere.[30, 31] The basic principles of its operation are as follows.

Our FTMW spectrometer is based on the instrument designed by Balle and Flygare.[20] Firstly, a microwave cavity is formed by two spherical aluminum mirrors, held within a vacuum chamber as depicted in Figure 2.8. One mirror is fixed to the front flange of the chamber, while the second mirror is movable and can be tuned with a Motor Mike DC actuator into resonance with the external MW radiation to give a standing wave pattern between the mirrors. The vacuum chamber is evacuated with a diffusion pump, backed by a mechanical pump. This combination gives pressures < 1 mTorr in the chamber, essentially eliminating collisions between species in the free-jet expansion and warm background gas. The pulsed nozzle is mounted near the centre of the fixed mirror, and the free-jet expansion propagates parallel to the MW cavity axis.[32]

The coherent MW pulse is generated using a MW synthesizer with an operating range of 1 to 20 GHz. The pulse length is regulated by two *p-i-n* diode switches. Typical MW pulse lengths for the study of He_N–cyanoacetylene clusters were ~0.2 μs for $N = 1$ *a*-type transitions and ~1.5 μs for $N = 1$ *b*-type transitions, and 0.2 - 0.9 μs for $N =$ 2 to 31. The MW pulse is coupled into the MW cavity via a wire hook antenna, and the molecular emission signal is detected with the same antenna. The coherent MW pulse is used to excite the molecular ensemble and the subsequent spontaneous coherent molecular emission signal is measured as a function of time. The signal is amplified and down-converted to radio frequencies, then 4k, 8k, 16k, or 32k data points are collected at a 10 ns sampling rate. The digitized signal is averaged and then Fourier transformed to

obtain a frequency spectrum. The MW diode detector connected to the movable mirror is used to tune the cavity into resonance with the excitation pulse frequency prior to each experiment. The bandwidth of the cavity is ~1 MHz.

Having the MW cavity axis and the propagation of the free-jet expansion parallel allows efficient capturing of the molecular emission signal, leading to enhanced sensitivity of this configuration compared to one where the expansion is perpendicular to the cavity axis. The emission signal radiates spherically from the travelling molecules, and both the "forward" and "backward" components are detected. In the Fourier transformed frequency spectrum the rotational transition lines appear as Doppler doublets as illustrated in Figure 2.9. The transition frequency is the average of the Doppler pair. For a Ne expansion the typical full width at half height linewidth is 7 kHz, and the estimated accuracy is better than ± 1 kHz.[31] The velocity of a gas is inversely proportional to the square root of its mass. A Ne expansion (T_o = 300 K) takes ~0.38 ms to travel 30 cm, a typical operating length of our MW cavity. An expansion of He atoms traverses the cavity in ~0.17 ms. The shorter observation time of species in a He expansion causes broadening of rotational transition frequencies and typical linewidths in a He expansion are ~21 kHz and the estimated accuracy of the frequencies is ± 2 kHz. The timing of each MW experiment is controlled by a pulse generator. Figure 2.10 shows the timing sequence typically used for the study of He_N–cyanoacetylene complexes. Starting from time t = 0, a pulse opens the nozzle and the gas sample expands into the cavity. The MW $\pi/2$ pulse is then coupled into the cavity, converting the initial population difference between the two energy levels of interest into a macroscopic polarization of the

molecular ensemble. A protective switch prevents the strong excitation MW pulse from damaging the sensitive detection amplifier. Once the excitation pulse has decayed from the cavity, the protective switch is opened and the molecular emission signal plus the remaining cavity background signal is recorded. In order to record the background signal of the cavity, this entire sequence is preceded by the same sequence but without a molecular pulse. The molecular emission signal is then obtained by subtracting the background signal from the (molecule + background) signal. This constitutes one cycle in our experiment.

When MW-MW double resonance experiments are conducted a second MW synthesizer, with an operating frequency range of 1 to 40 GHz, is used to broadcast continuous radiation into the cavity through a horn antenna. This radiation propagates perpendicular to the cavity axis, as illustrated in Figure 2.11, for two different horn setups. Setup **A** illustrates the horn placement for constructive MW-MW DR experiments. Here, the horn was placed inside the cavity, as near as possible to the nozzle. This provides a near homogenous electromagnetic field of MW frequency near the nozzle, pumping population from a lower to a higher rotational energy level. Setup **B** was suggested by Brendel and Mäder,[33] and Markov *et al.*[31] The horn is located outside the vacuum chamber and the MW radiation is broadcasted through a teflon window. The horn is oriented with the longer axis parallel to the MW cavity axis, a 90° rotation of the horn for setup **B** compared to **A**. The relative orientation of the horn and distance from the expansion causes the molecules in the expansion to experience an inhomogeneous electromagnetic field in setup **B**. This electromagnetic field is located further in the

expansion, corresponding to a spacial region where macroscopic polarization of the molecular ensemble would normally exist.

2.4 Figures

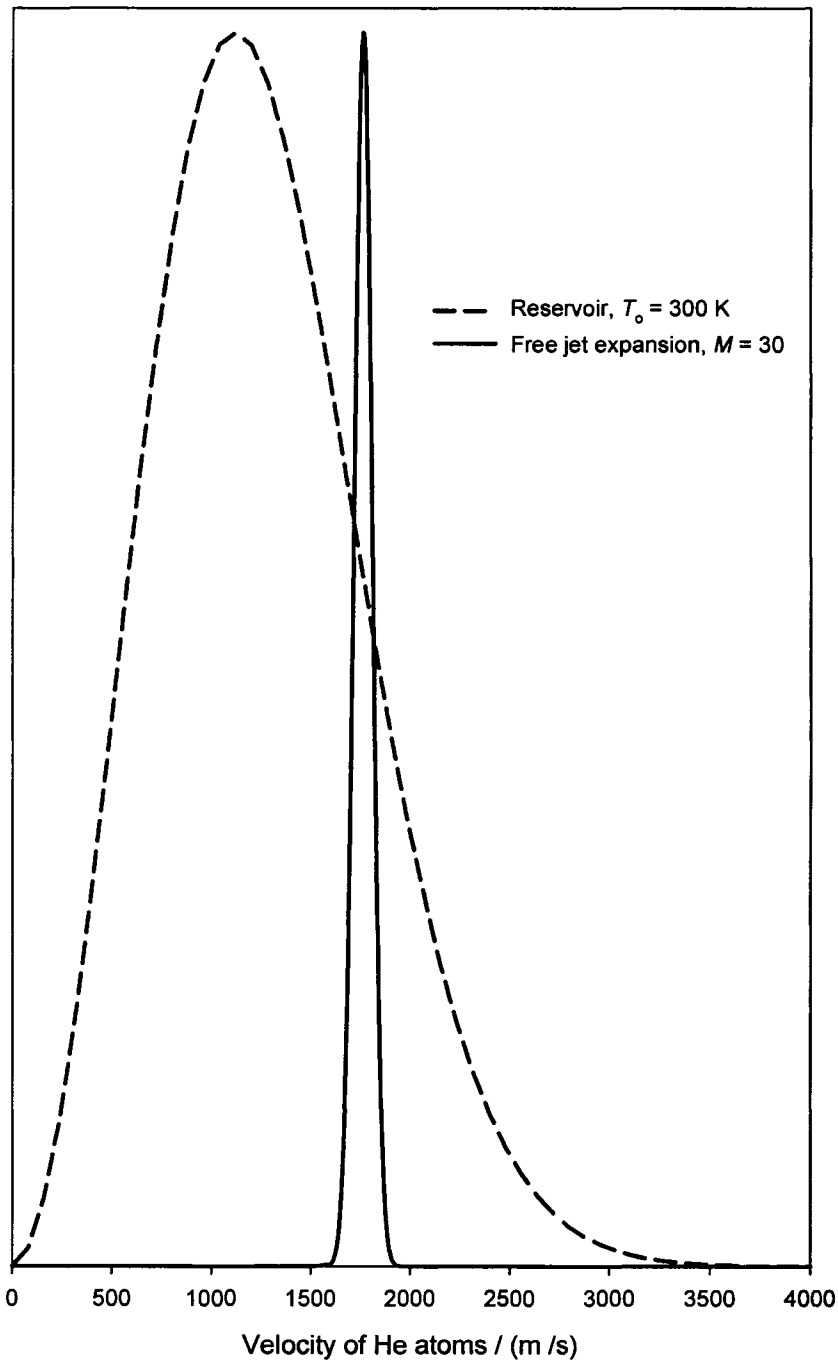

Figure 2.1 The velocity distribution of He atoms from a reservoir at $T_0 = 300$ K and in a supersonic expansion with $M = 30$. The curves are normalized to unity at the most probable velocity.

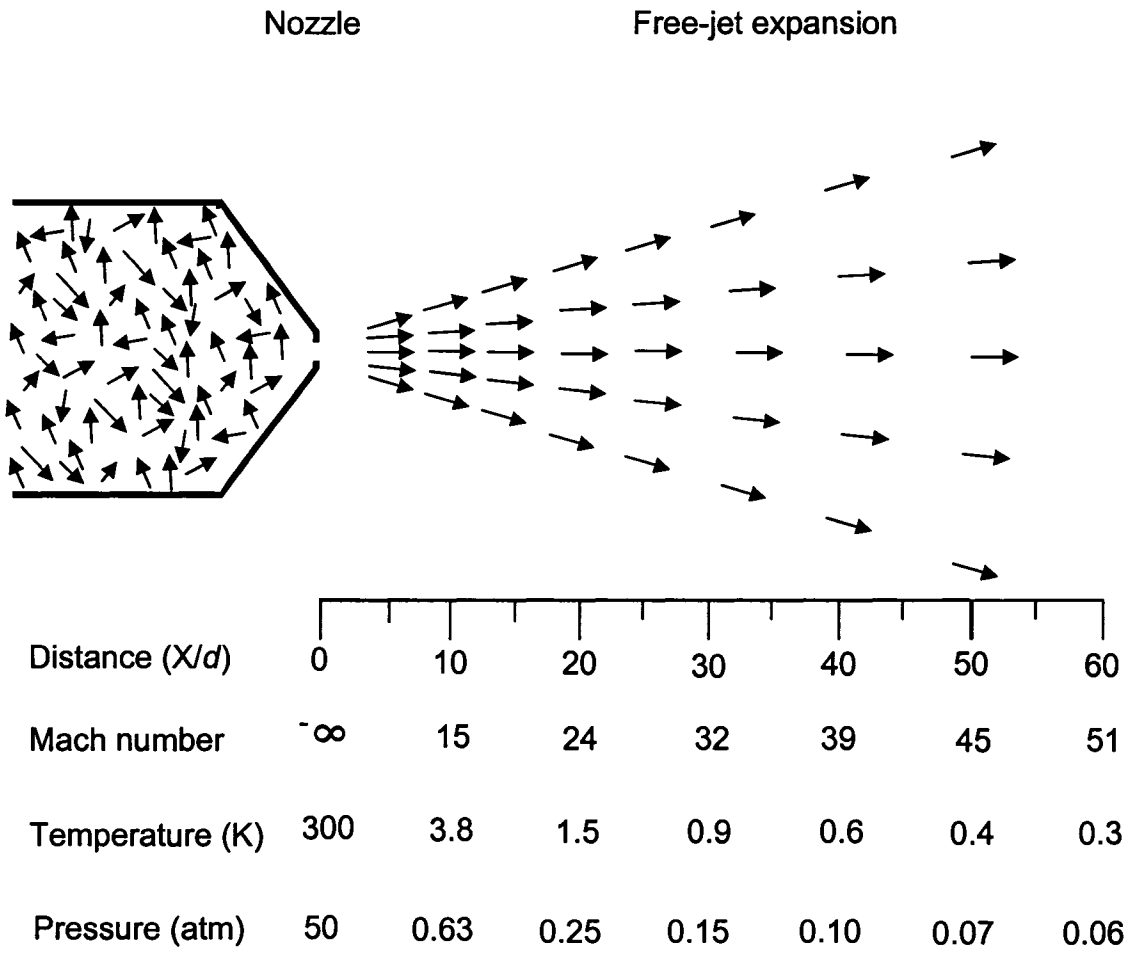

Figure 2.2 A schematic diagram of a free-jet expansion of He atoms. The velocities of the atoms are represented by the arrows. Shown below the nozzle is a scale of the distance from the nozzle X/*d* in units of the nozzle diameter *d*. For an expansion from a reservoir at T_0 = 300 K and P_0 = 50 atm, Mach numbers, temperature and the pressure of the expanding gas are given for various distances from the nozzle.

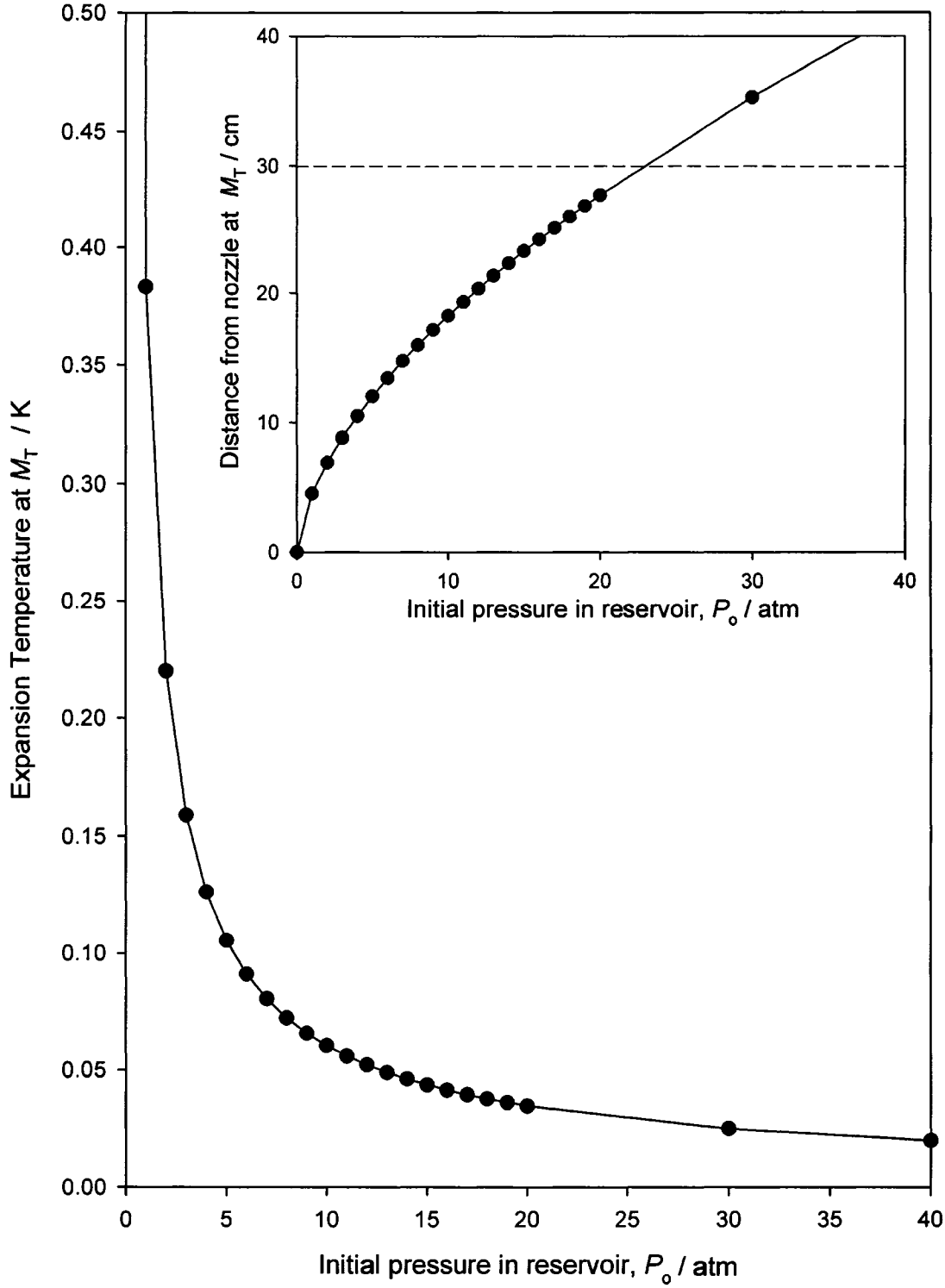

Figure 2.3 He expansion temperature at M_T versus reservoir pressure P_o, using a hard-sphere model. The distance from the nozzle when M_T is reached is inset. The dashed line at 30 cm marks the normal operating length of our microwave cavity.

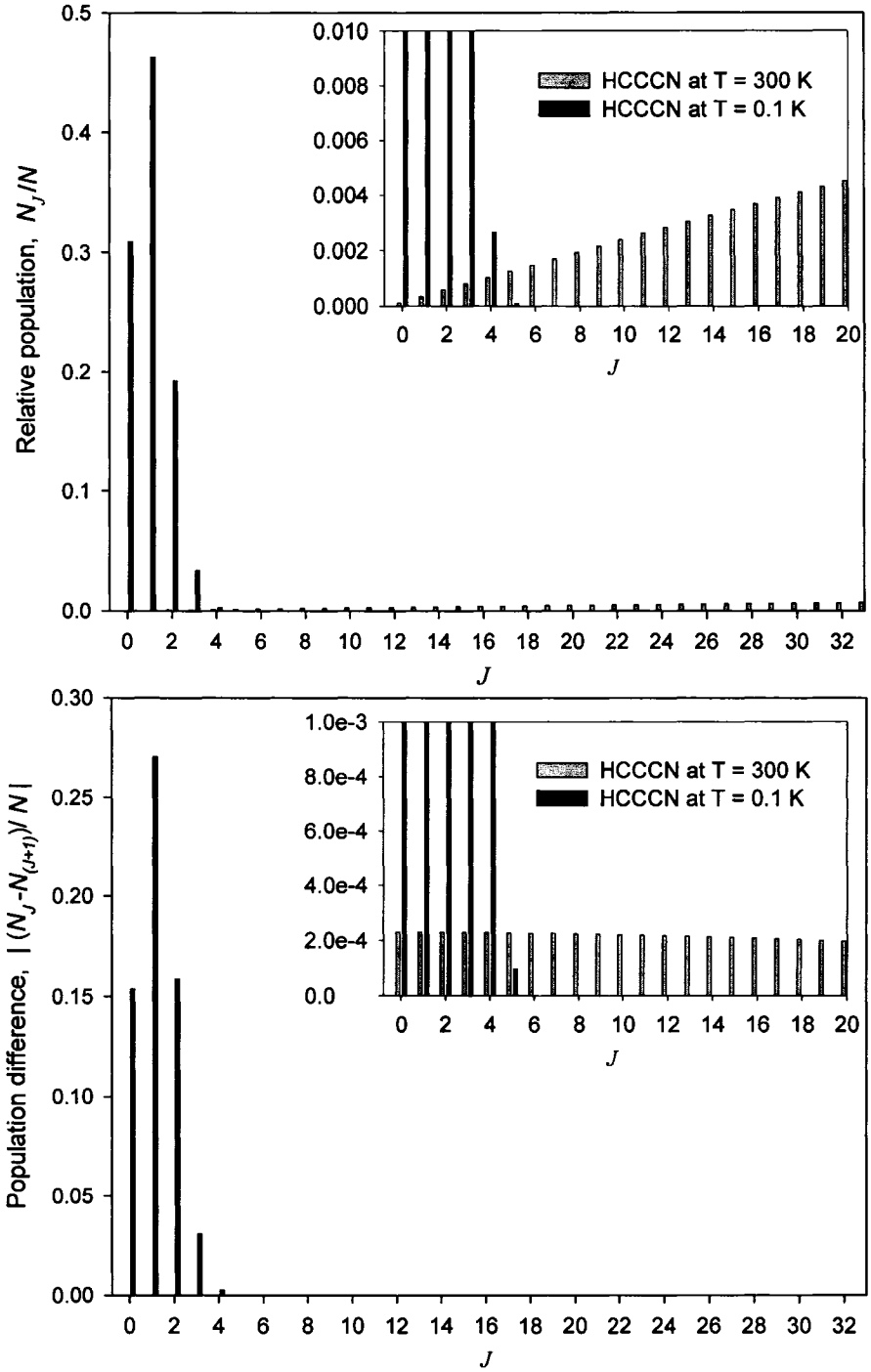

Figure 2.4 Normalized population information for rotational energy levels $J = 0$ to 33, at a rotational temperature of 300 K and 0.1 K. The upper plot shows the population of the rotational energy levels of HCCCN, normalized so that $\sum_J N_J = 1$. The lower plot shows the magnitude of the difference in population between J and J+1. A plot of $J = 0$ to 20, with the dependent axis enlarged, is inset in both the upper and lower plots to show the values for HCCCN at 300 K.

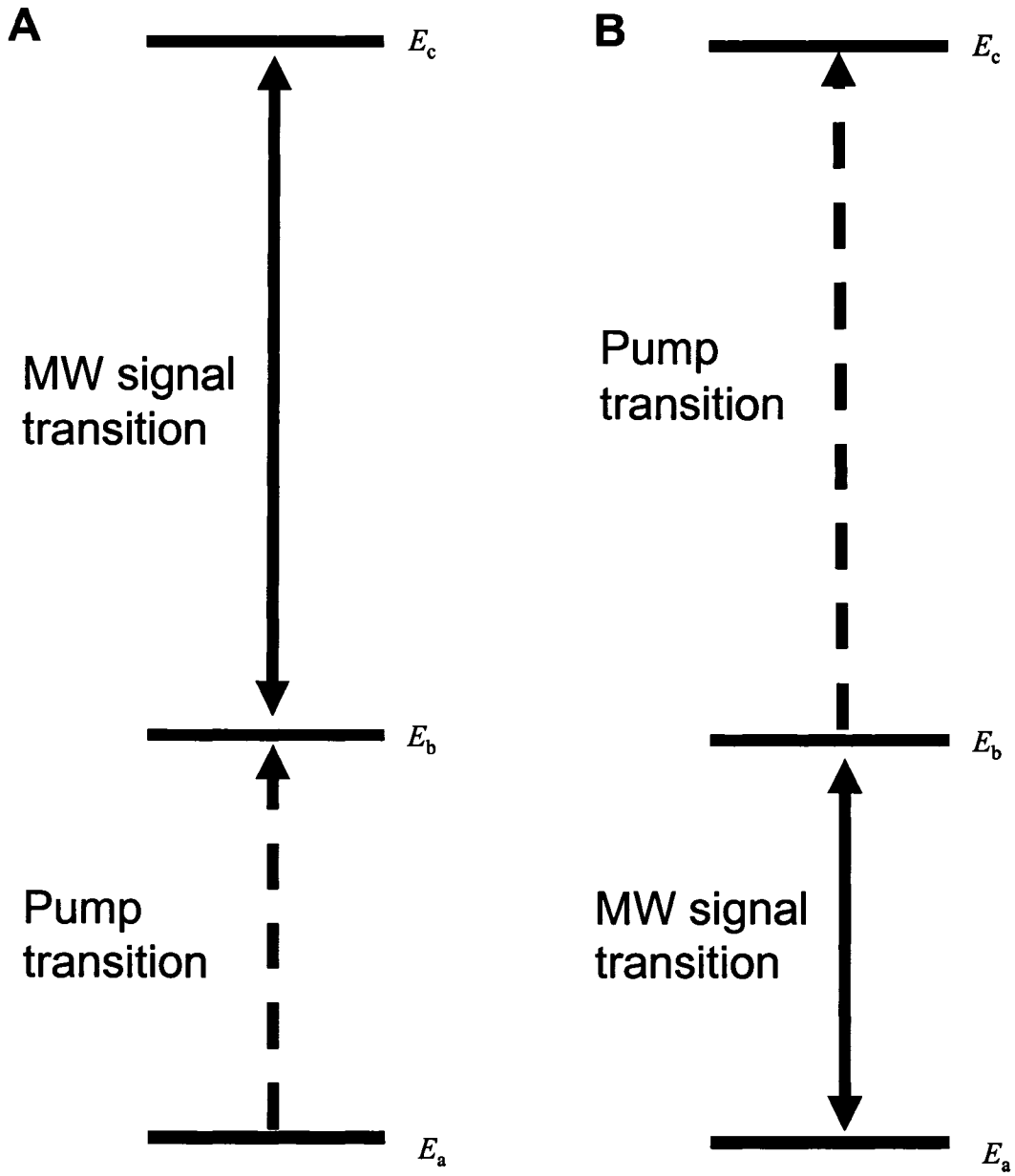

Figure 2.5 Illustration of the MW-MW double resonance (DR) schemes used in this work. (**A**) a constructive pumping scheme where the signal intensity of the observed transition of frequency $(E_c\text{-}E_b)/\hbar$ is increased by pumping population from E_a to E_b. (**B**) a destructive pumping scheme whereby the coherent emission signal with frequency $(E_b\text{-}E_a)/\hbar$ is destroyed by broadcasted radiation with frequency $(E_c\text{-}E_b)/\hbar$.

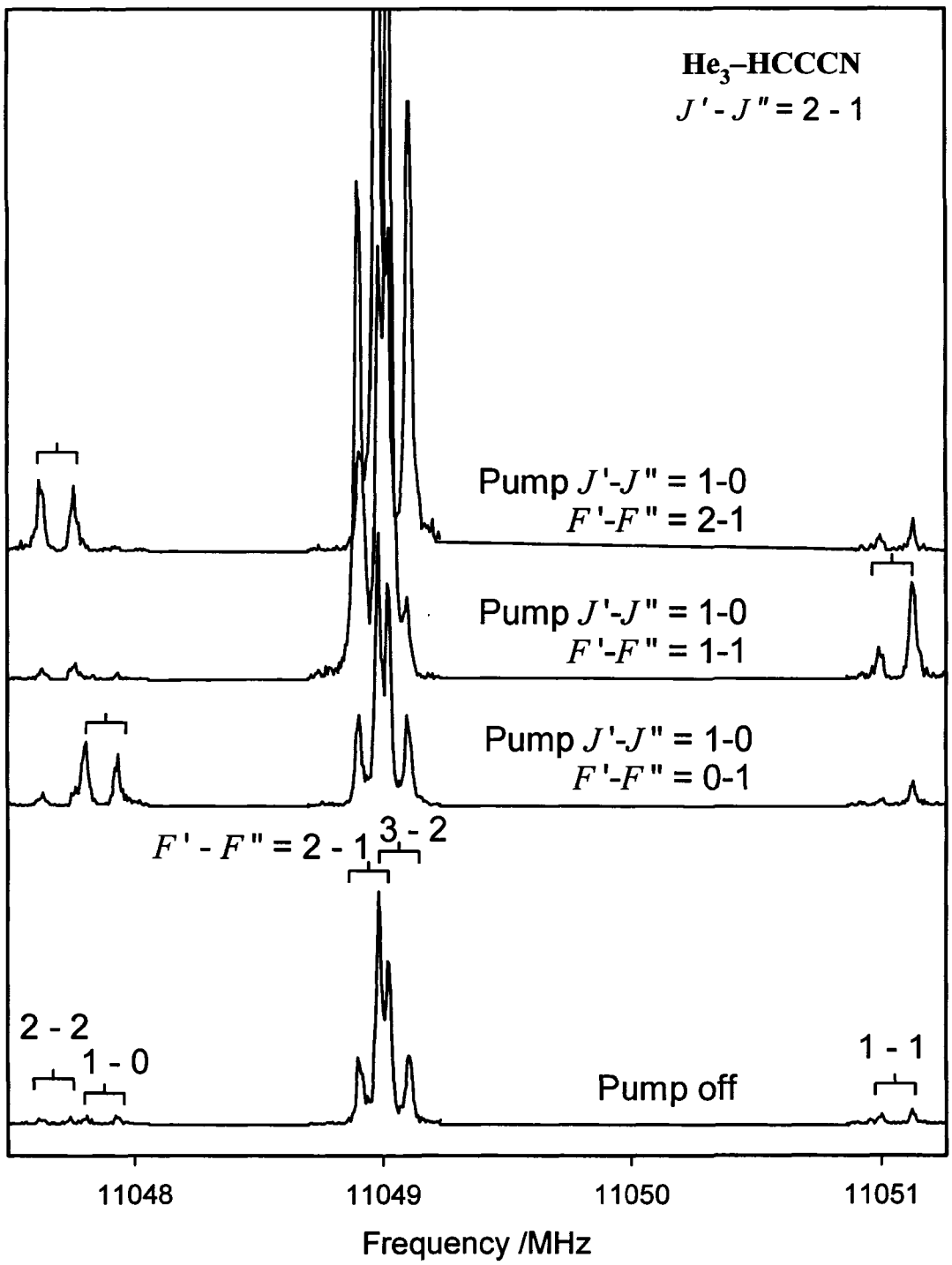

Figure 2.6 A representative spectrum showing the effect of constructive MW-MW DR experiments. The nuclear quadrupole hyperfine components of the He_3–HCCCN $J = 1\text{-}0$ rotational transition were pumped, leading to corresponding increases in the $J = 2\text{-}1$ rotational signal.

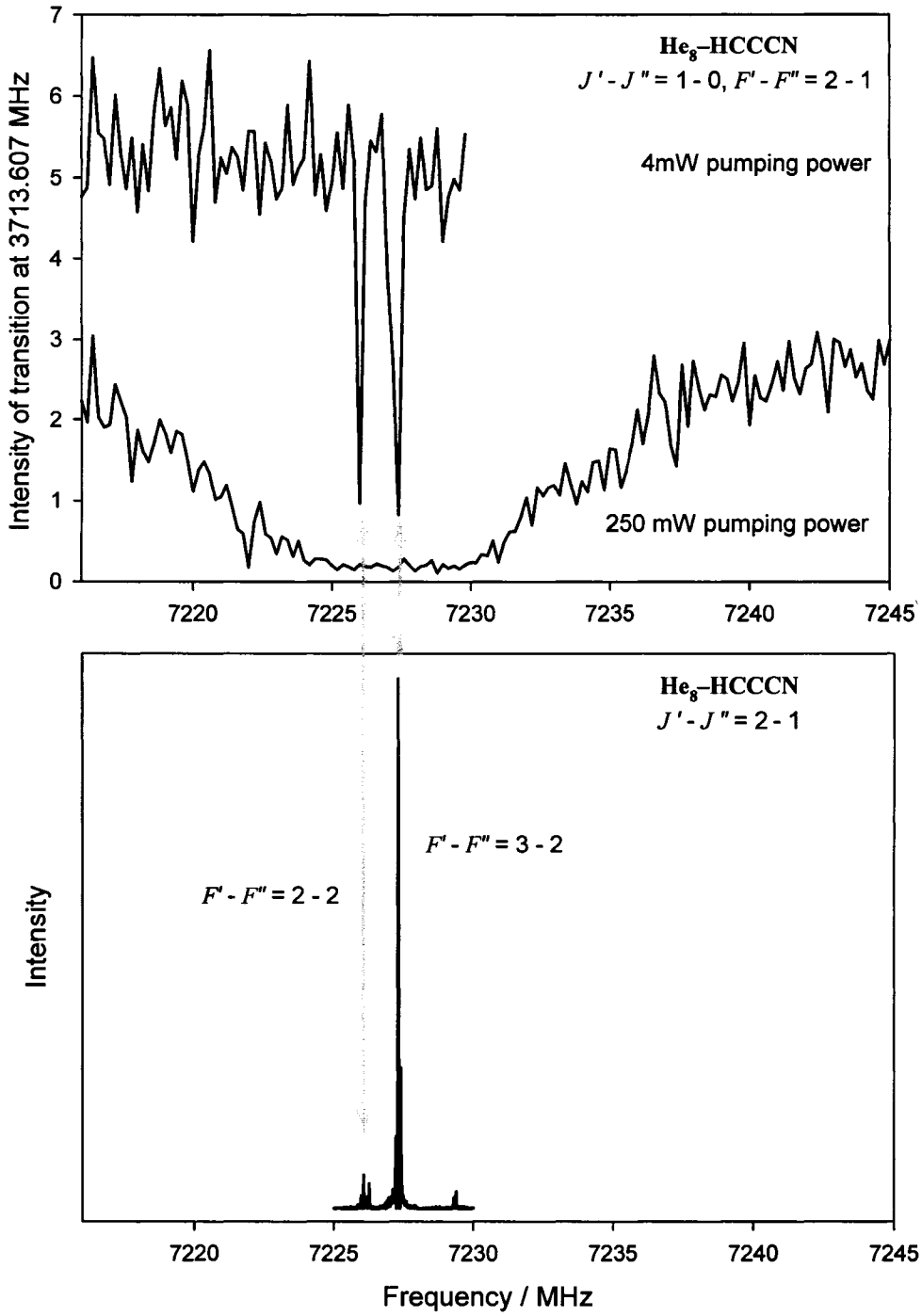

Figure 2.7 A representative spectrum showing the effect of destructive MW-MW DR experiments. The emission signal of the $F = 2\text{-}1$ nuclear quadrupole hyperfine component of the He_8–HCCCN $J = 1\text{-}0$ rotational transition was destroyed when the frequencies of the $F = 2\text{-}2$ and $3\text{-}2$ components of the $J = 2\text{-}1$ transition were pumped with 4 mW power. With higher pumping power the monitored emission signal was reduced for all pumped frequencies, and destroyed over the entire range of the $J = 2\text{-}1$ transition.

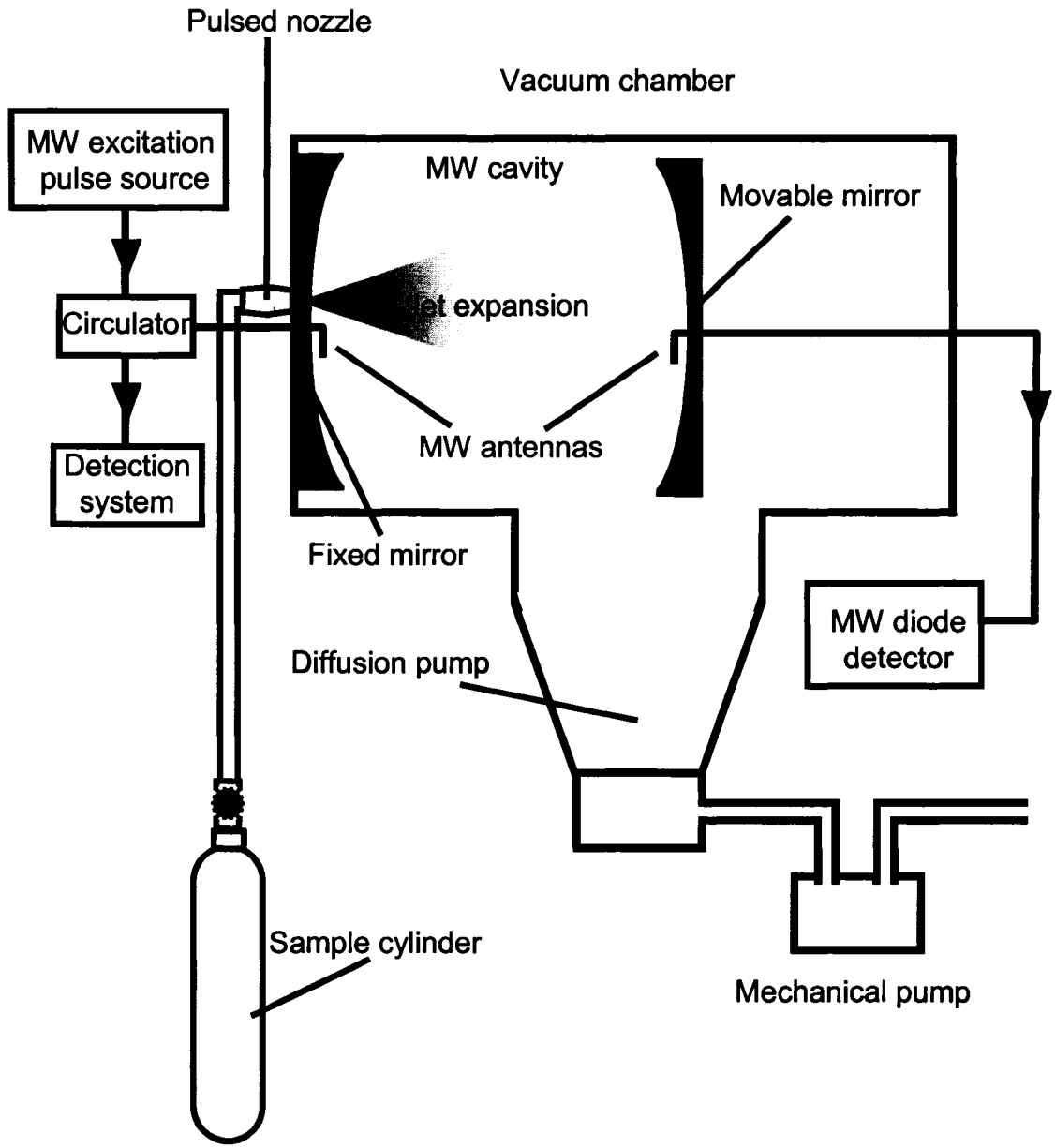

Figure 2.8 A simplified illustration of the mechanical setup of the FTMW spectrometer.

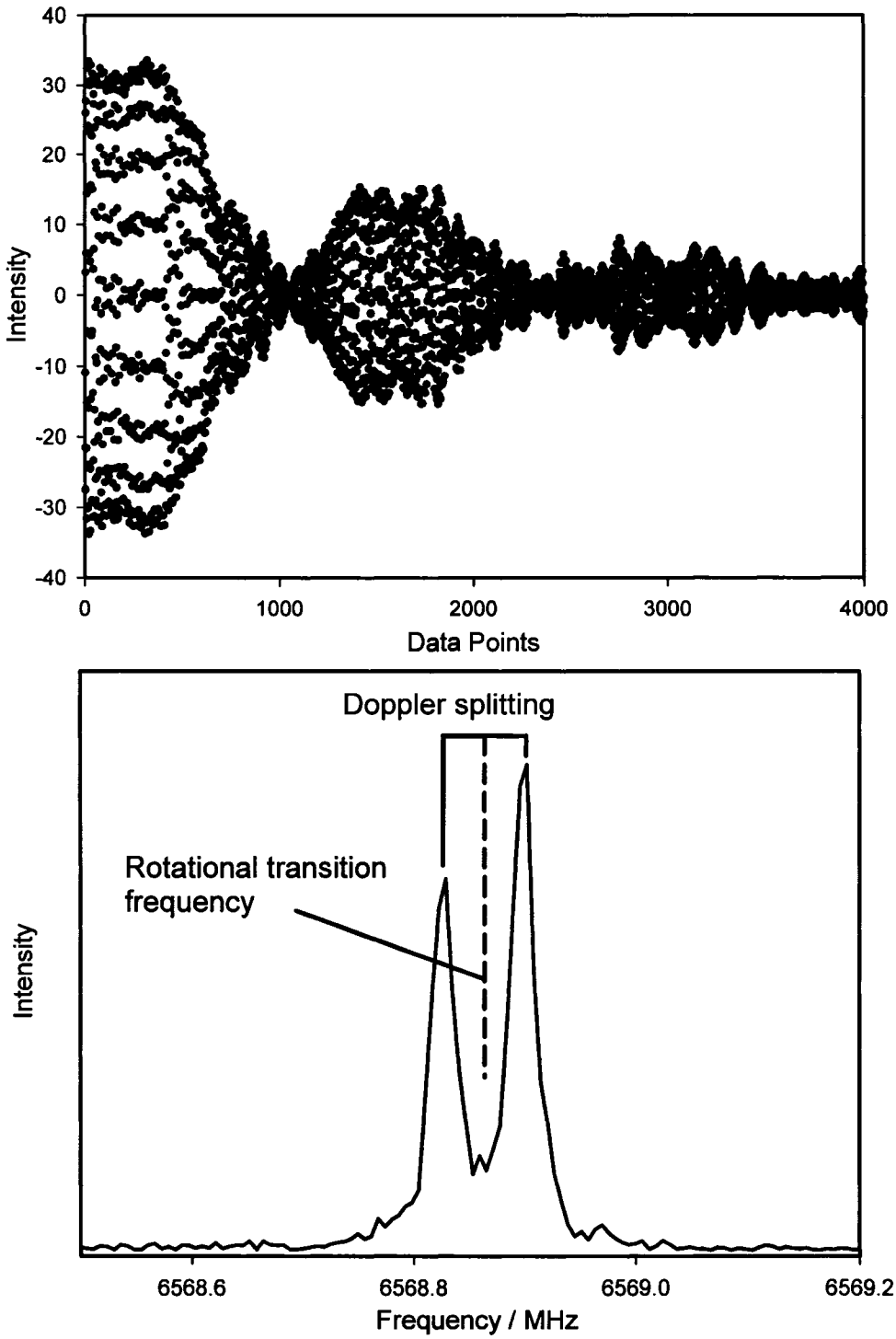

Figure 2.9 The digitized molecular emission signal and Fourier transformed frequency spectrum of the $J = 2\text{-}1$ rotational transition of He_9–$HCCC^{15}N$. The signal was recorded using a 10 ns sampling rate and was averaged for 100 cycles.

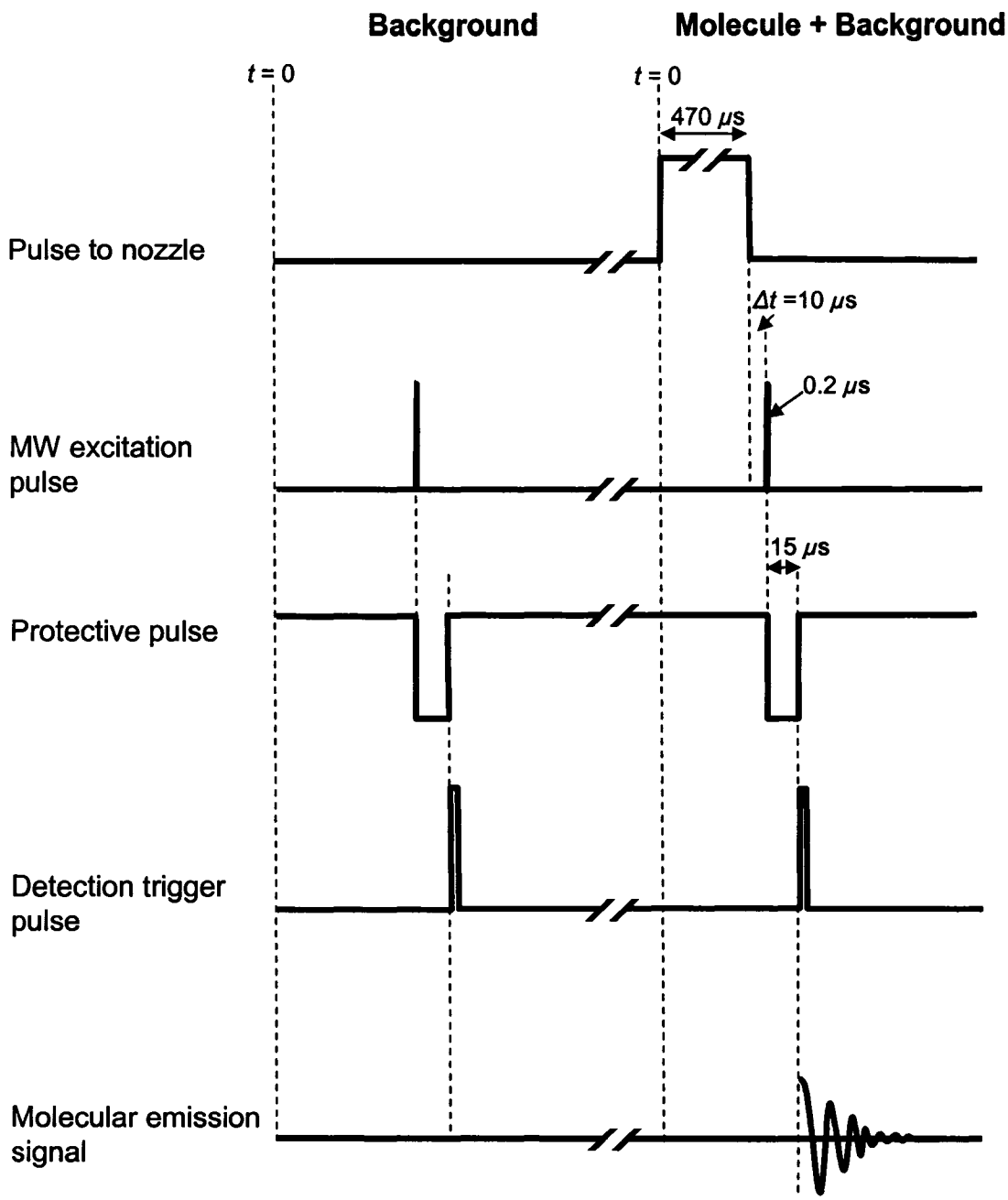

Figure 2.10 The timing sequence used to record the molecular emission signal of He_N–cyanoacetylene clusters. The molecular emission signal is obtained by subtracting the background signal from the (molecule + background) signal.

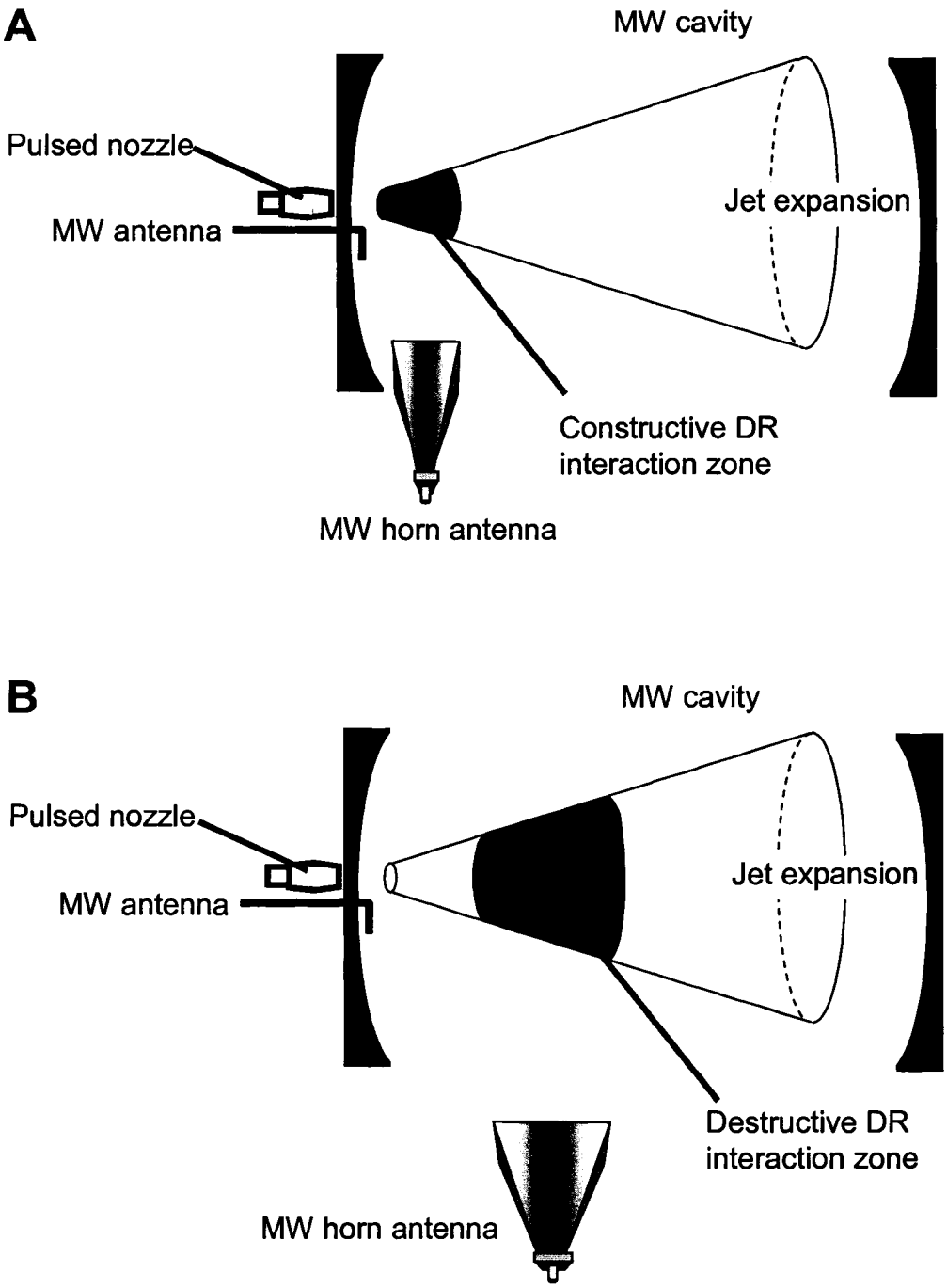

Figure 2.11 A schematic diagram illustrating the interaction zones between molecules in the free-jet expansion and broadcasted MW-MW double resonance (DR) radiation. In setup **A**, the horn is placed inside the vacuum chamber, as near as possible to the nozzle. In setup **B**, the horn is located outside the vacuum chamber, near the middle of the expansion. The horn is rotated 90° in setup **A** compared to **B**.

2.5 References

1. C. Moreau and C. J. Bongrand, Ann. Chim. **14**, 47 (1920).

2. F. A. Miller and D. H. Lemmon, Spectrochim. Acta **23A**, 1415 (1967).

3. P. D. Mallinson and A. Fayt, Mol. Phys. **32**, 473 (1976).

4. A. C. Legon, Ann. Rev. Phys. Chem. **34**, 275 (1983).

5. R. E. Smalley, L. Wharton, and D. H. Levy, Acc. Chem. Res. **10**, 139 (1977).

6. D. H. Levy, Ann. Phys. Chem. **31**, 197 (1980).

7. T. A. Miller, Science **223**, 545 (1984).

8. J. P. Toennies and K. Winkelmann, J. Chem. Phys. **66**, 3965 (1977).

9. B. B. Hamel and D. R. Wills, Phys. Fluids **5**, 829 (1966).

10. C. E. Klots, J. Chem. Phys. **72**, 192 (1980).

11. D. R. Miller, in *Atomic and Molecular Beam Methods, Vol 1*, edited by G. Scoles (Oxford University Press, Oxford 1988).

12. H. W. Liepmann and A. Roshko, *Elements of Gas Dynamics* (Wiley, New York 1957).

13. J. B. Anderson and J. B. Fenn, Phys. Fluids **8**, 780 (1965).

14. D. R. Miller, J. P. Toennies, and K. Winkelmann, *9th Symposium on Rarefied Gas Dynamics Vol 2*, edited by M. Becker and M. Feibig (DFVLR Press 1974) C 9-1.

15. A. Amirav, U. Even, and J. Jortner, Chem. Phys. **51**, 31 (1980).

16. R. P. Mariela, S. K. Neoh, and D. R. Hersbach, J. Chem. Phys. **67**, 2981 (1977).

17. R. L. DeLeon and J. S. Muenter, Chem. Phys. Lett. **111**, 147 (1984).

18. S. M. Beck, M. G. Livermann, D. L. Monts, and R. F. Smalley, J. Chem. Phys. **70**, 232 (1979).

19. S. Thorwirth, H. S. P. Müller, and G. Winnewisser, J. Mol. Spec. **204**, 133 (2000).

20. T. J. Balle and W.H. Flygare, Rev. Sci. Instrum. **52**, 33 (1981).

21. J. Braun, P. K. Day, J. P. Toennies, G. Witte, and E. Neher, Rev. Sci. Instrum.**68**, 3001 (1997).

22. A. E. Castleman Jr. and R. G. Keese, Science **241**, 36 (1988).

23. J. Tang and A. R. W. McKellar, J. Chem. Phys. **119**, 5467 (2003).

24. J. Ekkers and W. H. Flygare, Rev. Sci. Instrum. **47**, 448 (1976).

25. W. H. Flygare, *Pulsed Fourier Transform Microwave Spectroscopy* in *Fourier, Hadamard, and Hilbert Transforms in Chemistry*, edited by A. G. H. Marshall (Plenum Press, New York 1982) pp 207-270.

26. H. Dreizler, Ber. Bunsenges. Phys. Chem. **99**, 1451 (1995).

27. H. Dreizler, Mol. Phys. **59**, 1 (1986).

28. C. H. Townes and A. L. Schawlow, *Microwave Spectroscopy*, (Dover Publications, New York 1975) pp 21-24.

29. U. Wotzel, W. Stahl, and H. Mäder, Can. J. Phys. **75**, 821 (1997).

30. Y. Xu and W. Jäger, J. Chem. Phys. **106**, 7968 (1997).

31. V. N. Markov, Y. Xu, and W. Jäger, Rev. Sci. Instrum. **69**, 4061 (1998).

32. J.-U. Grabow and W. Stahl, Z. Naturforsch. Teil. A **45**, 1043 (1990).

33. K. Brendel and H. Mäder, private communication.

3

The weakly bound He–cyanoacetylene dimer: high-resolution microwave spectra

This chapter details the first microwave rotational spectroscopic study of He–cyanoacetylene. Section 3.1 gives the experimental details for the spectroscopic study of the He–cyanoacetylene dimer. Results of the rotational investigation of He–HCCCN, He–DCCCN, and He–HCCC^{15}N, are discussed in section 3.2. Transitions corresponding to less abundant ^{13}C-containing isotopomers are also reported. Section 3.3 contains an analysis of the spectroscopic observations made for the He–cyanoacetylene van der Waals dimer.

3.1 Experimental details

He–cyanoacetylene dimers were generated using a pulsed supersonic expansion

through a General Valve nozzle with a cone shaped exit (series 9, orifice Ø = 0.8 mm). The sample mixtures were composed of low concentrations of cyanoacetylene, typically 0.5 to 2%, in He at backing pressures between 6 and 10 atm. Studies of the ^{13}C-containing isotopes were conducted using ~0.2% cyanoacetylene in He at 30 atm of backing pressure. The pure rotational transitions of the He–cyanoacetylene complexes were measured with a Balle-Flygare type Fourier transform microwave spectrometer.[1] Constructive microwave-microwave double resonance experiments[2] were used to enhance the signal intensity of weaker transitions and to confirm the quantum number assignments, as described in Section 2.3. These experiments were employed to observe weak hyperfine structure components for some $J = 3$-2 transitions. This technique was also used to confirm the presence of shared energy levels for sequential transitions.

3.2 Experimental results and spectroscopic analysis

Cyanoacetylene has a relatively large dipole moment, $\mu = 3.73$ D,[3] compared to other linear molecules of similar molecular mass ($\mu_{(NNO)} = 0.16$ D,[4] $\mu_{(OCS)} = 0.72$ D,[5] $\mu_{(HCN)} = 2.99$ D[6]). The He–cyanoacetylene van der Waals dimer has a T-shaped geometry and therefore has a rotational spectrum that is characteristically that of an asymmetric top. Figure 3.1 shows the He–HCCCN van der Waals dimer in its principal inertial axis system along with the structural parameters used to describe the complex. A large component of the cyanoacetylene dipole moment projects along the a-axis in the principal inertial axis system. A smaller projection of the dipole moment falls along the b-axis. I was able to

measure intense rotational transition frequencies that correspond to end-over-end, or *a*-type rotational transitions, where the transition dipole moment falls along the *a*-axis. The smaller dipole along the *b*-axis allowed me to measure weaker *b*-type rotational transitions.

The spectroscopic parameters of each isotopomer were fit to the measured transition frequencies with Pickett's least squares fitting program SPFIT,[7] using Watson's *A*-reduced Hamiltonian for a near-prolate asymmetric top of the form:[8]

$$H = \tfrac{1}{2}(B+C)J^2 + [A - \tfrac{1}{2}(B+C)]J_a^2 + \tfrac{1}{2}(B-C)(J_b^2 - J_c^2) - \Delta_J J^4 - \Delta_{JK} J_a^2 J^2 - \Delta_K J_a^4 - \delta_J J^2(J_b^2 - J_c^2) - \delta_K[J_a^2(J_b^2 - J_c^2) + (J_b^2 - J_c^2)J_a^2] \quad (3\text{-}1)$$

Rotational transitions of each isotopomer of He–cyanoacetylene were fit separately.

Details about the rotational transitions of the three main isotopomers, He–HCCC^{15}N, He–HCCCN, and He–DCCCN, are given in the following pages. Rotational transitions corresponding to several different ^{13}C containing isotopomers were observed, and these are discussed in Section 4.1 *d*.

a) He–HCCC^{15}N dimer

The rotational spectrum of He–HCCC^{15}N is the simplest of the three main He–cyanoacetylene isotopomers studied. None of the nuclei in this dimer has a spin greater than $I = ½$. The rotational transitions of He–HCCC^{15}N display only Doppler splitting (due to the coaxial propagation of the beam expansion with the microwave radiation). The *a*-type $J_{KaKc}' - J_{KaKc}'' = 1_{01}-0_{00}$ transition is shown in Figure 3.2.

For He–HCCC^{15}N, ten rotational transitions were detected and studied. I measured seven *a*-type and three *b*-type transitions which are reported in Table 3.1. Figure 3.3 is an energy level diagram showing the rotational energy levels of He–HCCC^{15}N, with arrows indicating the measured transitions. The vertical arrows correspond to *a*-type transitions ($\Delta K_a = 0$, $\Delta K_c = \pm 1$), while the diagonal arrows between *K*-stacks are *b*-type transitions ($\Delta K_a = \pm 1$, $\Delta K_c = \pm 1$). The detection of both *a*- and *b*-type transitions made it possible to fully characterize the rotational energy levels of the He-cyanoacetylene dimer. There is no projection of the permanent dipole moment along the *c*-axis in the principal inertial frame, thus *c*-type transitions ($\Delta K_a = \pm 1$, $\Delta K_c = 0$) are not allowed for this planar complex.

Assignment of the measured frequencies to transitions between particular rotational energy levels of He–HCCC^{15}N was accomplished by a variety of methods. Firstly, very good predictions for this complex were obtained prior to commencing the spectral search. Frequencies of the allowed rotational energy transitions were predicted from calculated *ab initio* potential energy surfaces. These surfaces, discussed in detail in the following chapter, were scaled in a manner that gave the best fit to the rotational transitions of both He–HCCCN and He–DCCCN. This significantly reduced the frequency range scanned during spectral searches, and gave a starting point for spectral assignment. The assignment was substantiated by the presence of a closed loop among the studied transitions. This means that the frequencies of $J_{KaKc} = (1_{01}\text{-}0_{00}) + (2_{02}\text{-}1_{01}) - (1_{11}\text{-}0_{00})$ gives exactly the frequency of $J_{KaKc} = 2_{02}\text{-}1_{11}$, thus confirming that these transitions are correctly assigned. Further confirmation of the quantum number

assignment was achieved using microwave-microwave double resonance experiments to corroborate the presence of shared rotational energy levels between two observed transitions. Measured rotational transition frequencies were fit to a distortable rotor model, and the resulting rotational parameters are presented in Table 3.2.

b) He–HCCCN dimer

On the scale of the diagram, the relative position of the rotational energy levels of He–HCCCN does not differ noticeably from those depicted in Figure 3.3 for He–HCCC^{15}N. The presence of a ^{14}N nucleus (I = 1) in the dimer, however, does result in a more complex observable spectrum. The angular momentum of a quadrupolar nucleus couples with the rotational angular momentum of the rotor. The resulting total angular momentum, $\boldsymbol{F}$, can be expressed as the vector summation of the rotational angular moment, $\boldsymbol{J}$, and the spin of the quadrupolar nucleus, $\boldsymbol{I}$. Consequently, each observed rotational transition of He–HCCCN displays a unique signature of ^{14}N nuclear quadrupolar hyperfine structures.

In total, twelve rotational transitions were observed within the K_a = 0, ±1 stacks: seven strong *a*-type transitions and five much weaker *b*-type transitions. Figures 3.4 and 3.5 are composite spectra for the *a*- and *b*-type J'-J'' = 1-0 transition of He–HCCCN, respectively. Among the measured transitions, three closed loops can be formed, supporting the quantum number assignments. Along with the distinctive nuclear quadrupole hyperfine structures observed, this helped confirm the quantum number assignments. Constructive microwave-microwave double resonance experiments were

performed both to confirm the assignment, and to allow the detection of weak transitions.

Comparing the spectra in Figures 3.4 and 3.5, the relative intensities (given by the number of cycles required to obtain the shown signal to noise ratios) of the *a*- and *b*-type transitions are indicative of a much larger projection of the HCCCN dipole moment along the *a*-axis of the complex. The pure rotational transition frequencies of the He–HCCCN van der Waals dimers are reported in Table 3.3. The nuclear quadrupole hyperfine structures were fit using the $\boldsymbol{J} + \boldsymbol{I}_{^{14}N} = \boldsymbol{F}$ coupling scheme for He–HCCCN. The root mean square (rms) error is 3.4 kHz for the 56 frequencies fit; the resulting spectroscopic parameters are given in Table 3.2.

c) He–DCCCN dimer

Rotational transitions of the He–DCCCN dimer are further complicated by an additional quadrupolar nucleus, compared to He–HCCCN. Here, the hyperfine structures due to ^{14}N ($I = 1$) are split again by the additional angular momentum of the D nucleus ($I = 1$). For example, the J_{KaKc}'-J_{KaKc}'' = 1_{01}-0_{00} transition, shown in Figure 3.6, is split into three main components by the ^{14}N nucleus. The spin of the D nucleus causes splitting of much smaller magnitude. Much of the deuterium hyperfine structure in nine rotational transitions was resolved; the corresponding frequencies are reported in Table 3.4. The spectroscopic parameters were determined as described above, using the $\boldsymbol{J} + \boldsymbol{I}_{^{14}N} = \boldsymbol{F}_1$, $I_D + \boldsymbol{F}_1 = \boldsymbol{F}_2$ coupling scheme, and are given in Table 3.2. Overall, the observed transition intensities are lower in the deuterated species compared to the main isotopomer. This can be attributed to the increased splitting of the rotational transitions

by the additional quadrupolar nucleus. Also, the relative intensities of the hyperfine structure components are affected by the additional splitting, as can be seen by comparing Figures 3.4 and 3.6.

d) Various ^{13}C containing isotopomers

Our instrument is sensitive enough to detect the $J_{KaKc} = 1_{01}$-0_{00} transition of ^{13}C containing isotopomers in natural abundance (1.11%). For He–H^{13}CCCN, He–HC^{13}CCN, and He–HCC^{13}CN, both the measured $J_{KaKc} = 1_{01}$-0_{00} transition frequencies and the fitted ^{14}N nuclear quadrupole hyperfine coupling constant are given in Table 3.5. Composite spectra of the $J_{KaKc} = 1_{01}$-0_{00} transition of He–HC^{13}CCN and He–HCC^{13}CN are presented in Figure 3.7. These two isotopomers have only a small difference in their moments of inertia, since the ^{13}C atom in both species lie very near to the centre of mass of the He-cyanoacetylene dimer. During searches for the He–HCCC^{15}N dimer, the $J_{KaKc} = 1_{01}$-0_{00} transitions for He–H^{13}CCC^{15}N, He–HC^{13}CC^{15}N, and He–HCC^{13}C^{15}N were observed. In addition to the already low natural abundance of ^{13}C, the probability of observing these complexes was further reduced by the presence of only 10% ^{15}N in our enriched cyanoacetylene mixture. The transition frequencies of the doubly substituted dimers are also given in Table 3.5.

3.3 Analysis of the rotational spectroscopic parameters of He–cyanoacetylene

The floppy nature of the He–HCCCN van der Waals complex is evident given that six distortion constants were required to fit the observed transitions of the normal isotopomer. A good indication of the magnitude of the large amplitude zero-point vibrational motions is given by the inertial defect, $\Delta = I_C - I_B - I_A$. In the case of a perfectly rigid, planar rotor $\Delta = 0$. For the He–HCCCN complex, $\Delta = 14.41$ amu Å^2. In the heavier rare-gas analogs Ar–HCCCN and Ne–HCCCN, $\Delta = 3.66$ amu Å^2,[9] and $\Delta = 5.62$ amu Å^2,[10] respectively. Rare-gas ball-stick systems show increasing inertial defect as the mass of the rare-gas atom decreases. The rare gas–OCS series of Ar–, Ne– , and He–OCS also shows increasing inertial defect, with $\Delta = 2.83$ amu Å^2,[11] $\Delta = 4.37$ amu Å^2, [11] and $\Delta = 7.95$ amu Å^2,[12] respectively. He atom containing complexes exist at the extreme of weakly bound systems and so are expected to be highly non-rigid. The He–HCCCN complex is even less rigid than the comparable He–OCS dimer.

The intermolecular potential energy surface of the interaction between a He atom and cyanoacetylene is the most accurate description of this weakly bound dimer. Various computational methods have been developed to capture interaction potential energy surfaces of van der Waals dimers, and *ab initio* potential energy surfaces are discussed in the following chapter. Despite the magnitude of the zero-point motions, however, fitting the rotational transitions of He–cyanoacetylene to a semi-rigid rotor model can provide useful information about the effective structure and dynamics of the dimer. An effective

structure of the He–cyanoacetylene van der Waals dimer was determined using Kisiel's STR*ucture* FIT*ting to rotational data* program.[13] The position of the He atom within the dimer was fitted using the A, B, and C rotational constants of the HCCC^{15}N, HCCCN and DCCCN containing dimers, and B+C of the measured ^{13}C-containing cyanoacetylene isotopomers. With bond lengths of the cyanoacetylene molecule frozen at ground vibrational state values reported by Tyler and Sheridan,[14] an average position of the He atom was determined to be R = 3.93 ± 0.05 Å and θ = 80.1° ± 1.3°, using rotational parameters of all nine He–cyanoacetylene isotopomers observed. He–OCS was determined to have a T-shaped ground state geometry, with a van der Waals bond length of 3.93 Å from the OCS centre of mass, at an angle of 109.7° from the sulfur-end of the molecule. The van der Waals bond length of the more tightly bound He–NNO dimer was determined to be 3.3915 Å.[15] In the case of the He–NNO dimer it was not possible to determine the van der Waals angle experimentally.

We can use the ^{14}N quadrupole coupling constants (see Table 3.2) to determine an average orientation of the HCCCN monomer respect to the principal inertial axis system of the complex. Assuming that the electric field gradients of the free HCCCN or DCCCN molecules are unchanged upon the formation of the van der Waals bond, we can determine an average angle θ_a between the molecular axis and the a-axis:

$$\chi_{aa} = \frac{1}{2}\chi_0 < 3\cos^2\theta_a - 1 > \qquad (3\text{-}2)$$

and

$$\chi_{bb} = \frac{1}{2}\chi_0 < 3\ \sin^2\theta_a - 1 >, \qquad (3\text{-}3)$$

The ^{14}N coupling constant of isolated HCCCN, χ_0, is -4.31924 (1) MHz.[3] For free DCCCN, $\chi_0(^{14}N)$ = -4.316 (3) MHz.[16] For He–HCCCN , the θ_a values obtained from these two relations are θ_a = 6.3° and 6.6°, respectively. For He–DCCCN, θ_a = 5.8° and 5.1°. The difference between the values of θ_a obtained using χ_{aa} and χ_{bb} are due in part to the floppiness of the complex, but also to the uncertainty in determining the coupling constants of the van der Waals dimers. The high relative uncertainty in both χ_{aa} (D) and χ_{bb} (D) obtained using the D hyperfine structures makes this nucleus a poor choice for determining θ_a (θ_a = 13.8° and 1.7° from χ_{aa} and χ_{bb}, respectively).

The assumption of unchanged field gradient at the site of the ^{14}N nucleus upon complex formation can be verified by comparing the χ_{cc} coupling constants with χ_0 of the free monomer. For a rigid, planar complex, $-2\chi_{cc} = \chi_0$. From the spectroscopic parameters used to fit the rotational transitions of He–HCCCN (see Table 3.2), $-2\chi_{cc}$ for the ^{14}N nucleus is -4.3324 (6) MHz, while χ_0 is -4.31924 (1) MHz (Ref. 3). The small discrepancy can be attributed to the large amplitude motions, similar to the effect seen in the Ar-N_2 complex.[17] Likewise the transitions of He–DCCCN were fit such that $-2\chi_{cc}$ for the ^{14}N and D nuclei are -4.350 (2) MHz and 0.188 (4) MHz (see Table 3.2), while χ_0 for these nuclei are -4.316 (3) MHz and 0.2288 (55) MHz (Ref. 16), respectively. The small difference between $-2\chi_{cc}$ and χ_0 of ^{14}N for both isotopomers confirm that the electric field gradient along the cyanoacetylene molecule is essentially unchanged by

complex formation. The larger difference between $-2\chi_{cc}$ and χ_0 for the D nucleus in DCCCN can be attributed to the larger relative uncertainty in the D nuclear quadrupole coupling constants.

3.4 Summary

The He–cyanoacetylene van der Waals dimer was investigated by pure rotational spectroscopy. Three isotopomers, He–HCCCN, He–DCCCN, and He–HCCC^{15}N, were studied in depth, with a minimum of nine transitions observed for each of these species in the microwave frequency region. Transitions were observed for six other ^{13}C containing isotopomers. Analysis of the observed rotational transitions are consistent with a T-shaped geometry for the He–cyanoacetylene van der Waals dimer. The spectroscopic transitions observed are those of a very flexible complex, as evidenced by the large number of distortion parameters required to fit the rotational transitions to the model of a distortable rotor. A fit of the determined rotational parameters to a structure geometry gives a van der Waals bond length of 3.93 ± 0.05 Å between the He atom and the cyanoacetylene centre of mass, at an angle of $80.1 \pm 1.3°$ from the N-end of the molecule. The large inertial defects determined for He–HCCCN, He–DCCCN, and He–HCCC^{15}N show that He–cyanoacetylene dimer undergoes large amplitude zero-point vibrational motions.

3.5 Tables

Table 3.1 Measured transition frequencies of He–HCCC^{15}N.

$J_{KaKc}' - J_{KaKc}''$	ν_{obs} (MHz)	$\Delta\nu^a$ (kHz)
$1_{10} - 1_{01}$	7324.3956	0.0
$1_{01} - 0_{00}$	7579.0819	0.9
$2_{02} - 1_{11}$	9131.6274	-0.9
$1_{11} - 0_{00}$	13333.6703	-0.9
$2_{12} - 1_{11}$	13525.5255	-0.0
$2_{02} - 1_{01}$	14886.2194	0.9
$2_{11} - 1_{10}$	16652.1052	0.0
$3_{13} - 2_{12}$	20154.2996	0.0
$3_{03} - 2_{02}$	21684.7757	0.0
$3_{12} - 2_{11}$	24803.1685	0.0

[a] $\Delta\nu = \nu_{obs} - \nu_{calc}$, where ν_{calc} is calculated using the fitted rotational parameters.

Table 3.2 Determined rotational parameters for the He–HCCC^{15}N, He–HCCCN, and He–DCCCN van der Waals dimers. All values are in MHz, unless specified otherwise.

	He–HCCC^{15}N	He–HCCCN	He–DCCCN
A	10486.6 (1)	10518.56 (4)	10456.4 (9)
B	4635.57 (5)	4773.10 (2)	4349.900 (3)
C	2946.39 (5)	3002.14 (2)	2910.329 (1)
Δ_J	0.707 (1)	0.8106 (4)	-0.5698 (5)
Δ_{JK}	12.814 (6)	12.841 (2)	19.275 (2)
Δ_K	132.0 (1)	135.67 (4)	64.43 (9)
δ_J	0.14648 (7)	0.1699 (3)	0.0504 (1)
δ_K	30.30 (2)	32.38 (1)	
ϕ_J	0.00591 (1)	0.007045 (4)	
χ_{aa} (^{14}N)	–	-4.2409 (6)	-4.250 (1)
χ_{bb} (^{14}N)	–	2.0747 (6)	2.075 (2)
χ_{aa} (D)	–	–	0.209 (3)
χ_{bb} (D)	–	–	-0.115 (4)
rms error[a]	0.57 kHz	3.43 kHz	5.30 kHz
Δ[b]	14.3 amu Å^2	14.4 amu Å^2	9.1 amu Å^2

[a] The root mean square (rms) error for the total fit, including the nuclear quadrupole hyperfine structure of the nine transitions observed.
[b] $\Delta = I_C - I_B - I_A$.

Table 3.3 Measured transition frequencies of He–HCCCN.

$J_{KaKc}' - J_{KaKc}''$	$F' - F''$	ν_{obs} (MHz)	$\Delta\nu^a$ (kHz)	$J_{KaKc}' - J_{KaKc}''$	$F' - F''$	ν_{obs} (MHz)	$\Delta\nu^a$ (kHz)
	1 - 0	7288.0397	- 3.1		2 - 0	17106.6275	- 3.6
	2 - 2	7289.2994	- 2.1		2 - 2	17107.2731	- 7.8
	0 - 1	7289.6022	3.2		1 - 1	17107.6745	5.8
$1_{10} - 1_{01}$	1 - 2	7289.9489	- 2.4	$2_{11} - 1_{10}$	3 - 2	17107.9487	1.0
	2 - 1	7290.5767	3.0		1 - 2	17108.3189	0.5
	1 - 1	7291.2217	- 1.8		1 - 0	17109.2940	0.9
	1 - 1	7770.8776	1.0		1 - 0	19483.6988	6.3
	2 - 1	7772.1505	1.7		2 - 2	19484.5137	- 4.0
$1_{01} - 0_{00}$	0 - 1	7774.0567	- 0.6	$2_{12} - 1_{01}$	3 - 2	19485.2150	1.1
					2 - 1	19485.7853	- 4.6
	1 - 1	9154.1236	8.3		1 - 1	19486.8742	1.1
	3 - 3	9154.4836	- 3.2				
$2_{11} - 2_{02}$	2 - 2	9155.1537	- 1.9		3 - 3	20604.2546	- 1.6
					3 - 2	20604.9522	- 0.2
	2 - 1	9591.5649	1.4	$3_{13} - 2_{12}$	2 - 1	20605.3084	- 5.5
	2 - 2	9592.1865	0.7		4 - 3	20605.3285	2.2
$2_{02} - 1_{11}$	3 - 2	9593.5224	0.9		2 - 2	20606.4023	5.1
	1 - 0	9595.1922	- 5.0				
					3 - 3	22154.6411	- 1.4
	0 - 1	13420.4555	- 0.7		2 - 1	22155.7215	- 1.4
	2 - 1	13421.3910	1.2	$3_{03} - 2_{02}$	3 - 2	22155.9758	- 2.4
$1_{11} - 0_{00}$	1 - 1	13422.0097	- 2.5		4 - 3	22155.9990	6.5
					2 - 2	22157.7994	- 1.3
	2 - 1	13834.6513	- 3.1				
	2 - 2	13835.2720	- 4.7		3 - 3	25464.4687	- 4.9
	2 - 1	13835.7433	5.7		3 - 2	25465.1440	3.6
$2_{12} - 1_{11}$	3 - 2	13835.9750	2.1	$3_{12} - 2_{11}$	2 - 1	25465.4980	- 3.8
	1 - 0	13837.2936	0.1		4 - 3	25465.5129	3.2
					2 - 2	25466.5414	2.0
	2 - 2	15241.4254	- 1.4				
	1 - 0	15241.5990	2.9				
	2 - 1	15242.7049	5.9				
$2_{02} - 1_{01}$	3 - 2	15242.7637	1.3				
	1 - 2	15243.5017	- 2.9				
	1 - 1	15244.7762	- 0.6				

[a] $\Delta\nu = \nu_{obs} - \nu_{calc}$, where ν_{calc} is calculated using the fitted rotational parameters.

Table 3.4 Measured transition frequencies of He–DCCCN.

J_{KaKc}' - J_{KaKc}''	F_1F_2' - F_1F_2''	ν_{obs} (MHz)	$\Delta\nu^a$ (kHz)	J_{KaKc}' - J_{KaKc}''	F_1F_2' - F_1F_2''	ν_{obs} (MHz)	$\Delta\nu^a$ (kHz)
	11-12	7261.4197	3.3		22-22	14299.1563	-4.8
	12-12	7261.4558	5.6		23-23	14299.1778	0.9
	10-11	7261.4763	-21.5		12-01	14299.3526	4.8
1_{01}-0_{00}	21-10	7262.6803	-5.3		11-01	14299.3835	4.8
	23-12	7262.7167	6.7		23-12	14300.4359	-0.8
	22-11	7262.7540	-3.6	2_{02}-1_{01}	22-11	14300.4946	-7.7
	01-12	7264.6346	0.5		34-23	14300.5162	1.4
					11-10	14302.5081	-6.9
	23-12	8295.1063	-0.3		12-12	14302.5264	-5.3
2_{02}-1_{11}	34-23	8297.0615	3.0		11-12	14302.5626	-0.1
	33-22	8297.1446	1.6		11-11	14302.6059	9.5
	23-12	13022.5679	-0.8		23-12	15898.4850	0.5
	23-23	13023.1838	1.0		23-23	15899.1263	-3.9
	32-21	13023.8556	-0.7		32-21	15899.7701	-0.8
2_{12}-1_{11}	34-23	13023.8834	4.7	2_{11}-1_{10}	34-23	15899.7978	4.7
	33-22	13023.9364	4.4		33-22	15899.8499	2.4
	12-01	13025.2133	1.4		12-01	15901.1512	-2.2
					11-01	15901.1702	-0.7
	01-12	13265.2300	3.7				
	22-11	13266.1407	0.6		34-23	19027.3271	-7.9
	23-12	13266.1687	2.4	2_{12}-1_{01}	32-21	19027.3505	0.3
1_{11}-0_{00}	21-10	13266.1839	4.4		23-12	19027.8965	-2.4
	10-11	13266.7522	-2.0				
	12-12	13266.7816	1.3		34-34	19422.9434	4.5
	11-12	13266.8029	3.9		34-23	19423.6347	-0.1
				3_{13}-2_{12}	23-12	19423.9800	-14.4
					45-34	19424.0103	2.0
					44-33	19424.0347	8.1
					34-34	20910.8352	-1.9
					23-12	20911.9232	-1.8
				3_{03}-2_{02}	22-11	20911.9489	4.5
					34-23	20912.1681	-6.9
					45-34	20912.2059	7.1
					23-23	20914.0191	-0.9

[a] $\Delta\nu = \nu_{obs} - \nu_{calc}$, where ν_{calc} is calculated using the fitted rotational parameters.

Table 3.5 Measured $J_{KaKc} = 1_{01} - 0_{00}$ transition frequencies of ^{13}C isotopomers of He–HCCCN and He–HCCC^{15}N.

Isotopomer	$F' - F''$	ν_{obs} (MHz)	$\Delta\nu^a$ (kHz)	Unsplit centre (MHz)	χ_{aa} (^{14}N) (MHz)
	1 - 1	7549.2499	-1.6		
He–H^{13}CCCN	2 - 1	7550.5297	2.7	7550.3131	-4.239 (2)
	0 - 1	7552.4294	-1.1		
	1 - 1	7737.4838	-0.3		
He–HC^{13}CCN	2 - 1	7738.7562	0.5	7738.5437	-4.239 (2)
	0 - 1	7740.6631	-0.2		
	1 - 1	7744.3069	-0.5		
He–HCC^{13}CN	2 - 1	7745.5817	0.8	7745.3683	-4.245 (2)
	0 - 1	7747.4910	-0.3		
He–H^{13}CCC^{15}N	–	7361.6284	–	–	–
He–HC^{13}CC^{15}N	–	7544.7070	–	–	–
He–HCC^{13}C^{15}N	–	7556.0753	–	–	–

[a] $\Delta\nu = \nu_{obs} - \nu_{calc}$, where ν_{calc} is calculated using the fitted rotational parameters.

3.6 Figures

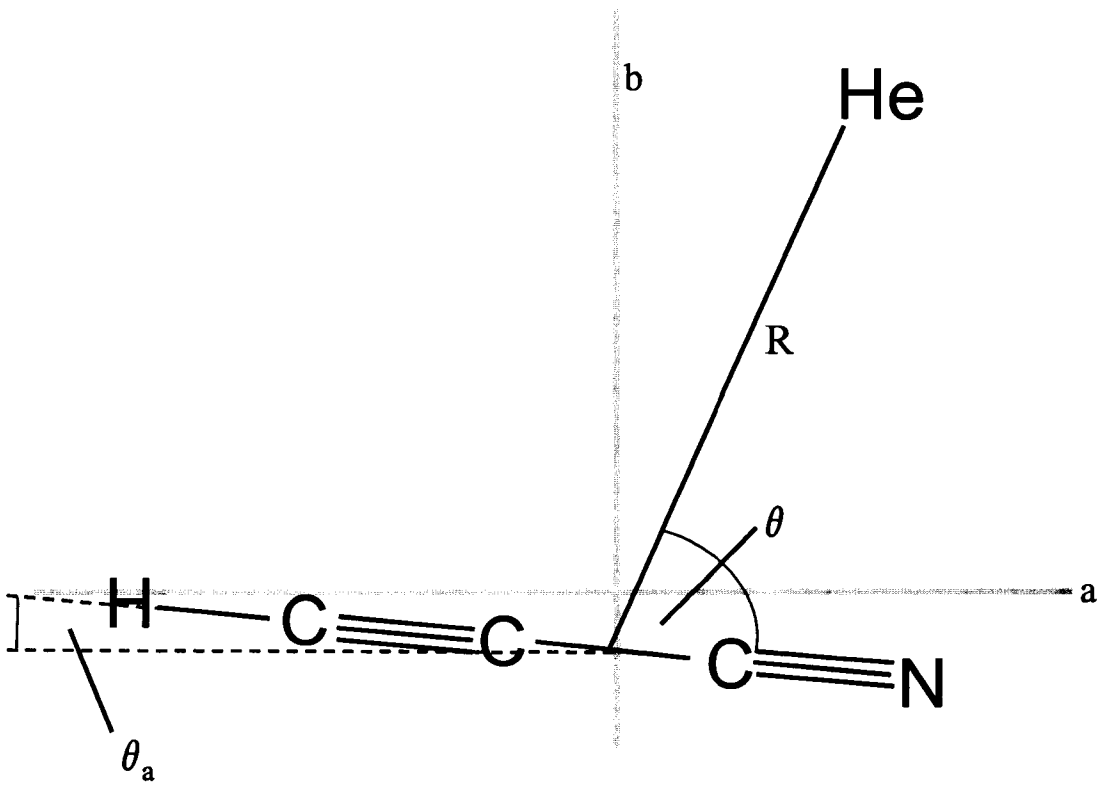

Figure 3.1 The structural parameters used to describe the geometry of He–HCCCN, superimposed on the principal inertial axis system. R is the distance between the He atom and the centre of mass of the HCCCN molecule. θ is the angle between R and the HCCCN axis, where $\theta = 0°$ corresponds to the HCCCN–He linear configuration. The angle between the HCCCN axis and the molecule fixed a-axis is θ_a.

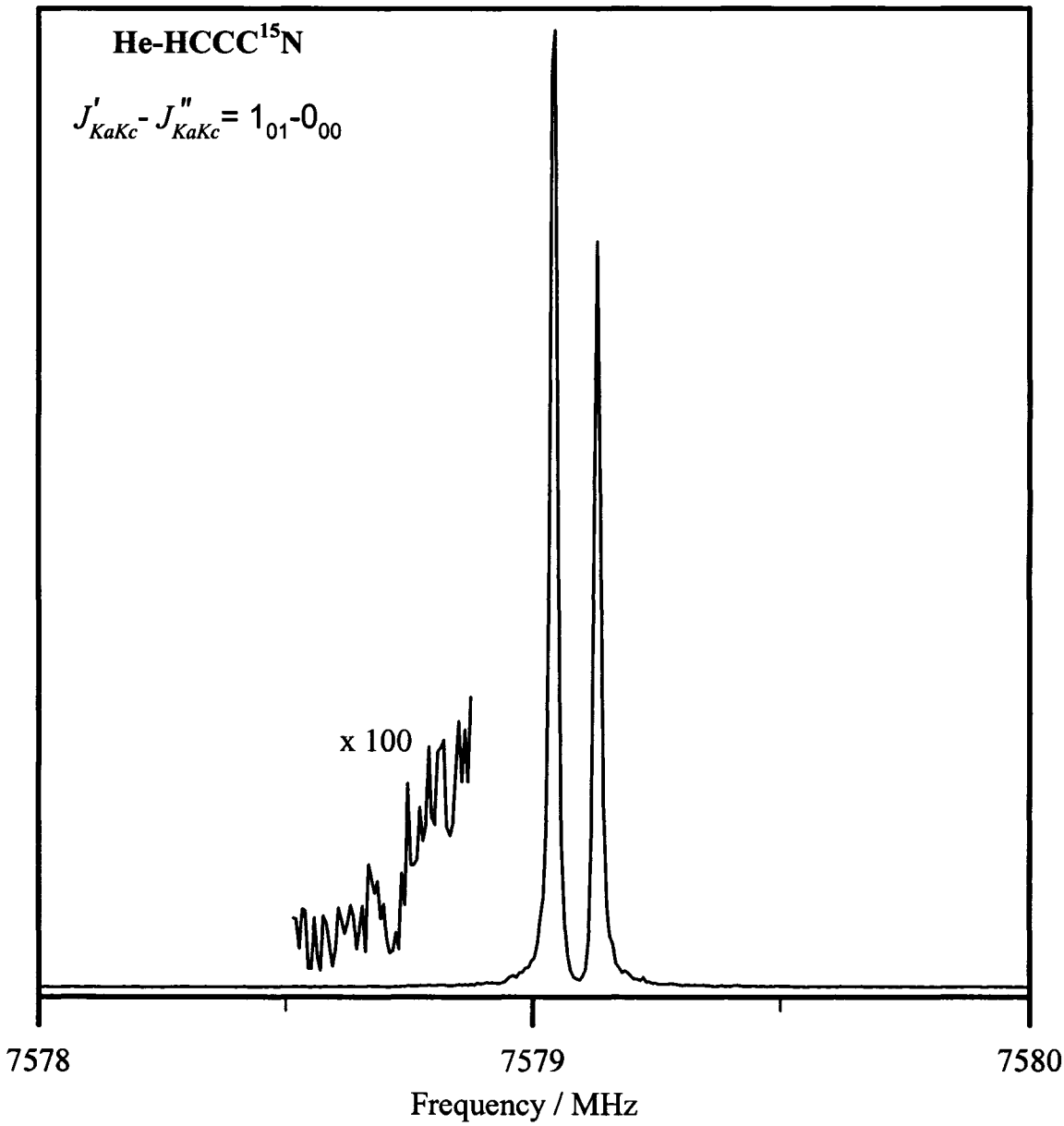

Figure 3.2 Spectrum of the $J_{KaKc} = 1_{01}$-0_{00} *a*-type transition of He–HCCC^{15}N, recorded at a 10 ns sample interval, summed over 10 cycles. A portion of the baseline has been enlarged to show the signal to noise ratio.

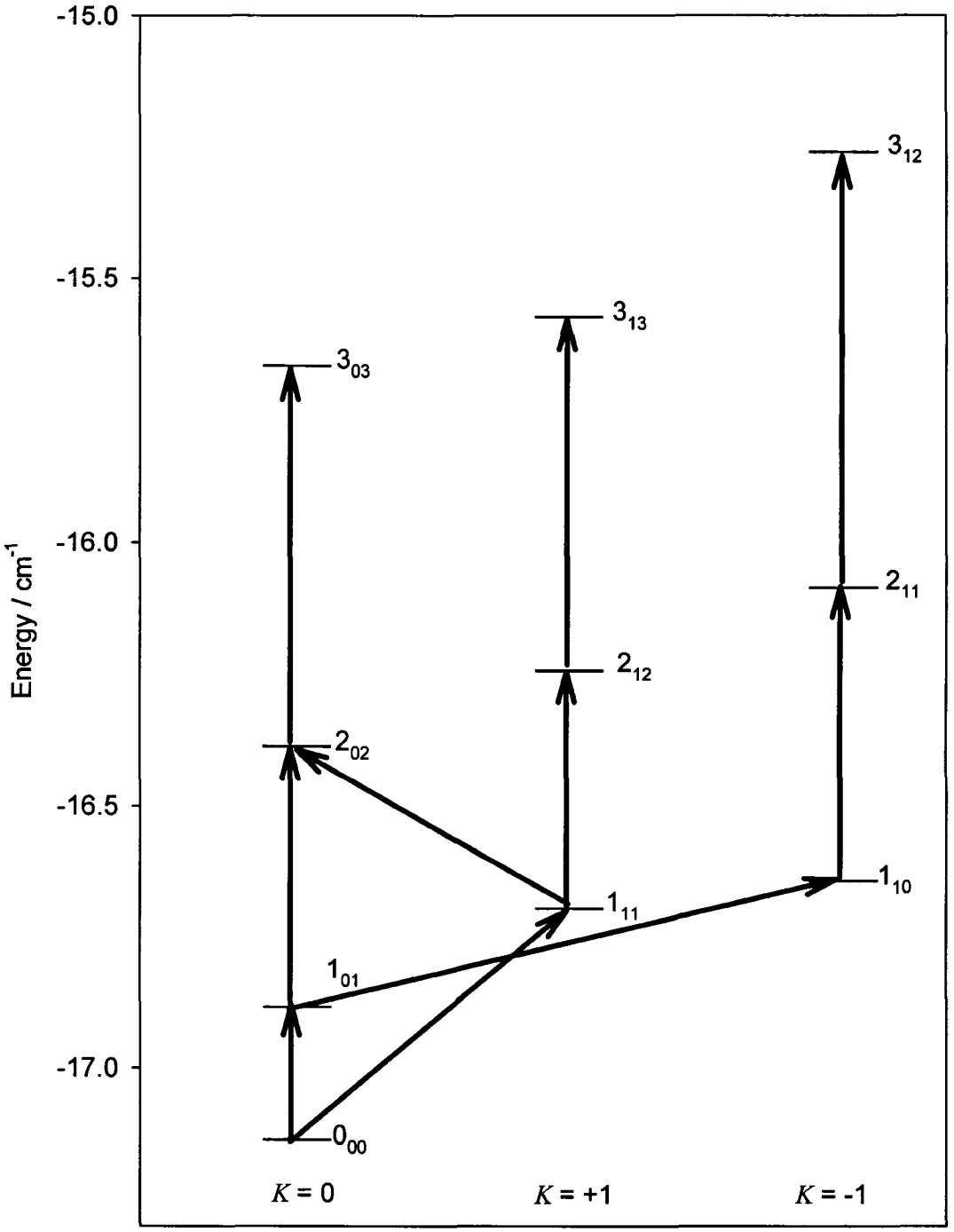

Figure 3.3 A rotational energy level diagram for He–HCCC^{15}N, including energy levels up to $J = 3$. Energy levels are denoted using J_{KaKc} notation and the $K = 0$, +1 and -1 stacks are shown separated. Arrows indicate the microwave rotational transitions that were measured for this complex.

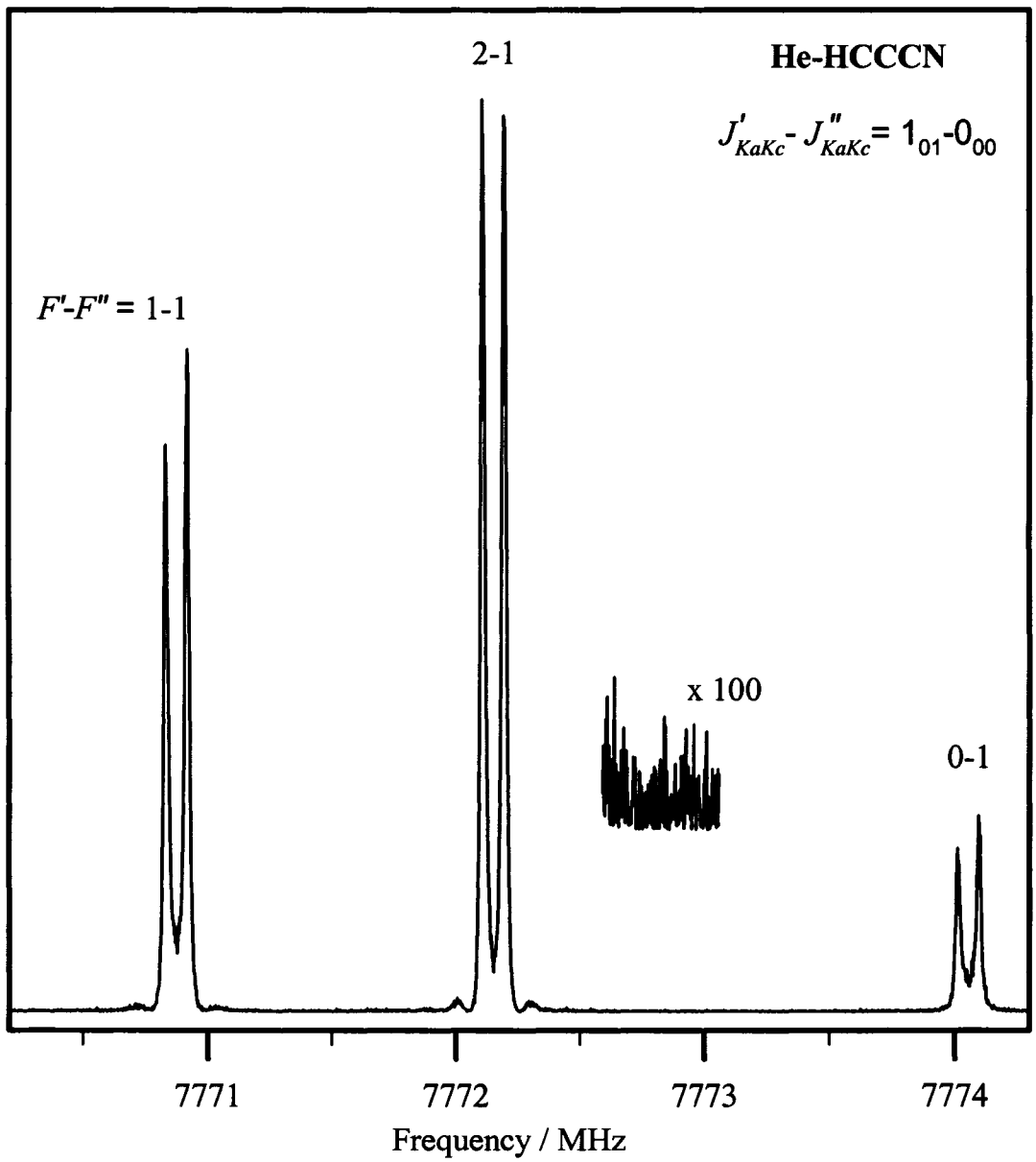

Figure 3.4 Composite spectrum of the $J_{KaKc} = 1_{01}$-0_{00} *a*-type transition of He–HCCCN. Three individual spectra were recorded at a 60 ns sample interval, summed over 10 cycles. A portion of the baseline has been enlarged to show the signal to noise ratio.

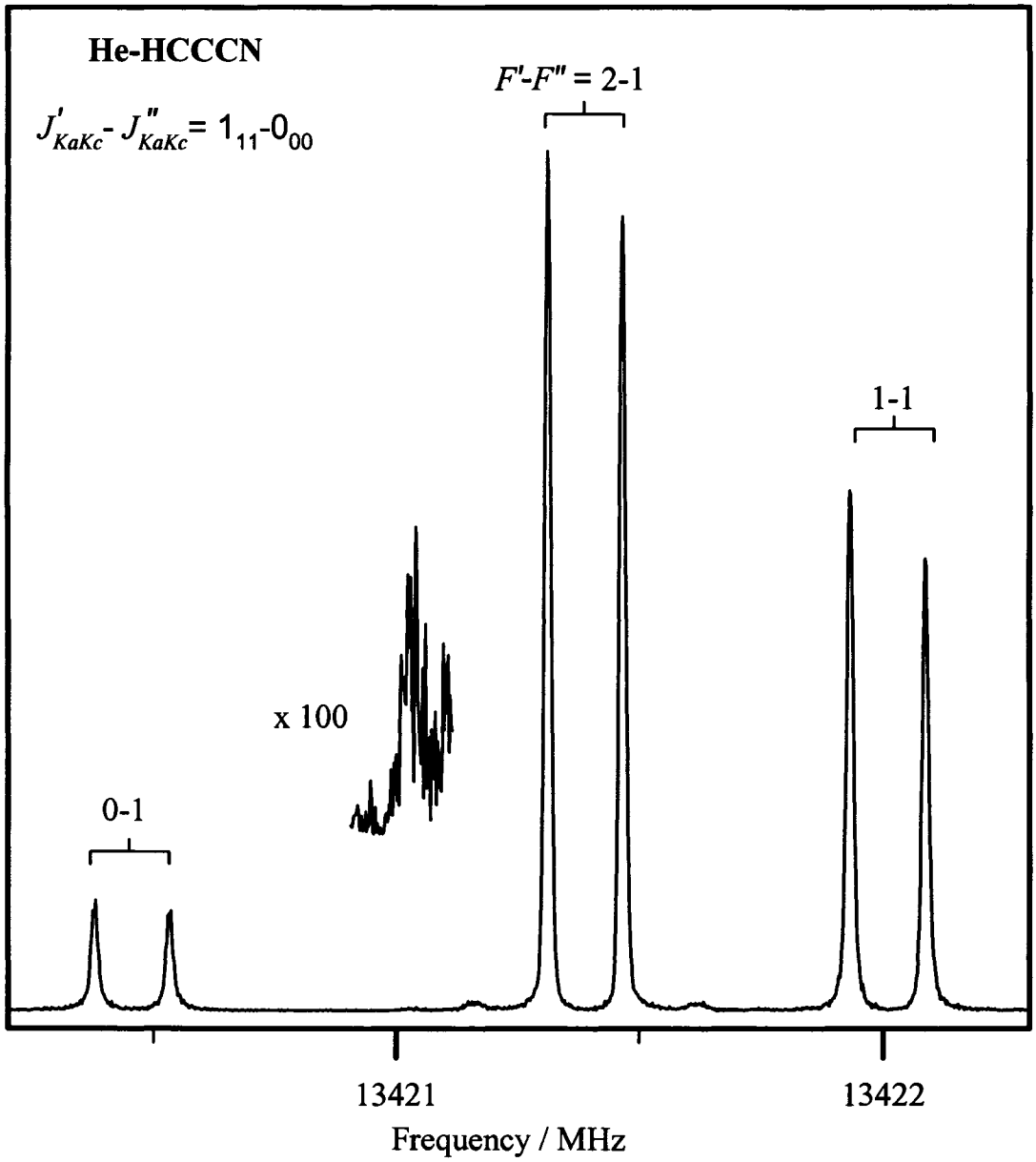

Figure 3.5 Composite spectrum of the $J_{KaKc} = 1_{11}$-0_{00} *b*-type transition of He–HCCCN. Three individual spectra were recorded at a 60 ns sample interval, summed over 200 cycles. A portion of the baseline has been enlarged to show the signal to noise ratio.

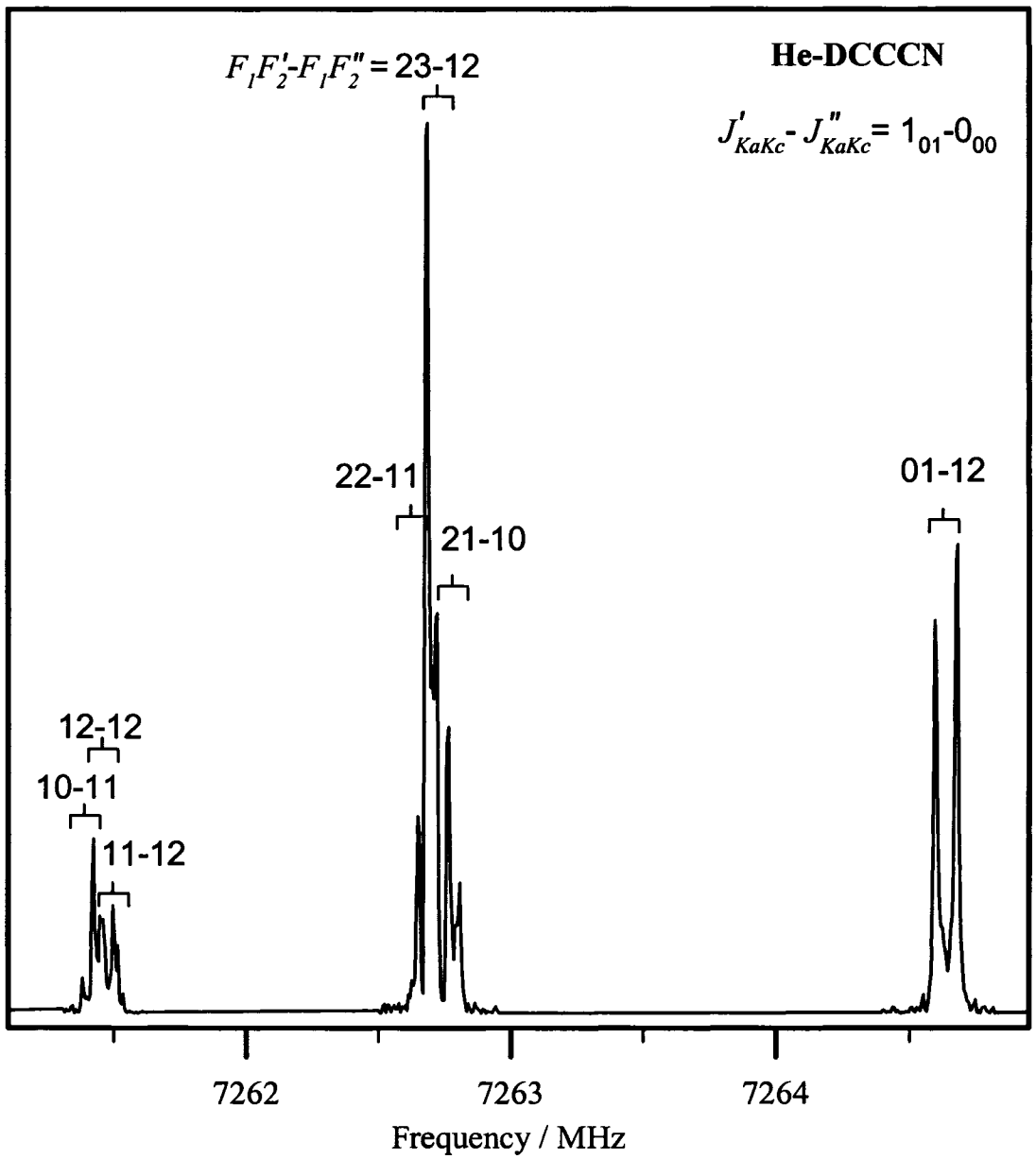

Figure 3.6 Composite spectrum of the $J_{KaKc} = 1_{01}$-0_{00} *a*-type transition of He–DCCCN. Three individual spectra were recorded at a 10 ns sample interval, summed over 10 cycles. The ^{14}N and D nuclear hyperfine structure components are labelled using the $\boldsymbol{J} + \boldsymbol{I}_{^{14}\mathrm{N}} = \boldsymbol{F}_1$, $\boldsymbol{F}_1 + \boldsymbol{I}_{\mathrm{D}} = \boldsymbol{F}_2$ coupling scheme.

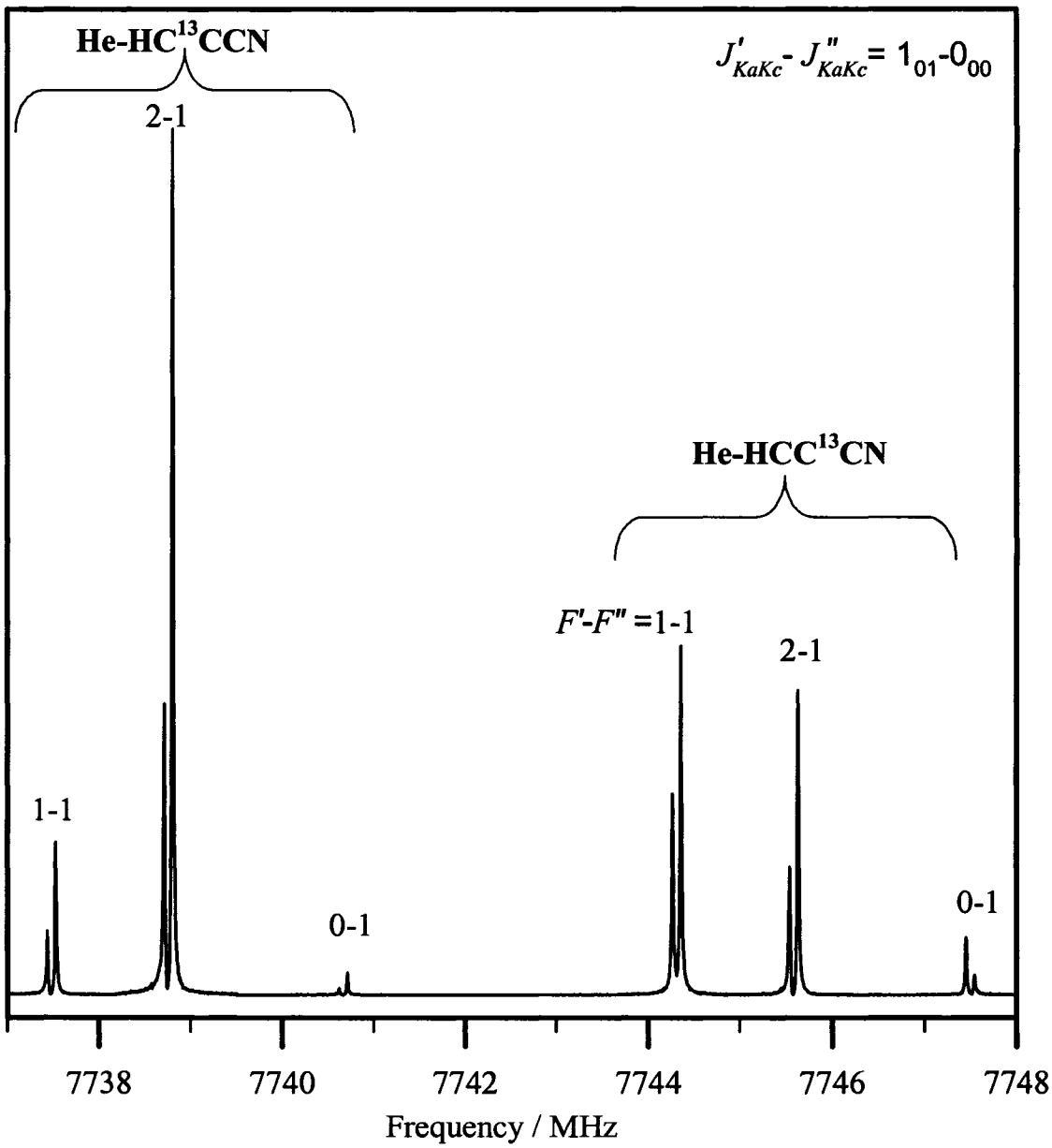

Figure 3.7 Composite spectrum of the $J_{KaKc} = 1_{01}$-0_{00} *a*-type transition of He–$HC^{13}CCN$ and He–$HCC^{13}CN$. Six individual spectra were recorded at a 10 ns sample interval, summed over 100 cycles.

3.7 References

1. Y. Xu and W. Jäger, J. Chem. Phys. **106**, 7968 (1997).
2. V. Markov, Y. Xu, and W. Jäger, Rev. Sci. Instrum. **69**, 4061 (1998).
3. R. L. DeLeon and J. S. Muenter, J. Chem. Phys. **82**, 1702 (1985).
4. L. H. Scharpen, J. S. Muenter, and V. W. Laurie, J. Chem. Phys. **53**, 2513 (1970).
5. J. S. Muenter, J. Chem. Phys. **48**, 4544 (1968).
6. B. N. Bhattacharya and W. Gordy, Rev., **119**, 144 (1960).
7. H. M. Pickett, J. Mol. Spec. **148**, 371 (1991).
8. J. K. G. Watson, J. Chem. Phys. **48**, 4517 (1968).
9. A. Huckauf and W. Jäger, J. Chem. Phys. **119**, 7749 (2003).
10. A. Huckauf and W. Jäger, manuscript in preparation.
11. F. J. Lovas and R. D. Suenram, J. Chem. Phys. **87**, 2010 (1987).
12. K. Higgins and W. Klemperer, J. Chem. Phys. **110**, 1383 (1999).
13. Z. Kisiel, J. Mol. Spectrosc. **218**, 58 (2003).
14. J. K. Tyler and J. Sheridan, Trans. Faraday Society **59**, 266 (1963).
15. X. G. Song, Y. Xu, P.-N. Roy, and W. Jäger, J. Chem. Phys. **121**, 12308 (2004).
16. E. Fliege, H. Dreizler, and B. Kleibömer, J. Mol. Struct. 97, 225 (1983).
17. J. Hutson, Mol. Phys. **84**, 184 (1995).

4

The weakly bound He–cyanoacetylene dimer: *ab initio* intermolecular potential energy surface

Intermolecular potential energy surfaces (PESs) are an attempt to accurately describe weakly bound dimers. *Ab initio* calculations are one possible approach to capturing these interaction surfaces. Six *ab initio* He–cyanoacetylene PESs, calculated using both supermolecular and perturbation methods, are discussed in this chapter. I calculated three surfaces using the coupled cluster method. The other three surfaces were determined by Akin-Ojo and coworkers.[1] These six PESs are compared to ascertain how well they capture the properties of the He–cyanoacetylene interaction. I want to determine how well generally-available basis sets and theory capture the dispersion energy of He–cyanoacetylene. My second goal is to establish a scaling procedure that can easily be implemented to aid in spectroscopic searches of extremely weakly bound

dimers.

Section 4.1 details some considerations that are necessary when selecting both computational methods and basis sets for determining the PES of a weakly bound dimer. I assess the ability of my chosen method and basis sets to capture correlation energy by calculating the potential energy curve of the He_2 dimer, in Section 4.2. Section 4.3 describes the three potential energy surfaces calculated for this study. Both my PESs and those of Akin-Ojo and coworkers (Ref. 1) are evaluated to determine how well they reproduce the observed rotational transitions (Section 4.5).

4.1 *Ab initio* potential energy surfaces (PESs) of van der Waals dimers

In a supermolecule calculation the interaction energy ΔE_{int} is determined by the difference between the energy of the complex AB and the energies of the monomers A and B separately:

$$\Delta E_{int} = E_{AB} - (E_A + E_B) \quad (4\text{-}1)$$

This interaction energy can be divided into Hartree-Fock (or self-consistent field), ΔE^{HF}, and electron correlation ΔE^{cor} contributions:

$$\Delta E_{int} = \Delta E^{HF} + \Delta E^{cor} \quad (4\text{-}2)$$

While Coulomb interactions are accounted for in the Hartree-Fock approach, electrons cannot avoid each other and, thus, this method over-estimates electron-electron repulsion. Post-Hartree-Fock methods correct this by taking into account the correlated movement of electrons.[2] A good description of a weakly bound system can be achieved

by computing an intermolecular PES. The method and basis set chosen must capture the correlation energy, however, as this accounts for the binding of these complexes.

It is important to choose a method that is size-consistent; the supermolecule energy at infinite separation is equal to the sum of the monomer energies determined separately. Two generally available, size-consistent methods are the coupled-cluster (CC) theory and the many-body perturbation (MBPT) theory.[3, 4] Coupled-cluster theory is very effective at capturing correlation energy, though it is more computationally expensive than MBPT.[4]

Dunning and coworkers' augmented correlation-consistent (aug-cc)[5, 6, 7] basis sets provide an efficient numerical method to capture correlation energy. They contain polarization functions with high angular momentum which are necessary to capture dispersion energy,[3] and are available in a variety of sizes (double-zeta (VDZ), triple-zeta (VTZ), quadruple-zeta (VQZ), *etc.*). These basis sets were selected for calculating the He–cyanoacetylene surfaces. In addition, bond functions,[4] smaller basis sets located mid-way between the monomers, increase the efficiency of the calculation. They reduce the need to include high angular momentum functions centred on the nuclei while still recovering the correlation interaction energy of the system.[4, 8]

4.2 Capturing electron correlation energy: the He–He dimer

In order to assess the ability of my chosen method and basis sets to capture electron correlation, the intermolecular PES of He_2 was calculated with both CC and

MBPT methods. Figure 4.1 shows the potential energy curve of the He_2 dimer determined using CC theory. As expected, the Hartree-Fock (HF) interaction energy is repulsive for all internuclear separations R. The semiempirical Aziz potential,[9] constructed by fitting a functional form directly to experimental data, is a good lower limit for the He_2 potential energy curve. Using aug-cc-pVTZ basis sets supplemented with $\{3s2p2d1f1g\}$ bond functions (denoted as aVTZ+BF), and the coupled cluster with single and double excitations (CCSD[10]) level of theory, the majority of the electron correlation energy is recovered compared to the Aziz potential (Ref. 9). If non-iterative triple excitations are included, using either the CCSD(T)[11, 12] or CCSD-T[13] definitions, a further increase in binding energy is observed. In fact, if the basis set is enlarged to aug-cc-pVQZ with $\{3s2p2d1f1g\}$ bond functions (aVQZ+BF) at the CCSD(T) level, only a slight lowering of the binding energy results (Figure 4.1 inset). This suggests that for the He_2 dimer the basis set was nearly saturated when the aVTZ+BF basis set was used. The attractive portions of the CCSD(T) and CCSD-T curves are within 4% of the Aziz semiempirical potential.

Table 4.1 gives the interaction, correlation, and Hartree-Fock energies at the potential minimum for He_2 potential energy curves determined using both the CC and MBPT methods. There are some results which should be noted. Firstly, when the basis set is augmented by adding diffuse polarization functions (compare VTZ+$\{3s2p2d1f1g\}$ and aVTZ+$\{3s2p2d1f1g\}$) there is an increase in the amount of correlation energy captured, regardless of the computational method chosen. When the size of the basis sets is increased from aVTZ+$\{3s2p2d1f1g\}$ to aVQZ+$\{3s2p2d1f1g\}$ only a small increase in

accuracy is observed, while the computational expense increases rapidly. Secondly, inclusion of triple excitations (compare CCSD to CCSD(T), CCSD-T, or MBPT4) are necessary to capture the interaction energy, yet only increase computation time slightly. The MBPT4 calculation is slightly more efficient than the CCSD(T); however, the consequent potential energy curve is of lower accuracy. Using the CCSD(T) method with aVTZ+{3*s*2*p*2*d*1*f*1*g*} basis sets is a good compromise between efficiency and accuracy of calculations for the He_2 dimer.

A final reference potential is included in Table 4.1. In order to reproduce known properties of the He_2 dimer, the hybrid He_2 potential energy curve[14] was constructed by fitting Korona *et al.*'s[15] symmetry adapted perturbation theory (SAPT) PES to a variety of mathematical forms.[16, 17, 18] Binding energies get larger and bond lengths get shorter as we go from MBPT4 to CCSD(T) to SAPT, though they are all roughly the same level of theory. The potential minimum of the hybrid SAPT surface is lower than that of the Aziz semiempirical surface (Ref. 9). While this suggests a higher accuracy, as more correlation energy is captured by the hybrid surface, this surface may predict a dimer that is too tightly bound. In fact, the hybrid SAPT surface underestimates the He_2 bond length, 44.87 Å,[14] compared to experimental value, 62 ± 10 Å.[19]

4.3 *Ab initio* calculation of the He–cyanoacetylene PES

Binding interactions between a He atom and cyanoacetylene are dominated by dispersion forces. *Ab initio* calculations for this type of van der Waals complex require

high levels of theory and large basis sets to model these forces. CCSD(T)[11, 12] has been shown to be an effective technique for determining the interaction energies of He atom containing van der Waals systems.[20, 21] For example, Pedersen *et al.* determined ground state intermolecular potential energy surfaces for He–, Ne–, and Ar–cyclopropane using CCSD(T) and aug-cc-pVDZ basis sets extended with $3s3p2d1f1g$ bond functions.[20] Their potential energy surfaces showed good agreement with microwave experiments on the Ne– and Ar–cyclopropane dimers.[22]

For the He–cyanoacetylene calculations, bond functions with the following α-coefficients were used: *sp* 0.9, 0.3, 0.1; *d* 0.3, 0.2; *fg* 0.3 (Refs. 4, 8, and 20), based on their previous success in producing potential energy surfaces of microwave accuracy. The bond functions were located midway between the atom and the centre of mass of the molecule. The bond lengths of cyanoacetylene were frozen at the calculated [CCSD(T), aug-cc-pVQZ] linear equilibrium values: r(H–C) = 1.0736 Å, r(C≡C) = 1.2094 Å, r(C–C) = 1.3810 Å and r(C≡N) = 1.1637 Å. The supermolecule, single point interaction energies were calculated using MOLPRO 2002.3 and MOLPRO 2002.6.[23] Basis set superposition error was corrected using the full counterpoise correction technique of Boys and Bernardi.[24]

A grid was created by calculating the single point energies of the He–cyanoacetylene complex. Figure 3.1 shows the structural parameters used to describe the relative positions of the He atom and cyanoacetylene. The separation, *R*, between the He atom and the cyanoacetylene centre of mass was allowed to range from 2 to 12 Å. Single point energies were calculated every 0.25 Å along *R*. For linear

configurations of the complex, the He atom was superimposed upon the molecule at small R. To minimize this effect, the angle between R and the cyanoacetylene molecular axis (θ) ranged from 2° to 178°. Calculations were performed every 11°, with $\theta = 0°$ corresponding to the linear HCCCN–He configuration. In total, the potential energy surface of the He–cyanoacetylene was composed of 697 single points. Microwave rotational experiments are most sensitive to the portions of the potential well near the global minimum. However, larger He_N–cyanoacetylene clusters (where $N = 2,3,4...$) probe other regions of the potential energy surface, particularly the regions at both ends of the molecule and at larger R. Calculating a dense grid along each θ-slice gave a potential energy surface suitable for determining properties of larger He_N–cyanoacetylene clusters.

Three potential energy surfaces were calculated at the CCSD(T) level of theory. The initial surface used the aug-cc-pVTZ basis set with bond functions (denoted aVTZ+BF), as described above. Placing the bond functions halfway between the He atom and the cyanoacetylene centre of mass means that near linear configurations of He–HCCCN were calculated with the bond functions superimposed on the molecule for small R. A second surface, using the aug-cc-pVTZ basis but without bond functions (denoted aVTZ) was calculated in order to gauge this effect. Finally, to test if larger basis sets were an efficient way to improve the accuracy of the PES, a third surface was calculated using the aug-cc-pVQZ basis set with bond functions (denoted aVQZ+BF). The number of points were reduced to avoid linear dependencies of the basis set at near-linear configurations. Single point energies were determined every 0.25 Å from $R = 2$ to

12 Å for most θ-slices. At the N-end, energies were calculated every 0.25 Å from $R = 3$ to 12 Å and $R = 2.25$ to 12 Å for $\theta = 2°$ and 13°, respectively. At the H-end, energies were calculated every 0.25 Å from $R = 2.25$ to 12 Å and $R = 5$ to 12 Å for $\theta = 167°$ and 178°, respectively. The first calculated point of each θ-slice is situated on the repulsive wall of the potential energy surface, above 0 cm^{-1}. The single point energies of the three determined PESs are given in Appendix A, Tables A.1, A.2, and A.3.

Topological features of my three surfaces and those of Ref. 1 differ only slightly and are summarized in Table 4.2. Each PES of He–cyanoacetylene has two minima; the global minimum occurs at an approximately T-shaped geometry, while a broad secondary minimum corresponds to the He–HCCCN linear configuration. A saddle point forms the barrier between the global and the secondary minima. At the HCCCN–He linear configuration the surfaces rise to a saddle point. A contour plot of the aVTZ+BF surface is shown in Figure 4.2.

The bound state energies supported by the He–cyanoacetylene potential energy surface were determined using the program JACOBI.[25] The energies of the rotational energy levels, up to $J = 3$, for the ground vibrational state of He–HCCCN, He–DCCCN and He–HCCC^{15}N are given in Appendix B (Tables B.1, B.2, and B.3, respectively).

4.4 The Akin-Ojo surfaces

A theoretical study of five He–cyanoacetylene PESs has been published by Akin-Ojo and co-workers.[1] This study compares potential energy surfaces calculated using

symmetry-adapted perturbation theory (SAPT), Møller-Plesset partitioning of the Hamiltonian at the second (MBPT2) and fourth (MBPT4) order, and the coupled-cluster method with single and double excitations and noniterative inclusion of triple excitations [CCSD(T)]. Bound rotational energy levels, in both the ground and first excited van der Waals vibrational state, were determined for each surface and these values were used to predict the ro-vibrational spectrum of He–HCCCN. For brevity, I will limit my discussion to only their three most accurate surfaces: MBPT4, CCSD(T), and SAPT.

4.5 Properties and accuracy of the He–cyanoacetylene PESs

The perceived quality of a PES depends on what information one wants to elicit from it. As microwave spectroscopists, we need surfaces of "microwave accuracy," surfaces that faithfully reproduce the interactions that affect low rotational energy levels. The small mass of He atoms means that we probe energy levels that lie higher than 50% of the binding well-depth. Comparing rotational transitions predicted by a variety of surfaces to those observed spectroscopically is a useful quantitative approach. Predicting rotational transition frequencies, and using them to fit the parameters of the same rotational Hamiltonian as used for the experimental spectra (Equation 3-1), gives a qualitative idea of which portions of the interaction potential are well reproduced by a given surface. The resulting 'theoretical' rotational and centrifugal distortion constants allow us to comment on the general properties of the calculated potential energy surfaces.

a) Quantitative comparison: predicting He–HCCCN rotational transitions

Quantitatively, all six PESs are very similar (as can be ascertained from the topological information given in Table 4.2). Differences between surfaces, such as the widths of local minima, the steepness of the repulsive wall, and other subtle features of each potential energy surface, greatly impact the accuracy of predicted rotational transitions of the van der Waals complex.

Table 4.3 gives experimental hypothetical unsplit centre frequencies and the spectral parameters determined in the fit of the 12 observed He–HCCCN microwave rotational transitions. This table also reports the rotational transition frequencies predicted from my three potential energy surfaces calculated at the CCSD(T) level, and the spectroscopic parameters used to fit them in the manner described in Section 3.2. Comparing the two triple zeta surfaces, aVTZ and aVTZ+BF, we see that the addition of bond functions results in a dramatic improvement in the correspondence between the predicted transition frequencies ν_{PES} and the experimentally observed ν_{obs}. The relative difference between predicted and experimental frequencies is given by:

$$\%\overline{\Delta\nu} = \sqrt{\frac{\Sigma_i \, (\%\Delta\nu_i)^2}{n}} \qquad (4\text{-}3)$$

where $\%\Delta\nu = 100 \times (\nu_{PES} - \nu_{obs})/\nu_{obs}$, and n is the number of transitions. The surface without bond functions, aVTZ, has a relative difference $\%\overline{\Delta\nu} = 3.2\%$. Supplementing the basis set with bond functions causes this difference to decrease to only 0.9%. The

addition of bond functions results in an increased steepness of the repulsive wall of the aVTZ+BF surface compared to the aVTZ surface. This is most noticeable near the global minimum at the T-shaped configuration. The location of minimum potential energy along a given θ-slice is essentially unchanged when bond functions are included. Overall, the aVTZ+BF surface has a wider binding well in the radial direction, because it becomes attractive at smaller R than the aVTZ surface.

By increasing the basis sets to quadruple zeta with bond functions, the predicted rotational transition frequencies continue to improve towards the experimental values, though the changes are much less spectacular. For aVQZ+BF, the difference between the predicted and experimental transitions is reduced to 0.5%. This PES is only slightly deeper than the aVTZ+BF surface and the locations of the radial minima are unchanged. On the aVQZ+BF surface, the steep repulsive wall becomes negative at only slightly smaller R than for the aVTZ+BF PES. The radial width of the binding wells of these two surfaces are almost equal. This suggests that the basis set is already becoming saturated with aVTZ+BF basis sets, and further small improvements are made only at great computational expense.

Using the energy levels reported in Ref. (1), I calculated the frequencies of the He–HCCCN rotational transitions observed in the microwave region for the surfaces reported by Akin-Ojo and co-workers. The values for the three most accurate surfaces are given in Table 4.4. The same spectroscopic fitting procedure as used for the experimental frequencies was then performed. The CCSD(T) surface from Ref. (1) has $\%\overline{\Delta\nu}$ = 2.1 % which is twice that of the aVTZ+BF surface. This CCSD(T) surface was

calculated with user defined basis sets and a less polarizable set of bond functions, $3s2p1d$,[26] as compared to the $3s3p2d1f1g$ (Ref. 20) functions I selected. As discussed in Ref. (1), the SAPT, CCSD(T), and MBPT4 methods correspond to roughly similar levels of theory. Both the MBPT4 and SAPT surfaces have smaller relative differences, 1.5% and 1.6%, than the Akin-Ojo CCSD(T) surface.

b) Pseudo-diatomic rotor interpretation of rotational parameters

In order to determine which parts of the intermolecular potential are captured by each surface, I will interpret the determined spectroscopic parameters of the surfaces. Comparing experimental and theoretical rotational and distortion constants has been used to gauge in what manner a potential surface captures and fails to capture the interactions of interest.[27]

If a complex is approximated as a pseudo-diatomic rotor then certain spectroscopic parameters have interpretable physical significance. In this model, $[(B + C)/2]^{-1}$ is proportional to an effective pseudo-diatomic separation. The magnitude of the calculated parameter $(B + C)/2$ suggests that all the potential energy surfaces reproduce the average separation between the HCCCN molecule and the He atom fairly well. The SAPT surface (see Table 4.4) is the most tightly bound, $(B + C)/2 = 3905$ MHz, compared to the experimental value of 3888 MHz. The four CCSD(T) surfaces predict a slightly longer bond than the experimental value, with $(B + C)/2$ ranging from 3872 MHz (aVTZ), to 3882 MHz (aVQZ+BF). The trend towards shorter pseudo-diatomic bond lengths, with increasing basis set size in the surfaces calculated at the CCSD(T) level,

reflects relative features of the potential energy surfaces, as described above. Note that both my aVTZ+BF surface and the CCSD(T) surface of Ref. (1) have $(B + C)/2 = 3879$ MHz, though the determined values for $\%\overline{\Delta\nu}$ of the surfaces are quite varied. This indicates that predicted He–HCCCN microwave transitions are sensitive to more than just the position of the global minimum of the potential energy surface.

The difference between the surfaces becomes clear when we examine the predicted flexibility of the He–HCCCN dimer. The value of the centrifugal distortion constant Δ_J is mainly determined by the radial anisotropy of the PES. From experiment, Δ_J is 0.8106 (4) MHz. When different methods are compared, as in Table 4.4, general trends are established. The SAPT surface, the PES with the smallest pseudo-diatomic separation, also results in a fairly rigidly bound complex with $\Delta_J = 0.2838$ (8) MHz. The three CCSD(T) surfaces supplemented by bond functions all predict a more radially flexible dimer (see Tables 4.3 and 4.4), while the aVTZ surface predicts the most flexible bond, $\Delta_J = 1.8682$ (4) MHz, of the six surfaces.

The spectroscopic parameters $B - C$ and Δ_{JK} depend on the angular anisotropy of the potential energy surface and can be regarded as measures of the large amplitude bending motions of the complex. $B - C$ is a measure of the van der Waals bond bending amplitude, while Δ_{JK} describes how the bending motion changes as the van der Waals bond undergoes centrifugal distortion. The experimental values are $B - C = 1771$ MHz and $\Delta_{JK} = 12.841$ (2) MHz. Comparing the PESs calculated using CCSD(T) method, all four surfaces overestimate the amplitude of the angular excursions from the equilibrium

configuration, as B - C is larger than observed in each case. All the CCSD(T) surfaces, therefore, underestimate the angular anisotropy to some degree. The aVQZ+BF and aVTZ+BF surfaces both capture the interaction between the radial stretching and angular bending motions well, with Δ_{JK} = 12.711 (5) MHz and 12.765 (5) MHz, respectively. Neither the aVTZ nor the CCSD(T) surface of Ref. (1) captures the angular properties of interaction between He and HCCCN particularly well. This is seen not only in the larger predicted Δ_{JK} values of 13.540 (2) MHz and 18.123 (4) MHz, but also in B - C of 2090 MHz and 1861 MHz, respectively. The SAPT surface shows high angular anisotropy, B - C = 1690 MHz, which is not surprising as it is the most tightly bound of the six surfaces.

The MBPT4 surface has high angular anisotropy, as B - C = 1736 MHz is slightly smaller than observed spectroscopically. The spectroscopic fit of the predicted rotational transitions gave negative Δ_J and large Δ_{JK} values, Δ_J = -0.1951 (7) MHz, Δ_{JK} = 20.397 (4) MHz. A "negative" Δ_J does not imply that the van der Waals bond gets more rigid with increasing rotational energy. When both Δ_J and Δ_{JK} are considered together, the MBPT4 surface is interpreted as one that favours bending motions to stretching motions at higher rotational energy.

c) Improving the recovery of correlation energy from variational methods

Variational *ab initio* methods underestimate the binding energy of van der Waals complexes and, therefore, the calculated potential energy surfaces are too shallow. All the surfaces examined in this paper accurately capture the separation between the He

atom and the HCCCN molecule. Considering both the quality of predicted rotational transition frequencies and the ability to reproduce the spectroscopic parameters, the aVTZ+BF and aVQZ+BF potential energy surfaces, determined using CCSD(T) theory, are arguably the best surfaces to use in microwave spectroscopic searches. The surfaces could be further improved, however, by recouping some of the lost binding energy. Several procedures for scaling surfaces have been reported previously. Higgins and Klemperer multiplied the He–OCS surface by 10%, resulting in a steeper repulsive wall, a deeper well and improved agreement of the rotational transition frequencies.[28] Howson and Hutson "morphed" the He–OCS potential energy surface by scaling both the energy and intermolecular distance in a multi-parameter fitting procedure.[29] For more symmetric van der Waals complexes (such as Xe-N_2), there are examples of extremely effective procedures in which a scaling function is chosen such that the best agreement between predicted and observed spectroscopic parameters can be achieved.[30] The latter two techniques are possible only after rotational spectra have been measured. I am interested in a simple, general procedure, such as the energy scaling, which can be performed in advance of a spectroscopic search.

Each CCSD(T) He–cyanoacetylene PES predicted a pseudo-diatomic separation, interpreted using $(B + C)/2$, that was similar to the experimental values of He–HCCCN. Each surface underestimated the angular anisotropy, as the B - C values were larger than that obtained from the experimental fit. Scaling a surface by multiplying the energy by a constant factor leaves the positions of the minima and saddle points unchanged, yet increases the angular anisotropy. Would scaling the energy of the aVTZ+BF surface

allow us to recover some of this accuracy, both in spectroscopic parameters and in predicted transitions?

As it turns out, these are slightly different goals. Table 4.5 gives both the predicted unsplit rotational transition frequencies and the fitted spectroscopic parameters of He–HCCCN for the unscaled and two scaled aVTZ+BF surfaces. Scaling the energy of the aVTZ+BF surface by only 3% is sufficient to reduce B - C to the experimental value. Because the scaling occurs globally, the relative change in radial versus angular anisotropy is small, resulting in only a minute change in Δ_{JK}. In general, the rest of the distortion constants improve towards the experimental spectroscopic parameters upon scaling. The one notable exception is Δ_J, which is reduced to only half its experimental value as the radial anisotropy is increased. The relative difference between the predicted and experimental transitions is improved with scaling by a factor of 1.03, to $\%\overline{\Delta\nu} = 0.7\%$ from 0.9%.

When individual transition frequencies are compared, it is clear that the CCSD(T) surfaces systematically predict He–HCCCN rotational transitions at lower frequency than those observed experimentally. Deepening the well of the surface improves this correspondence. When the well is further deepened, a threshold factor is reached after which no further improvements in $\%\overline{\Delta\nu}$ are observed. For the aVTZ+BF surface the best correspondence between predicted and experimental transitions is seen when the surface is scaled by 12%. This reduces $\%\overline{\Delta\nu}$ to 0.2%, which improves on that of the unscaled aVQZ+BF surface ($\%\overline{\Delta\nu} = 0.5\%$). It should be noted that for optimum

correspondence with experimental transitions, the aVQZ+BF surface needed to be scaled by only 8% ($\%\overline{\Delta\nu} = 0.1\%$).

The efficacy of this simple scaling technique is supported by He–DCCCN and He–HCCC^{15}N results. Tables 4.6 and 4.7 give the experimental and theoretical rotational transitions and parameters for He–DCCCN and He–HCCC^{15}N, respectively. Scaling the aVTZ+BF surface by constant factors for both He–DCCCN (Table 4.8) and He–HCCC^{15}N (Table 4.9) gives similar improvements in predicted rotational transitions and parameters as for the He–HCCCN. Again, the 3% deepening of the well improved the agreement with the experimental parameters. The best fit to the unsplit transition frequencies is observed when the well is deepened by 12%. The relative difference between the experimental and predicted transitions were the same for He–DCCCN as for He–HCCCN, $\%\overline{\Delta\nu} = 0.7\%$ and 0.2% for the 1.03 × and 1.12 × (aVTZ+BF) surfaces, respectively. For He–HCCC^{15}N, $\%\overline{\Delta\nu}$ was lowered from 0.7% to 0.6% and 0.3% by scaling the aVTZ+BF surface 1.03 × and 1.12 ×, respectively. In fact, the spectral search for the He–HCCC^{15}N isotopomer (using a sample enriched to 10% HCCC^{15}N) was greatly facilitated by using the predicted rotational transitions from the scaled surfaces. Improved inertial defect values for all isotopomers, $\Delta = 1/C - 1/B - 1/A$, provide additional support that energy scaling is a suitable approach to ameliorate variational *ab initio* PESs.

While aVQZ+BF is undoubtably a more accurate intermolecular potential energy surface than aVTZ+BF, the extra computational expense is not justified, given the

efficacy of a simple scaling procedure. The similar improvement between experimental and theoretical correspondence for He–HCCCN, He–DCCCN, and He–HCCC^{15}N upon scaling confirms that energy scaling is an appropriate choice for improving PESs calculated using variational methods.

4.6 Conclusions

I compared my observed frequencies of He–HCCCN, He–DCCCN, and He-HCCC^{15}N with those predicted by six *ab initio* PESs. From the preceding discussion, I offer some concluding remarks:

Different computational methods and basis sets result in surfaces that can have very similar topological features, but different predicted rotational transition frequencies. The CCSD(T) method and aV*n*Z basis sets (where n = T or Q) supplemented by bond functions, gave PESs of near microwave accuracy. Adding bond functions has greater impact on the properties of the determined PES than increasing the basis set size from aVTZ to aVQZ. A simple scaling procedure applied to the aVTZ+BF PES is sufficient to improve both the predicted spectroscopic parameters and rotational transition frequencies, so that the accuracy was equal to, or surpassed, those of the aVQZ+BF surface. As well, scaling the surface to get the best fit for the observed He–HCCCN transitions allowed the weaker He–DCCCN and He–HCCC^{15}N transitions to be found with relative ease. These observations may facilitate future spectral searches for weakly bound dimers, particularly in the microwave region.

Microwave rotational spectroscopy typically probes a region corresponding to less than 2 cm^{-1} of the potential energy well. One of the motivating factors in comparing my PESs and those of Akin-Ojo *et al.*[1] to the observed microwave transitions was to establish which aspects of the He–cyanoacetylene interaction were well captured by each. A further test of all these surfaces will occur when they are used to determine properties of larger He_N–cyanoacetylene clusters. In particular, the higher order cluster calculations will locate helium density at both the He–HCCCN and HCCCN–He linear configurations. This will test portions of the He–cyanoacetylene PES that are unprobable in studies of the weakly bound dimer.

4.7 Tables

Table 4.1 The interaction, Hartree-Fock, and electron correlation energies for the He_2 dimer at the potential minimum, R_{min}. The average time required to calculate a single point is given. Calculations were carried out at a resolution of $R = 0.001$ Å near the potential minimum for the first nine entries.

	R_{min} (Å)	ΔE^{int} (cm^{-1})	ΔE^{HF} (cm^{-1})	ΔE^{cor} (cm^{-1})	Calculation time (s)
Basis sets: **VTZ +BF**					
CCSD	3.017	-6.1360	4.9992	-11.3519	6.0
MBPT4	2.991	-6.7078	5.6419	-12.3497	4.5
CCSD(T)	2.984	-6.9475	5.8285	-12.7760	6.4
Basis sets: **aVTZ +BF**					
CCSD	3.018	-6.3630	5.0054	-11.3684	13.5
MBPT4	2.992	-7.0147	5.6451	-12.6598	10.0
CCSD(T)	2.984	-7.2983	5.8577	-13.1560	14.6
CCSD-T	2.984	-7.2988	5.8577	-13.1565	19.2
Basis sets: **aVQZ +BF**					
CCSD	3.0130	-6.3813	5.1015	-11.4828	75.1
CCSD(T)	2.978	-7.3575	5.9979	-13.3554	80.1
Aziz *et al.* Semiempirical[a]	2.9702	-7.609	–	–	–
Hybrid SAPT[b]	2.96463	-7.6878	–	–	–

[a] From Ref. (9).
[b] A composite PES, from Ref. (14) and references therein.

Table 4.2 Topographic features of various He–HCCCN potential energy surfaces, calculated at a resolution of $R = 0.05$ Å and $\theta = 0.5°$. The entries are given as [R (Å), θ (°), E^{int} (cm^{-1})].

	Saddle point 1	Global minimum	Saddle point 2	Secondary minimum
aVTZ	5.35, 0, -19.37	3.40, 85.0, -37.95	4.30, 122.5, -20.53	5.60, 180, -29.25
aVTZ+BF	5.30, 0, -21.33	3.35, 85.0, -43.37	4.25, 124.0, -23.00	5.60, 180, -30.20
aVQZ+BF	5.30, 0, -21.37	3.30, 85.5, -43.78	4.20, 122.5, -23.39	5.65, 180, -30.59
MBPT4[a]	5.31, 0, -20.55	3.34, 86.2, -43.14	4.32, 125.2, -23.00	5.58, 180, -29.80
SAPT[a]	5.28, 0, -21.82	3.27, 86.4, -48.68	4.24, 126.1, -27.04	5.56, 180, -31.37
CCSD(T)[a]	5.31, 0, -20.72	3.35, 86.4, -41.79	4.30, 124.4, -22.72	5.57, 180, -30.29

[a] Values from potential fits reported by Akin-Ojo *et al.* in Ref. (1).

Table 4.3 Hypothetical unsplit centre line frequencies and rotational parameters of He–HCCCN from experiment and potential energy surfaces. All values are in MHz, unless specified.

J_{KaKc}'-J_{KaKc}''	Experiment	aVQZ +BF		aVTZ+BF		aVTZ	
	ν_{obs} [a]	ν_{PES}	$\%\Delta\nu$ [b]	ν_{PES}	$\%\Delta\nu$ [b]	ν_{PES}	$\%\Delta\nu$ [b]
1_{10}-1_{01}	7289.6	7207.9	-1.1	7159.6	-1.8	6823.5	-6.4
1_{01}-0_{00}	7771.9	7761.1	-0.1	7756.0	-0.2	7736.9	-0.5
2_{11}-2_{02}	9154.6	9092.1	-0.7	9053.5	-1.1	8823.9	-3.6
2_{02}-1_{11}	9593.1	9663.1	0.7	9701.4	1.1	10033.1	4.6
1_{11}-0_{00}	13421.5	13315.7	-0.8	13257.1	-1.2	12809.8	-4.6
2_{12}-1_{11}	13835.7	13804.2	-0.2	13835.7	-0.3	13628.5	-1.5
2_{02}-1_{01}	15242.7	15217.7	-0.2	15202.5	-0.2	15106.1	-0.9
2_{11}-1_{10}	17107.7	17101.8	0.0	17107.7	-0.1	17106.5	0.0
2_{12}-1_{01}	19485.3	19358.8	0.6	19485.3	-1.0	18701.5	-4.0
3_{13}-2_{12}	20605.2	20560.3	-0.2	20533.6	-0.3	20287.9	-1.5
3_{03}-2_{02}	22156.0	22104.8	-0.2	22072.2	-0.4	21805.5	-1.6
3_{12}-2_{11}	25465.4	25456.0	0.0	25443.8	-0.1	25422.1	-0.2
$\%\overline{\Delta\nu}$ [c]			0.5		0.9		3.2
Rotational Parameters							
A	10518.56 (4)	10443.45 (9)		10382.48 (8)		10270.11 (8)	
B	4773.10 (2)	4781.91 (5)		4779.77 (5)		4917.37 (3)	
C	3002.14 (2)	2981.79 (4)		2978.81 (4)		2827.27 (3)	
Δ_J	0.8106 (4)	0.6032 (9)		0.6132 (9)		1.8682 (4)	
Δ_{JK}	12.841 (2)	12.711 (5)		12.765 (5)		13.540 (2)	
Δ_K	135.67 (4)	154.9 (1)		147.32 (9)		422.49 (8)	
δ_J	0.1699 (3)	0.19024 (6)		0.18791(6)		0.47987 (6)	
δ_K	32.38 (1)	36.30 (2)		35.26 (2)		83.94 (1)	
ϕ_J	0.007045 (4)	0.020294 (8)		0.019305 (8)		0.037560 (9)	
$(B + C)/2$	3888	3882		3879		3872	
$B - C$	1771	1800		1801		2090	
Δ [d]	14.4 amu Å^2	15.4 amu Å^2		15.3 amu Å^2		26.8 amu Å^2	

[a] ν_{obs} is the hyperfine-free centre frequency obtained from the quadrupole fit.

[b] $\%\Delta\nu = 100 \times(\nu_{PES} - \nu_{obs})/\nu_{obs}$.

[c] $\%\overline{\Delta\nu} = [\Sigma_i (\%\Delta\nu_i)^2 /n]^{0.5}$, where n is the number of transitions.

[d] $\Delta = 1/C - 1/B - 1/A$.

Table 4.4 Rotational parameters of He–HCCCN of three PESs reported in Ref. (1). All values are in MHz, unless specified. The rotational constants were calculated using only the frequencies of the 12 transitions observed in this work.

	SAPT	CCSD(T)	MBPT4
A	10784.59 (4)	10214.80 (5)	10221.35 (2)
B	4750.30 (4)	4810.10 (3)	4745.42 (2)
C	3060.4 (3)	2948.68 (3)	3009.48 (2)
Δ_J	0.2838 (8)	0.7654 (7)	-0.1951 (7)
Δ_{JK}	15.008 (5)	18.123 (4)	20.397 (4)
Δ_K	123.35 (5)	180.40 (6)	85.41 (3)
δ_J	0.06246 (6)	0.24983 (6)	0.12492 (6)
δ_K	21.36 (2)	37.65 (1)	14.03 (1)
ϕ_J	0.003192 (7)	0.010811 (8)	0.005415 (8)
$(B + C)/2$	3905	3879	3877
$B - C$	1690	1861	1736
Δ[a]	11.9 amu Å^2	16.9 amu Å^2	12.0 amu Å^2
$\%\overline{\Delta\nu}$[b]	1.6	2.1	1.5

[a] $\Delta = 1/C - 1/B - 1/A$.

[b] $\%\Delta\nu = [\Sigma_i(\%\Delta\nu_i)^2/n]^{0.5}$, where n is the number of transitions and $\%\Delta\nu = 100 \times(\nu_{PES} - \nu_{obs})/\nu_{obs}$.

Table 4.5 Hypothetical unsplit centre line frequencies and rotational parameters of He–HCCCN from unscaled and scaled potential energy surfaces. Experimental values are provided for comparison. All values are in MHz, unless specified.

J_{KaKc}'-J_{KaKc}''	Experiment	aVTZ+BF		1.03 × (aVTZ+BF)		1.12 × (aVTZ+BF)	
	ν_{obs} [a]	ν_{PES}	$\%\Delta\nu$ [b]	ν_{PES}	$\%\Delta\nu$ [b]	ν_{PES}	$\%\Delta\nu$ [b]
1_{10}-1_{01}	7289.6	7159.6	-1.8	7186.9	-1.4	7263.7	-0.4
1_{01}-0_{00}	7771.9	7756.0	-0.2	7755.5	-0.2	7754.7	-0.2
2_{11}-2_{02}	9154.6	9053.5	-1.1	9067.9	-0.9	9110.0	-0.5
2_{02}-1_{11}	9593.1	9701.4	1.1	9666.6	0.8	9572.0	-0.2
1_{11}-0_{00}	13421.5	13257.1	-1.2	13296.4	-0.9	13405.1	-0.1
2_{12}-1_{11}	13835.7	13835.7	-0.3	13804.6	-0.2	13847.6	0.1
2_{02}-1_{01}	15242.7	15202.5	-0.2	15207.5	-0.2	15222.4	-0.1
2_{11}-1_{10}	17107.7	17107.7	-0.1	17088.6	-0.1	17068.7	-0.2
2_{12}-1_{01}	19485.3	19485.3	-1.0	19345.5	-0.7	19498.0	0.1
3_{13}-2_{12}	20605.2	20533.6	-0.3	20558.5	-0.2	20625.5	0.1
3_{03}-2_{02}	22156.0	22072.2	-0.4	22093.6	-0.3	22151.0	0.0
3_{12}-2_{11}	25465.4	25443.8	-0.1	25435.8	-0.1	25415.5	-0.2
$\%\overline{\Delta\nu}$ [c]			0.9		0.7		0.2
Rotational Parameters							
A	10518.56 (4)	10382.48 (8)		10391.41 (8)		10433.43 (7)	
B	4773.10 (2)	4779.77 (5)		4763.90 (5)		4727.06 (5)	
C	3002.14 (2)	2978.81 (4)		2993.69 (4)		3028.38 (4)	
Δ_J	0.8106 (4)	0.6132 (9)		0.4925 (9)		0.1531 (9)	
Δ_{JK}	12.841 (2)	12.765 (5)		12.289 (5)		10.973 (5)	
Δ_K	135.67 (4)	147.32 (9)		124.13 (9)		76.72 (8)	
δ_J	0.1699 (3)	0.18791(6)		0.16292 (6)		0.10978 (6)	
δ_K	32.38 (1)	35.26 (2)		30.75(2)		21.15 (2)	
ϕ_J	0.007045 (4)	0.019305 (8)		0.017782 (8)		0.018927 (8)	
$(B + C)/2$	3888	3879		3879		3878	
$B - C$	1771	1801		1770		1699	
Δ [d]	14.4 amu Å^2	15.3 amu Å^2		14.1 amu Å^2		11.5 amu Å^2	

[a] ν_{obs} is the hyperfine-free centre frequency obtained from the quadrupole fit.
[b] $\%\Delta\nu = 100 \times(\nu_{PES} - \nu_{obs})/\nu_{obs}$.
[c] $\%\overline{\Delta\nu} = [\Sigma_i(\%\Delta\nu_i)^2 /n]^{0.5}$, where n is the number of transitions.
[d] $\Delta = 1/C - 1/B - 1/A$.

Table 4.6 Hypothetical unsplit centre line frequencies and rotational parameters of He–DCCCN from experiment and potential energy surfaces. All values are in MHz unless specified.

J_{KaKc}'-J_{KaKc}''	Experiment	aVQZ +BF		aVTZ+BF		aVTZ	
	ν_{obs} [a]	ν_{PES}	$\%\Delta\nu$ [b]	ν_{PES}	$\%\Delta\nu$ [b]	ν_{PES}	$\%\Delta\nu$ [b]
1_{01}-0_{00}	7262.5	7266.3	0.1	7260.6	0.0	7242.9	-0.3
2_{02}-1_{11}	8296.7	8413.8	1.4	8463.4	2.0	8809.5	6.2
2_{12}-1_{11}	13023.6	13016.2	-0.1	12999.1	-0.2	12643.2	-4.7
1_{11}-0_{00}	13266.3	13157.6	-0.8	13086.6	-1.4	12854.7	-1.3
2_{02}-1_{01}	14300.4	14305.2	0.0	14289.3	-0.1	14209.7	-0.6
2_{11}-1_{10}	15899.5	15927.8	0.2	15921.8	0.1	15931.1	0.2
2_{12}-1_{01}	19027.4	18907.5	-0.6	18825.1	-1.1	18254.9	-4.1
3_{13}-2_{12}	19423.9	19415.1	0.0	19386.5	-0.2	19166.0	-1.3
3_{03}-2_{02}	20912.2	20904.7	0.0	20871.4	-0.2	20655.5	-1.2
$\overline{\%\Delta\nu}$ [c]			0.6		0.9		3.0
Rotational Parameters							
A	10456.4 (9)	10471.3 (14)		10403.8 (2)		10017.6 (4)	
B	4349.900 (3)	4356.515 (19)		4356.294 (3)		4390.972 (7)	
C	2910.329 (1)	2904.648 (11)		2899.084 (2)		2846.632 (4)	
Δ_J	-0.5698 (5)	-1.386 (8)		-1.392 (1)		-1.539 (3)	
Δ_{JK}	19.275 (2)	23.64 (5)		23.683 (8)		32.83 (2)	
Δ_K	64.43 (9)	176.0 (13)		173.9 (2)		162.3 (4)	
δ_J	0.0504 (1)	- 0.1206 (3)		-0.1265 (1)		0.2000 (1)	
$(B + C)/2$	3630	3631		3628		3619	
$B - C$	1440	1452		1457		1544	
Δ [d]	9.1 amu Å^2	9.7 amu Å^2		9.7 amu Å^2		12.0 amu Å^2	

[a] ν_{obs} is the hyperfine-free centre frequency obtained from the quadrupole fit.
[b] $\%\Delta\nu = 100 \times(\nu_{PES} - \nu_{obs})/\nu_{obs}$.
[c] $\overline{\%\Delta\nu} = [\Sigma_i(\%\Delta\nu_i)^2 /n]^{0.5}$, where n is the number of transitions.
[d] $\Delta = 1/C - 1/B - 1/A$.

Table 4.7 Line frequencies and rotational parameters of He–HCCC^{15}N from experiment and potential energy surfaces. All values are in MHz, unless specified.

J_{KaKc}'-J_{KaKc}''	Experiment	aVQZ +BF		aVTZ+BF		aVTZ	
	ν_{obs} [a]	ν_{PES}	$\%\Delta\nu$ [b]	ν_{PES}	$\%\Delta\nu$ [b]	ν_{PES}	$\%\Delta\nu$ [b]
1_{10}-1_{01}	7324.4	7253.5	-0.9	7204.9	-1.6	6866.0	-6.2
1_{01}-0_{00}	7579.1	7560.1	-0.3	7555.2	-0.3	7536.6	-0.6
2_{02}-1_{11}	9131.6	9169.2	0.4	9208.4	0.8	9545.8	4.5
1_{11}-0_{00}	13333.7	13239.0	-0.7	13180.6	-1.1	12735.2	-4.5
2_{12}-1_{11}	13525.5	13484.1	-0.3	13469.0	-0.4	13315.4	-1.6
2_{02}-1_{01}	14886.2	14848.1	-0.3	14833.8	-0.4	14744.4	-1.0
2_{11}-1_{10}	16652.1	16625.3	-0.2	16620.1	-0.2	16629.9	-0.1
3_{13}-2_{12}	20154.3	20095.5	-0.3	20069.9	-0.4	19834.5	-1.6
3_{03}-2_{02}	21684.8	21620.3	-0.3	21589.9	-0.4	21344.2	-1.6
3_{12}-2_{11}	24803.2	24763.6	-0.2	24752.3	-0.2	24734.6	-0.3
$\overline{\%\Delta\nu}$ [c]			0.4		0.7		3.0
Rotational Parameters							
A	10486.6 (1)	10423.8 (1)		10363.1 (1)		10415.434 (1)	
B	4635.57 (5)	4637.02 (5)		4635.14 (5)		4811.076 (3)	
C	2946.39 (5)	2925.18 (5)		2922.22 (5)		2733.579 (2)	
Δ_J	0.707 (1)	0.4899 (9)		0.5042 (9)		1.9344 (2)	
Δ_{JK}	12.814 (6)	12.512 (6)		12.557 (6)		11.6348 (5)	
Δ_K	132.0 (1)	151.42 (1)		144.1 (1)		587.508 (2)	
δ_J	0.14648 (7)	0.16789 (7)		0.16593 (7)		0.42179 (7)	
δ_K	30.30 (2)	33.97 (2)		33.02 (2)		101.689 (1)	
ϕ_J	0.00591 (1)	0.019274 (8)		0.018229 (8)		0.039644 (8)	
$(B + C)/2$	3791	3781		3779		3772	
$B - C$	1689	1712		1713		2077	
Δ [d]	14.3 amu Å^2	15.3 amu Å^2		15.1 amu Å^2		31.3 amu Å^2	

[a] $\%\Delta\nu = 100 \times(\nu_{PES} - \nu_{obs})/\nu_{obs}$.

[b] $\overline{\%\Delta\nu} = [\Sigma_i(\%\Delta\nu_i)^2 /n]^{0.5}$, where n is the number of transitions.

[c] The root mean square (rms) error for the total fit of the 10 transitions observed.

[d] $\Delta = 1/C - 1/B - 1/A$.

Table 4.8 Hypothetical unsplit centre line frequencies and rotational parameters of He–DCCCN from unscaled and scaled potential energy surfaces. Experimental values are provided for comparison. All values are in MHz, unless specified.

J_{KaKc}'-J_{KaKc}''	Experiment	aVTZ+BF		1.03 × (aVTZ+BF)		1.12 × (aVTZ+BF)	
	ν_{obs} [a]	ν_{PES}	$\%\Delta\nu$ [b]	ν_{PES}	$\%\Delta\nu$ [b]	ν_{PES}	$\%\Delta\nu$ [b]
1_{01}-0_{00}	7262.5	7260.6	0.0	7260.3	0.0	7259.8	0.0
2_{02}-1_{11}	8296.7	8463.4	2.0	8428.0	1.6	8332.0	0.4
2_{12}-1_{11}	13023.6	12999.1	-0.2	13013.6	-0.1	13052.4	0.2
1_{11}-0_{00}	13266.3	13086.6	-1.4	13125.4	-1.1	13232.6	-0.3
2_{02}-1_{01}	14300.4	14289.3	-0.1	14293.2	-0.1	14304.8	0.0
2_{11}-1_{10}	15899.5	15921.8	0.1	15915.0	0.1	15897.6	0.0
2_{12}-1_{01}	19027.4	18825.1	-1.1	18878.8	-0.8	19025.2	0.0
3_{13}-2_{12}	19423.9	19386.5	-0.2	19408.8	-0.1	19468.7	0.2
3_{03}-2_{02}	20912.2	20871.4	-0.2	20888.1	-0.1	20932.8	0.1
$\overline{\%\Delta\nu}$ [c]			0.9		0.7		0.2
Rotational Parameters							
A	10456.4 (9)	10403.8 (2)		10434.7 (2)		10521.5 (4)	
B	4349.900 (3)	4356.294 (3)		4350.543 (3)		4335.597 (5)	
C	2910.329 (1)	2899.084 (2)		2904.622 (1)		2919.603 (2)	
Δ_J	-0.5698 (5)	-1.392 (1)		-1.3535 (9)		-1.263 (2)	
Δ_{JK}	19.275 (2)	23.683 (8)		22.316 (5)		18.92 (1)	
Δ_K	64.43 (9)	173.9 (2)		174.1 (2)		174.8 (3)	
δ_J	0.0504 (1)	-0.1265 (1)		-0.14607 (6)		-0.20297 (9)	
$(B + C)/2$	3630	3628		3628		3628	
$B - C$	1440	1457		1446		1416	
Δ [d]	9.1	9.7		9.4		8.5	

[a] ν_{obs} is the hyperfine-free centre frequency obtained from the quadrupole fit.
[b] $\%\Delta\nu = 100 \times(\nu_{PES} - \nu_{obs})/\nu_{obs}$.
[c] $\overline{\%\Delta\nu} = [\Sigma_i(\%\Delta\nu_i)^2 / n]^{0.5}$, where n is the number of transitions.
[d] $\Delta = 1/C - 1/B - 1/A$.

Table 4.9 Line frequencies and rotational parameters of He–HCCC^{15}N from unscaled and scaled potential energy surfaces. Experimental values are provided for comparison. All values are in MHz, unless specified.

J_{KaKc}'-J_{KaKc}''	Experiment	aVTZ+BF		1.03 × (aVTZ+BF)		1.12 × (aVTZ+BF)	
	ν_{obs} [a]	ν_{PES}	$\%\Delta\nu$ [b]	ν_{PES}	$\%\Delta\nu$ [b]	ν_{PES}	$\%\Delta\nu$ [b]
1_{10}-1_{01}	7324.4	7204.9	-1.6	7232.3	-1.3	7310.0	-0.2
1_{01}-0_{00}	7579.1	7555.2	-0.3	7555.5	-0.3	7554.1	-0.3
2_{02}-1_{11}	9131.6	9208.4	0.8	9175.2	0.5	9078.2	-0.6
1_{11}-0_{00}	13333.7	13180.6	-1.1	13220.0	-0.9	13327.7	-0.0
2_{12}-1_{11}	13525.5	13469.0	-0.4	13485.6	-0.3	13525.7	0.0
2_{02}-1_{01}	14886.2	14833.8	-0.4	14839.7	-0.3	14851.8	-0.2
2_{11}-1_{10}	16652.1	16620.1	-0.2	16614.5	-0.2	16593.9	-0.3
3_{13}-2_{12}	20154.3	20069.9	-0.4	20095.5	-0.3	20157.8	0.0
3_{03}-2_{02}	21684.8	21589.9	-0.4	21611.1	-0.3	21661.4	-0.1
3_{12}-2_{11}	24803.2	24752.3	-0.2	24747.1	-0.2	24724.5	-0.3
$\overline{\%\Delta\nu}$ [c]			0.7		0.6		0.3
Rotational Parameters							
A	10486.6 (1)	10363.1 (1)		10372.7 (1)		10415.87 (8)	
B	4635.57 (5)	4635.14 (5)		4620.80 (5)		4585.68 (5)	
C	2946.39 (5)	2922.22 (5)		2936.45 (5)		2968.91 (5)	
Δ_J	0.707 (1)	0.5042 (9)		0.3967 (9)		0.085 (1)	
Δ_{JK}	12.814 (6)	12.557 (6)		12.053 (6)		10.690 (6)	
Δ_K	132.0 (1)	144.1 (1)		121.6 (1)		75.39 (9)	
δ_J	0.14648 (7)	0.16593 (7)		0.14391 (7)		0.09691 (7)	
δ_K	30.30 (2)	33.02 (2)		28.835 (2)		19.89 (2)	
ϕ_J	0.00591 (1)	0.018229 (8)		0.017003 (8)		0.018734 (8)	
$(B + C)/2$	3791	3779		3779		3777	
$B - C$	1689	1713		1684		1617	
Δ [d]	14.3 amu Å^2	15.1 amu Å^2		14.0 amu Å^2		11.5 amu Å^2	

[a] $\%\Delta\nu = 100 \times(\nu_{PES} - \nu_{obs})/\nu_{obs}$.

[b] $\overline{\%\Delta\nu} = [\Sigma_i (\%\Delta\nu_i)^2 / n]^{0.5}$, where n is the number of transitions.

[c] The root mean square (rms) error for the total fit of the 10 transitions observed.

[d] $\Delta = 1/C - 1/B - 1/A$.

4.8 Figures

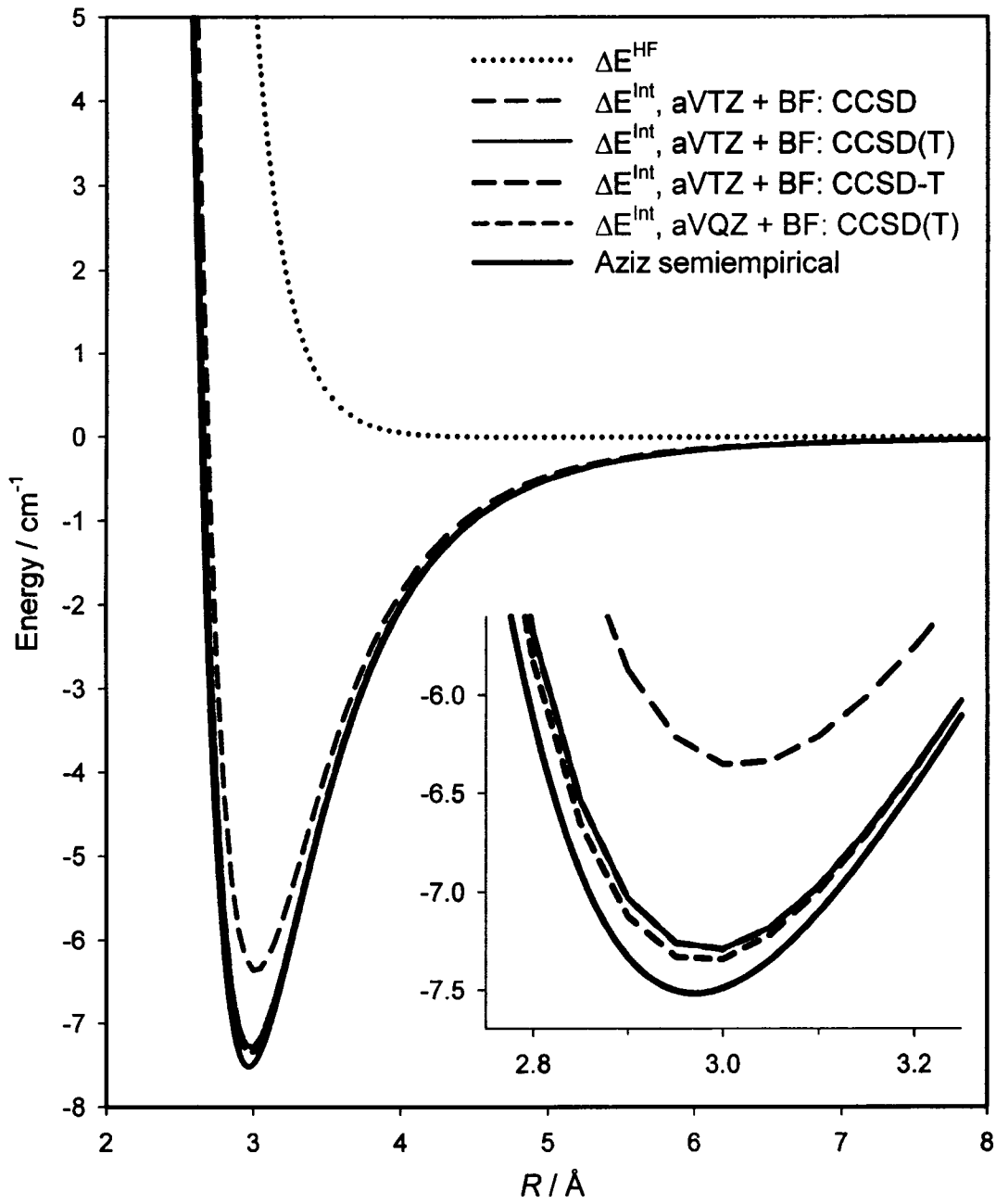

Figure 4.1 He_2 potential energy curves: using the coupled cluster method at various levels, Hartree-Fock theory, and a semiempirical potential obtained by direct fitting to experimental data (Ref. 9). The Hartree-Fock potential energy curve is repulsive for all values of R. An enlarged image of the region near the potential minimum, inset, demonstrates the similarities between the CCSD(T) and CCSD-T surfaces.

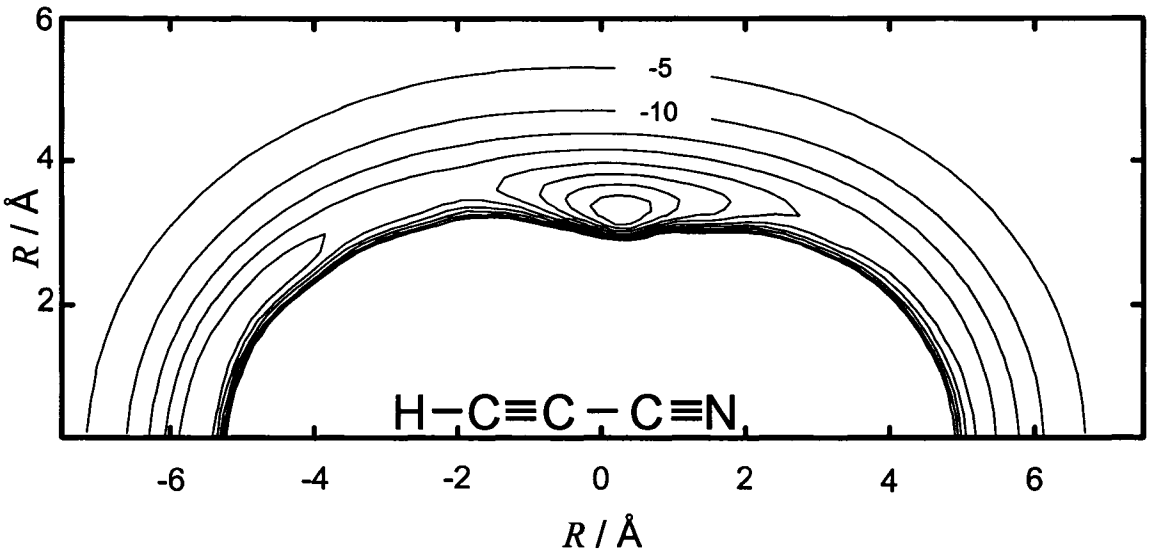

Figure 4.2 Contour plot of the aVTZ + BF potential energy surface of the interaction between a He atom and cyanoacetylene. The contours are separated by 5 cm^{-1}. For parameters of the characteristic points see Table 4.2.

4.9 References

1. O. Akin-Ojo, R. Bukowski, and K. Szalewicz, J. Chem. Phys. **119**, 8379 (2003).

2. H.-J. Werner and P. J. Knowles, in *Molpro: Getting started with Molpro Version* 2002.6 (University of Birmingham, 2001) p 2.

3. J. M. Hutson, in *Rovibrational Bound States in Polyatomic Molecules*, edited by M. M. Law, I. A. Atkinson, and J. M. Hutson (Collaborative Computation Project on Heavy Particle Dynamics, Daresbury, UK, 1999).

4. F.-M. Tao and Y.-K. Pan, J. Chem. Phys. **97**, 4989 (1992).

5. T. H. Dunning, Jr., J. Chem. Phys. **90**, 1007 (1989).

6. R. A. Kendall, T. H. Dunning, Jr., and R. J. Harrison, J. Chem. Phys. **96**, 1358 (1992).

7. D. E. Woon and T. H. Dunning, Jr., J. Chem. Phys. **98**, 1358 (1993).

8. F.-M. Tao, J. Chem. Phys. **98**, 3049 (1992).

9. R. A. Aziz, F. R. W. McCourt, and C. C. K. Wong, Mol. Phys. **61**, 1487 (1987).

10. C. Hampel, K. A. Peterson, and H.-J. Werner, Chem. Phys. Lett. **190**, 1 (1992).

11. K. Raghavachari, G. W. Trucks, J. A. Pople, and M. Head-Gordon, Chem. Phys. Lett. **157**, 479 (1989).

12. K. Raghavachari, G. W. Trucks, J. A. Pople, and M. Head-Gordon, J. Chem. Phys. **115**, 8431 (2001).

13. M. J. O. Deegan and P. J. Knowles, Chem. Phys. Lett. **227**, 321 (1994).

14. A. R. Janzen and R. A. Aziz, J. Chem. Phys. **107**, 914 (1997).

15. T. Korona, H. L. Williams, R. Bukowski, B. Jeziorski, and K. Szalewicz, J. Chem. Phys. **106**, 1 (1997).

16. K. T. Tang and J. P. Toennies, J. Chem. Phys. **80**, 3726 (1984).

17. D. M. Ceperley and H. J. Partridge, J. Chem. Phys. **84**, 820 (1986).

18. D. Bishop and J. Pipin, Int. J. Quantum. Chem. **45**, 349 (1993).

19. F. Luo, G. C. McBane, G. Kim, C. F. Giese, and W. R. Gentry, J. Chem. Phys. **98**, 3564 (1993).

20. T. B. Pederson, B. Fernández, H. Koch, and J. Makarewicz, J. Chem. Phys. **115**, 8431 (2001).

21. S. M. Cybulski and R. R. Toczylowski, J. Chem. Phys. **111**, 10520 (1999).

22. Y. Xu and W. Jäger, J. Chem. Phys. **106**, 7968 (1997).

23. MOLPRO, a package of *ab initio* programs designed by H.-J. Werner and P. J. Knowles, version 2002.3, R. D. Amos, *et al.*; MOLPRO, a package of *ab initio* programs designed by H.-J. Werner and P. J. Knowles, version 2002.6, R. D. Amos, *et al.*

24. S. F. Boys and F. Bernardi, Mol. Phys. **19**, 553 (1970).

25. X. G. Song, Y. Xu, P.-N. Roy and W. Jäger, J. Chem. Phys. **121**, 12308 (2004).

26. E. M. Mas, K. Szalewicz, R. Bukowski, and B. Jeziorski, J. Chem. Phys. **107**, 4207 (1997).

27. W. Jäger, G. Armstrong, M. C. L. Gerry, F. Y. Naumkin, F. Wang, and F. R. W. McCourt, J. Chem. Phys. **109**, 5420 (1998).

28. K. Higgins and W. Klemperer, J. Chem. Phys. **110**, 1383 (1999).

29. J. M. Howson and J. M. Hutson, J. Chem. Phys. **115**, 5059 (2001).

30. Q. Wen and W. Jäger, J. Chem. Phys. **122**, 214310 (2005).

5

Introduction to larger He_N–molecule clusters

5.1 Unusual properties of superfluid ^4He

Helium was first liquified in 1908. Subsequent research into the properties of this liquid quickly yielded anomalous results when compared to other noble liquids. In 1928 Wolfke and Keesom suggested that liquid helium must exist as two distinct states; a phase stable at higher temperatures, He I, behaving as an ordinary fluid and a second phase stable at low temperature, He II, that is unlike classical fluids.[1] This hypothesis clarified earlier discoveries and spurred the search for additional indications that liquid helium displayed unusual properties.

A phase diagram of ^4He, projected on the pressure-temperature plane, is given in Figure 5.1. When compared to the phase diagram of an ordinary fluid, Figure 5.1 inset,

there are significant differences. Solid, liquid, and gaseous ^{4}He never exist in equilibrium, as its phase diagram lacks a triple point. Applied pressure of 25 atm is required to solidify the very weakly interacting ^{4}He at 0 K. Classically, all motion stops at absolute zero. Quantum mechanics concedes that if atoms are sufficiently weakly interacting, with large zero-point motions, they will remain liquid at absolute zero. Most significantly, there is a liquid-liquid phase transition, named the λ-line. This transition occurs at T_λ = 2.176 K, under saturated vapour pressure, and is not associated with a latent heat of the system.

Above the λ-temperature, He I behaves like a normal fluid. However, the phase transition to He II marks the onset of very unusual behaviour.[2, 3, 4] Two of these dramatic effects were termed "frictionless flow" and the "fountain effect." When Kapitza measured the drop in pressure as He II flowed through a thin gap between two plates, he determined that the viscosity of He II is at least 1500 times smaller than that of He I.[5] The velocity of an ordinary fluid through a capillary is proportional to the pressure difference across the capillary, and inversely proportional to the viscosity of the fluid. Since He II flowed through thin capillaries with no measurable pressure difference, Kapitza concluded that the viscosity of He II was essentially zero or that He II was "superfluid." The fountain effect[6] was discovered after extraordinarily high heat conduction was observed in He II.[7, 8] The fountain is generated using a tube packed with emory powder, immersed in liquid He II. When the powder is irradiated, a steady jet of He streams from the top of the tube, as illustrated in Figure 5.2. In He II, heat transfer is accompanied by matter transfer.

In the two-fluid model,[9, 10] superfluid He II is made up of two fluids which are simultaneously present and interpenetrating; a superfluid and a normal fluid. The superfluid is highly coherent ensemble in which all the atoms are described by a single wavefunction, and by definition carry no entropy. The non-viscous superfluid fraction has a mass density ρ_s. The normal fluid has density ρ_n, and is assumed to carry all the thermal excitations of the liquid ^{4}He. The total mass density ρ of the liquid is given by:

$$\rho = \rho_s + \rho_n \tag{5-1}$$

At absolute zero, the entire liquid is superfluid and $\rho = \rho_s$. At some critical temperature, T_c, the superfluid fraction disappears and $\rho = \rho_n$. For $0 \leq T \leq T_c$, the temperature determines the unique proportion of normal to superfluid density, as shown in Figure 5.3.

The two-fluid model gives a phenomenological explanation for frictionless flow through thin capillaries. The superfluid fraction flows through the opening with zero viscosity, while the normal component of the fluid is prevented from passing through the small gap. The two-fluid model can also explain the "fountain effect." The emory powder forms tiny pores through which the superfluid fraction flows, but not the normal fraction. When the tube is heated, a temperature and pressure difference develops between the tube and the surrounding ^{4}He bath. The normal fluid, which carries all the entropy of the liquid, is trapped within the tube and the pressure difference causes the fluid to stream out of the top of the capillary. The superfluid fraction, however, continues to flow through the "entropy trap" into the tube. As the ratio of ρ_n / ρ_s is determined by temperature, the fountain effect is maintained as long as the emory powder is irradiated.

5.2 The Andronikashvili experiment

Landau suggested an experiment by which the presence of two distinct fractions of He II could be verified.[11] Following this suggestion, Andronikashvili directly observed normal and superfluid He II, and studied the temperature dependence of the ρ_n / ρ_s ratio.[12] A vessel containing a stack of thin plates was constructed, as illustrated in Figure 5.4,[13] and rotated in He II. The effective inertia of the vessel was measured at various temperatures. A maximum value was observed at the λ-point where $\rho = \rho_n$, corresponding to the moment of inertia of the vessel plus all the He II adhering to the plates. Only the normal component of He II is dragged by a moving object. The frictionless superfluid component is not carried along and as the temperature is lowered, the density of the superfluid fraction increases. At T = 0 K a minimal moment of inertia value is obtained corresponding to that of the plates alone. Experimentally, a temperature of 1.76 K was achieved. Figure 5.5 gives the density of the normal fraction compared to the total density, ρ_n / ρ.[11, 12, 14] These early values of ρ_n / ρ ranged from 100% at the λ-point to 30% at T = 1.76 K, where the superfluid fraction dominates the total density of He II.

In what is termed the "microscopic Andronikashvili experiment," Grebenev, Toennies, and Vilesov demonstrated that superfluidity can exist in finite ^{4}He systems.[15] Rovibrational transitions of an OCS molelcule embedded within pure ^{4}He-droplets (~10^4 atoms) were resolved, similar to the spectrum expected of an isolated, gaseous rotor. The observed moment of inertia of the OCS molecules was higher by a factor of 2.7 than

that of the free molecule. The authors devised an elegant experiment to show that the observed behaviour of OCS in a ^{4}He-nanodroplet was due to the bosonic nature of the ^{4}He-droplet. ^{3}He, a fermion, becomes superfluid only below $T_c = 0.003$ K. The temperature of a nanodroplet (0.38 K) allows the majority of ^{4}He atoms to become superfluid, but is above the T_c for ^{3}He atoms. A single broad peak was observed for the rovibrational spectrum of OCS embedded within pure ^{3}He-nanodroplets, shown in Figure 5.6 **A**. This would be expected of a chromophore solvated by a normal fluid. When ^{4}He atoms were added to the ^{3}He nanodroplets, however, the OCS rovibrational peaks narrowed (Figure 5.6, **B** through **F**). Once 60 ^{4}He atoms surrounded the OCS molecule (Figure 5.6 **E**), the rovibrational spectrum consisted of resolved peaks, similar to a gas-phase spectrum.[15] The authors proposed that the superfluid fraction of the ^{4}He allowed the OCS chromophore to rotate unimpeded, while the increased moment of inertia was due to normal He II density being dragged by the rotor. In this manner, they reproduced the Andronikashvili experiment,[12] on a microscopic scale. The authors of Ref. 15 suggested that a minimum of 60 ^{4}He atoms were required to form a superfluid.

5.3 Systematic solvation of a molecule with He atoms

Determining the onset of superfluidity in ^{4}He nanodroplets is different than in a bulk system. In bulk phase, the ρ_n / ρ_s ratio has a unique value at a given temperature. He-nanodroplets with more than ~1000 atoms have temperature $T = 0.38$ K. Surface excitations reduce the efficiency of evaporative cooling of smaller nanodroplets, causing

an elevated droplet temperature of approximately 0.45 K for He nanodroplets of less than 1000 atoms.[16] As temperature determines the ρ_n / ρ_s ratio, an increasing ρ_s can be achieved by increasing the average droplet size. Studying the onset of superfluidity in He-nanodroplets would require forming increasingly small clusters. There are inherent difficulties in this approach, and reliable results exist only for minimum cluster sizes of 330 ^{4}He atoms (Ref. 16), much larger than the proposed value of 60 ^{4}He atoms.

Systematically solvating a molecule with He atoms was proposed as an alternative approach for investigating the onset of superfluidity.[17] Studies of He–molecule van der Waals dimers, such as He–OCS,[18] He–N_2O,[19, 20] He–HCN,[21] He–HCCCN,[22] *etc.*, are being increasingly reported. Larger He_N–molecule clusters (N = 2, 3, 4, 5,...), however, are difficult to form in the gas-phase. By careful manipulation of both the sample and nozzle conditions, increasingly large He_N–molecule clusters (N = 2, 3,.. up to 72 for OCS,[17, 23, 24, 25] to 19 for N_2O,[26, 27] to 20 for CO,[28] and to 17 for CO_2[29]) have been generated using pulsed molecular beams and studied using IR and microwave spectroscopy. In these studies, the effective B rotational constant initially lowers, as the moment of inertia of the He_N–molecule increases with the addition of subsequent He atoms. For He_N–OCS,[17, 23, 24] the B rotational constant becomes smaller than the nanodroplet value[15] for N = 6, shown in Figure 5.7. This means that the B rotational constant must "turn-around," or that the moment of inertia must decrease for larger N. This decoupling of helium density was observed for He_N–N_2O, although the first minimum in B was significantly higher than the nanodroplet value.[26, 27] The effective rotational constant continued to oscillate above the nanodroplet B value[30] (Figure 5.7),

meaning that the effective moment of inertia for N up to 19 remains lower than that of N_2O in a ^{4}He nanodroplet.[26, 27, 30] The behaviour of the rotational constant and vibrational shifts of increasingly large clusters are drastically varied depending on the dopant molecule studied.

Theories to explain and predict the behaviour of the B rotational constant with increasing cluster size have been advanced in recent years. Projection operator imaginary-time spectral evolution (POITSE) calculations[31, 32, 33] predict that the behaviour of B versus N will follow one of two scenarios: i) the inertia of a heavy rotor (e.g., OCS) will increase 2-3 times upon solvation with helium, and this solvated inertia is reached before the first solvation shell is complete, ii) the inertia of a light rotor (e.g., HCN) will increase only fractionally, and converge to the nanodroplet B value much more slowly. This is explained by the concept of "adiabatic following." Heavy dopant molecules, which rotate slowly when excited and generally have stronger, more anisotropic interactions with He atoms, will drag solvating helium density as they rotate. Lighter rotors, rotating faster and with less anisotropic interactions with He, will drag only a small fraction of this amount. Whaley and co-workers suggest that a slow convergence to nanodroplet inertia values for light rotors is due to interactions between molecular rotations and bulk phase excitations, which would only occur in large clusters.[32, 34, 35]

Results from reptation quantum Monte Carlo (RQMC) calculations,[36] however, dispute this interpretation. To disentangle the effects of molecular inertia from interaction potential anisotropy, the rotational dynamics of OCS and HCN were each

simulated using the inertia of the other molecule.[37] The strength and anisotropy of the potential was found to determine both convergence to the nanodroplet regime and the increase in molecular inertia upon solvation with He.[37] Also, RQMC calculations for He_N–OCS (for N up to 50) predicted oscillatory behaviour of B with increasing N,[37] defying the theory of fast convergence to the nanodroplet regime for heavy rotors. Recent rovibrational and rotational results for He_N–OCS with N up to 72 supports these computational findings.[25] Although B initially dropped below the nanodroplet B value, the rotational constant of the clusters was found to increase for larger N and showed oscillatory behaviour of B above the limiting nanodroplet B value.[25] The computational study showed that the interaction potential between He and a molecule determines in which fashion B rotational constants of large clusters converge to the ^{4}He nanodroplet value.

5.4 Quantum exchange and the onset of superfluidity

The increase in the B rotational constant observed in He_N–N_2O for $N > 8$ (Refs. 26 and 27) indicates that helium density is decoupling from the rotating system. This manifestation of frictionless behaviour can be considered an indicator of superfluidity in ^{4}He. The bosonic nature of ^{4}He atoms allows them to simultaneously occupy a single quantum state: one of the conditions that defines the superfluid phase. Bose-Einstein statistics dictate that the wavefunction of bosons must be symmetric with respect to exchange of identical particles. If we exchange two bosons, the sign of the wavefunction

of the system does not change. Similarly, Fermi-Dirac statistics govern fermions, although exchanging two identical fermions changes the sign of the wavefunction.

Theoretical chemists and physicists are investigating the role of quantum exchange in the onset of superfluidity. One approach has been to compare the properties of He_N–N_2O clusters determined from calculations that treat the He atoms as either classical or quantum particles.[27, 38] Finite-temperature path integral Monte Carlo (PIMC) calculations do not explicitly include exchange. When ^{4}He atoms are treated as distinguishable particles which obey Boltzmann statistics, the determined properties of He_N–N_2O correspond to what would be expected if the system obeyed classical physics. When quantum exchange is allowed, ^{4}He atoms obey Bose-Einstein statistics.[27, 38] Figure 5.8 shows the experimental B values of He_N–N_2O as filled triangles and the PIMC B values as open squares (Boltzmann statistics) and open circles (Bose-Einstein statistics) for increasing N. Classically, we expect the moment of inertia of He_N–N_2O to increase as the number of He atoms adhering to the N_2O molecule increases. What is observed in Figure 5.8 is slightly more complicated. Overall, there is a downward trend for PIMC (Boltzmann) B values with increasing N. Increased B values at $N = 7$, 10, 11, 15, and 17 are attributed to rearrangements of the ^{4}He density around N_2O. For $N = 3$ to 7, the inclusion of quantum exchange (open circles in Figure 5.8) gives nearly identical B values as when Boltzmann statistics are used. For He_N–N_2O clusters with $N > 8$, the B values calculated with and without exchange diverge. It is at this point that Bose-Einstein statistics become important for determining the properties of He_N–N_2O clusters. The ratio of the superfluid density to total ^{4}He density (ρ_s / ρ) around N_2O starts to become

significant at $N = 8$, as shown in Figure 5.9, for both experiment and theory.[27] The B turn-around, for both experiment and calculations including exchange, occurs at $N = 9$.[27, 38] This highlights the impact that Bose-Einstein statistics has on helium decoupling, the hallmark of microscopic superfluidity.

5.5 Does rotor length influence the onset of superfluidity?

All the dopant molecules discussed in the previous sections are linear molecules, composed of a maximum of three atoms. Systematically solvating a longer molecule will provide additional information on the role that dopant length plays in the solvation process and the onset of superfluidity. One measure of the extent of a molecule can be obtained by summing the bond lengths of the ground vibrational state and the van der Waals radii of the terminal atoms of the molecule. At 7.55 Å, HCCCN is more than one Angstrom longer than OCS (6.09 Å) or N_2O (5.38 Å). The large dipole moment of this molecule (μ = 3.71 D) makes it possible to observe large He_N–cyanoacetylene clusters with our microwave spectrometer, even at low abundance. Synthesizing the compound in house allows isotopic substitution, increasing the amount of information obtainable. For all these reasons, cyanoacetylene is an intriguing choice as a chromophore for microscopic solvation with ^{4}He.

The rovibrational [39, 40, 41] and rotational [42] spectra of HCCCN embedded in superfluid ^{4}He nanodroplet have been reported. The observed spectra show a lowering of the rotational constant of HCCCN in the droplet (B = 1573.7 (7) MHz),[39] as compared

to the free molecule (B = 4549.05859 (4) MHz).[43] This provides a limiting B rotational constant value for very large clusters. Determining the behaviour of B versus N for increasingly large He_N–HCCCN clusters will clarify how rotor length influences the convergence towards droplet values and the onset of superfluidity.

PIMC calculations by Roy and Blinov for He_N–HCCCN clusters predict when exchange will become important.[44] Figure 5.10 shows the evolution of B with N for He_N–HCCCN, as determined from PIMC calculations that consider He atoms as distinguishable particles and as particles that undergo exchange.[44] For $N < 5$ the B rotational constants of He_N–HCCCN determined with and without considering exchange are nearly identical. For $N \geq 5$, B values diverge. This is in stark contrast to the shorter He_N–N_2O clusters, where the B values determined with and without exchange do not diverge until $N = 8$ (Figure 5.8).[27] PIMC calculations of the helium density for He_N–N_2O and He_N–HCCCN provide some insight into this discrepancy.[27, 38, 44] For N_2O, the first five He atoms form a ring around the equator of the molecule, where the global minimum of the He–N_2O PES is located (Figure 5.11 **A**).[38] Due to atom-atom repulsion, the addition of a sixth He atom causes helium density to spill into the secondary minimum of the He–N_2O PES, located at the oxygen-end of the molecule (Figure 5.11 **B**).[38] PIMC calculations for He_5–HCCCN show all the helium density is localized in the global minimum (Figure 5.11 **C**).[44] The increased length of cyanoacetylene means that the distance is longer between the global minimum (corresponding to a T-shaped geometry) and the local minimum (at the H-end of the molecules) of the He–HCCCN PES, when compared to N_2O. Attractive forces between the He atoms on the ring and those located

at the secondary minimum are reduced. It becomes energetically favourable for the sixth He atom in He_6–HCCCN to remain localized on the ring (Figure 5.11 **D**).[44] In the path integral formalism,[45] exchanges with a large projected area on a given axis mean there is a reduction in the moment of inertia along that axis (Ref. 38). The higher relative density of helium on the equatorial ring, compared to that localized on either end of a linear molecule, causes the first long exchange cycles to occur between He atoms localized in the equatorial ring. For He_N–N_2O, the spilling of helium density to the oxygen-end reduces the helium density available to take part in long exchange cycles. The increased helium density on the ring for He_6–HCCCN compared to He_6–N_2O corresponds to an earlier evidence of exchange for He atoms in He_N–HCCCN compared to He_N–N_2O. These computational findings suggest that the longer rotor length of HCCCN compared to N_2O will result in different behaviour as these two molecules are solvated with He atoms. The results of the spectroscopic investigation of He_N–cyanoacetylene clusters are detailed in the following chapter.

5.6 Figures

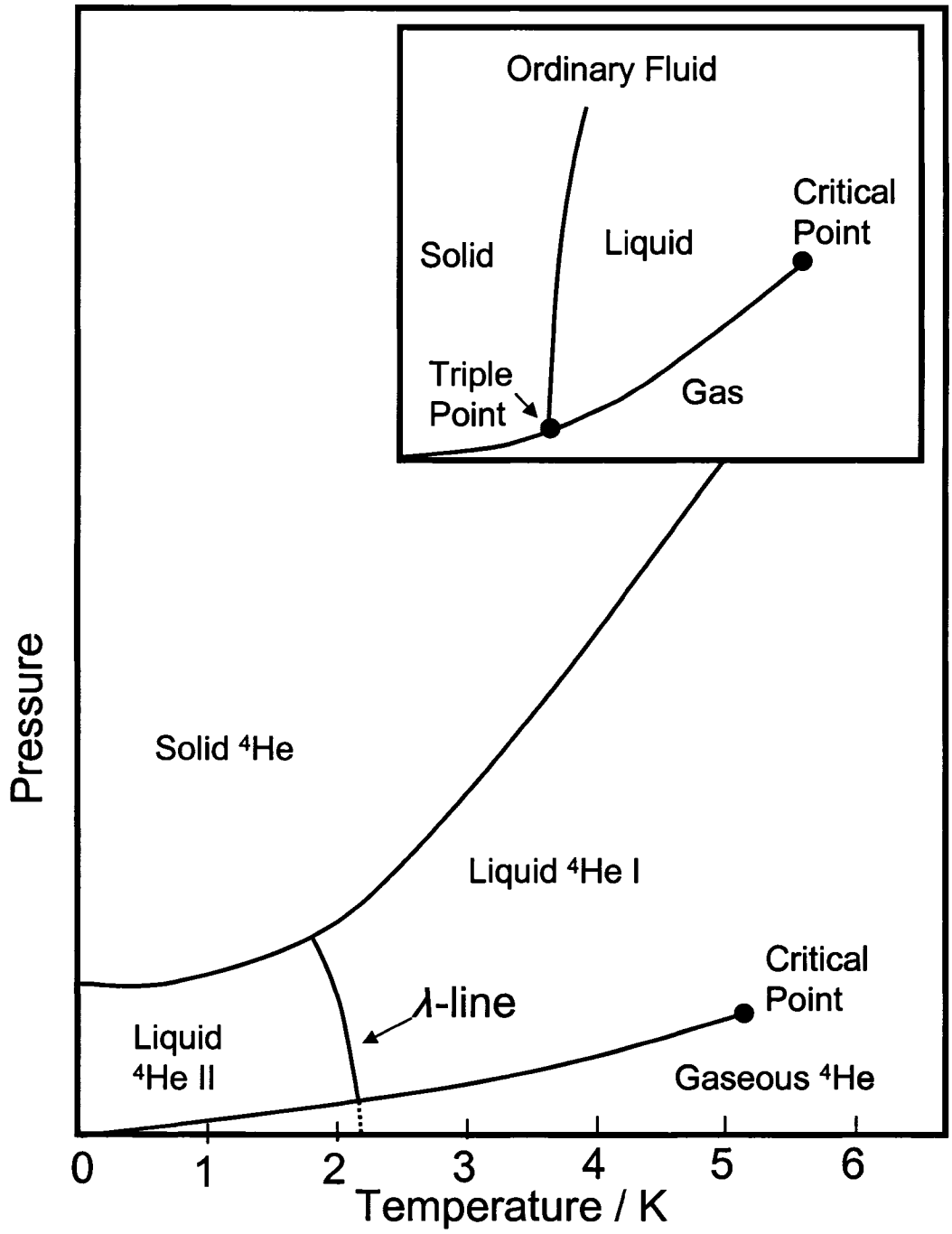

Figure 5.1 The pressure-temperature phase diagram of ^{4}He, compared to that of an ordinary fluid (inset).

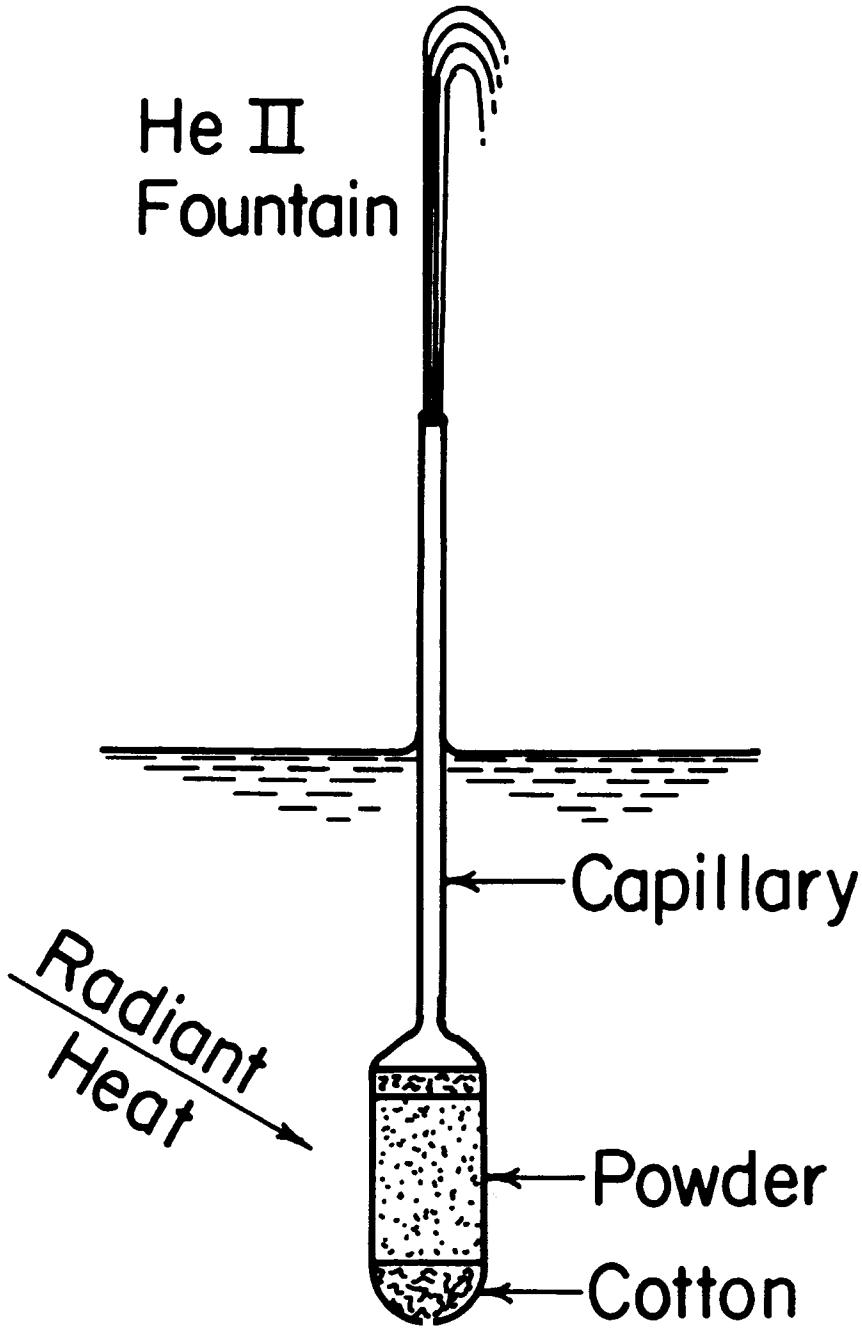

Figure 5.2 Schematic illustration of the He II fountain effect. Radiation incident on a tube packed with fine emory powder causes a jet of He to project from the top. This jet will continue for as long as the powder is irradiated. Illustration reproduced from Ref. 3.

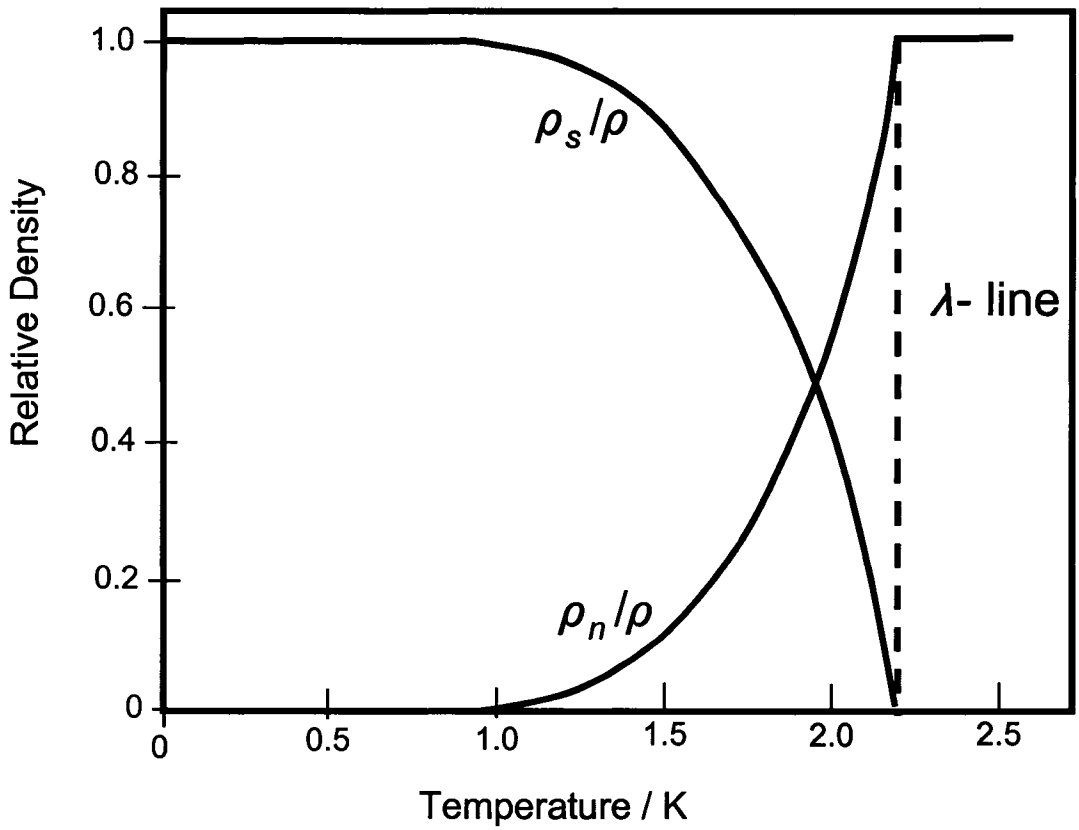

Figure 5.3 Superfluid and normal fluid density of He II as a function of temperature.

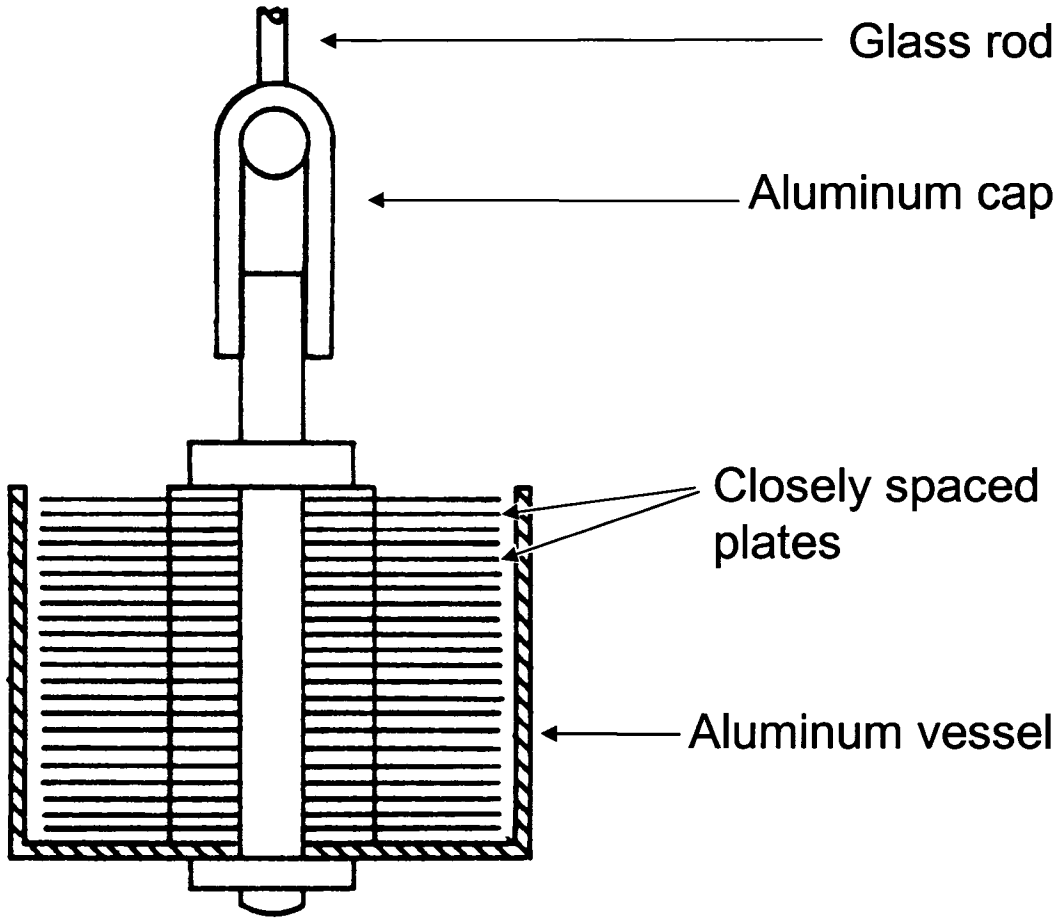

Figure 5.4 The experimental stacked plates apparatus used by Andronikashvili to determine the ratio of normal to superfluid density in He II. Illustration reproduced from Ref. 13.

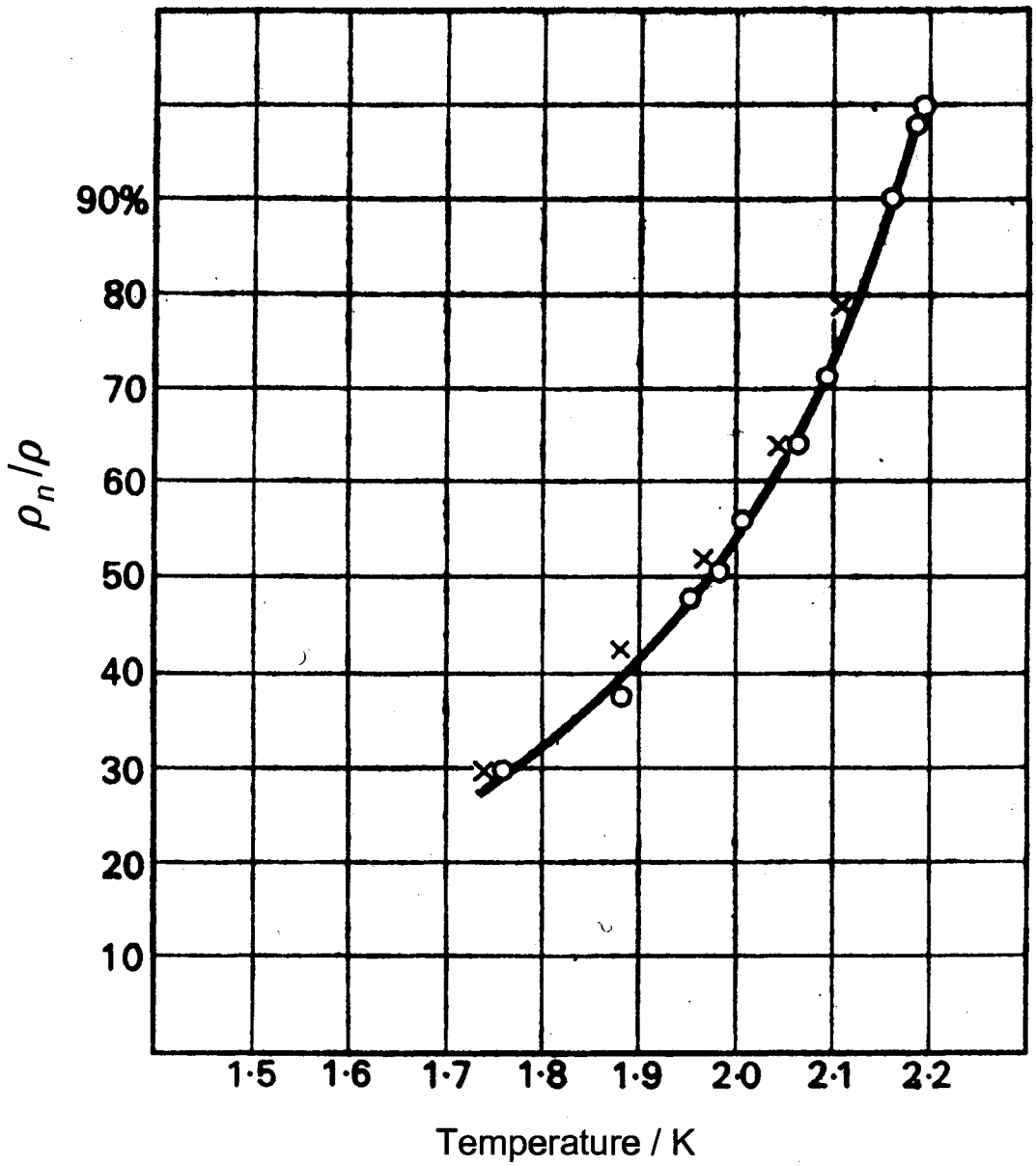

Figure 5.5 The experimental ratio of normal fluid density to the total density of He II, ρ_n/ρ. The Andronikashvili values, determined by moment of inertia measurements, are given by the circles. The ρ_n/ρ ratio determined by measurements of the velocity of second sound in He II (Ref. 14) agree well with the Andronikashvili experiment, (crosses). Landau's theoretical values (Ref. 11) are given by the solid curve. Figure reproduced from Ref. 12.

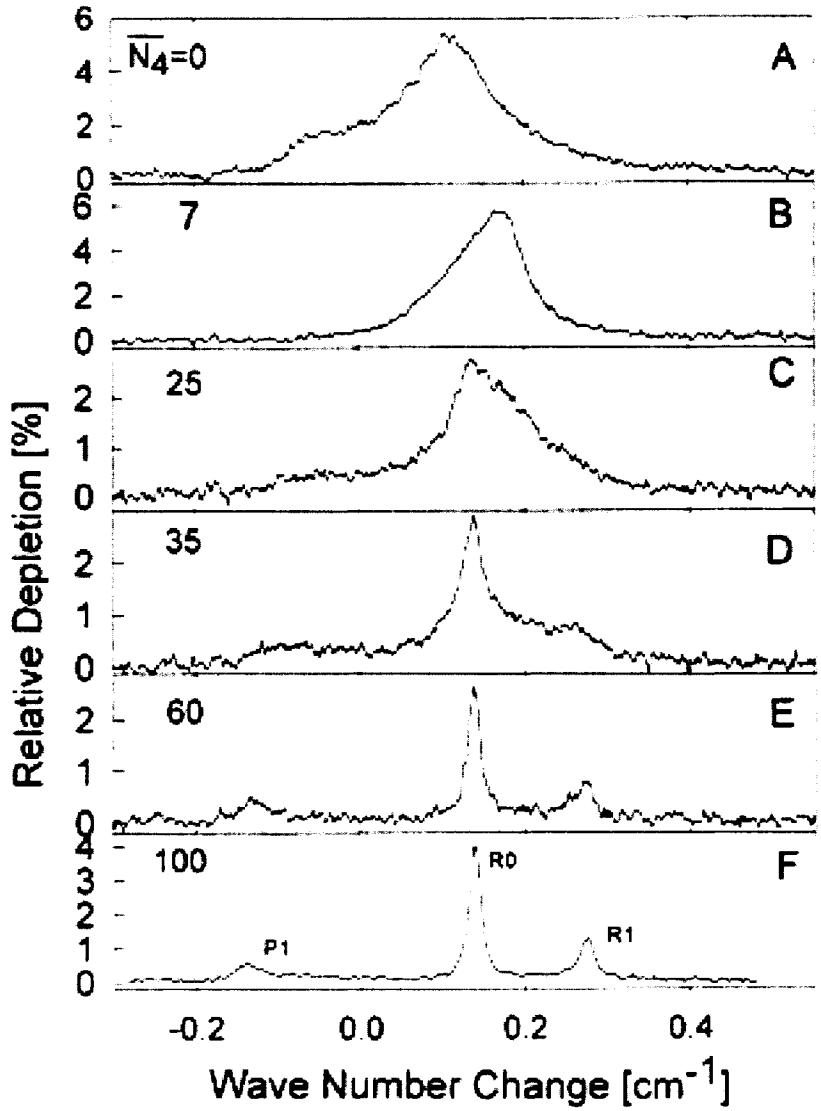

Figure 5.6 A series of OCS spectra embedded within ^{3}He nanodroplets, doped with an increasing average number $\overline{N_4}$ of ^{4}He atoms ($\overline{N_4}$ = 0 (**A**), 7 (**B**), 25 (**C**), 35 (**D**), 60 (**E**), and 100 (**F**)). The change in wave number is with respect to the origin of OCS in ^{4}He nanodroplets, ν_0 = 2061.71 cm^{-1}. Spectra reproduced from Ref. 15.

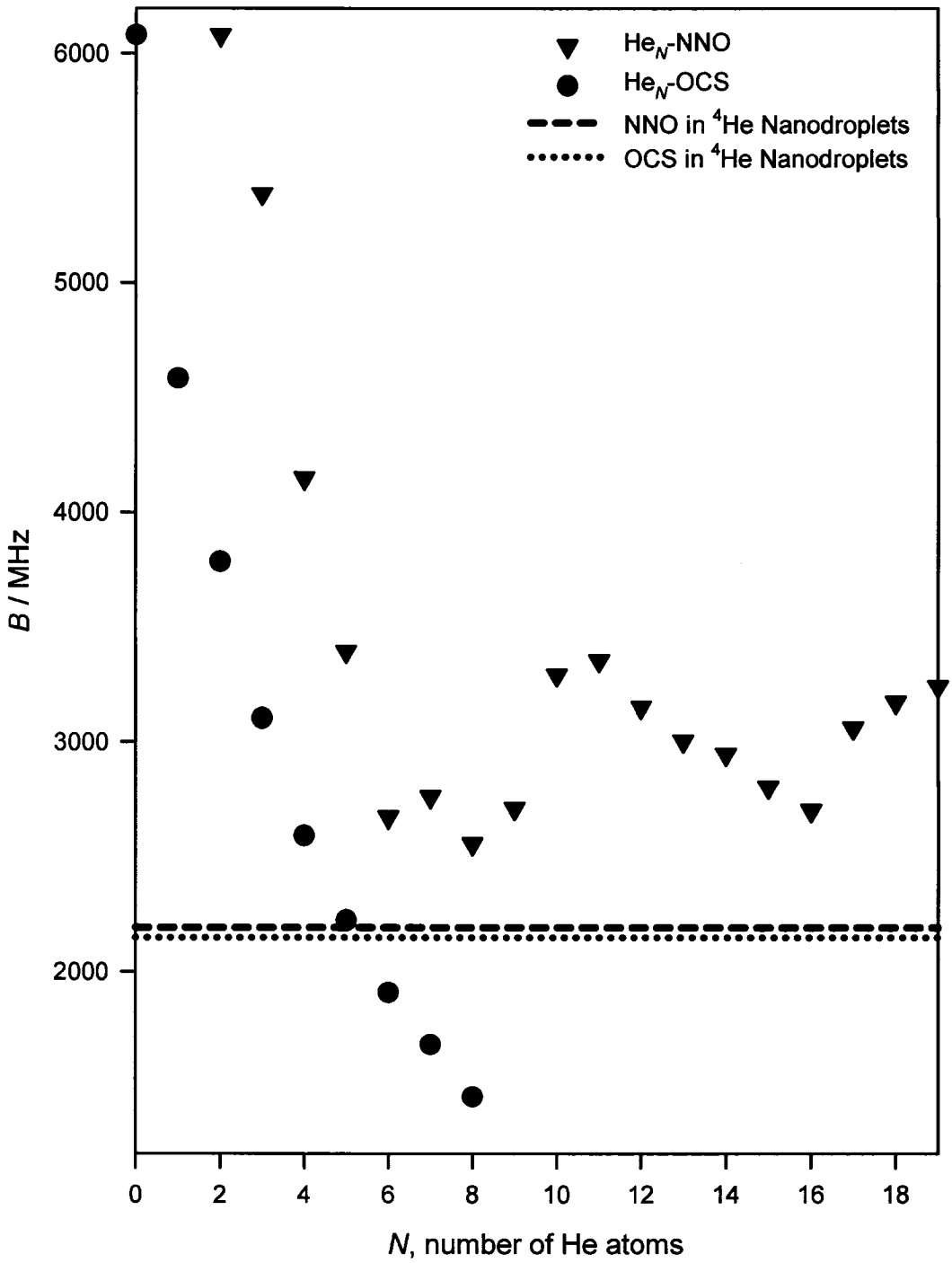

Figure 5.7 The evolution of B of He_N–N_2O (Ref. 26, 27) and He_N–OCS (Ref. 17, 23, 24) with increasing numbers of He atoms, N. The limiting N_2O (Ref. 30) and OCS (Ref. 15) ^{4}He nanodroplet values are given as dashed horizontal lines.

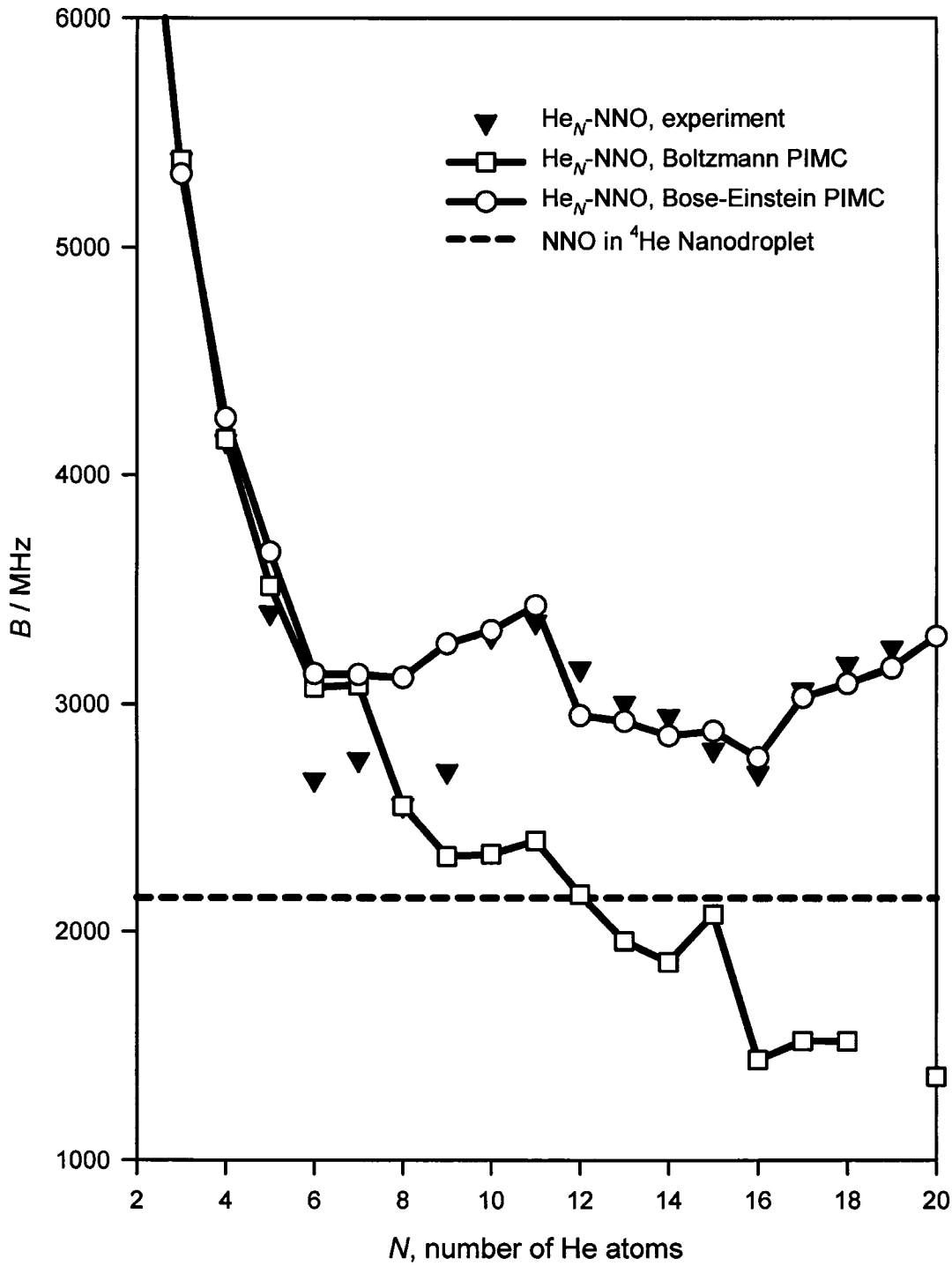

Figure 5.8 Evolution of B with N for He_N–N_2O, from experiment (Refs. 26 and 27), Boltzman PIMC calculations (Ref. 27), and Bose-Einstein PIMC calculations (Ref. 27). The values of B determined from theory diverge at $N = 8$, indicating that exchange becomes important for He_N–N_2O clusters with $N > 8$.

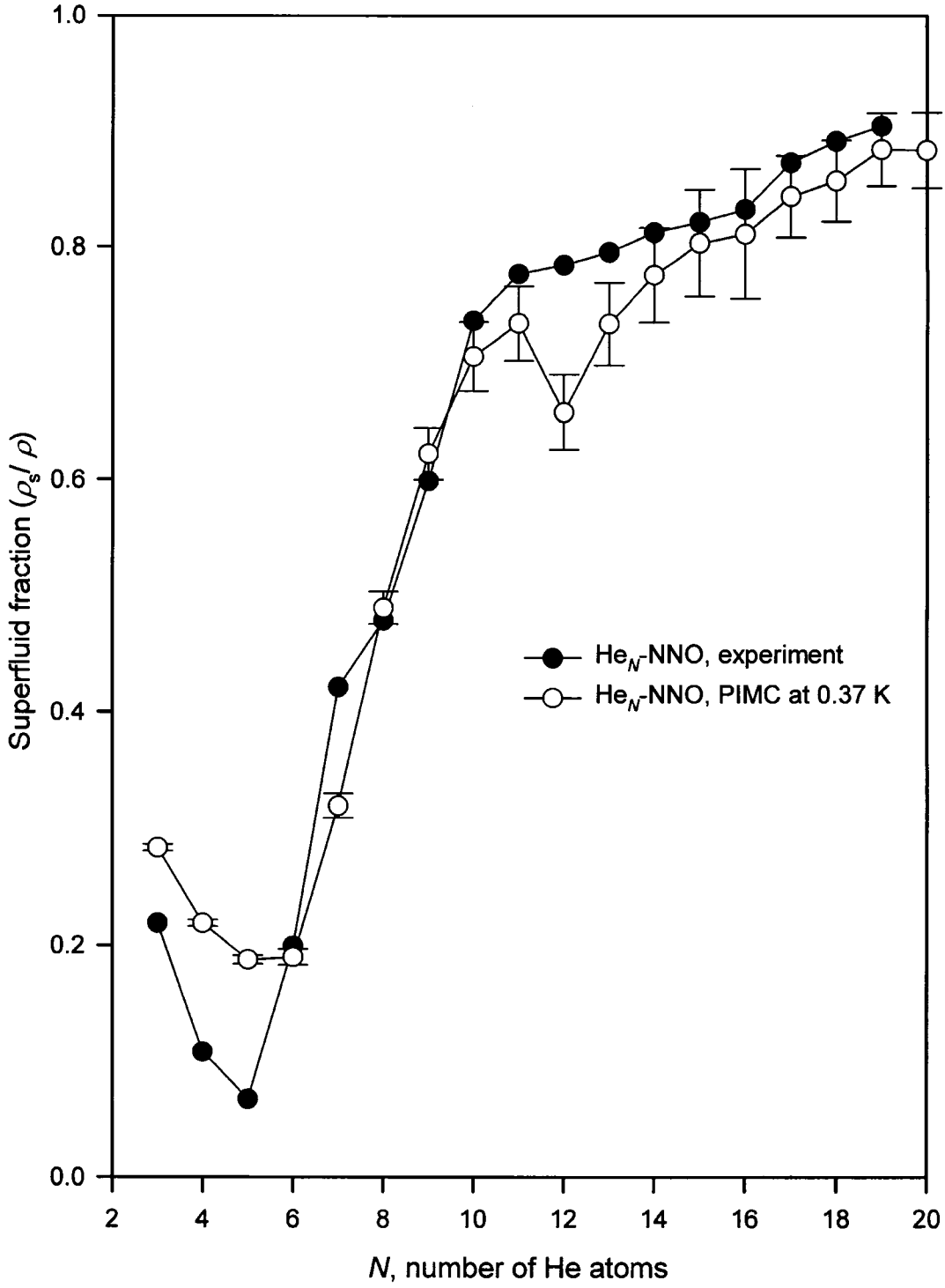

Figure 5.9 The ratio of superfluid to total ^{4}He density (ρ_s/ρ) for He_N–N_2O with N, from both experiment and PIMC calculations (from Ref. 27).

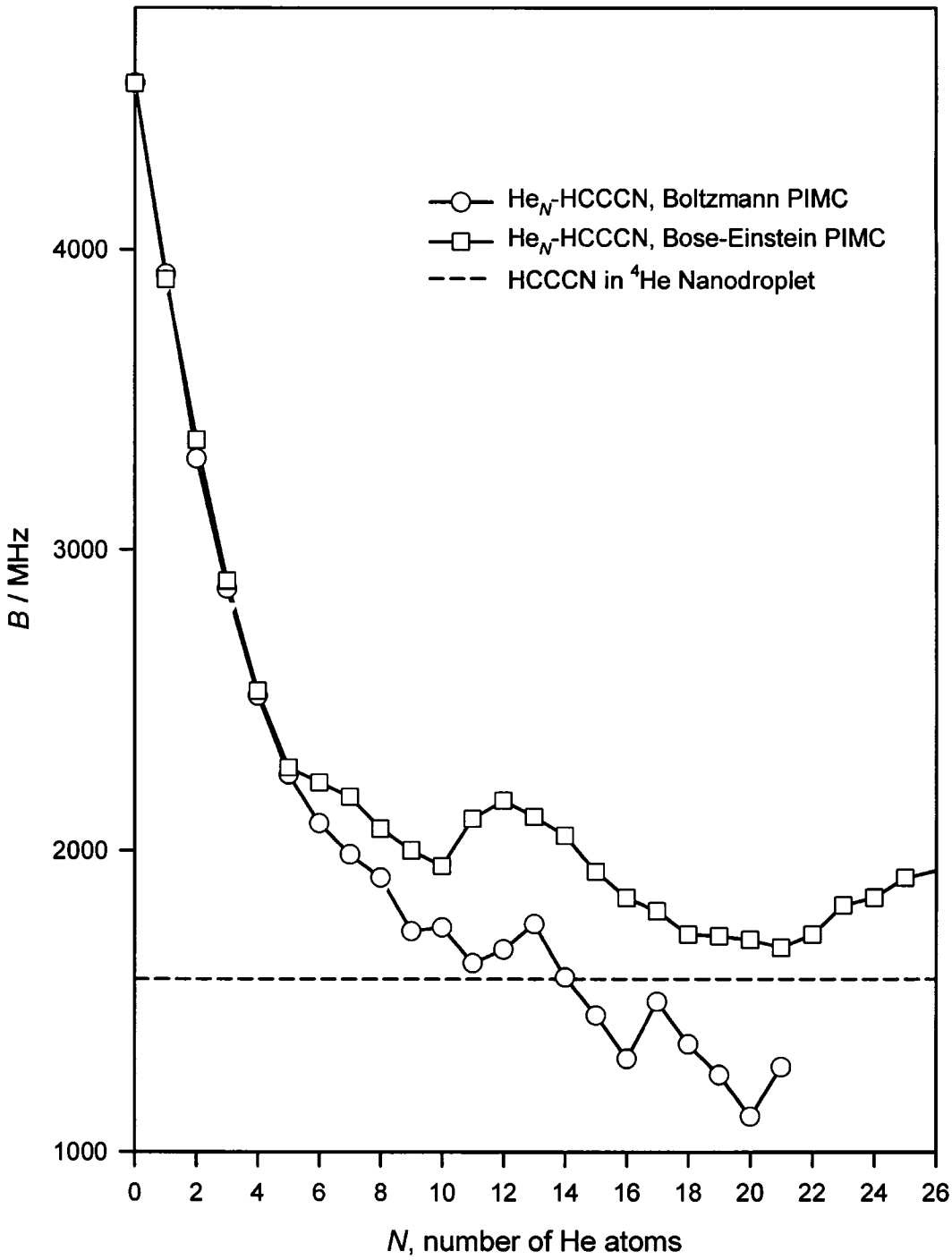

Figure 5.10 The evolution of B for He_N–HCCCN with N, for calculations using Boltzmann and Bose-Einstein Statistics (Ref. 44). Error bars are smaller than the symbols.

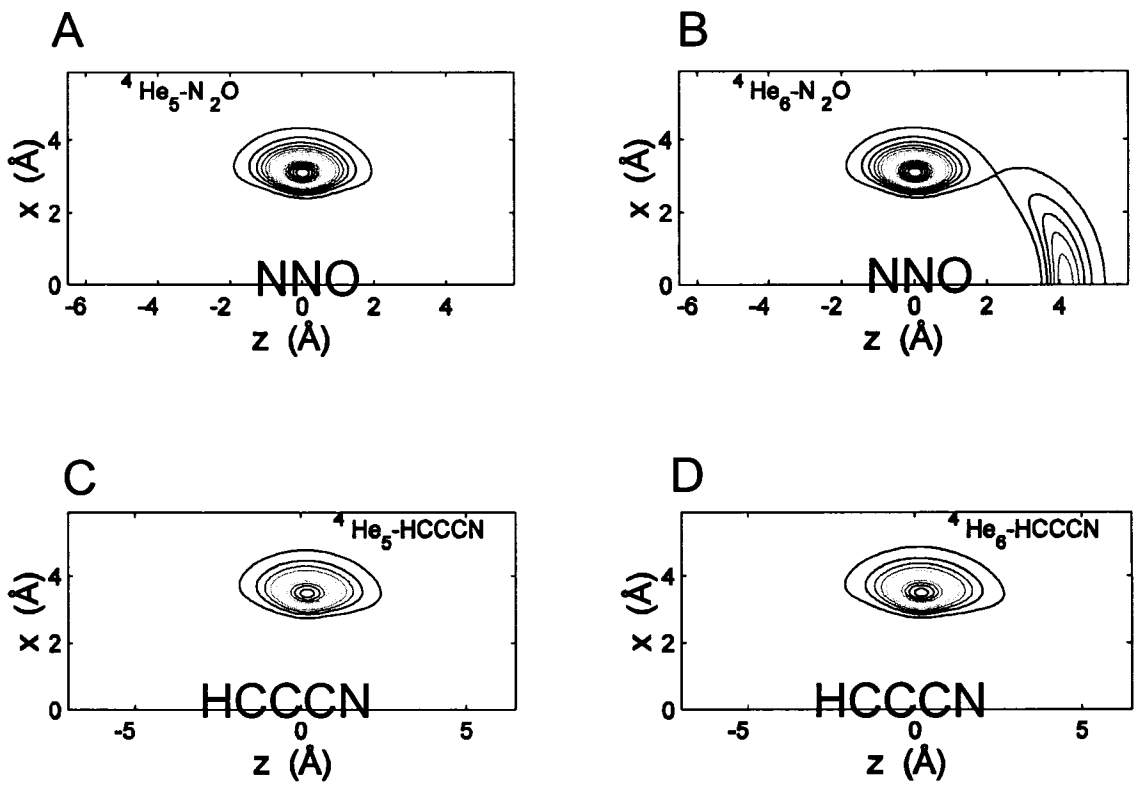

Figure 5.11 Contour plots of the helium density around (**A**) He_5–N_2O (Ref. 38), (**B**) He_6–N_2O (Ref. 38), (**C**) He_5–HCCCN (Ref. 44), and (**D**) He_6–HCCCN (Ref. 44) from PIMC calculations at T = 0.37 K. The contour lines represent increments of 0.01 $Å^{-3}$, starting with 0.005 $Å^{-3}$.

5.7 References

1. W. H. Keesom and M. Wolfke, *Two Different Liquid States of Helium* in *Helium 4*, edited by Z. M. Galasiewicz (Pergamon Press, Oxford, 1971).

2. W. E. Keller, *Helium-3 and Helium-4* (Plenum Press, New York, 1969).

3. P. Nozières and D. Pines, *The Theory of Quantum Liquids: Superfluid Bose Liquids* (Addison-Wesley Publishing Company, Inc., Redwood City, CA, 1990).

4. R. J. Donnelly, *Experimental Superfluidity* (University of Chicago Press, Chicago, 1967).

5. P. Kapitza, Nature **141**, 74 (1938).

6. J. F. Allen and H. Jones, Nature **141**, 243 (1938).

7. W. H. Keesom and A. P. Keesom, Physica **3**, 359 (1936).

8. J. F. Allen, R. Peierls, and M. Z. Uddin, Nature **140**, 62 (1937).

9. F. London, Nature **141**, 643 (1938).

10. L. Tisza, Nature **141**, 913 (1938). L. Tisza, Phys. Rev. **72**, 838 (1947).

11. L. Landau, J. Phys. **5**, 71 (1941).

12. E. Andronikashvili, J. Phys. (U. S. S. R.) **10**, 201 (1946).

13. J. F. Annett, *Superconductivity, Superfluids and Condensates* (Oxford University Press, Oxford 2004).

14. V. Peshkov, J. Phys. (U. S. S. R.) **10**, 389 (1946).

15. S. Grebenev, J. P. Toennies, and A. F. Vilesov, Science **279**, 2083 (1998).

16. M. Hartmann, N. Pörtner, B. Sartakov, J. P. Toennies, and A. F. Vilesov, J. Chem. Phys. **110**, 5109 (1999).

17. J. Tang, Y. Xu, A. R. W. McKellar, and W. Jäger, Science **297**, 2030 (2002).

18. K. Higgins and W. Klemperer, J. Chem. Phys **110**, 1383 (1999).

19. X. G. Song, Y. Xu, P.-N. Roy, and W. Jäger, J. Chem. Phys. **121**, 12308 (2004).

20. J. Tang and A. R. W. McKellar, J. Chem. Phys. **117**, 2586 (2002).

21. K. Harada, K. Tanaka, T. Tanaka, S. Nanbu, and M. Aoyagi. J. Chem. Phys. **117**, 7401 (2002).

22. W. C. Topic and W. Jäger, J. Chem. Phys. **123**, 064303 (2005).

23. Y. Xu and W. Jäger, Chem. Phys. Lett. **350**, 417 (2001).

24. Y. Xu and W. Jäger, J. Chem. Phys. **119**, 5457 (2003).

25. Y. Xu, W. Jäger, and A. R. W. McKellar, submitted for publication.

26. Y. Xu, W. Jäger, J. Tang, and A. R. W. McKellar, Phys. Rev. Lett. **91**, 163401-1 (2003).

27. Y. Xu, N. Blinov, W. Jäger, and P.-N. Roy, J. Chem. Phys. **124**, 081101 (2006).

28. J. Tang and A. R. W. McKellar, J. Chem. Phys. **119**, 754 (2003).

29. J. Tang, A. R. W. McKellar, F. Mezzacapo, and S. Moroni, Phys. Rev. Lett. **92**, 145503-1 (2004).

30. K. Nauta and R. E. Miller, J. Chem. Phys. **115**, 10254 (2001).

31. F. Paesani, A. Viel, F. A. Gianturco, and K. B. Whaley, Phys. Rev. Lett. **90**, 073401 (2003).

32. Y. Kwon, P. Huang, M. V. Patel, D. Blume, and K. B. Whaley, J. Chem. Phys. **113**, 6469 (2000).

33. J. P. Toennies and A. F. Vilesov, Angew. Chem., Int. Ed. **43**, 2622 (2004).

34. A. Viel and K. B. Whaley, J. Chem. Phys. **115**, 10186 (2001).

35. R. Zillich and K. B. Whaley, Phys. Rev. B **69**, 104517 (2004).

36. S. Baroni and S. Moroni, Phys. Rev. Lett. **82**, 4745 (1999).

37. S. Paolini, S. Fantoni, S. Moroni, and S. Baroni, J. Chem. Phys. **123**, 114306 (2005).

38. S. Moroni, N. Blinov, and P.-N. Roy, J. Chem. Phys. **121**, 3577 (2004).

39. C. Callegari, I. Reinhard, K. K. Lehmann, G. Scoles, K. Nauta, and R. E. Miller, J. Chem. Phys. **113**, 4636 (2000).

40. C. Callegari, A. Conjusteau, I. Reinhard, K. K. Lehmann, and G. Scoles, J. Chem. Phys. **113**, 10535 (2000).

41. J. M. Merritt, G. E. Douberly, and R. E. Miller, J. Chem. Phys. **121**, 1309 (2004).

42. I. Reinhard, C. Callegari, A. Conjusteau, K. K. Lehmann, and G. Scoles, Phys. Rev. Lett. **82**, 5036 (1999).

43. S. Thorwirth, H. S. P. Müller, and G. Winnewisser, J. Mol. Spec. **204**, 133 (2000).

44. N. Blinov and P.-N. Roy, private communication.

45. P. Sindzinger, M. L. Klein, and D. M. Ceperley, Phys. Rev. Lett. **63**, 1601 (1989).

6

He_N–cyanoacetylene clusters: high-resolution microwave spectra

This chapter details the microwave rotational spectroscopic study of He_N–cyanoacetylene clusters, for values of N ranging from 2 to 31. Section 6.1 describes the experimental setup used for the investigation of larger helium–cyanoacetylene clusters. The criteria used for the N assignment of the He_N–HCCCN clusters are discussed in Section 6.2, while the heavier isotopomers are discussed in Section 6.3. Analysis of the spectroscopic results for the asymmetric He_2-cyanoacetylene trimer (Section 6.4) are considered separately from prolate symmetric top clusters of size ranging from $N = 3$ to 31 (Section 6.5). The superfluid fractions and the evolution of B with N for He_N–cyanoacetylene and He_N–N_2O are contrasted, to gauge the impact of rotor length on the onset of superfluidity (Section 6.9).

6.1 Experimental details

The He_N–cyanoacetylene clusters were generated using a pulsed supersonic expansion through a General Valve nozzle with a cone shaped exit (series 9, orifice Ø = 0.8 mm). The sample mixtures used were composed of < 0.1% cyanoacetylene in He backing gas. The cyanoacetylene isotopomers were synthesized using the procedure described in Section 2.1. Rotational transition of the clusters with N = 2-17 and 26-31 were observed and their frequencies measured. The J = 1-0 frequencies of the clusters with N = 18-25 were too low to be observed with our Fourier transform microwave spectrometer. For He_N–cyanoacetylene clusters with N = 2 to 5, backing pressures ranging from 15 to 25 atm were employed for spectroscopic searches and measurements. For clusters with N = 6 to 17, the J = 1 - 0 rotational transitions were studied with backing pressures of 30 to 70 atm. For these cluster sizes the J = 2-1 transitions were studied at backing pressures of 25 to 48 atm. To form the largest He_N–HCCCN clusters ($N \geq 26$), both high pressure (~100 to 120 atm) and a cooled nozzle were required. The assignment of N values will be further discussed in the following section.

Spectroscopic searches for the J'-J'' = 1-0 transition of He_N–cyanoacetylene clusters with $N \geq 2$ were performed in the conventional manner. The excitation frequency was stepped through a desired frequency range, in increments of approximately 0.2 MHz. For each step, the mirror separation was reduced and the resonant frequency of the microwave cavity was determined by a scanning program. Searches for J = 2-1 for N = 2 to 6 where performed using this scanning technique. For larger clusters, N = 7 to

17 and 26 to 31, destructive MW-MW double resonance experiments were used to search for the $J = 2\text{-}1$ transitions. For these experiments (described in more detail in Section 2.3), a known rotational transition is monitored, while a second frequency is broadcast using a horn antenna, perpendicular to the axis of the microwave cavity. When searching for the $J = 2\text{-}1$ transition of a particular cluster, the $J = 1\text{-}0$ transition was monitored while the frequency broadcast by the horn antenna was scanned. When the broadcasted frequency coincided with the $J = 2\text{-}1$ transition of that He_N–cyanoacetylene cluster, the coherence of the monitored $J = 1\text{-}0$ transition was destroyed, and the observed intensity of the $J = 1\text{-}0$ transition was reduced (shown in Figure 2.7). The main advantage of this searching technique is that only transitions of the cluster of interest are observed and, in particular, only those that have a rotational energy level in common with the $J = 1\text{-}0$ transition monitored. This provides conclusive evidence that the two rotational transitions belong to the same He_N-cyanoacetylene complex. Since a known transition is continuously observed, this technique also confirms that the experimental conditions are within the range required to generate and observe the cluster of interest. For $N = 6$ to 17, the $J = 2\text{-}1$ rotational transition was measured after being located by destructive MW-MW double resonance, using the FTMW instrument in the usual manner. For $N = 26$ to 31, the frequency of two nuclear quadrupole hyperfine components of the $J = 2\text{-}1$ transition ($F_1F_2' - F_1F_2'' = 2\text{-}2$ and $3\text{-}2$) were determined by observing the decrease in the $J = 1\text{-}0$, $F = 2 - 1$ hyperfine component, while stepping the double resonance frequency by 0.1 MHz. The estimated accuracy of the $J = 2\text{-}1$ hyperfine components measured with this technique is 50 kHz, versus an estimated

accuracy of 7 kHz for those determined in the conventional manner.

6.2 Assignment of cluster size: He_N–HCCCN

As He atoms are added around a cyanoacetylene molecule, classical physics predicts that the moment of inertia of subsequent cluster sizes will increase. In this scenario, the frequency of the He_N–cyanoacetylene clusters would decrease steadily with increasing N. For $1 < N < 6$, the frequency of the $J = 1$-0 transition decreased by 9% to 15% with the addition of subsequent He atoms, corresponding to a decrease in frequency of 360 MHz to 1200 MHz. During the spectral search for He_6–HCCCN, however, it became evident that more complex behaviour was eminent. The search for the $J = 1$-0 transition of He_6–HCCCN revealed two transitions, both with the nuclear quadrupole hyperfine structures of the $J = 1$-0 transition of a HCCCN containing cluster, but separated by less than 10 MHz. Attributing each observed rotational transition to the He_N–cyanoacetylene cluster with the correct number of He atoms proved to be one of the most complex aspects of this project.

The N value assignment of He_N–molecule clusters is performed by careful study of the relative behaviour of the transition intensities of different clusters when experimental conditions are changed. More specifically, studies of dependence of rovibrational transition intensities on backing pressure or nozzle temperature, performed in the infrared spectral region, are particularly useful for assigning N values.[1, 2, 3, 4] The bandwidth of the IR instrument allows many cluster sizes to be simultaneously studied as the experimental

conditions are manipulated. Larger clusters are formed in greater abundance as the backing pressure is increased, or as the nozzle temperature is lowered. Careful adjustments of the molecular expansion conditions allow the precise conditions that generate new He_N–molecule clusters to be identified (Ref. 3 contains many examples of this technique). Previous microwave studies of He_N–molecule clusters for $N > 3$ have been aided by supporting infrared information for the N value assignment.[1, 4, 5, 6] For He_N–N_2O, IR data was available for N up to 9 (Ref. 4).

Insufficient overlap between strong HCCCN vibrational transitions and available laser frequency coverage prevented the study of corresponding rovibrational transitions for the He_N–HCCCN clusters for $N \geq 1$. For He_N–HCCCN for $N > 5$, N assignment was based on both microwave studies and predictions of the $J = 1\text{-}0$ and 2-1 rotational transitions from ground state calculations by Moroni.[7]

a) The dependence of the J = 1-0 transition signal on backing pressure

Many sets of detailed pressure dependence studies of the $J = 1\text{-}0$ rotational transitions were conducted for all He_N–HCCCN clusters with $N \leq 17$. Each set of pressure dependence studies was performed using a single sample, at high pressure. The valve to the main sample reservoir was closed and a single transition was measured for 100 averaging cycles, to obtain the signal to noise ratio. Over the course of 100 cycles, the sample pressure dropped an average of 1 atm. These experiments were continued until the transition could not be distinguished from background noise. The valve to the main sample reservoir was re-opened and the rotational transition was measured again (at

essentially the initial pressure) to ensure that the signal intensity returned to its initial value. The cavity was then tuned into resonance with the next transition of interest, and the experiments were repeated. A set of studies consists of all the pressure dependence studies conducted using a single sample and performed consecutively. Only studies from within a single set will be compared, as sample concentration can influence the intensities of the rotational transitions of He_N–cyanoacetylene clusters.

Figure 6.1 is a plot of the observed signal to noise for the F = 2-1 component of the J = 1-0 transition of four He_N–HCCCN clusters. The frequencies of the rotational transitions monitored were 3783.9821 MHz (filled circles), 3777.5867 MHz (open circles), 3515.3637 MHz (filled triangles), and 3502.4541 MHz (open triangles). In contrast to IR studies, direct comparison of signal intensities in different frequency regions can be misleading for microwave experiments. The narrow bandwidth of the microwave instrument means that only one rotational transition may be monitored at a time. Also, the observed transition strength will depend on the resonance of the cavity at that particular frequency (a property that varies greatly for frequencies between 3.2 and 4.0 GHz). For this reason, it is only appropriate to directly compare the intensity and pressure dependence of rotational transitions that are close in frequency. The transitions at 3783.9821 MHz (filled circles) and 3777.5867 MHz (open circles) are both quite strong. Under the sample conditions of this study, the transition at 3783.9821 MHz grows in at ~20 atm, reaches maximum strength at 43 atm and slowly decreases for higher backing pressures. In contrast, the transition at 3777.5867 MHz grows in at ~35 atm and reaches maximum strength at 49 atm. Both the high pressure needed to observe

the cluster and the rapid increase in signal strength to a maximum are indicators that the transition at 3777.5867 MHz is due to a cluster which is significantly larger than that at 3783.9821 MHz. The higher signal to noise ratio of the transition at 3783.9821 MHz indicates that this cluster is always formed in higher abundance than the cluster that gives rise to the transition at 3777.5867 MHz. The decline in signal to noise for the 3783.9821 MHz transition above 43 atm suggests competitive formation of larger clusters at the expense of smaller ones at high pressure. The transition at 3783.9821 MHz was assigned to He_6–HCCCN while that at 3777.5867 MHz was eventually assigned to He_{14}–HCCCN.

The observed signal strengths of the transitions at 3515.3637 MHz and 3502.4541 MHz are much weaker than the pair discussed above. For our instrument operating in the 3.2 to 4.0 GHz frequency region, a general trend is that cavity resonance decreases with decreasing frequency. For this reason, it is impossible to make even qualitative statements about the relative abundance of the clusters that give rise to the transitions at ~3.5 GHz compared to either He_6–HCCCN or He_{14}–HCCCN. In fact, even the pressures at which these two pairs of clusters are first observed cannot be directly compared; the lower resonance of the cavity at lower frequency means the instrument is less sensitive in this region. With this in mind, Figure 6.1 shows that the transition at 3515.3637 MHz is first observed at ~35 atm and reaches a maximum signal to noise ratio at 47 atm. The transition at 3502.4541 MHz is not observable until ~44 atm and does not obtain a maximum signal to noise before 59 atm. The pressure at which the signal to noise reaches a maximum value is independent of cavity resonance considerations. These transitions were assigned to He_{10}–HCCCN and He_{15}–HCCCN, respectively.

On the basis of pressure dependence studies alone, discriminating between small clusters (N = 1 - 6) was relatively straight forward. In one study comparing clusters of N = 1-4, He–HCCCN was detectable at 3.8 atm, He_2–HCCCN at 4.7 atm, He_3–HCCCN at 6.1 atm, and He_4–HCCCN at 13.4 atm using only 10 averaging cycles. He_N– HCCCN clusters of N = 8-10 had sequential pressure dependence in terms of cluster formation and pressure at which maximum signal to noise ratio was achieved. Under experimental conditions favouring larger He_N–HCCCN clusters, N = 13 and 14 were found to form sequentially at 31 atm and 34 atm, respectively. Under the same conditions, He_{15}–HCCCN and He_{16}–HCCCN were often formed at very similar pressures (~ 40 atm). The respective assignment of these two clusters was based on the steeper pressure dependence of the He_{16}–HCCCN signal to noise ratio when compared to the smaller He_{15}–HCCCN cluster. The formation pressure of both these complexes is significantly higher than that of all smaller clusters. He_{17}–HCCCN was only detected when the backing pressure exceeded 45 atm. However, due to the low signal intensity (resulting from small instrumental cavity modes at low frequencies) detailed pressure dependence studies were not performed for this cluster. Very large He_N–HCCCN clusters with N = 26-31 were not observed when the backing pressure was less than 80 atm. Transitions corresponding to these clusters were first observed with a room temperature nozzle, and a sample pressure of 115 atm. These signals disappeared if the sample pressure dropped below 90 atm.

Pressure dependence studies of the He_N–HCCCN J = 1-0 rotational transitions eventually assigned to N = 7, 11, and 12 did not allow a definitive N assignment based on

this method alone. The cluster size assignment of a majority of the He_N–HCCCN clusters investigated, however, could be accomplished by solely studying the pressure dependence of their J = 1-0 rotational transition intensities. This cluster size assignment was further supported by the studies of the dependence of the J = 1-0 transition intensity on HCCCN concentration and on nozzle temperature.

b) The dependence of the J = 1-0 transition signal on sample concentration

Comparing the pressure dependence of transitions that were similar in frequency was invaluable in making the N assignment. There were, however, some anomalous clusters whose pressure dependence made them difficult to assign. Specifically, transitions that are now assigned to He_7–HCCCN have signal intensities that depend on pressure in a manner similar to those assigned to He_{12}–, He_{13}–, and He_{14}– HCCCN. Figure 6.2 shows a pressure dependence study that compared He_8–HCCCN (3713.6078 MHz), He_7–HCCCN (3927.4571 MHz), and He_{12}–HCCCN (3978.5747 MHz). While the instrument is slightly more sensitive at 3.9 GHz than 3.7 GHz, He_8–HCCCN first appeared at ~23 atm while the transitions assigned to He_7–HCCCN were not observed until ~30 atm. The transition assigned to He_{12}–HCCCN appears at a slightly higher pressure, ~33 atm. The final assignment of He_7– HCCCN and He_{12}–HCCCN was made by consideringt the relative effect that sample concentration had on their signal intensities.

Measurements of the J = 1-0 signal intensity for different sample concentrations allowed a rough separation of observed transitions: clusters that can be formed with concentrations > 0.05% HCCCN (N = 1 to ~10), and those which show improved signal

intensity with concentrations < 0.05 % HCCCN (N > ~14). The relative behaviour of the signal intensities of the rotational transitions at 3927.4571 MHz and 3978.5747 MHz with samples of different concentrations was the main motivation for assigning these transitions to He_7–HCCCN and He_{12}–HCCCN, respectively. The largest clusters, N = 26 to 31, were only observed when sample concentrations were < 0.03% HCCCN.

c) The dependence of the J = 1-0 transition signal on nozzle cooling

Figure 6.3 shows the signal improvement achieved for He_{26}–HCCCN when the nozzle was cooled to -20 °C (253.15 K) compared to the same cluster studied with identical pressure and sample composition, but with a nozzle operating at room temperature. Similar improvement in signal intensity was observed for N = 27 to 31. For clusters of $N \leq 17$, no improvement in signal intensity was observed when nozzle cooling was implemented.

d) Ground State predictions of J = 1-0 and 2-1

Ground State reptation quantum Monte Carlo (RQMC)[8, 9] calculations by Moroni also helped with the N assignment of He_N–HCCCN clusters.[7] Ground State values for the J = 1-0 and J = 2-1 rotational transitions of He_N–HCCCN for N = 3 to 23, 25, 27, and 30 became available while I was conducting spectral searches for clusters with N > 7.[7] These predictions were able to help guide and refine the spectral search. The absolute correspondence between the predicted transition frequencies and those observed in the microwave frequency region ranged significantly, from a minimum difference of 18 MHz

for He_6–HCCCN to a maximum of 400 MHz for He_{15}–HCCCN, for the J = 1-0 rotational transition. The qualitative behaviour of the transition frequencies with the addition of successive helium atoms proved an invaluable aide to both spectral searches and N value assignment for the He_N-HCCCN clusters. Figure 6.4 gives the J = 1-0 and J = 2-1 rotational transition frequencies, both from ground state calculations and those observed experimentally, of He_N–HCCCN clusters versus their assigned N values, for N = 1 to 17, and 26 to 31.

The relative assignment of the clusters N = 26 through N = 31 is based on the trend of the frequency of the rotational transitions. The B value of the clusters for N between 18 and 25, inclusive, renders their J = 1-0 rotational transitions too low in frequency to observe with our spectrometer. In order for larger clusters to be observed, the B value must begin to increase at some cluster size. Once the experimental conditions allowed the growth of new (larger) clusters, the rotational transition of lowest frequency was assigned to the smallest new cluster. The absolute assignment of this transition to N = 26 was aided by the transition frequencies predicted by Ground State calculations (Ref. 7). The J = 1-0 transition frequency from Ground State calculations for N = 15, 16, and 17 were an average of 387 MHz higher in frequency than the measured values. For the larger clusters, Ground State predictions were available for N = 25, 27, and 30. If the lowest large cluster were assigned to N = 25, the average difference between the calculated and measured J = 1-0 frequencies of N = 25, 27, and 30 is 265 MHz. If this transition was assigned to N = 26, the average frequency difference for N = 27 and 30 was 361 MHz, and to N = 27, the difference is 484 MHz. Assigning the lowest observed

transition to $N = 26$ is a compromise between over- and underestimating the correspondence between the Ground State frequencies and measured transitions. The relative ordering of clusters $N = 26$ through 31 is essentially certain, although I estimate that the actual cluster sizes could vary by ± 1.

6.3 Assignment of cluster size: He_N–DCCCN and He_N–$HCCC^{15}N$

The search for the He_N–DCCCN and He_N–$HCCC^{15}N$ clusters was conducted using B rotational constants predicted by scaling of the He_N–HCCCN B values. The fitted B rotational constants of He_N–HCCCN allow the effective inertia of the helium density observed experimentally to be determined:

$$I_{He\ (effective)} = I_{He_N\text{-}HCCCN} - I_{HCCCN} \qquad (6\text{-}1)$$

where $I_{HCCCN} = k/B_{HCCCN}$ and $I_{He_N\text{-}HCCCN} = k/B_{He_N\text{-}HCCCN}$. Here, k is a conversion factor (505 379 MHz amu Å^2), B_{HCCCN} is the rotational constant of the free HCCCN molecule in MHz, and $B_{He_N\text{-}HCCCN}$ is the rotational constant of the cluster with N He atoms in MHz and I_{HCCCN} is expressed in units of amu Å^2. Adding the moment of inertia of the isotopomer of interest, $I_{isotopomer}$, to $I_{He\ (effective)}$, yields a good prediction of the rotational constant for a given cluster upon isotopic substitution. The B rotational constants predicted for He_N–DCCCN and He_N–$HCCC^{15}N$ clusters in this manner were less than 50 MHz and 24 MHz away from the experimentally determined constants, respectively. It was less difficult to make N assignments for the heavier isotopomers for

this reason. When ambiguity arose, the final N assignment was made by considering the distortion parameter, D, of the clusters in question. The distortion parameters are always smaller for a heavier isotopomer He_N–cyanoacetylene cluster, compared to the analogous HCCCN cluster. The D of He_N–HCCCN was used as an upper threshold value, to aid in assigning the N values of the heavier isotopomers.

6.4 He_2–cyanoacetylene: experimental results and spectroscopic analysis

A microwave spectral search for He_2–molecule trimers is arduous, given the narrow band width of the microwave instrument (~0.2 MHz) and the difficulty encountered predicting rotational transition frequencies of these floppy complexes.[5, 10] For trimers containing heavier atoms, such as Ar_2–OCS[11] and Ne_2–OCS,[12] spectra are normally predicted using a pairwise additive model for the trimer geometry. The effective bond lengths in the corresponding dimers are used to predict A, B, and C rotational constants for the trimer. The helium dimer has a ground state separation of 62 ± 10 Å,[13] much longer than that of a He–molecule dimer. During spectral searches for He_2–OCS, the trimer was initially assumed to be a planar complex, held together by the He–OCS interaction alone.[5, 10] The dihedral angle ϕ is defined as the angle between one He atom, the OCS centre of mass (c.m.), the sulfur atom and the second He atom. In this model ϕ was 180°, as the trimer geometry was assumed to be determined solely by the He–OCS interaction. The J = 1-0 transition of He_2–OCS was found within 100 MHz of

the predicted frequency, but the $J = 2\text{-}1$ transition was eventually found more than 1 GHz lower than predicted.[5, 10] The geometry of the He_2–OCS trimer was determined to be non-planar, but rather that of a floppy asymmetric top, with an approximate value of $\phi = \sim 118°$.[2]

For the spectral search of He_2–cyanoacetylene, I assumed a bent geometry for the trimer with $\phi = 120°$, with the dihedral angle formed by one He atom, the cyanoacetylene c.m., the N-nucleus and the second He atom. The resulting predictions for the $J_{KaKc} = 1_{01}\text{-}0_{00}$ and $J_{KaKc} = 2_{02}\text{-}1_{01}$ transitions were found to be more than 700 MHz and 900 MHz too low, respectively. The measured $J_{KaKc} = 1_{01}\text{-}0_{00}$ and $2_{02}\text{-}1_{01}$ transition frequencies of He_2–cyanoacetylene trimers are given in Table 6.1.

The spectroscopic parameters of each He_2–cyanoacetylene isotopomer were fit to the measured transition frequencies with Pickett's least squares fitting program SPFIT,[14] using Watson's *A*-reduced Hamiltonian for a prolate asymmetric top.[15] Rotational transitions of each isotopomer of He–cyanoacetylene were fit separately. The two rotational transitions observed for each of He_2–HCCCN, He_2–HCCC^{15}N, and He_2–DCCCN, allowed the *B* and *C* rotational constants to be fit. The *A* rotational constant was frozen at 10 000 MHz, a large value consistent with that expected by a near-prolate asymmetric top. For He_2–H^{13}CCCN, He_2–HC^{13}CCN, and He_2–HCC^{13}CN, only a single rotational transition was observed, allowing $(B + C)/2$ to be fit, while *A* was frozen at 10 000 MHz. The fitted spectroscopic parameters are given in Table 6.1.

Figure 6.5 shows the He_2–HCCCN van der Waals trimer in its principal inertial axis system, along with the structural parameters used to describe the complex. Like

He_2–OCS, He_2–cyanoacetylene is a floppy, prolate asymmetric top. While not strictly appropriate, assuming the trimer is a rigid complex does allow an effective geometry of He_2–cyanoacetylene to be calculated. An effective structure of the He_2–cyanoacetylene van der Waals trimer was determined using Kisiel's STR*ucture* FIT*ting to rotational data* program.[16] ϕ was fitted using the B and C rotational constants of the $HCCC^{15}N$, HCCCN and DCCCN containing trimers, and $B + C$ of the measured ^{13}C-containing cyanoacetylene isotopomers. The bond lengths of the cyanoacetylene molecule were frozen at ground vibrational state values reported by Tyler and Sheridan.[17] The distance between each He atom and the cyanoacetylene centre of mass, R, and the angle between R and the cyanoacetylene molecular axis θ were frozen at the values determined for the He–cyanoacetylene dimer, $R = 3.93 \pm 0.05$ Å and $\theta = 80.1 \pm 1.3°$. Using the rotational parameters of six He_2–cyanoacetylene isotopomers, ϕ was found to be $144.9 \pm 7.7°$.

6.5 He_N–cyanoacetylene, $N \geq 3$: experimental results and spectroscopic analysis

The measured $J = 1$-0 and $J = 2$-1 transition frequencies of He_N–HCCCN ($N = 3$-17 and 26-31), He_N–$HCCC^{15}N$ ($N = 3$-16), and He_N–DCCCN ($N = 3$-15) are given in Tables 6.2, 6.3, and 6.4, respectively. The nuclear quadrupole hyperfine structures due to the ^{14}N nucleus ($I = 1$) were resolved for the $J = 1$-0 and $J = 2$-1 transitions of clusters containing HCCCN and DCCCN. Additional splitting due to the D nucleus ($I = 1$) was observed for the rotational transitions of He_N–DCCCN clusters, as shown for

He_4–DCCCN in Figure 6.6. The smaller magnitude of the D nuclear quadrupole moment compared to that of the ^{14}N nucleus, prevented these hyperfine structure from being fully resolved for some clusters. The D hyperfine structure and the Doppler splitting collapsed into a single, unresolvable peak in some cases, shown in the spectrum of He_8–DCCCN in Figure 6.6. The measured frequency of a partially resolved peak was attributed to a D nuclear quadrupole hyperfine component, when Doppler splitting was unresolvable. When the nuclear quadrupole hyperfine structures due to D could not be resolved even partially (for example, $N = 10$, 11, 12, 14, and 15 for He_N–DCCCN), the centre of the resulting broad peak was taken to be that of the ^{14}N nuclear quadrupole component.

The spectroscopic parameters of each He_N–cyanoacetylene isotopomer were fit to the measured transition frequencies, with Pickett's least squares fitting program SPFIT.[18] For N ≥ 3, the clusters were assumed to be prolate symmetric tops, whose transition frequencies can be adequately described by the rotational energy levels of a linear molecule:

$$\nu_{(J+1)\leftarrow J} = 2B(J+1) - 4D(J+1)^3 \qquad (6\text{-}2)$$

where $\nu_{(J+1)\leftarrow J}$ is the frequency of the transition between the J and $(J+1)$ rotational energy levels. The two transitions observed for each He_N–cyanoacetylene cluster, $J = 1$-0 and $J = 2$-1, allowed a fit of both the B rotational constant and the D distortion parameter, using Pickett's fitting program SPFIT.[18] The nuclear quadrupole hyperfine structures were fit using the $\boldsymbol{J} + \boldsymbol{I}_{^{14}N} = \boldsymbol{F}$ coupling scheme for He_N–HCCCN clusters. The $\boldsymbol{J} + \boldsymbol{I}_{^{14}N} = \boldsymbol{F}_1$, $\boldsymbol{I}_D + \boldsymbol{F}_1 = \boldsymbol{F}_2$ coupling scheme was used for He_N–DCCCN clusters. The

fitted rotational parameters of He_N–$HCCC^{15}N$, He_N–HCCCN, and He_N–DCCCN are given in Tables 6.2, 6.4, and 6.5, respectively. All He_N–DCCCN clusters were assigned quantum numbers corresponding to rotational energy levels split by two quadrupolar nuclei. When the D nuclear quadrupole hyperfine structure was not resolved, the $\boldsymbol{J} + \boldsymbol{I}_{^{14}N} = \boldsymbol{F}_1$, $\boldsymbol{I}_D + \boldsymbol{F}_1 = \boldsymbol{F}_2$ coupling scheme was used but χ_{aa} (D) was set to 0.0 MHz during the fitting procedure.

6.6 The evolution of B with N for He_N–cyanoacetylene

The B rotational constant is inversely proportional to the moment of inertia with respect to the b-axis in the principal inertial axis system. For the free HCCCN molecule, B = 4549.05859 (4) MHz.[19] If He_N–cyanoacetylene clusters obeyed classical physics, the moment of inertia would be expected to increase as the number of He atoms increased. Figure 6.7 shows the evolution of the B rotational constant and D distortion constant of He_N–HCCCN, He_N–$HCCC^{15}N$, and He_N–DCCCN, versus N. For all three isotopomers, B decreases smoothly with each additional He atom added to the cluster for N = 3 to 6. At N = 7, B increases, indicating that going from He_6– to He_7–cyanoacetylene results in a net reduction in the effective moment of inertia with respect to the b-axis. B decreases for N = 8 and 9, but begins to increase again at N = 10. This reduction in moment of inertia with respect to the b-axis with the addition of successive He atoms continues until B reaches a maximum at N = 13. A steady decrease in B then occurs for N = 14-17, after which the J = 1-0 transition frequencies dropped out of the range of our instrument. It is

assumed that this decrease in B continues to a minimum value, after which a second "turn-around" occurs and an increase in B is observed. This second turn-around was confirmed for He_N–HCCCN, as B values for $N = 26$ to 31 were determined. The B rotational constant of HCCCN in a ^{4}He nanodroplet is 1573.7 (7) MHz,[20] lower than that of He_{31}–HCCCN. The B values for $N = 26$ to 31 seem to increase smoothly towards an undetermined maximum value. To converge to the limiting B value of a ^{4}He nanodroplet, B must attain at least one more maximum value at N, after which the moment of inertia will begin to increase.

In Figure 6.8, $I_{He\ (effective)}$ (defined in equation 6-1) is compared to the moment of inertia of the helium density around He_N–HCCCN, determined using PIMC calculations.[21] The PIMC calculations treat the helium atoms as distinguishable particles, which obey Boltzmann statistics. In this scenario, the moment of inertia of the helium density around HCCCN increases with the addition of successive He atoms. Experimental values, however, begin to deviate at $N = 6$ from the moment of inertia of the calculated helium density. At $N = 7$, the effective He moment of inertia decreases. From this point on, the experimental and calculated values of the inertia of helium density around HCCCN diverge completely. This illustrates how significantly the observed B versus N behaviour of He_N–cyanoacetylene clusters deviates from that expected for a system that obeys Boltzmann statistics.

6.7 The geometry and stability of He_N–cyanoacetylene clusters

Relative positions of the He atoms within He_N–OCS (Refs. 1, 2, 5) and He_N–N_2O (Refs. 4, 6) have been deduced using both IR bandshift values and complimentary isotopic information from high resolution MW studies. A lack of IR transitions for He_N–cyanoacetylene makes a definitive determination of the cluster geometries impossible using only the experimental evidence acquired in the MW frequency region. Studying the solvation of three isotopomers of cyanoacetylene with He atoms, however, does allow some insight into the distribution of the helium density for certain values of N.

a) N = 3 to 6

The change in moment of inertia that accompanies that addition of a helium atom can be used to elicit structural information about the He_N–cyanoacetylene clusters:

$$\Delta I = I_N - I_{(N-1)} \qquad (6\text{-}3)$$

where I_N is the effective moment of inertia of the He_N-cyanoacetylene cluster and $I_{(N-1)}$ is that of the next smallest cluster. The results are shown in Figure 6.9 for He_N–HCCCN, He_N–HCCC^{15}N, and He_N–DCCCN. For N = 3 to 5, ΔI of the three cyanoacetylene isotopomers are nearly identical, indicating that the projection of these He atoms onto the cyanoacetylene axis lies very close to the c.m. of the HCCCN linear molecule. DCCCN and HCCC^{15}N have essentially the same mass. A different distribution of this mass means that the c.m. of DCCCN is shifted 0.06 Å closer towards the hydrogen end compared to HCCCN, while for HCCC^{15}N it is shifted 0.04 Å towards the nitrogen end compared to

HCCCN. Adding He atoms to a ring centred on the HCCCN c.m. would result in each additional He atom increasing the cluster moment of inertia by similar amounts for each N, but also for all three isotopomers. This corresponds to each He atom occupying an equivalent position, taking an equatorial position around the axis of the cyanoacetylene molecule as for He–cyanoacetylene. The separation between adjacent He atoms decreases as each successive He atom joins the ring. Figure 6.7 shows that the centrifugal distortion constant of each cluster decreases for $N = 3$ to 5, indicating that the increased interactions between He atoms on the ring leads to stabilization of the cluster. These stabilizing interactions reach a maximum at $N = 5$.

The sixth atom in both He_6–N_2O (Refs. 4, 6) and He_6–OCS (Refs. 1, 2, 5) has been found to occupy a position near the secondary minimum of the He–N_2O or He–OCS potential energy surface. For both species, IR bandshift information and isotopic studies in the microwave frequencies region showed that the sixth He atom was located further from the centre of mass of the linear molecule than the first five He atoms. This is accompanied by an increase in the distortion constant of $N = 6$ compared to $N = 5$ by a factor of ~24 for He_N–N_2O,[4] and ~11 for He_N–OCS.[1] For He_N–HCCCN, the cluster distortability increases only by a factor of ~4 for $N = 6$ compared to $N = 5$, and slightly less for the heavier isotopomers. The addition of a sixth He atom to He_5–cyanoacetylene decreases the stability of the cluster, but to a lesser degree than that observed for He_6–N_2O or He_6–OCS. The ΔI values for all isotopomers of He_6–cyanoacetylene are essentially the same, as seen in Figure 6.9. In contrast to the N_2O– and OCS–He clusters, this suggests that the projection of the sixth He atom in He_6–cyanoacetylene

onto the axis of the molecule is close to the centre of mass of cyanoacetylene. I propose that the geometry of He_6–cyanoacetylene corresponds to a somewhat diffuse equatorial ring of six He atoms around the cyanoacetylene axis. This geometry is pictured in Figure 6.9.

b) N = 7

The addition of a seventh He atom to the He_6–cyanoacetylene cluster causes a net decrease in the effective inertia of the cluster. This is seen as an increase in *B* for He_7–cyanoacetylene compared to He_6–cyanoacetylene in Figure 6.7. The decrease in the moment of inertia of He_7–cyanoacetylene compared to He_6–cyanoacetylene is due to a redistribution of the helium density around the molecule, similar to that observed for He_7–N_2O.[4, 6] ΔI is quite varied for the isotopomers, and it is from these values that we can make deductions about the structure of He_7–cyanoacetylene. The differences in ΔI for the isotopomers suggest that this He atom is located further from the cyanoacetylene c.m. If the seventh He atom adds to the hydrogen end, the c.m. of the He_7–cyanoacetylene cluster will shift towards the hydrogen end. As the c.m. of He_7–DCCCN is closer to the hydrogen end than that of He_7–HCCC^{15}N, adding the seventh He atom to this end should have caused a smaller change in ΔI for He_7-DCCCN compared to He_7–HCCC^{15}N. Indeed, it is observed that ΔI = -8.8 amu Å^2 for He_7–HCCC^{15}N, but is only -5.7 amu Å^2 for He_7-DCCCN . Based on these findings, I suggest that the seventh He atom is located near the hydrogen end of the cyanoacetylene molecule. This geometry is associated with an increase in the distortability of the

He_7–cyanoacetylene cluster, as demonstrated by the increase in D by a factor of ~5 when going from $N = 6$ to $N = 7$. The intermolecular PES of He–cyanoacetylene has a broad secondary minimum located at the H-end of the cyanoacetylene molecule, as discussed in Chapter 4 and illustrated in Figure 4.2. Localization of helium density in the secondary minimum of the He–molecule PES was observed for both He_6–OCS[1, 2, 5] and He_6–N_2O,[4, 6] once the equatorial ring has been filled. The addition of the seventh He atom to a position near the secondary minimum of the He–cyanoacetylene PES is, thus, consistent with these findings.

c) $N = 8$ to 13

It is difficult to make too definitive statements about the geometry of the clusters $N = 8$ to 11, given the limited experimental information available. ΔI values for He_9– and He_{10}–DCCCN are omitted from Figure 6.9, as only one transition was found for He_9–DCCCN. For He_{11}– and He_{12}–cyanoacetylene, however, the ΔI values of the three isotopomers begin to converge. This suggests that the c.m. of the clusters with $N = 11$ and 12 are once again shifting back towards the c.m. of the linear molecules. At $N = 13$, once again the ΔI of the three isotopomers are identical, indicating that projection of the thirteenth He atom onto the cyanoacetylene axis coincides almost exactly with the c.m. of HCCCN. There is a sudden drop in D for He_{13}–cyanoacetylene (see Figure 6.7), indicating that this cluster size is particularly stable compared to $N = 8$-12.

d) $N > 13$

After a peak in D for $N = 14$, the stability of the clusters increases for $N = 15$, 16, and 17, as shown in Figure 6.7. The minute differences in ΔI, in Figure 6.9, for the isotopomers at $N = 14$ and 15, hint that these He atoms are added close to the c.m. of the cyanoacetylene isotopomers. There is insufficient isotopomer experimental information from which to theorize as to the location of the additional He atoms for $N > 15$.

e) Helium density determination from PIMC calculations

The cluster geometries inferred from isotopomeric data support calculations of the helium density around HCCCN for various cluster sizes, determined from PIMC calculations performed at 0.37 K.[21] In Figure 6.10, two dimensional contour plots of the helium density around HCCCN are illustrated for $N = 5$, 6, 7, 10, 13, 17 (Ref. 21). The HCCCN molecule lies along the z-axis in these representations, and x is distance from the HCCCN c.m., along the *b*-axis. For both $N = 5$ and 6 (Figure 6.10 **A** and **B**, respectively), the helium density remains localized in an equatorial position, very near to the HCCCN c.m. If these plots are rotated 360° about the z-axis, they trace out a ring of helium density around the cyanoacetylene molecule. The addition of the sixth He atom results in a ring that is more diffuse than that determined for He_5–HCCCN. This is supported experimentally by the increase in D between $N = 5$ and 6. He_7–HCCCN (Figure 6.10 **C**) shows some helium density localized at the H-end of the cyanoacetylene, and this is also supported by the relative ΔI of He_7–DCCCN and He_7–HCCC^{15}N. For clusters of $N = 8$ to 10, helium density was found to build-up at the H-end of the

molecule, as indicated for He_{10}–HCCCN in Figure 6.10 **D**. The ΔI values of the three isotopomers begin to converge for $N = 11, 12, 13$. The PIMC calculations for these clusters show increasing helium density accumulating at the H-end of the molecule, but also that the region near the N-end of HCCCN is beginning to be coated with helium density. Figure 6.10 **E** shows that helium density can be found at the N-end of the molecule, at $N = 13$. Taken together with ΔI of the isotopomers, this suggests that He atoms are not being added as hard spheres, to one end of the molecule or the other. Instead, helium density is added simultaneously to the H- and N-ends of the molecule for He_{13}–HCCCN. For clusters with $N > 13$, a gradual increase in the helium density at both ends of the cluster is observed, as shown in Figure 6.10 **F** for He_{17}–HCCCN. The PIMC helium density calculations for He_N–cyanoacetylene clusters are both supported by the spectroscopic evidence, and are able to expand upon the proposed geometries suggested by studies of the isotopomers of cyanoacetylene.

6.8 Superfluid behaviour of He_N–cyanoacetylene clusters

A decoupling of helium density from the rotating molecule is considered a clear indicator of superfluid behaviour. In a bulk phase sample, superfluid He II is frictionless. This would suggest that every time the addition of a He atom to a He_N–molecule cluster results in a net decrease in the effective cluster moment of inertia, superfluid behaviour of He is being observed.

Figure 6.7 shows clear oscillations in the evolution of B with N for

He_N–cyanoacetylene. These oscillations indicate that helium density is decoupled from rotating clusters for large N. Determining the onset of superfluid behaviour of helium in He_N–molecule clusters is one of the main motivations for studying the solvation of a molecule with He atoms. The ratio of superfluid to normal helium density, ρ_s/ρ, can be determined for He_N–HCCCN clusters:

$$\rho_s/\rho = \frac{I_{He\ (Boltzmann)} - I_{He\ (effective)}}{I_{He\ (Boltzmann)}} \qquad (6\text{-}4)$$

where $I_{He\ (Boltzmann)}$ is the classical moment of inertia of helium density rotating with HCCCN from PIMC calculations,[21] and $I_{He\ (effective)}$ is defined in equation 6-1. Figure 6.11 shows the superfluid fraction for He_N–HCCCN (N = 1-17 and 26-31). The superfluid ratio from PIMC calculations for He atoms which obey Bose-Einstein statistics are also plotted in Figure 6.11. The superfluid fraction for N = 2 to 5, for both the experimental and calculated values, is not zero. The discussion in Ref. 6 attributes this to finite-size effects that are present even for Boltzmann statistics, and not as evidence of actual superfluid density in He_N–N_2O cluster with $N < 5$. The same is assumed to apply to He_N–cyanoacetylene clusters for N = 2-5. Figure 6.11 shows that the superfluid fraction increases quite rapidly from 0.16 at N = 5, to 0.83 by N = 13. The superfluid fraction remains essentially constant at ~0.83 for N = 13 to 17. We pick up again with N = 26 to 31, and the superfluid fraction increases smoothly from 0.91 to 0.95.

6.9 Rotor length and the onset of superfluidity in He_N–molecule clusters

As the length of cyanoacetylene (4.80 Å) is more than twice the length of N_2O (2.31 Å) it is informative to compare these systems to gauge the effect that rotor length has on the onset of superfluidity. Figure 6.12 shows the evolution of B with N for He_N–N_2O (Refs. 4, 6) and He_N–HCCCN. Clusters of interest have been labelled **A**, **B**, **C**, and **D** in the figure.

Label **A** refers to $N = 7$ for both the N_2O and HCCCN clusters. The peak in B for both He_7–N_2O and He_7–HCCCN is due to a redistribution of helium density, and is not due to quantum effects. **B** denotes the first turn-around in B which can be attributed to superfluid behaviour of the helium density. This occurs at $N = 9$ for the N_2O clusters, but for the longer rotor turn-around does not occur until He_{10}–HCCCN. In the N_2O system, this first turn-around in B corresponds to a superfluid fraction of ~0.5 (Ref. 6), shown in Figure 5.9. For He_N–HCCCN clusters, 50% of the helium density has already become superfluid by $N = 7$. First B turn-around does not occur until the superfluid fraction reaches 0.69, at He_{10}–HCCCN. The longer HCCCN rotor requires not only more He atoms to reach the first turn-around, but a larger superfluid fraction. As discussed in Chapter 5, the onset of long exchange cycles in PIMC calculations begins once the density of He is sufficiently high.[9] These long exchange cycles are first observed between He atoms on the ring, where the helium density is the highest in small He_N–molecule clusters, and denote the decoupling of helium density from the rotating system.[22] It is interesting to note that the increased helium density on the ring of six He atoms around

cyanoacetylene, compared to the five atom ring around N_2O (Refs. 4, 6), seems to increase the rate at which He atoms become superfluid. However, the longer cyanoacetylene rotor, compared to N_2O, requires more He atoms to become superfluid before a turn-around in B occurs.

The effective B values increase between the **B** and **C** labels. For N_2O clusters, the **C** local maximum in B happens at He_{11}–N_2O. Figure 5.9 shows the rate of increase in the superfluid fraction of the He_N–N_2O clusters slows for $N = 11$ to 16, having reached ~0.8 for He_{11}–N_2O (Ref. 6). Point **C** occurs at $N = 13$ for the He_N–cyanoacetylene clusters. Figure 6.11 shows that $N = 13$ is also the herald cluster size that marks the beginning of a region with no increase in the superfluid fraction. For $N = 13$, 14, 15, 16, and 17, the superfluid fraction remains essentially constant at a value of ~0.83. The $J = 1$-0 transitions of the He_N–cyanoacetylene clusters dropped below the operating frequency of our instrument for $N > 17$. The lighter He_N–N_2O clusters remained measurable, and the decrease in B to a local minimum at $N = 16$ is reported in Ref. 6. Point **D** marks the second turn-around in B. This was observed for He_{17}–N_2O, and Ground State calculations predict that this happens at He_{23}–HCCCN (Ref. 7, plotted in Figure 6.4). Between He_{16}– and He_{17}–N_2O, the superfluid fraction jumps from 0.83 to 0.87. Calculations of the chemical potential show a change in slope between $N = 16$ and 17 for He_N–N_2O clusters.[9] The chemical potential is a measure of the change in energy of the He_N–N_2O cluster as successive atoms are added. This change in the slope indicates that adding a He atom to a cluster with $N = 11$ to 16 is associated with a higher change in the cluster energy than adding a He atom to a cluster with $N = \sim 17$ or higher. Around $N =$

17, the first solvation shell of He is completed around N_2O and the second shell begins to fill. Helium density in the second solvation shell increases the superfluid fraction of He atoms in the first shell, as seen by the increase in the superfluid fraction at ~He_{17}–N_2O. Neither the filling of the first solvation shell or the inauguration of a second shell were directly observed for He_N-HCCCN clusters. I can be certain that this occurs, however, since I was able to measure the rotational transitions of clusters after the second turn-around. The rotational transitions assigned to $N = 26$ to 31 have an estimated accuracy of ± 1 He atom. They are, nonetheless, part of the second shell of solvating helium density. Between $N = 17$ and 26, the superfluid fraction of He around HCCCN increases from 0.83 to 0.91. The superfluid fraction continues to increase with the addition of more He atoms, resulting in 95% of the helium density reaching superfluidity by He_{31}–HCCCN.

Microwave and computational studies of He_N–N_2O clusters, for $N = 2$ to 19, showed that superfluidity built up in stages.[6, 9] Similar steps in the superfluid fraction were observed for He_N–cyanoacetylene clusters. The differences in the onset of superfluidity for the two rotors, in terms of both the cluster size at which the points **B**, **C**, and **D** were achieved and the superfluid fraction required to have a first turn-around in B, can be attributed to the differences in the length of N_2O and HCCCN. More helium density is required to coat or form a complete solvation shell around HCCCN than N_2O, and this is reflected in the evolution of B with N for the corresponding clusters.

6.10 Summary

The pure rotational transitions of He_N–cyanoacetylene for $N = 2$ to 17 and 26 to 31 were investigated by microwave spectroscopy. While the HCCCN, $HCCC^{15}N$, and DCCCN isotopomers were primarily investigated, the $J = 1\text{-}0$ rotational transition of ^{13}C containing HCCCN isotopomers was measured for $N = 2$. The He_2–cyanoacetylene trimer was found to have rotational transitions corresponding to those of a floppy, asymmetric top. By assuming that each He atom occupied a position equivalent to that determined for He–cyanoacetylene, the He–cyanoacetylene c.m.–He angle, ϕ, was determined to be $144.9 \pm 7.7°$.

The rotational transitions for clusters of $N > 2$ are effectively those of a prolate symmetric top. The B and D rotational parameters of a linear molecule were fitted to the transition frequencies for the cyanoacetylene clusters with three He atoms and greater. The B rotational constant provides information about the effective distribution of mass with respect to the b-axis, while D serves as a measure of the flexibility of the cluster. Isotopomeric information suggests that, in contrast to He_N–OCS and He_N–N_2O, a stable equatorial ring of six He atoms is formed around the cyanoacetylene. The seventh He atom most likely adds to the hydrogen end of the cyanoacetylene.

The evolution of B with N for He_N–cyanoacetylene clusters shows that the effective moments of inertia of the clusters did not necessarily increase, as expected by classical physics, as the number of He atoms in the clusters increased. This is evidence that some helium density is decoupling from the rotating chromophore, behaving in a

manner expected for superfluid He II in the bulk phase. The earliest manifestation of superfluidity in He_N–cyanoacetylene clusters happens at $N = 10$. The apparent moment of inertia of this cluster is actually less than that of He_9–cyanoacetylene.

The superfluid fraction of the helium density of He_N–HCCCN clusters was found to increase rapidly for $N > 5$. At $N = 13$, however, the superfluid fraction stabilized at ~0.83 for the addition of the 14th, 15th, 16th, and 17th He atoms. The superfluid fraction was found to increase smoothly for $N = 26$ to 31, the largest observed He_N–HCCCN clusters. The maximum superfluid fraction observed experimentally was 0.948 for He_{31}–HCCCN.

The relative evolution of B with N for He_N–cyanoacetylene and He_N–N_2O, shows that the onset of superfluidity is delayed when a longer rotor is solvated with He atoms. Results from Ground State calculations suggest that the first solvation shell of He is complete for He_{22}–cyanoacetylene (Ref. 7), six more He atoms than are required to form the first solvation shell around N_2O. These results indicate rotor length does affect the cluster size at which superfluid behaviour in He_N–molecule clusters is observed, but also that the onset of superfluidity occurs via a similar mechanism for both He_N–N_2O and He_N–cyanoacetylene.

6.11 Tables

Table 6.1 Measured transition frequencies and fitted rotational parameters for He_2–cyanoacetylene complexes. The microwave accuracy of the fit to the measured rotational transitions (rms fit) is given in kHz.

	Rotational Transitions			Rotational Parameters	
		ν_{obs} (MHz)	$\Delta\nu^a$ (kHz)		(MHz)
	$J_{KaKc} = 1_{01} - 0_{00}$			A	10000.0 (fixed)
				B	4370.180 (2)
	F= 1-1	6607.5026	-19.8	C	2238.389 (1)
	2-1	6608.7751	-3.0		
	0-1	6610.6846	22.8	χ_{aa} (^{14}N)	-4.186 (1)
He_2–HCCCN	$J_{KaKc} = 2_{02} - 1_{01}$				
	F= 2-2	12716.2441	42.6		
	1-0	12716.2687	-66.9		
	2-1	12717.4828	25.6		
	3-2	12717.5425	43.9		
	1-1	12719.4299	-45.1	rms error	38.4 kHz
	$J_{KaKc} = 1_{01} - 0_{00}$			A	10000.0 (fixed)
				B	4243.002 (3)
		6467.6931	0.0	C	2224.692 (2)
He_2–HCCC^{15}N	$J_{KaKc} = 2_{02} - 1_{01}$				
		12491.1393	0.0	rms error	0.0 kHz
	$J_{KaKc} = 1_{01} - 0_{00}$			A	10000.0 (fixed)
				$(B+C)/2$	3220.8988 (3)
He_2–H^{13}CCCN	F= 1-1	6440.7356	-0.8		
	2-1	6442.0143	5.2	χ_{aa} (^{14}N)	-4.236 (2)
	0-1	6443.9139	-4.5		
				rms error	3.5 kHz
	$J_{KaKc} = 1_{01} - 0_{00}$			A	10000.0 (fixed)
				$(B+C)/2$	3291.3340 (3)
He_2–HC^{13}CCN	F= 1-1	6581.6056	-0.2		
	2-1	6582.8808	0.4	χ_{aa} (^{14}N)	-4.249 (2)
	0-1	6584.7923	-0.2		
				rms error	0.3 kHz

Table 6.1 (continued)

	Rotational Transitions			Rotational Parameters	
		ν_{obs} (MHz)	$\Delta\nu^a$ (kHz)		(MHz)
	$J_{KaKc} = 1_{01} - 0_{00}$			A	10000.0 (fixed)
				$(B+C)/2$	3294.6790 (3)
He_2–$HCC^{13}CN$	F= 1-1	6588.2954	-2.8		
	2-1	6589.5712	0.3	χ_{aa} (^{14}N)	-4.249 (2)
	0-1	6591.4826	2.4		
				rms error	0.5 kHz
	$J_{KaKc} = 1_{01} - 0_{00}$			A	10000.0 (fixed)
				B	4035.397 (1)
	F_1F_2=12-12	6224.8227	-15.2	C	2190.521 (1)
	10-11	6224.8646	-3.2		
	21-10	6226.0949	-3.0	χ_{aa} (^{14}N)	-4.219 (1)
	23-12	6226.1263	6.6	χ_{aa} (D)	0.187 (3)
	22-11	6226.1622	0.1		
	01-12	6228.0431	14.7		
He_2–DCCCN	$J_{KaKc} = 2_{02} - 1_{01}$				
	F_1F_2=22-22	12084.8310	36.1		
	23-23	12084.8620	53.2		
	12-01	12084.8981	-59.4		
	11-01	12084.9438	-41.4		
	23-12	12086.0603	-0.5		
	34-23	12086.1194	-4.0		
	33-22	12086.1743	41.2		
	12-12	12088.0929	-25.3	rms error	29.6 kHz

[a] $\Delta\nu = \nu_{obs} - \nu_{calc}$

Table 6.2 Measured transition frequencies of He_N–HCCCN clusters. The relationship between the $J = 1\text{-}0$ and $J = 2\text{-}1$ transitions of each cluster was confirmed using microwave-microwave double resonance.

	$J = 1\text{-}0$			$J = 2\text{-}1$		
	$F' - F''$	ν_{obs} (MHz)	$\Delta\nu^a$ (kHz)	$F' - F''$	ν_{obs} (MHz)	$\Delta\nu^a$ (kHz)
He_3 – HCCCN	1-1	5585.7558	0.3	2-2	11047.6875	5.3
	2-1	5587.0221	-2.1	1-0	11047.8833	-10.4
	0-1	5588.9294	1.8	2-1	11048.9626	11.7
				3-2	11049.0383	-3.3
				1-1	11051.0625	-3.3
He_4 – HCCCN	1-1	4764.9762	0.5	2-2	9504.7310	0.3
	2-1	4766.2421	-1.3	1-0	9504.9396	-2.5
	0-1	4768.1458	0.8	2-1	9506.0026	4.3
				3-2	9506.0883	-0.6
				1-1	9508.1099	-1.5
He_5 – HCCCN	1-1	4140.3975	-0.3	2-2	8274.1359	-0.2
	2-1	4141.6624	0.4	1-0	8274.3468	-0.1
	0-1	4143.5587	-0.1	2-1	8275.3991	-1.3
				3-2	8275.4925	1.8
				1-1	8277.5076	-0.3
He_6 – HCCCN	1-1	3782.7249	0.7	2-2	7534.1417	-1.4
	2-1	3783.9821	-0.6	1-0	7534.3527	-0.3
	0-1	3785.8708	0.0	2-1	7535.4057	4.1
				3-2	7535.4897	-1.9
				1-1	7537.4991	-0.5
He_7 – HCCCN	1-1	3926.2012	0.0	2-2	7677.8373	0.6
	2-1	3927.4571	-0.6	1-0	7678.0463	0.1
	0-1	3929.3434	0.6	2-1	7679.0960	2.7
				3-2	7679.1797	-3.4
				1-1	7681.1879	0.0

Table 6.2 (continued)

	$J = 1\text{-}0$			$J = 2\text{-}1$		
	$F'\text{-}F''$	ν_{obs} (MHz)	$\Delta\nu^a$ (kHz)	$F'\text{-}F''$	ν_{obs} (MHz)	$\Delta\nu^a$ (kHz)
	1-1	3712.3609	-0.9	2-2	7226.0148	1.9
He_8 – HCCCN	2-1	3713.6078	0.6	1-0	7226.2152	-5.4
	0-1	3715.4758	0.3	2-1	7227.2640	5.7
				3-2	7227.3474	0.1
				1-1	7229.3320	-2.3
He_9 – HCCCN	1-1	3444.6446	-0.5	2-2	6683.5780	2.2
	2-1	3445.8803	0.3	1-0	6683.7809	-0.8
	0-1	3447.7328	0.1	2-1	6684.8085	-2.2
				3-2	6684.8993	0.4
				1-1	6686.8698	0.5
He_{10} – HCCCN	1-1	3514.1183	-0.7	2-2	6821.8385	4.5
	2-1	3515.3637	-0.6	1-0	6822.0337	-8.0
	0-1	3517.2340	1.4	2-1	6823.0798	0.5
				3-2	6823.1747	6.4
				1-1	6825.1520	-3.3
He_{11} – HCCCN	1-1	3570.2827	-0.6	2-2	6928.1656	-1.9
	2-1	3571.5473	1.0	1-0	6928.3757	-2.4
	0-1	3573.4408	-0.4	2-1	6929.4346	4.1
				3-2	6929.5235	2.7
				1-1	6931.5335	-2.5
He_{12} – HCCCN	1-1	3977.3101	-1.0	2-2	7752.6164	1.1
	2-1	3978.5747	0.9	1-0	7752.8263	0.5
	0-1	3980.4682	0.1	2-1	7753.8760	-2.0
				3-2	7753.9683	0.1
				1-1	7755.9830	0.2
He_{13} – HCCCN	1-1	4081.7630	-1.3	2-2	7986.2276	3.5
	2-1	4083.0310	1.9	1-0	7986.4320	-3.0
	0-1	4084.9259	-0.6	2-1	7987.4868	-2.1
				3-2	7987.5805	1.3
				1-1	7989.5975	0.3

Table 6.2 (continued)

	$J = 1\text{-}0$			$J = 2\text{-}1$		
	$F' - F''$	ν_{obs} (MHz)	$\Delta\nu^a$ (kHz)	$F' - F''$	ν_{obs} (MHz)	$\Delta\nu^a$ (kHz)
He_{14} – HCCCN	1-1	3776.3244	0.3	2-2	7341.3129	-0.3
	2-1	3777.5867	-0.6	1-0	7341.5236	-0.2
	0-1	3779.4828	0.3	2-1	7342.5764	0.0
				3-2	7342.6675	0.8
				1-1	7344.6818	-0.4
He_{15} – HCCCN	1-1	3501.1903	-0.7	2-2	6827.6794	0.9
	2-1	3502.4541	0.7	1-0	6827.8871	-1.9
	0-1	3504.3475	0.1	2-1	6828.9380	-2.9
				3-2	6829.0361	5.0
				1-1	6831.0443	-1.1
He_{16} – HCCCN	1-1	3367.9990	1.4	2-2	6581.9588	7.9
	2-1	3369.2600	-0.1	1-0	6582.1495	-11.9
	0-1	3371.1529	-1.3	2-1	6583.2087	-4.7
				3-2	6583.3117	8.1
				1-1	6585.3185	0.5
He_{17} – HCCCN	1-1	3211.5809	-0.6	2-2	6278.6610	-0.8
	2-1	3212.8461	1.6	1-0	6278.8733	0.9
	0-1	3214.7383	-1.0	2-1	6279.9239	-0.9
				3-2	6280.0153	0.3
				1-1	6282.0307	0.5
He_{26} – HCCCN	1-1	3278.7282	-1.4	2-2	6393.65	0.3
	2-1	3279.9925	2.4	3-2	6395.00	-0.3
	0-1	3281.8803	-1.0			
He_{27} – HCCCN	1-1	3440.8800	-1.6	2-2	6718.90	24.8
	2-1	3442.1438	2.6	3-2	6720.20	-24.8
	0-1	3444.0299	-1.0			
He_{28} – HCCCN	1-1	3578.3849	-0.6	2-2	6999.20	-23.0
	2-1	3579.6502	1.1	3-2	7000.60	23.0
	0-1	3581.5445	-0.4			
He_{29} – HCCCN	1-1	3688.1995	0.7	2-2	7226.35	4.4
	2-1	3689.4659	-1.1	3-2	7227.70	-4.4
	0-1	3691.3700	0.4			

Table 6.2 (continued)

	$J = 1\text{-}0$			$J = 2\text{-}1$		
	$F' - F''$	ν_{obs} (MHz)	$\Delta\nu^a$ (kHz)	$F' - F''$	ν_{obs} (MHz)	$\Delta\nu^a$ (kHz)
He_{30} – HCCCN	1-1	3771.2963	-0.4	2-2	7400.10	29.8
	2-1	3772.5663	0.7	3-2	7401.40	-29.8
	0-1	3774.4690	-0.3			
He_{31} – HCCCN	1-1	3830.4990	-0.2	2-2	7524.40	-20.0
	2-1	3831.7687	0.3	3-2	7525.80	20.0
	0-1	3833.6726	-0.1			

[a] $\Delta\nu = \nu_{obs} - \nu_{calc}$

Table 6.3 Rotational transition frequencies and calculated rotational parameters of He_N–$HCCC^{15}N$ clusters, given in MHz. The rms error is 0.0 kHz for each cluster, since two rotational parameters were determined from two rotational transition frequencies. The relationship between the $J = 1\text{-}0$ and $J = 2\text{-}1$ transitions of each cluster was confirmed using microwave-microwave double resonance.

	B (MHz)	D (MHz)	$J = 1\text{-}0$ (MHz)	$J = 2\text{-}1$ (MHz)
$He_3 - HCCC^{15}N$	2754.2109 (7)	4.79667 (9)	5489.2352	10863.3503
$He_4 - HCCC^{15}N$	2350.8949 (7)	1.01471 (9)	4697.7310	9317.1089
$He_5 - HCCC^{15}N$	2046.2822 (7)	0.29272 (9)	4091.3945	8175.7618
$He_6 - HCCC^{15}N$	1871.8311 (7)	1.24317 (9)	3738.6895	7447.5430
$He_7 - HCCC^{15}N$	1934.6889 (7)	6.89937 (9)	3841.7804	7517.9760
$He_8 - HCCC^{15}N$	1843.4809 (7)	8.04442 (9)	3654.7841	7116.5021
$He_9 - HCCC^{15}N$	1708.3238 (7)	8.26364 (9)	3383.5931	6568.8589
$He_{10} - HCCC^{15}N$	1739.6841 (7)	8.17235 (9)	3446.6789	6697.2215
$He_{11} - HCCC^{15}N$	1760.1192 (7)	8.49233 (9)	3486.2690	6768.7221
$He_{12} - HCCC^{15}N$	1956.4125 (7)	8.03521 (9)	3880.6842	7568.5233
$He_{13} - HCCC^{15}N$	2006.5945 (7)	7.05524 (9)	3984.9680	7800.6103
$He_{14} - HCCC^{15}N$	1859.8387 (7)	8.41122 (9)	3686.0326	7170.1960
$He_{15} - HCCC^{15}N$	1726.3787 (7)	6.99462 (9)	3424.7790	6681.6871
$He_{16} - HCCC^{15}N$	1661.7310 (7)	6.12394 (9)	3298.9662	6450.9579

Table 6.4 Measured transition frequencies of He_N–DCCCN clusters. The relationship between the $J = 1\text{-}0$ and $J = 2\text{-}1$ transitions of each cluster was confirmed using microwave-microwave double resonance.

	$J = 1\text{-}0$			$J = 2\text{-}1$		
	$F_1F_2{}' - F_1F_2{}''$	ν_{obs} (MHz)	$\Delta\nu^a$ (kHz)	$F_1F_2{}' - F_1F_2{}''$	ν_{obs} (MHz)	$\Delta\nu^a$ (kHz)
	12 - 12	5310.90320	3.3	23 - 23	10522.4307	-3.9
	21 - 10	5312.12360	-3.9	12 - 01	10522.6286	-8.4
He_3 – DCCCN	23 - 12	5312.16320	9.6	11 - 01	10522.6786	7.1
	22 - 11	5312.19370	-11.5	23 - 12	10523.6933	5.0
	01 - 12	5314.07390	2.4	34 - 23	10523.7913	3.6
				12 - 12	10525.7996	-9.0
				12 - 11	10525.8510	5.7
	11 - 12	4565.3232	6.7	23 - 23	9109.8526	1.6
	12 - 12	4565.3449	-3.2	12 - 01	9110.0491	-5.3
	10 - 11	4565.3912	-1.8	11 - 01	9110.0878	3.4
He_4 – DCCCN	21 - 10	4566.5735	-6.0	34 - 23	9111.2033	-0.2
	23 - 12	4566.6055	3.0	12 - 12	9113.2234	0.5
	22 - 11	4566.6481	0.8			
	01 - 12	4568.5171	0.5			
	12 - 12	3989.4021	6.4	23 - 23	7973.2374	1.4
	10 - 11	3989.4287	-7.1	12 - 01	7973.4365	-3.7
He_5 – DCCCN	21 - 10	3990.6226	-7.5	34 - 23	7974.5920	3.5
	23 - 12	3990.6562	5.3	12 - 12	7976.6061	-1.2
	22 - 11	3990.6943	3.3			
	01 - 12	3992.5624	-0.4			
	11 - 12	3664.6238	-4.1	22 - 22	7299.8406	-5.3
	12 - 12	3664.6423	-3.8	23 - 23	7299.8586	4.8
He_6 – DCCCN	21 - 10	3665.8859	2.9	12 - 01	7300.0567	-2.4
	23 - 12	3665.9068	9.8	21 - 10	7301.0702	2.4
	22 - 11	3665.9271	3.8	23 - 12	7301.0946	-10.1
	01 - 12	3667.7840	-8.7	34 - 23	7301.2084	9.2
				12 - 12	7303.2069	1.2

Table 6.4 (continued)

	J = 1-0			J = 2-1		
	F_1F_2 ′- F_1F_2 ″	ν_{obs} (MHz)	$\Delta\nu^a$ (kHz)	F_1F_2 ′- F_1F_2 ″	ν_{obs} (MHz)	$\Delta\nu^a$ (kHz)
	12 - 12	3721.5324	-11.4	23 - 23	7291.4250	7.4
	21 - 10	3722.7800	1.4	12 - 01	7291.6169	-5.9
He_7 – DCCCN	23 - 12	3722.8012	10.4	23 - 12	7292.6610	-3.7
	22 - 11	3722.8166	3.0	34 - 23	7292.7629	4.7
	01 - 12	3724.6747	-3.4	12 - 12	7294.7545	-2.5
	12 - 12	3522.0903	-3.7	22 - 22	6869.1556	-1.3
	21 - 10	3523.2931	-20.6	23 - 23	6869.1736	7.6
He_8 – DCCCN	23 - 12	3523.3502	20.5	12 - 01	6869.3572	-11.1
	22 - 11	3523.3640	3.9	21 - 10	6870.3691	9.9
	01 - 12	3525.2055	-0.0	23 - 12	6870.3991	-2.7
				34 - 23	6870.4976	1.7
				12 - 12	6872.4757	-4.1
				22 - 22	6357.6351	-10.3
				23 - 23	6357.6646	12.6
				12 - 01	6357.8506	-4.3
He_9 – DCCCN				21 - 10	6358.8573	3.1
				23 - 12	6358.8790	-6.1
				34 - 23	6358.9835	6.0
				12 - 12	6360.9530	-1.0
	12 - 12	3315.8458	-13.2	23 - 23	6455.8356	11.4
	23 - 12	3317.1127	10.3	12 - 01	6456.0289	-2.6
He_{10} – DCCCN	01 - 12	3318.9707	2.9	23 - 12	6457.0542	-13.4
				34 - 23	6457.1665	10.1
				12 - 12	6459.1348	-5.5
	12 - 12	3394.7787	-16.7	23 - 23	6593.8802	11.5
	23 - 12	3396.0726	15.1	12 - 01	6594.0644	-14.8
He_{11} – DCCCN	01 - 12	3397.9501	-0.9	23 - 12	6595.1338	3.0
				34 - 23	6595.2314	10.4
				12 - 12	6597.2247	-10.1
	12 - 12	3782.5838	-7.6	23 - 23	7382.4115	4.8
He_{12} – DCCCN	23 - 12	3783.8625	9.5	23 - 12	7383.6623	-6.1
	01 - 12	3785.7440	-1.9	34 - 23	7383.7598	1.3

Table 6.4 (continued)

	$J = 1\text{-}0$			$J = 2\text{-}1$		
	$F_1F_2{}' - F_1F_2{}''$	ν_{obs} (MHz)	$\Delta\nu^a$ (kHz)	$F_1F_2{}' - F_1F_2{}''$	ν_{obs} (MHz)	$\Delta\nu^a$ (kHz)
	12 - 12	3881.1224	-3.7	23 - 23	7604.8762	-2.6
He_{13} – DCCCN	21 - 10	3882.3692	4.7	21 - 10	7606.0864	-8.8
	23 - 12	3882.3907	12.8	23 - 12	7606.1285	-2.2
	22 - 11	3882.3943	-9.0	34 - 23	7606.2385	13.5
	01 - 12	3884.2695	-4.8			
He_{14} – DCCCN	12 - 12	3590.7349	-0.6	23 - 23	6988.5435	14.7
	23 - 12	3592.0128	8.8	12 - 01	6988.7262	-14.1
	01 - 12	3593.8988	-8.2	23 - 12	6989.7794	-17.9
				34 - 23	6989.8966	8.7
				12 - 12	6991.9203	8.5
He_{15} – DCCCN	12 - 12	3342.0823	-8.2	23 - 23	6523.3013	11.7
	23 - 12	3343.3624	10.4	12 - 01	6523.4933	-6.6
	01 - 12	3345.2424	-2.3	23 - 12	6524.5363	-14.8
				34 - 23	6524.6505	9.2
				12 - 12	6526.6546	0.5

[a] $\Delta\nu = \nu_{obs} - \nu_{calc}$

Table 6.5 Fitted rotational parameters and hypothetical unsplit centre frequencies of He_N–HCCCN clusters.

	B /MHz	*D* / MHz	χ_{aa} / MHz	rms fit / kHz
He_3–HCCCN	2803.7959 (4)	5.19477 (5)	-4.229 (1)	6.15
He_4–HCCCN	2385.1881 (4)	1.08607 (5)	-4.226 (1)	1.91
He_5–HCCCN	2071.3508 (4)	0.31259 (5)	-4.215 (1)	0.80
He_6–HCCCN	1894.5651 (4)	1.33934 (5)	-4.195 (1)	1.70
He_7–HCCCN	1978.2410 (4)	7.30846 (5)	-4.189 (1)	1.57
He_8–HCCCN	1873.3282 (4)	8.31420 (5)	-4.152 (1)	2.99
He_9–HCCCN	1740.0485 (4)	8.60573 (5)	-4.117 (1)	1.17
He_{10}–HCCCN	1774.8479 (4)	8.63475 (5)	-4.151 (1)	4.15
He_{11}–HCCCN	1803.4379 (4)	8.88504 (5)	-4.211 (1)	2.27
He_{12}–HCCCN	2006.0857 (4)	8.45202 (5)	-4.209 (1)	0.95
He_{13}–HCCCN	2056.2547 (4)	7.42281 (5)	-4.216 (1)	2.03
He_{14}–HCCCN	1906.3698 (4)	8.84071 (5)	-4.211 (1)	0.44
He_{15}–HCCCN	1765.7502 (4)	7.31437 (5)	-4.209 (1)	2.23
He_{16}–HCCCN	1697.4319 (4)	6.45358 (5)	-4.209 (1)	6.08
He_{17}–HCCCN	1618.4289 (4)	6.05596 (5)	-4.210 (1)	0.91
He_{26}–HCCCN	1653.611 (3)	6.860 (1)	-4.202 (2)	1.31
He_{27}–HCCCN	1734.610 (3)	6.822 (1)	-4.199 (2)	1.48
He_{28}–HCCCN	1802.918 (3)	6.600 (1)	-4.213 (2)	0.65
He_{29}–HCCCN	1857.203 (3)	6.287 (1)	-4.228 (2)	0.61
He_{30}–HCCCN	1898.124 (3)	5.974 (1)	-4.230 (2)	0.54
He_{31}–HCCCN	1927.230 (3)	5.726 (1)	-4.231 (2)	0.29

Table 6.6 Fitted rotational parameters and hypothetical unsplit centre frequencies of He_N–DCCCN clusters.

	B /MHz	D / MHz	$\chi_{aa}(^{14}N)$ / MHz	$\chi_{aa}(D)$ / MHz	rms fit / kHz
He_3 – DCCCN	2664.3270 (3)	4.17519 (4)	-4.234 (1)	0.226 (3)	6.73
He_4 – DCCCN	2285.0075 (3)	0.90353 (4)	-4.229 (1)	0.197 (3)	3.50
He_5 – DCCCN	1995.7571 (3)	0.26645 (4)	-4.227 (1)	0.176 (3)	4.65
He_6 – DCCCN	1835.3692 (3)	1.26141 (4)	-4.199 (1)	0.116 (2)	6.05[a]
He_7 – DCCCN	1874.0019 (3)	6.35428 (4)	-4.182 (1)	0.101 (4)	6.45[a]
He_8 – DCCCN	1776.2184 (3)	7.32699 (4)	-4.152 (1)	0.134 (2)	9.92[a]
He_9 – DCCCN	1589.7227 (1)	–	-4.135 (1)	0.097 (3)	7.72
He_{10} – DCCCN	1673.1744 (4)	7.36344 (5)	-4.145 (1)	–	9.60[b]
He_{11} – DCCCN	1714.3032 (4)	8.19007 (5)	-4.208 (1)	–	11.59[b]
He_{12} – DCCCN	1907.1228 (4)	7.65071 (6)	-4.206 (2)	–	5.94[b]
He_{13} – DCCCN	1954.2709 (3)	6.59206 (5)	-4.201 (2)	0.112 (3)	7.97[a]
He_{14} – DCCCN	1812.0452 (4)	8.07449 (5)	-4.229 (1)	–	11.33[b]
He_{15} – DCCCN	1685.0485 (4)	6.73884 (5)	-4.206 (1)	–	9.13[b]

[a] $J = 1\text{-}0$, $F_1F_2 = 23\text{-}12$ Doppler splitting not resolved, the measured frequency was assumed to be that of the centre (most intense) component.
[b] Unable to resolve the deuterium hyperfine structure, only ^{14}N nuclear quadrupole hyperfine structure (hfs) was fitted. The ^{14}N hfs frequencies were assumed to be the centre (most intense) component.

6.12 Figures

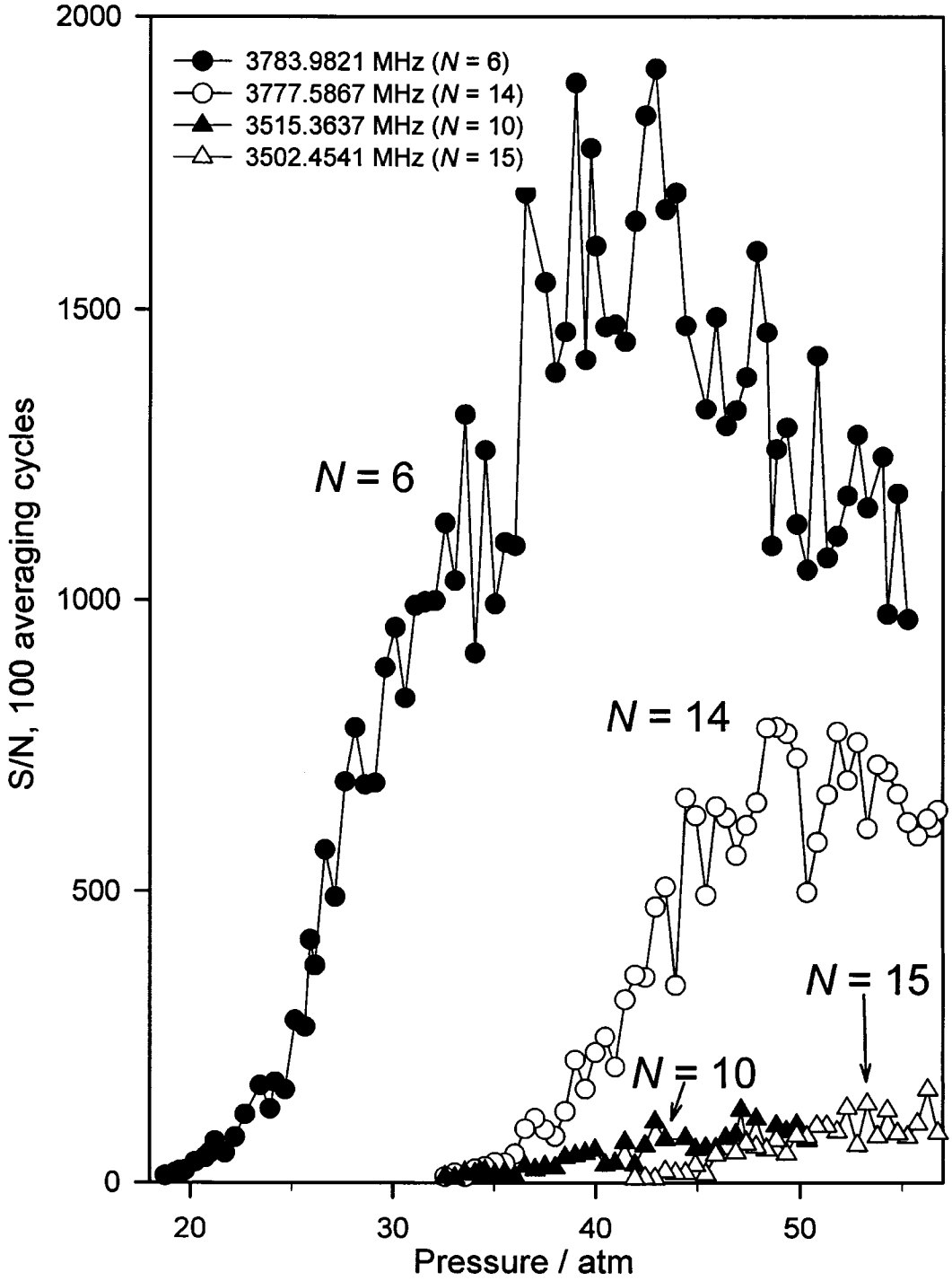

Figure 6.1 The dependence of the observed signal to noise of four He_N–HCCCN clusters on sample pressure. The $J = 1\text{-}0$ rotational transition, $F = 2\text{-}1$ hyperfine component, of each cluster was monitored.

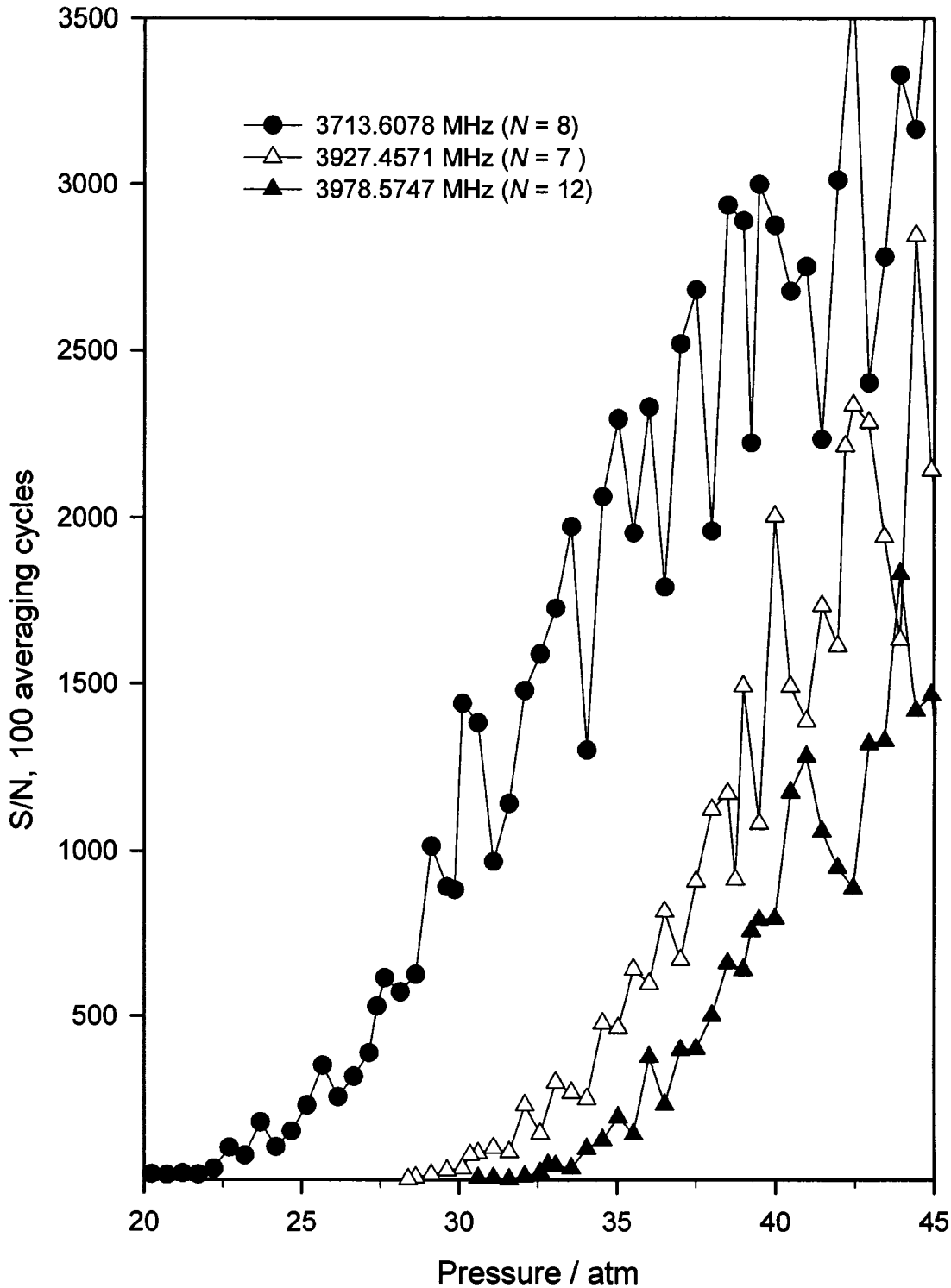

Figure 6.2 The dependence of the observed signal to noise of He_7–HCCCN, He_8–HCCCN, and He_{12}–HCCCN on sample pressure. The $J = 1$-0 rotational transition, $F = 2$-1 hyperfine component of each cluster was monitored.

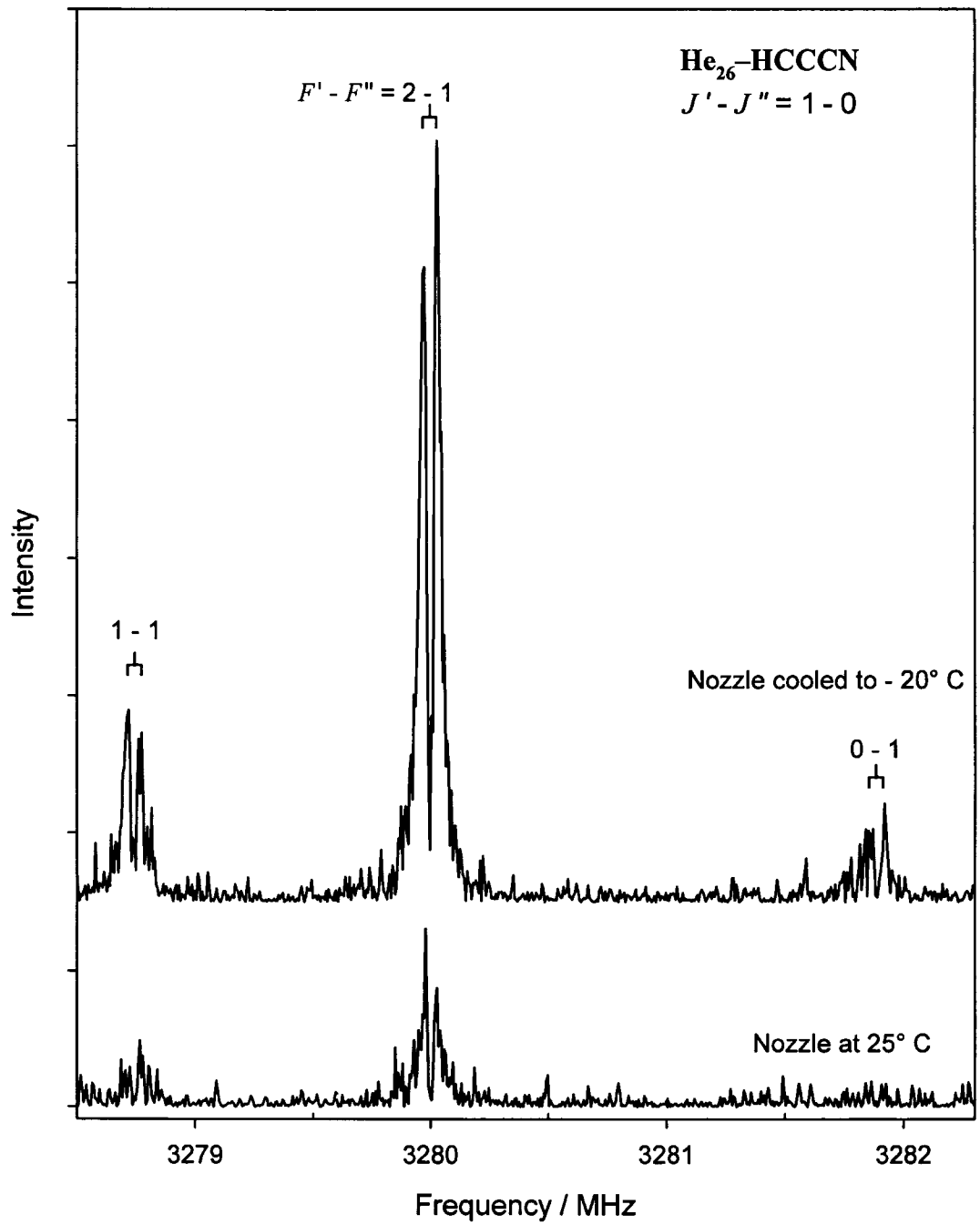

Figure 6.3 Composite spectrum of the $J = 1\text{-}0$ rotational transition of He_{26}–HCCCN. Improvement in signal strength was observed when the nozzle was cooled to -20 °C (253.15 K) compared to the same cluster studied with identical pressure and sample composition, but with a nozzle operating at room temperature. Three individual spectra were recorded at 10 ns sample intervals, and summed over 100 cycles to show the transition at each nozzle condition.

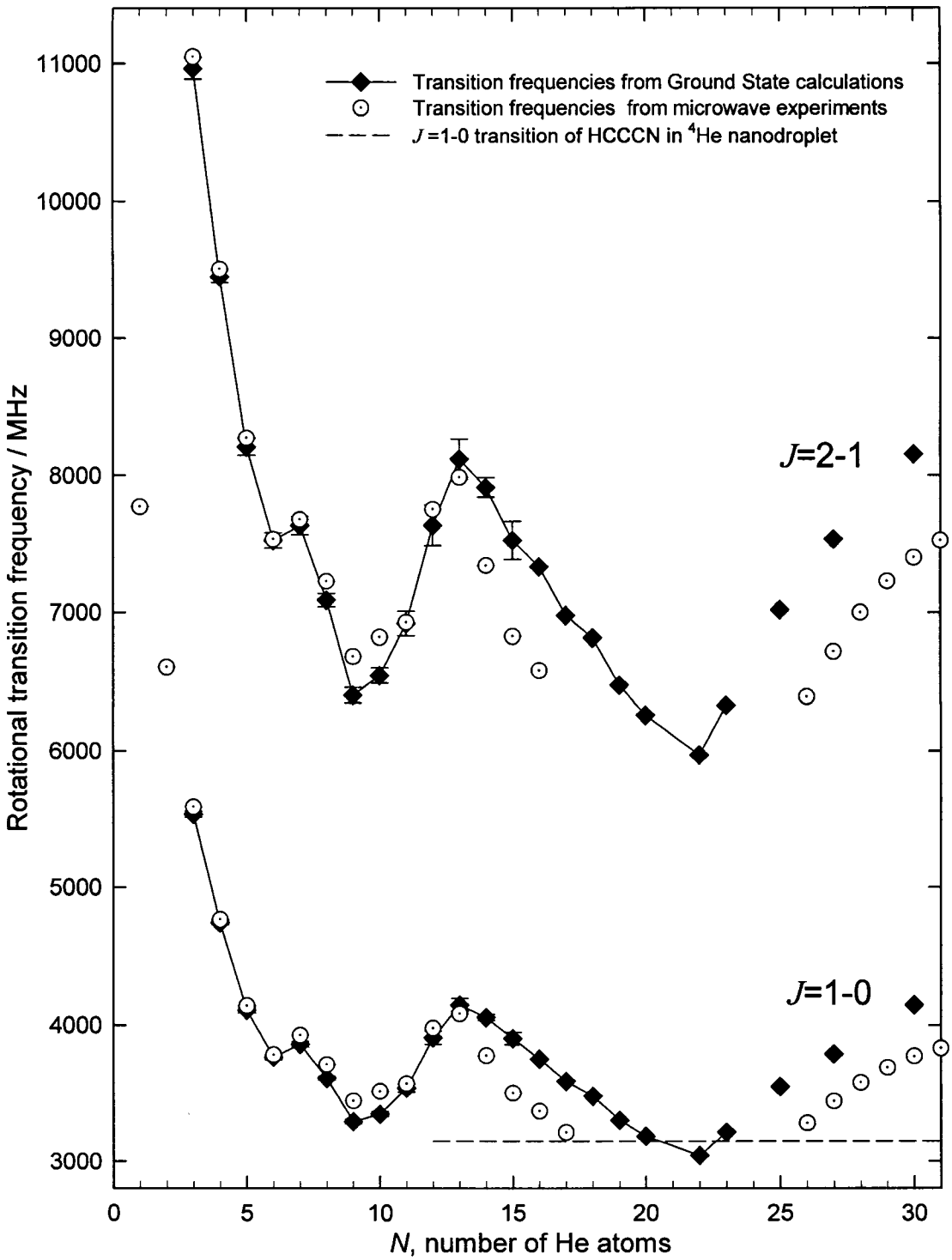

Figure 6.4 The frequencies of the $J = 1\text{-}0$ and $J = 2\text{-}1$ rotational transitions, from Ground State calculations (Ref. 7) and measured experimentally for He_N–HCCCN clusters versus N. The limiting ^{4}He nanodroplet value is given by the dashed line.

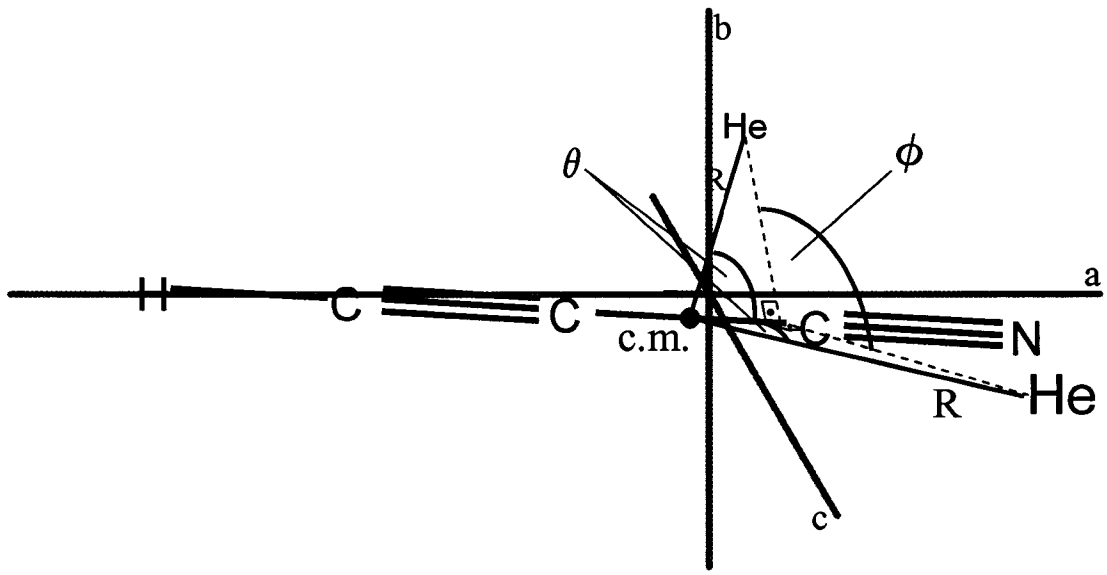

Figure 6.5 The structural parameters used to describe the geometry of He_2–HCCCN, superimposed on the principal inertial axis system. R is the distance between the He atom and the centre of mass of the HCCCN molecule. θ is the angle between R and the HCCCN axis, where $\theta = 0^{\circ}$ corresponds to the HCCCN–He linear configuration. The dihedral angle between one He atom, the HCCCN c.m., the N nucleus, and the second He atom is ϕ.

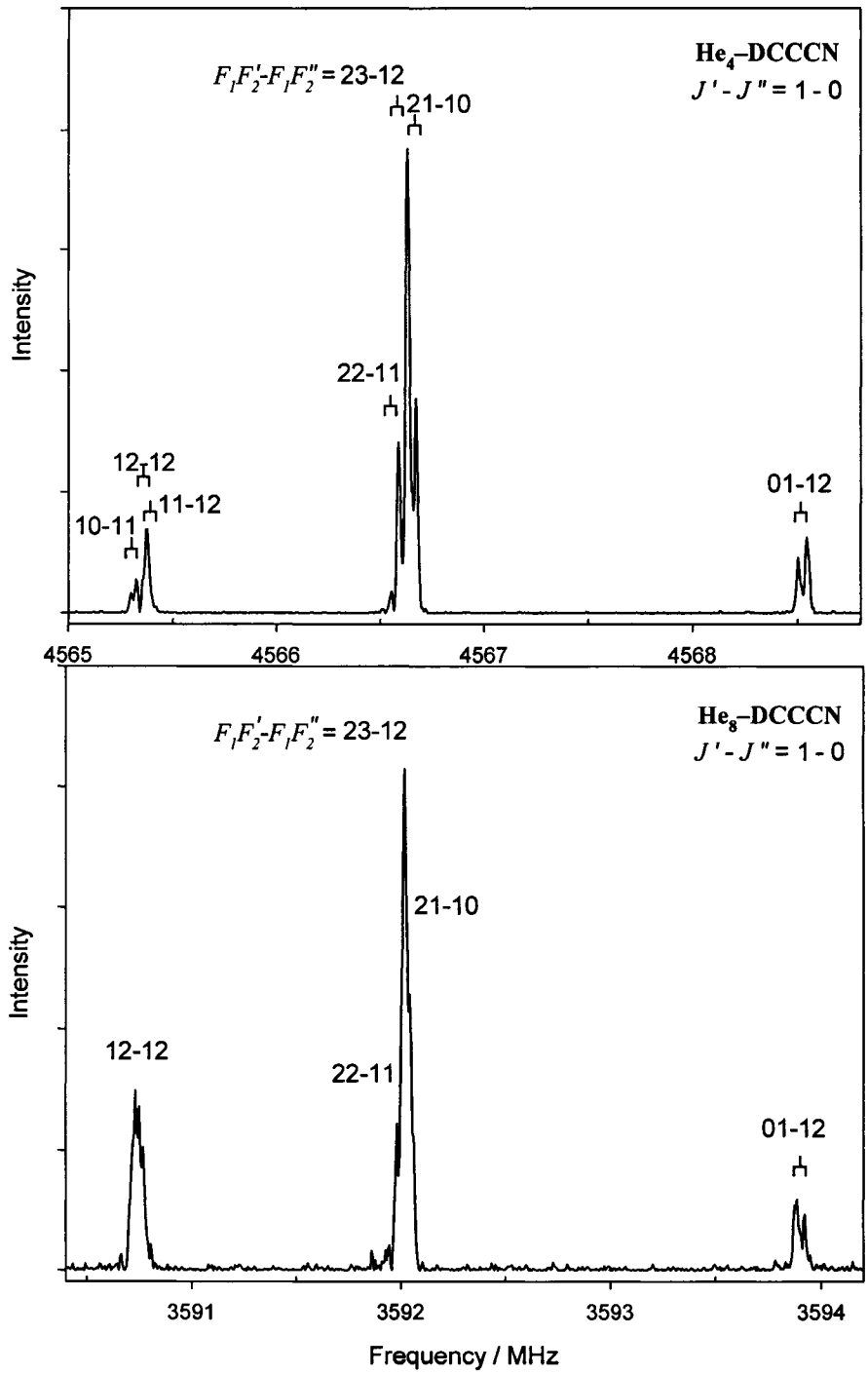

Figure 6.6 Composite spectrum of the $J = 1 - 0$ rotational transition of He_4–DCCCN and He_8–DCCCN, illustrating the varied degree to which it was possible to resolve D nuclear quadrupole hyperfine structures. Three individual spectra were recorded at 10 ns sample intervals, and summed over 50 cycles for He_4–DCCCN and 100 cycles for He_8–DCCCN.

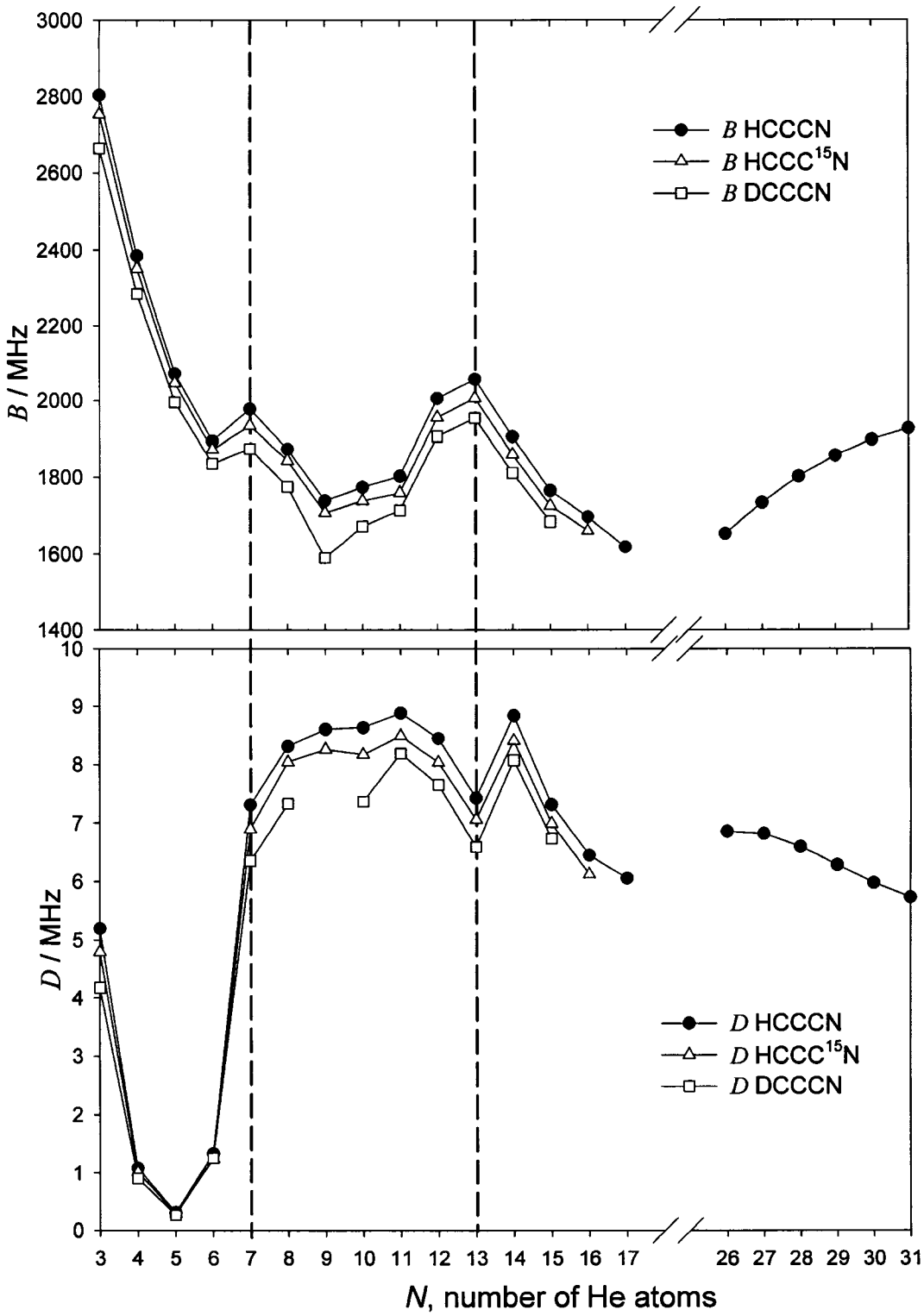

Figure 6.7 The behaviour of the B rotational constant with N, and D rotational parameter with N, for He_N–HCCCN, He_N–DCCCN and He_N–$HCCC^{15}N$.

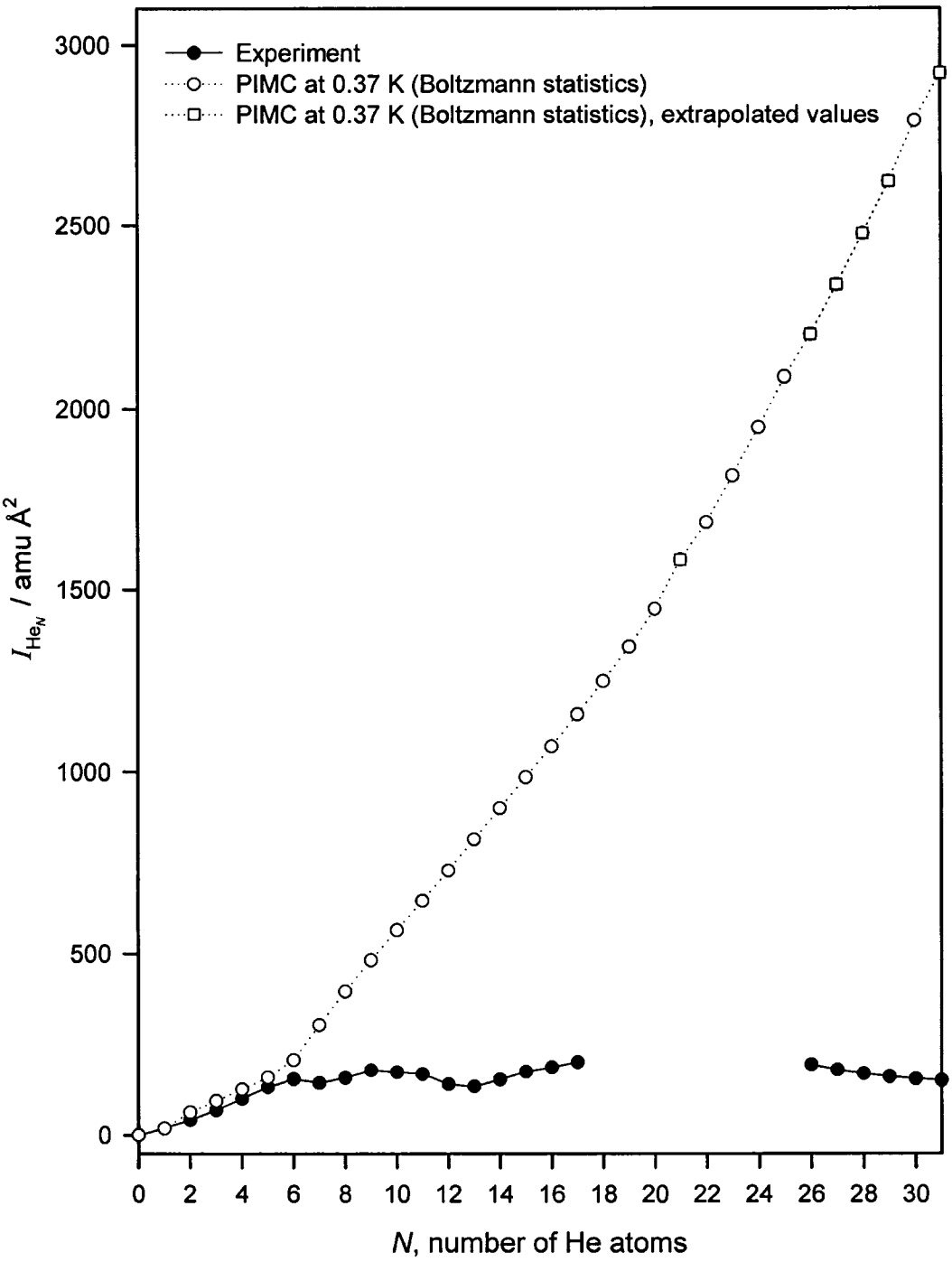

Figure 6.8 The effective helium moment of inertia with respect to the He_N–HCCCN *b*-axis, determined from the experimental *B* rotational constant, and determined from PIMC calculations of distinguishable particles (Ref. 21).

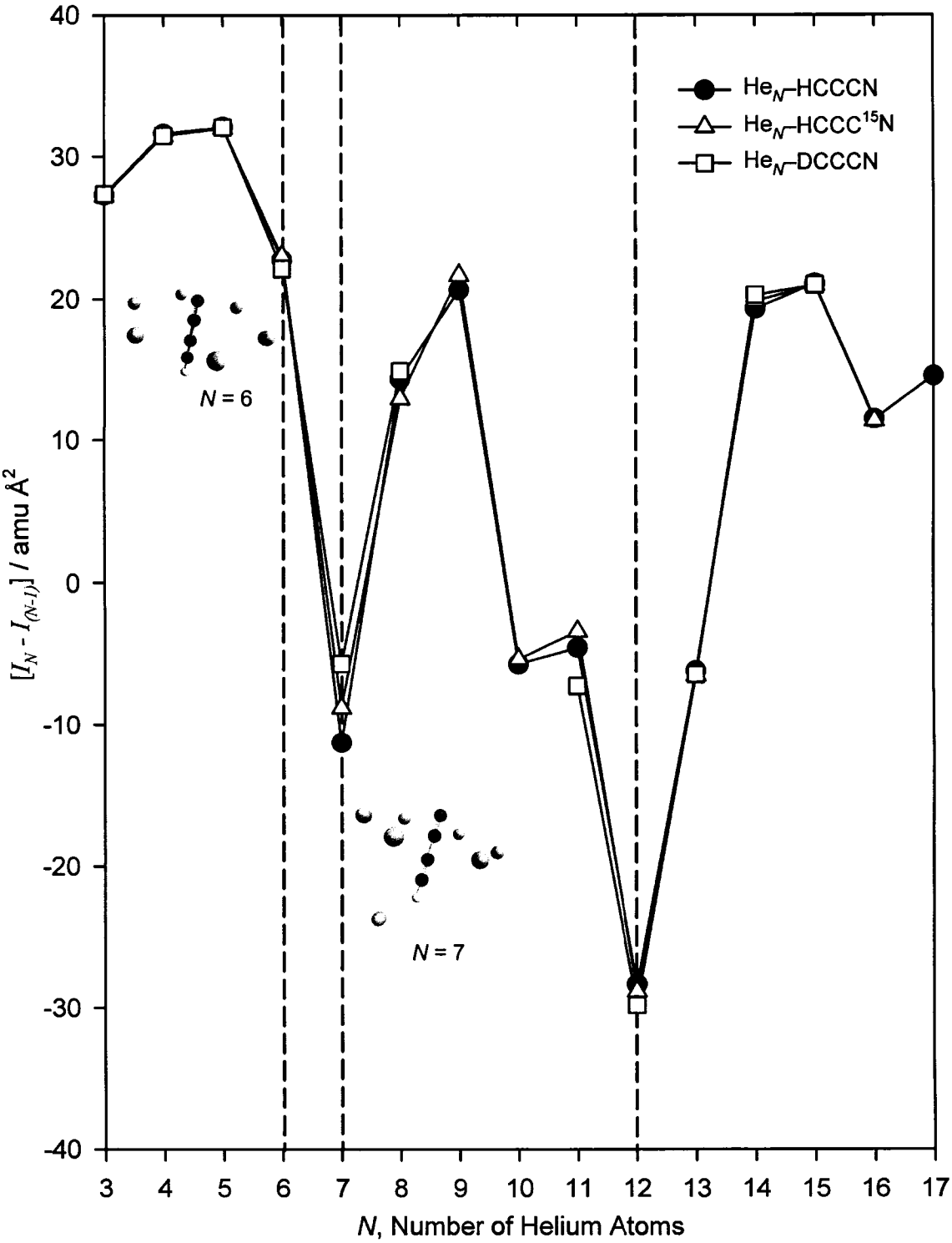

Figure 6.9 The change in moment of inertia for He_N–cyanoacetylene clusters with the addition of successive He atoms. Calculated as the difference in moment of inertia for He_N–cyanoacetylene and that of $He_{(N-1)}$–cyanoacetylene.

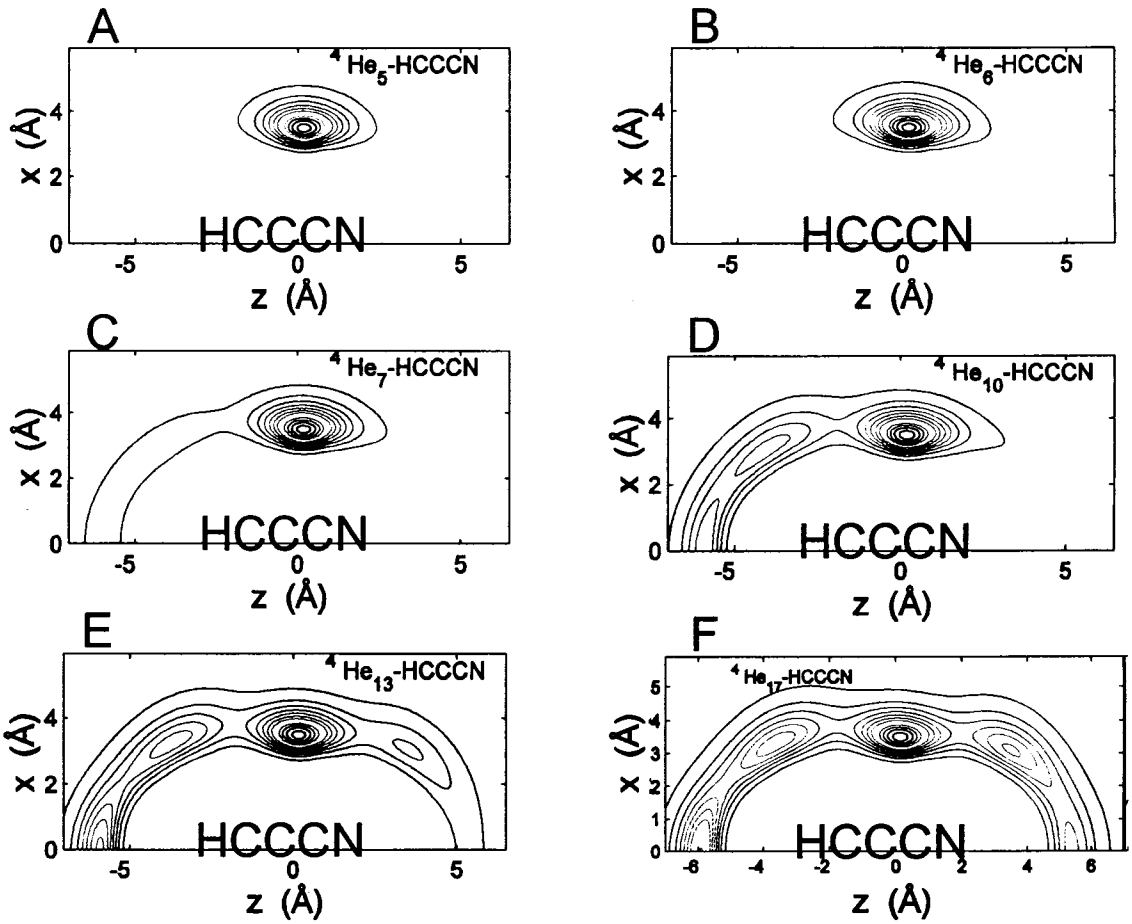

Figure 6.10 Contour plots of the helium density around (**A**) He_5–HCCCN, (**B**) He_6–HCCCN, (**C**) He_7–HCCCN, (**D**) He_{10}–HCCCN, (**E**) He_{13}–HCCCN, and (**F**) He_{17}–HCCCN from PIMC calculations at $T = 0.37$ K (Ref. 21). The contour lines represent increments of 0.01 Å^{-3}, starting with 0.005 Å^{-3}.

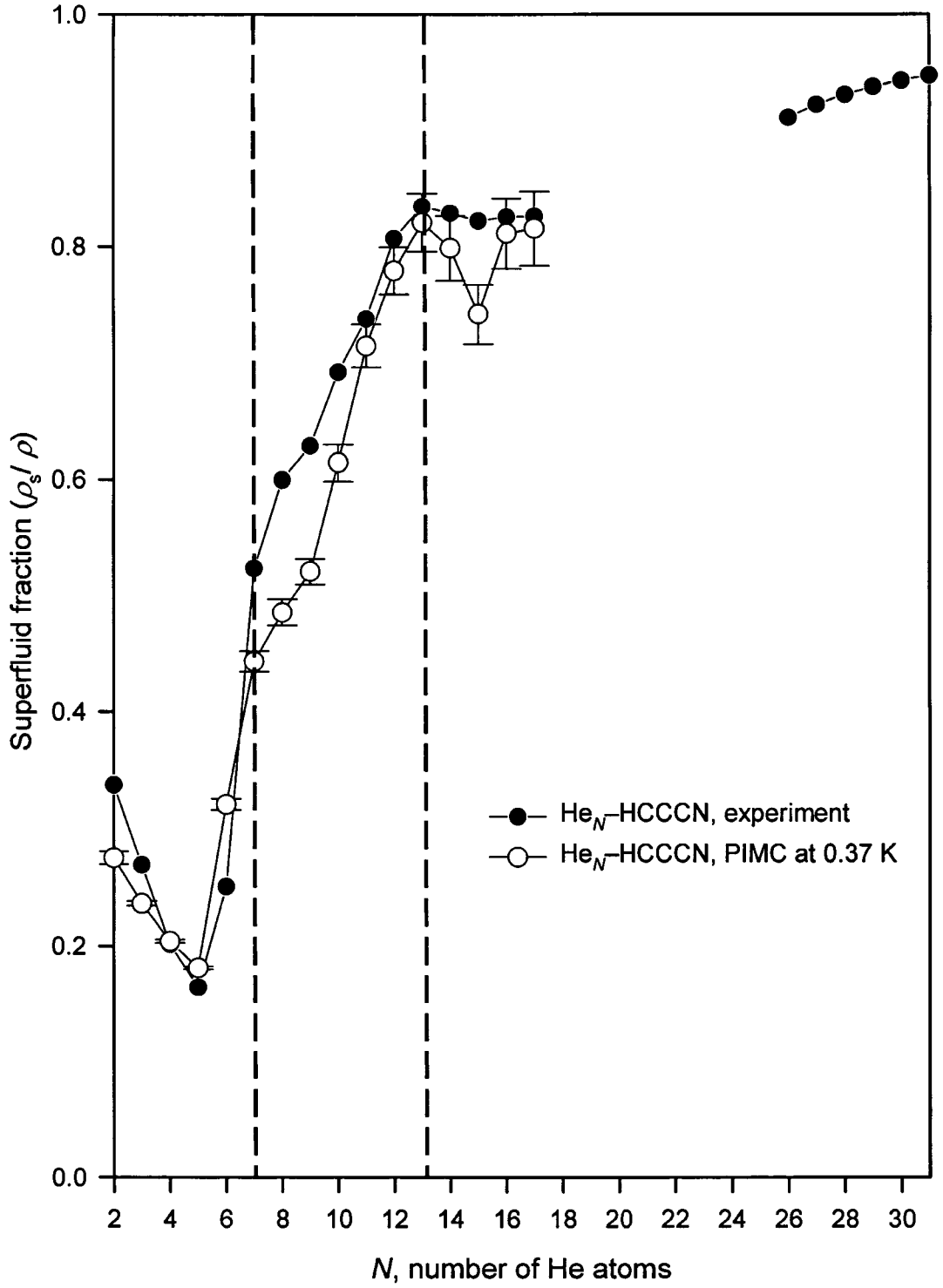

Figure 6.11 The ratio of superfluid to normal helium density in He_N–HCCCN clusters. The PIMC values shown were calculated for He atoms which obeyed Bose-Einstein statistics (Ref. 21). The dashed lines denote the cluster sizes for which local maxima in B were observed in Figure 6.7.

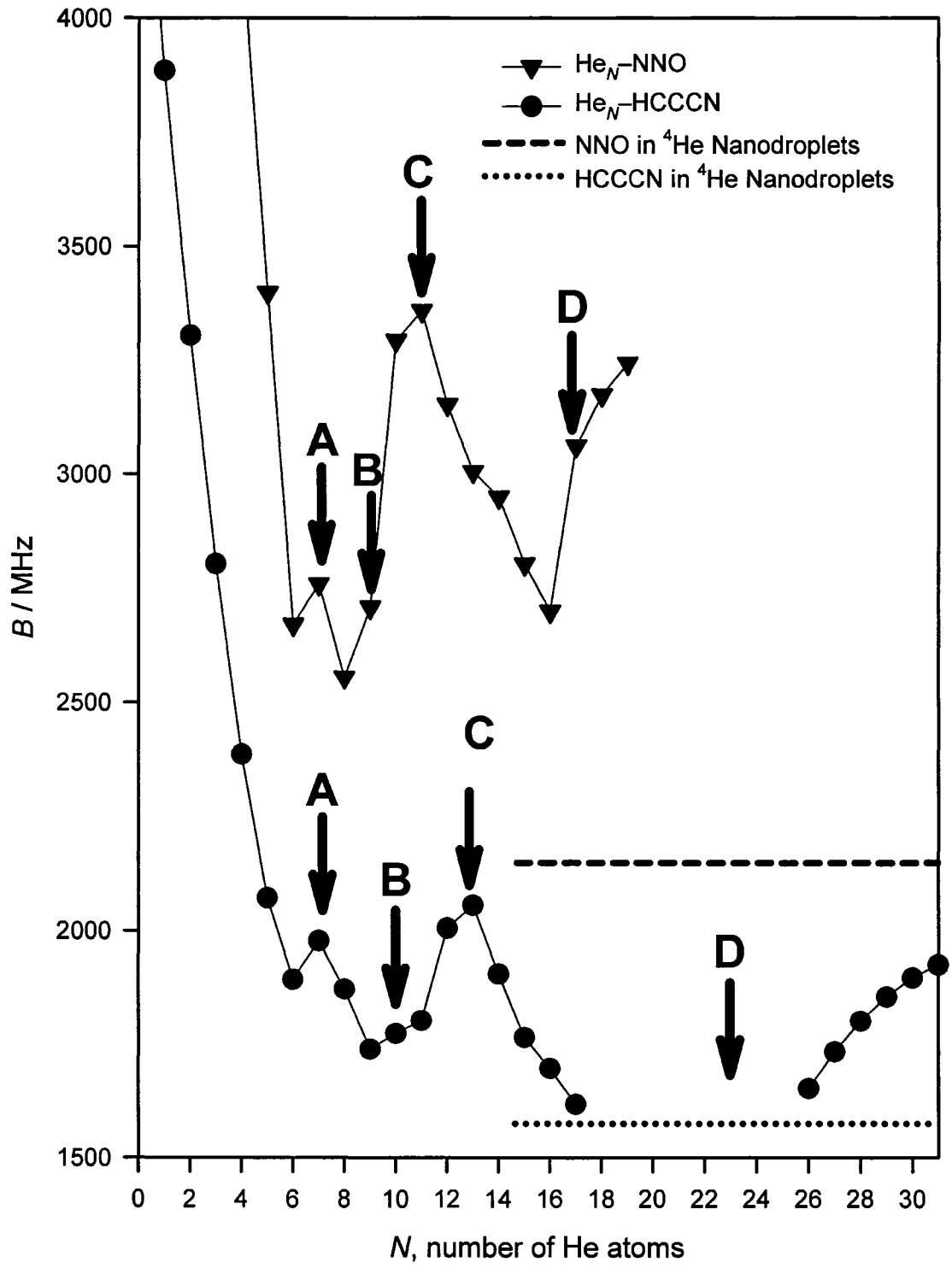

Figure 6.12 The evolution of B with N for He_N–N_2O (Refs. 4, 6) and He_N–HCCCN. **A**, **B**, **C**, and **D** refer to specific cluster sizes which are discussed in the text.

6.13 References

1. J. Tang, Y. Xu, A. R. W. McKellar, and W. Jäger, Science **297**, 2030 (2002).

2. J. Tang and A. R. W. McKellar, J. Chem. Phys. **119**, 5467 (2003).

3. J. Tang and A. R. W. McKellar, J. Chem. Phys. **119**, 754 (2003).

4. Y. Xu, W. Jäger, J. Tang, and A. R. W. McKellar, Phys. Rev. Lett. **91**, 163401 (2003).

5. Y. Xu and W. Jäger, J. Chem. Phys. **119**, 5457 (2003).

6. Y. Xu, N. Blinov, W. Jäger, and P. -N. Roy, J. Chem. Phys. **124**, 081101 (2006).

7. S. Moroni, private communication.

8. S. Moroni, A. Sarsa, S. Fantoni, K. E. Schmidt, and S. Baroni, Phys. Rev. Lett. **90**, 143401, (2003).

9. S. Moroni, N. Blinov, and P.-N. Roy, J. Chem. Phys. **121**, 3577 (2004).

10. Y. Xu and W. Jäger, Chem. Phys. Lett. **350**, 417 (2001).

11. Y. Xu, M. C. L. Gerry, J. P. Connelly, and B. J. Howard, J. Chem. Phys. **98**, 2735 (1993).

12. Y. Xu and W. Jäger, Phys. Chem. Chem. Phys. **2**, 3549 (2000).

13. F. Luo, C. F. Giese, and W. R. Gentry, J. Chem. Phys. **104**, 5467 (2003).

14. H. M. Pickett, J. Mol. Spectros. **148**, 371 (1991).

15. J. K. G. Watson, J. Chem. Phys. **48**, 4517 (1968).

16. Z. Kisiel, J. Mol. Spectrosc. **218**, 58 (2003).

17. J. K. Tyler and J. Sheridan, Trans. Faraday Society **59**, 266 (1963).

18. H. M. Pickett, J. Mol. Spectrosc. **148**, 371 (1991).

19. S. Thorwirth, H. S. P. Müller, and G. Winnewisser, J. Mol. Spectrosc. **204**, 133 (2000).

20. C. Callegari, I. Reinhard, K. K. Lehmann, G. Scoles, K. Nauta, and R. E. Miller, J. Chem. Phys. **113**, 4636 (2000).

21. N. Blinov and P. -N. Roy, private communication.

22. P. Sindzinger, M. L. Klein, and D. M. Ceperley, Phys. Rev. Lett. **63**, 1601 (1989).

7

Conclusions

Evidence of superfluidity in He_N–cyanoacetylene clusters was successfully detected using Fourier transform microwave spectroscopy. Numerous conclusions can be made about the results presented in Chapters 3, 4, and 6. Many of these are summarized in the corresponding chapters. Some general conclusions are presented here.

Firstly, from the pure rotational study of He_N–cyanoacetylene clusters it can be concluded that pulsed-nozzle Fourier transform microwave spectroscopy is a powerful technique with which to study the solvation of linear molecules with He atoms. The sensitivity of the microwave instrument was demonstrated by the observation of ^{13}C-containing isotopomers of He–HCCCN, He–HCCC^{15}N, and He_2–HCCCN at natural abundance. Observing the second two sets of isotopomers was especially significant, as

the cyanoacetylene sample was only enriched to 10% ^{15}N and the He_2–HCCCN trimer makes up only a small fraction of the species in our expansion. It is this sensitivity which allowed the rotational transition frequencies of larger He_N–cyanoacetylene clusters to be measured, even at frequencies significantly lower than the nominal operating range of our spectrometer, 4 to 26 GHz.

The second general conclusion follows from the first. Cyanoacetylene is well suited as a chromophore for investigating the onset of superfluidity in He clusters. The rotational spectroscopic study of the solvation of cyanoacetylene was feasible partly because of the strong permanent dipole moment of the molecule. It gave rise to strong rotational emission signals, allowing the detection of He_N–cyanoacetylene clusters that are produced only in low abundance. The strong rotational transitions of $N = 26$ to 31 indicate that larger He_N–cyanoacetylene clusters were already formed within our expansion.

The measured rotational transition frequencies of He_N–cyanoacetylene were used to fit the rotational parameters of a distortable asymmetric top model (for $N = 1$ and 2) or prolate symmetric top model (for $N \geq 3$). The evolution of the fitted B rotational constants with N was strikingly different than predicted by classical physics. An increase in the moment of inertia is intuitively expected as the He_N–cyanoacetylene clusters increase in size. A corresponding decrease in B with increasing N is thus predicted classically. The effective B values of He_N–cyanoacetylene clusters did decrease for small clusters with $N < 7$. An increase in B was observed for $N = 7$, which was attributed to the redistribution of helium density. A local minimum value of the B rotational constant

was attained at He_9–cyanoacetylene. The addition of a tenth He atom resulted in a net decrease in the moment of inertia of the cluster. The increase in B for He_{10}–cyanoacetylene marked the onset of oscillatory behaviour of the effective B rotational constant with increasing N. This is a clear indication that helium density decouples from the rotating cluster and is a hallmark of superfluidity in He containing systems. A local maximum value of B was reached for He_{13}–cyanoacetylene, after which the effective inertia of the clusters with N = 14-17 was found to increase with the addition of He atoms. It was assumed that some B values of He_N–cyanoacetylene clusters with N = 18-25 dropped below the limiting B value of HCCCN in ^{4}He nanodroplets. This necessitates that additional helium density decouples from the rotating cyanoacetylene molecule in larger clusters, if the effective moment of inertia of HCCCN in a nanodroplet is to be obtained. Though the J = 1-0 transition frequencies in this size cluster range were too low to measure with our instrument, the presence of a second "turn-around" of B was confirmed through spectroscopic investigation. Rotational transitions for clusters with N = 26 to 31 were observed, and their B values increased with increasing cluster size. B of the largest cluster observed spectroscopically, He_{31}–HCCCN, is significantly higher than B of HCCCN in a ^{4}He nanodroplet. This explicitly implies that further increases in the effective moment of inertia of He_N–cyanoacetylene clusters occur for N > 31. The oscillatory behaviour of B with N determined for He_N–cyanoacetylene clusters indicates the complexity of the solvation process in this system.

Using a relatively long molecular rotor for the spectroscopic investigation of the onset of superfluidity in He_N–molecule clusters has provided some interesting results.

He–cyanoacetylene was found to be extremely floppy compared to other He–molecule dimers, such as He–OCS and He–N_2O. It undergoes large amplitude motions, and the fit of its rotational transition frequencies to a semi-rigid rotor model required many distortion constants. The He_2–cyanoacetylene trimer is a very floppy asymmetric rotor, with a complicated rotational spectrum of which only two transitions were observed. The extreme non-rigidity of the dimer and trimer made the relatively tightly bound He_5–cyanoacetylene species remarkable. A ring of five He atoms in an equatorial position around cyanoacetylene, OCS or N_2O results in a fairly rigid cluster. While interactions between He atoms or between He atoms and a molecule may be weak, the accumulated effect of these weak interactions is significant. The localization of a sixth He atom in the equatorial ring for He_6–cyanoacetylene contributes to differences in the onset of superfluidity for He_N–cyanoacetylene clusters, compared to the shorter He_N–N_2O clusters. Specifically, the increased helium density in the ring lead to a faster increase in the superfluid fraction of He for small He_N–cyanoacetylene clusters ($N = 5$ to 13), compared to He_N–N_2O. The longer length of the cyanoacetylene, however, meant that additional He atoms were required to coat the rotor compared to N_2O, delaying the observation of the "turn-around" of the B rotational constant.

This work demonstrates that important information can be gleaned by the study of the solvation of a longer rotor with He atoms. It is my hope that it serves as a starting point for the study of even larger He_N–cyanoacetylene clusters, and inspires research into the properties of other species in a superfluid environment.

Appendix A

Table A.1 *Ab initio* single point energies (E_h) of the He–cyanoacetylene potential energy surface, calculated at CCSD(T) theory level with aVQZ basis sets supplemented with bond functions (α: *sp* 0.9, 0.3, 0.1; *d* 0.3;0.2; *fg* 0.3).

	θ = 2°	13°	24°	35°	46°	57°
R=2.00 Å			0.5207	0.2949	0.1256	0.0536
2.25 Å		0.9636	0.3717	0.1708	0.0656	0.0258
2.50 Å		0.5163	0.2477	0.0937	0.0325	0.0116
2.75 Å		0.3476	0.1439	0.0482	0.0152	4.9090e-3
3.00 Å	0.3119	0.1870	0.0733	0.0231	6.7251e-3	1.8687e-3
3.25 Å	0.1325	0.0848	0.0339	0.0103	2.7240e-3	5.7751e-4
3.50 Å	0.0536	0.0355	0.0145	4.2687e-3	9.5408e-4	7.4655e-5
3.75 Å	0.0213	0.0141	5.7731e-3	1.5719e-3	2.2910e-4	-9.2248e-5
4.00 Å	7.7437e-3	5.2510e-3	2.0841e-3	4.5982e-4	-3.4229e-5	-1.2672e-4
4.25 Å	2.6762e-3	1.7761e-3	6.2466e-4	4.4753e-5	-1.0766e-4	-1.1530e-4
4.50 Å	7.9169e-4	4.8409e-4	9.4997e-5	-8.4296e-5	-1.1082e-4	-9.2554e-5
4.75 Å	1.3943e-4	4.3886e-5	-6.9346e-5	-1.0605e-4	-9.2801e-5	-7.0597e-5
5.00 Å	-5.7463e-5	-8.0894e-5	-1.0114e-4	-9.3345e-5	-7.1930e-5	-5.2787e-5
5.25 Å	-9.7052e-5	-9.8078e-5	-9.1061e-5	-7.3474e-5	-5.4061e-5	-3.9287e-5
5.50 Å	-8.8706e-5	-8.4098e-5	-7.1881e-5	-5.5399e-5	-4.0246e-5	-2.9342e-5
5.75 Å	-6.9986e-5	-6.4976e-5	-5.4063e-5	-4.1162e-5	-2.9994e-5	-2.2084e-5
6.00 Å	-5.2452e-5	-4.8379e-5	-4.0031e-5	-3.0562e-5	-2.2500e-5	-1.6776e-5
6.25 Å	-3.8683e-5	-3.5676e-5	-2.9621e-5	-2.2827e-5	-1.7032e-5	-1.2871e-5
6.50 Å	-2.8420e-5	-2.6375e-5	-2.2065e-5	-1.7207e-5	-1.3021e-5	-9.9716e-6
6.75 Å	-2.1181e-5	-1.9661e-5	-1.6594e-5	-1.3106e-5	-1.0058e-5	-7.8003e-6
7.00 Å	-1.5910e-5	-1.4817e-5	-1.2617e-5	-1.0089e-5	-7.8434e-6	-6.1528e-6
7.25 Å	-1.2082e-5	-1.1296e-5	-9.7023e-6	-7.8437e-6	-6.1725e-6	-4.8919e-6
7.50 Å	-9.2872e-6	-8.7113e-6	-7.5402e-6	-6.1584e-6	-4.8976e-6	-3.9162e-6
7.75 Å	-7.2144e-6	-6.7888e-6	-5.9178e-6	-4.8780e-6	-3.9148e-6	-3.1548e-6
8.00 Å	-5.6610e-6	-5.3442e-6	-4.6865e-6	-3.8950e-6	-3.1497e-6	-2.5551e-6
8.25 Å	-4.4807e-6	-4.2420e-6	-3.7415e-6	-3.1291e-6	-2.5461e-6	-2.0793e-6
8.50 Å	-3.5783e-6	-3.3932e-6	-3.0085e-6	-2.5316e-6	-2.0720e-6	-1.6991e-6
8.75 Å	-2.8760e-6	-2.7361e-6	-2.4348e-6	-2.0592e-6	-1.6933e-6	-1.3931e-6
9.00 Å	-2.3259e-6	-2.2181e-6	-1.9810e-6	-1.6827e-6	-1.3893e-6	-1.1452e-6
9.25 Å	-1.8943e-6	-1.8076e-6	-1.6202e-6	-1.3796e-6	-1.1417e-6	-9.4241e-7
9.50 Å	-1.5487e-6	-1.4816e-6	-1.3297e-6	-1.1346e-6	-9.4012e-7	-7.7610e-7
9.75 Å	-1.2715e-6	-1.2175e-6	-1.0936e-6	-9.3453e-7	-7.7449e-7	-6.3857e-7
10.00 Å	-1.0466e-6	-1.0022e-6	-9.0096e-7	-7.7008e-7	-6.3752e-7	-5.2417e-7
10.25 Å	-8.6342e-7	-8.2628e-7	-7.4334e-7	-6.3357e-7	-5.2240e-7	-4.2865e-7
10.50 Å	-7.1178e-7	-6.8055e-7	-6.1184e-7	-5.2143e-7	-4.2897e-7	-3.4742e-7
10.75 Å	-5.8638e-7	-5.5944e-7	-5.0210e-7	-4.2542e-7	-3.4849e-7	-2.8006e-7
11.00 Å	-4.8130e-7	-4.5970e-7	-4.1061e-7	-3.4658e-7	-2.8071e-7	-2.2299e-7
11.25 Å	-3.9402e-7	-3.7515e-7	-3.3364e-7	-2.7904e-7	-2.2354e-7	-1.7480e-7
11.50 Å	-3.1941e-7	-3.0404e-7	-2.6896e-7	-2.2332e-7	-1.7523e-7	-1.3185e-7
11.75 Å	-2.5668e-7	-2.4389e-7	-2.1335e-7	-1.7415e-7	-1.3332e-7	-9.6879e-8
12.00 Å	-2.0347e-7	-1.9276e-7	-1.6646e-7	-1.3297e-7	-9.7386e-8	-6.6225e-8

Table A.1, continued

	$\theta = 68^{\circ}$	79°	90°	101°	112°	123°
R=2.00 Å	0.0259	0.0156	0.0136	0.0179	0.0316	0.0651
2.25 Å	0.0112	6.0286e-3	5.0911e-3	7.3773e-3	0.0146	0.0327
2.50 Å	4.4713e-3	2.0416e-3	1.6416e-3	2.7821e-3	6.3950e-3	0.0157
2.75 Å	1.5707e-3	4.9817e-4	3.4346e-4	8.8111e-4	2.5878e-3	7.1185e-3
3.00 Å	4.0399e-4	-3.4904e-5	-8.6511e-5	1.5178e-4	9.1317e-4	3.0179e-3
3.25 Å	-1.7466e-5	-1.7748e-4	-1.8938e-4	-9.2329e-5	2.2248e-4	1.1425e-3
3.50 Å	-1.3867e-4	-1.8389e-4	-1.8232e-4	-1.4823e-4	-3.3505e-5	3.3465e-4
3.75 Å	-1.4949e-4	-1.5187e-4	-1.4698e-4	-1.3901e-4	-1.0819e-4	1.6907e-5
4.00 Å	-1.2647e-4	-1.1579e-4	-1.1100e-4	-1.1269e-4	-1.1370e-4	-8.7666e-5
4.25 Å	-9.8176e-5	-8.5618e-5	-8.1814e-5	-8.6267e-5	-9.7031e-5	-1.0658e-4
4.50 Å	-7.3613e-5	-6.2763e-5	-5.9964e-5	-6.4545e-5	-7.6521e-5	-9.5374e-5
4.75 Å	-5.4554e-5	-4.6119e-5	-4.4121e-5	-4.7991e-5	-5.8346e-5	-7.6819e-5
5.00 Å	-4.0431e-5	-3.4154e-5	-3.2732e-5	-3.5770e-5	-4.3933e-5	-5.9167e-5
5.25 Å	-3.0141e-5	-2.5553e-5	-2.4542e-5	-2.6844e-5	-3.3028e-5	-4.4754e-5
5.50 Å	-2.2677e-5	-1.9332e-5	-1.8608e-5	-2.0329e-5	-2.4937e-5	-3.3700e-5
5.75 Å	-1.7234e-5	-1.4787e-5	-1.4261e-5	-1.5545e-5	-1.8969e-5	-2.5446e-5
6.00 Å	-1.3233e-5	-1.1430e-5	-1.1046e-5	-1.2009e-5	-1.4558e-5	-1.9344e-5
6.25 Å	-1.0262e-5	-8.9211e-6	-8.8520e-6	-9.3620e-6	-1.1274e-5	-1.4831e-5
6.50 Å	-8.0331e-6	-7.0273e-6	-6.8778e-6	-7.3653e-6	-8.8161e-6	-1.1476e-5
6.75 Å	-6.3428e-6	-5.5781e-6	-5.4363e-6	-5.8443e-6	-6.9499e-6	-8.9626e-6
7.00 Å	-5.0449e-6	-4.4578e-6	-4.3342e-6	-4.6660e-6	-5.5205e-6	-7.0601e-6
7.25 Å	-4.0411e-6	-3.5866e-6	-3.4930e-6	-3.7525e-6	-4.4183e-6	-5.6077e-6
7.50 Å	-3.2561e-6	-2.9010e-6	-2.8239e-6	-3.0335e-6	-3.5578e-6	-4.4863e-6
7.75 Å	-2.6373e-6	-2.3575e-6	-2.3009e-6	-2.4641e-6	-2.8811e-6	-3.6126e-6
8.00 Å	-2.1467e-6	-1.9237e-6	-1.8778e-6	-2.0108e-6	-2.3447e-6	-2.9259e-6
8.25 Å	-1.7538e-6	-1.5748e-6	-1.5371e-6	-1.6453e-6	-1.9156e-6	-2.3810e-6
8.50 Å	-1.4373e-6	-1.2925e-6	-1.2633e-6	-1.3514e-6	-1.5702e-6	-1.9453e-6
8.75 Å	-1.1808e-6	-1.0625e-6	-1.0622e-6	-1.1109e-6	-1.2898e-6	-1.5945e-6
9.00 Å	-9.7146e-7	-8.7440e-7	-8.5437e-7	-9.1396e-7	-1.0610e-6	-1.3099e-6
9.25 Å	-7.9993e-7	-7.1874e-7	-7.0200e-7	-7.5167e-7	-8.7267e-7	-1.0778e-6
9.50 Å	-6.5782e-7	-5.9050e-7	-5.7677e-7	-6.1962e-7	-7.1838e-7	-8.8740e-7
9.75 Å	-5.3988e-7	-4.8356e-7	-4.7112e-7	-5.0550e-7	-5.9003e-7	-7.3036e-7
10.00 Å	-4.4119e-7	-3.938e-7	-3.8367e-7	-4.1251e-7	-4.8315e-7	-6.0016e-7
10.25 Å	-3.5810e-7	-3.1848e-7	-3.0912e-7	-3.3405e-7	-3.9414e-7	-4.9200e-7
10.50 Å	-2.8972e-7	-2.5455e-7	-2.4800e-7	-2.6836e-7	-3.1897e-7	-3.9981e-7
10.75 Å	-2.3022e-7	-2.0100e-7	-1.9365e-7	-2.1186e-7	-2.5492e-7	-3.2487e-7
11.00 Å	-1.8018e-7	-1.5508e-7	-1.4945e-7	-1.6435e-7	-2.0108e-7	-2.6086e-7
11.25 Å	-1.3758e-7	-1.1550e-7	-1.1036e-7	-1.2358e-7	-1.5501e-7	-2.0456e-7
11.50 Å	-1.0070e-7	-8.2069e-8	-7.8309e-8	-8.9080e-8	-1.1661e-7	-1.6239e-7
11.75 Å	-6.9602e-8	-5.3322e-8	-4.9229e-8	-5.9019e-8	-8.2220e-8	-1.1766e-7
12.00 Å	-4.2215e-8	-2.8280e-8	-2.5325e-8	-3.3308e-8	-5.3879e-8	-8.8794e-8

Table A.1, continued

	θ = 134°	145°	156°	167°	178°
R=2.00 Å	0.1419	0.2808	0.4679		
2.25Å	0.0759	0.1674	0.3302	1.1604	
2.50 Å	0.0390	0.0976	0.2455	0.6864	
2.75 Å	0.0193	0.0548	0.1750	0.5912	
3.00 Å	9.0596e-3	0.0291	0.1103	0.4363	
3.25 Å	3.9852e-3	0.0145	0.0616	0.2548	
3.50 Å	1.5824e-3	6.6774e-3	0.0310	0.1283	
3.75 Å	5.1280e-4	2.7829e-3	0.0142	0.0584	
4.00 Å	7.6400e-5	9.8900e-4	5.9290e-3	0.0245	
4.25 Å	7.6182e-5	2.3632e-4	2.1731e-3	9.4189e-3	
4.50 Å	1.1142e-4	-3.9850e-5	6.2870e-4	3.2501e-3	
4.75 Å	1.0388e-4	-1.1598e-4	6.3792e-5	9.1457e-4	
5.00 Å	-8.4622e-5	-1.1782e-4	-1.0457e-4	1.1910e-4	2.7060e-4
5.25 Å	-6.5222e-5	-9.7693e-5	-1.2932e-4	-1.0429e-4	-3.7356e-5
5.50 Å	-4.9148e-5	-7.5107e-5	-1.1087e-4	-1.3639e-4	-1.3816e-4
5.75 Å	-3.6807e-5	-5.6063e-5	-8.5050e-5	-1.1559e-4	-1.3087e-4
6.00 Å	-2.7636e-5	-4.1507e-5	-6.2669e-5	-8.7028e-5	-1.0119e-4
6.25 Å	-2.0896e-5	-3.0817e-5	-4.5714e-5	-6.3024e-5	-7.3492e-5
6.50 Å	-1.5945e-5	-2.3072e-5	-3.3468e-5	-4.5325e-5	-5.2443e-5
6.75 Å	-1.2287e-5	-1.7460e-5	-2.4760e-5	-3.2834e-5	-3.7554e-5
7.00 Å	-9.5607e-6	-1.3363e-5	-1.8558e-5	-2.4114e-5	-2.7245e-5
7.25 Å	-7.5095e-6	-1.0340e-5	-1.4096e-5	-1.7981e-5	-2.0090e-5
7.50 Å	-5.9491e-6	-8.0807e-6	-1.0839e-5	-1.3605e-5	-1.5062e-5
7.75 Å	-4.7495e-6	-6.3742e-6	-8.4273e-6	-1.0431e-5	-1.1466e-5
8.00 Å	-3.8177e-6	-5.0708e-6	-6.6161e-6	-8.0927e-6	-8.8505e-6
8.25 Å	-3.0865e-6	-4.0608e-6	-5.2405e-6	-6.3452e-6	-6.9150e-6
8.50 Å	-2.5082e-6	-3.2733e-6	-4.1836e-6	-5.0233e-6	-5.4537e-6
8.75 Å	-2.0468e-6	-2.6532e-6	-3.3631e-6	-4.0086e-6	-4.3388e-6
9.00 Å	-1.6761e-6	-2.1614e-6	-2.7201e-6	-3.2227e-6	-3.4758e-6
9.25 Å	-1.3763e-6	-1.7591e-6	-2.2102e-6	-2.6047e-6	-2.8055e-6
9.50 Å	-1.1317e-6	-1.4532e-6	-1.8033e-6	-2.1150e-6	-2.2783e-6
9.75 Å	-9.3178e-7	-1.1895e-6	-1.4733e-6	-1.7250e-6	-1.8560e-6
10.00 Å	-7.6718e-7	-9.7911e-7	-1.2122e-6	-1.4143e-6	-1.5173e-6
10.25 Å	-6.3009e-7	-8.0380e-7	-9.9270e-7	-1.1684e-6	-1.2451e-6
10.50 Å	-5.1956e-7	-6.6551e-7	-8.1729e-7	-9.6206e-7	-1.0214e-6
10.75 Å	-4.2146e-7	-5.4258e-7	-6.7196e-7	-7.9033e-7	-8.3813e-7
11.00 Å	-3.4411e-7	-4.4585e-7	-5.5338e-7	-6.4325e-7	-6.8743e-7
11.25 Å	-2.7658e-7	-3.6323e-7	-4.5179e-7	-5.2871e-7	-5.6368e-7
11.50 Å	-2.1835e-7	-2.9242e-7	-3.6815e-7	-4.3163e-7	-4.6063e-7
11.75 Å	-1.7342e-7	-2.3487e-7	-2.9881e-7	-3.4953e-7	-3.7450e-7
12.00 Å	-1.2965e-7	-1.8347e-7	-2.3807e-7	-2.8065e-7	-3.0275e-7

Table A.2 *Ab initio* single point energies (E_h) of the He–cyanoacetylene potential energy surface, calculated at CCSD(T) theory level with aVTZ basis sets supplemented with bond functions (α: *sp* 0.9, 0.3, 0.1; *d* 0.3;0.2; *fg* 0.3).

	θ = 2°	13°	24°	35°	46°	57°
R=2.00 Å	21.6280	2.2170	0.5250	0.2967	0.1265	0.0541
2.25 Å	3.2559	0.9719	0.3746	0.1721	0.0661	0.0260
2.50 Å	0.8958	0.5205	0.2496	0.0945	0.0328	0.0118
2.75 Å	0.5716	0.3498	0.1451	0.0487	0.0154	4.9862e-3
3.00 Å	0.3135	0.1882	0.0740	0.0234	6.8331e-3	1.9079e-3
3.25 Å	0.1333	0.0855	0.0342	0.0105	2.7788e-3	5.9693e-4
3.50 Å	0.0540	0.0359	0.0147	4.3478e-3	9.8145e-4	8.4188e-5
3.75 Å	0.0211	0.0143	5.8698e-3	1.6094e-3	2.4265e-4	-8.7859e-5
4.00 Å	7.8622e-3	5.3371e-3	2.1277e-3	4.7751e-4	-2.7730e-5	-1.2486e-4
4.25 Å	2.7217e-3	1.8128e-3	6.4399e-4	5.3009e-5	-1.0479e-4	-1.1469e-4
4.50 Å	8.1105e-4	4.9965e-4	1.0363e-4	-8.0650e-5	-1.0971e-4	-9.2469e-5
4.75 Å	1.4771e-4	5.0330e-5	-6.5725e-5	-1.0465e-4	-9.2498e-5	-7.0740e-5
5.00 Å	-5.4619e-5	-7.8668e-5	-9.9904e-5	-9.2998e-5	-7.2018e-5	-5.3007e-5
5.25 Å	-9.6613e-5	-9.7672e-5	-9.0881e-5	-7.3578e-5	-5.4288e-5	-3.9515e-5
5.50 Å	-8.9102e-5	-8.4342e-5	-7.2095e-5	-5.5638e-5	-4.0484e-5	-2.9550e-5
5.75 Å	-7.0574e-5	-6.5404e-5	-5.4364e-5	-4.1406e-5	-3.0204e-5	-2.2271e-5
6.00 Å	-5.2967e-5	-4.8783e-5	-4.0297e-5	-3.0765e-5	-2.2680e-5	-1.6948e-5
6.25 Å	-3.9072e-5	-3.5986e-5	-2.9827e-5	-2.2995e-5	-1.7190e-5	-1.3033e-5
6.50 Å	-2.8802e-5	-2.6595e-5	-2.2221e-5	-1.7345e-5	-1.3166e-5	-1.0127e-5
6.75 Å	-2.1373e-5	-1.9823e-5	-1.6714e-5	-1.3226e-5	-1.0188e-5	-7.9458e-6
7.00 Å	-1.6020e-5	-1.4929e-5	-1.2714e-5	-1.0195e-5	-7.9656e-6	-6.2919e-6
7.25 Å	-1.2152e-5	-1.1377e-5	-9.7857e-6	-7.9451e-6	-6.2892e-6	-5.0266e-6
7.50 Å	-9.3391e-6	-8.7802e-6	-7.6219e-6	-6.2588e-6	-5.0133e-6	-4.0497e-6
7.75 Å	-7.2713e-6	-6.8612e-6	-6.0038e-6	-4.9818e-6	-4.0341e-6	-3.2907e-6
8.00 Å	-5.7328e-6	-5.4264e-6	-4.7838e-6	-4.0085e-6	-3.2764e-6	-2.6962e-6
8.25 Å	-4.5724e-6	-4.3411e-6	-3.8526e-6	-3.2568e-6	-2.6850e-6	-2.2269e-6
8.50 Å	-3.6879e-6	-3.5099e-6	-3.1346e-6	-2.6698e-6	-2.2199e-6	-1.8527e-6
8.75 Å	-3.0053e-6	-2.8674e-6	-2.5744e-6	-2.2072e-6	-1.8477e-6	-1.5537e-6
9.00 Å	-2.4722e-6	-2.3643e-6	-2.1325e-6	-1.8389e-6	-1.5503e-6	-1.3105e-6
9.25 Å	-2.0516e-6	-1.9657e-6	-1.7798e-6	-1.5426e-6	-1.3079e-6	-1.1111e-6
9.50 Å	-1.7148e-6	-1.6461e-6	-1.4959e-6	-1.3021e-6	-1.1096e-6	-9.4687e-7
9.75 Å	-1.4430e-6	-1.3872e-6	-1.2639e-6	-1.1051e-6	-9.4621e-7	-8.1093e-7
10.00 Å	-1.2205e-6	-1.1749e-6	-1.0730e-6	-8.1060e-7	-8.1060e-7	-6.9752e-7
10.25 Å	-1.0387e-6	-9.9995e-7	-9.1663e-7	-6.9737e-7	-6.9737e-7	-6.0251e-7
10.50 Å	-8.8724e-7	-8.5526e-7	-7.8579e-7	-6.0225e-7	-6.0225e-7	-5.2231e-7
10.75 Å	-7.6131e-7	-7.3522e-7	-6.7649e-7	-5.2272e-7	-5.2272e-7	-4.5468e-7
11.00 Å	-6.5579e-7	-6.3454e-7	-5.8535e-7	-4.5450e-7	-4.5450e-7	-3.9733e-7
11.25 Å	-5.6785e-7	-5.5055e-7	-5.0777e-7	-3.9778e-7	-3.9778e-7	-3.4810e-7
11.50 Å	-4.9388e-7	-4.7920e-7	-4.4344e-7	-3.4906e-7	-3.4906e-7	-3.0720e-7
11.75 Å	-4.3126e-7	-4.1820e-7	-3.8765e-7	-3.0729e-7	-3.0729e-7	-2.7110e-7
12.00 Å	-3.7778e-7	-3.6653e-7	-3.4097e-7	-2.7193e-7	-2.7193e-7	-2.4039e-7

Table A.2, continued

	θ=68°	79°	90°	101°	112°	123°
R=2.00 Å	0.0261	0.0158	0.0137	0.0181	0.0319	0.0656
2.25 Å	0.0113	6.1136e-3	5.1652e-3	7.4714e-3	0.0148	0.0330
2.50 Å	4.5399e-3	2.0819e-3	1.6762e-3	2.8286e-3	6.4801e-3	0.0158
2.75 Å	1.6045e-3	5.1665e-4	3.5892e-4	9.0344e-4	2.6329e-3	7.2178e-3
3.00 Å	4.1995e-4	-2.6888e-5	-7.9828e-5	1.6239e-4	9.3619e-4	3.0717e-3
3.25 Å	-1.0144e-5	-1.7442e-4	-1.8682e-4	-8.7288e-5	2.3413e-4	1.1707e-3
3.50 Å	-1.3559e-4	-1.8294e-4	-1.8160e-4	-1.4623e-4	-2.7829e-5	3.4917e-4
3.75 Å	-1.4835e-4	-1.5176e-4	-1.4695e-4	-1.3835e-4	-1.0562e-4	2.4267e-5
4.00 Å	-1.2621e-4	-1.1597e-4	-1.1120e-4	-1.1258e-4	-1.1262e-4	-8.4106e-5
4.25 Å	-9.8262e-5	-8.5866e-5	-8.2051e-5	-8.6366e-5	-9.6662e-5	-1.0492e-4
4.50 Å	-7.3815e-5	-6.3007e-5	-6.0193e-5	-6.4716e-5	-7.6469e-5	-9.4686e-5
4.75 Å	-5.4778e-5	-4.6338e-5	-4.4325e-5	-4.8181e-5	-5.8440e-5	-7.6595e-5
5.00 Å	-4.0644e-5	-3.4349e-5	-3.2927e-5	-3.5961e-5	-4.4090e-5	-5.9167e-5
5.25 Å	-3.0342e-5	-2.5732e-5	-2.4729e-5	-2.7035e-5	-3.3213e-5	-4.4865e-5
5.50 Å	-2.2860e-5	-1.9503e-5	-1.8783e-5	-2.0519e-5	-2.5137e-5	-3.3865e-5
5.75 Å	-1.7410e-5	-1.4956e-5	-1.4436e-5	-1.5737e-5	-1.9174e-5	-2.5637e-5
6.00 Å	-1.3403e-5	-1.1599e-5	-1.1223e-5	-1.2198e-5	-1.4760e-5	-1.9546e-5
6.25 Å	-1.0428e-5	-9.0892e-6	-8.8141e-6	-9.5494e-6	-1.1474e-5	-1.5037e-5
6.50 Å	-8.1934e-6	-7.1915e-6	-6.9880e-6	-7.5493e-6	-9.0068e-6	-1.1682e-5
6.75 Å	-6.4966e-6	-5.7401e-6	-5.5875e-6	-6.0212e-6	-7.1378e-6	-9.1682e-6
7.00 Å	-5.1955e-6	-4.6193e-6	-4.5050e-6	-4.8439e-6	-5.7093e-6	-7.2661e-6
7.25 Å	-4.1890e-6	-3.7465e-6	-3.6602e-6	-3.9293e-6	-4.6063e-6	-5.8124e-6
7.50 Å	-3.4040e-6	-3.0605e-6	-2.9953e-6	-3.2108e-6	-3.7459e-6	-4.6898e-6
7.75 Å	-2.7872e-6	-2.5180e-6	-2.4679e-6	-2.6419e-6	-3.0687e-6	-3.8136e-6
8.00 Å	-2.2992e-6	-2.0854e-6	-2.0472e-6	-2.1871e-6	-2.5301e-6	-3.1231e-6
8.25 Å	-1.9099e-6	-1.7390e-6	-1.7084e-6	-1.8224e-6	-2.1007e-6	-2.5729e-6
8.50 Å	-1.5991e-6	-1.4586e-6	-1.4336e-6	-1.5265e-6	-1.7510e-6	-2.1333e-6
8.75 Å	-1.3465e-6	-1.2308e-6	-1.2099e-6	-1.2857e-6	-1.4694e-6	-1.7775e-6
9.00 Å	-1.1401e-6	-1.0441e-6	-1.0264e-6	-1.0883e-6	-1.2380e-6	-1.4918e-6
9.25 Å	-9.7036e-7	-8.9011e-7	-8.7506e-7	-9.2609e-7	-1.0505e-6	-1.2558e-6
9.50 Å	-8.2997e-7	-7.6274e-7	-7.4911e-7	-7.9170e-7	-8.9390e-7	-1.0637e-6
9.75 Å	-7.1305e-7	-6.5638e-7	-6.4425e-7	-6.7938e-7	-7.6473e-7	-9.0528e-7
10.00 Å	-6.1519e-7	-5.6732e-7	-5.5697e-7	-5.8649e-7	-6.5711e-7	-7.7466e-7
10.25 Å	-5.3296e-7	-4.9188e-7	-4.8334e-7	-5.0712e-7	-5.6740e-7	-6.6618e-7
10.50 Å	-4.6332e-7	-4.2852e-7	-4.2113e-7	-4.4201e-7	-4.9209e-7	-5.7529e-7
10.75 Å	-4.0446e-7	-3.7516e-7	-3.6844e-7	-3.8544e-7	-4.2869e-7	-4.9911e-7
11.00 Å	-3.5333e-7	-3.2760e-7	-3.2338e-7	-3.3843e-7	-3.7475e-7	-4.3484e-7
11.25 Å	-3.1263e-7	-2.9165e-7	-2.8506e-7	-2.9763e-7	-3.2930e-7	-3.7980e-7
11.50 Å	-2.7511e-7	-2.5549e-7	-2.5208e-7	-2.6314e-7	-2.9017e-7	-3.3409e-7
11.75 Å	-2.4352e-7	-2.2833e-7	-2.2378e-7	-2.3340e-7	-2.5639e-7	-2.9450e-7
12.00 Å	-2.1688e-7	-2.0215e-7	-1.9937e-7	-2.0741e-7	-2.2781e-7	-2.6068e-7

Table A.2, continued

	θ = 134°	145°	156°	167°	178°
R=2.00 Å	0.1428	0.2827	0.4725	2.3171	31.0372
2.25 Å	0.0766	0.1687	0.3334	1.1676	4.7175
2.50 Å	0.0394	0.0985	0.2476	0.6915	1.6920
2.75 Å	0.0195	0.0554	0.1763	0.5944	2.3893
3.00 Å	9.1940e-3	0.0295	0.1112	0.4384	6.7126
3.25 Å	4.0589e-3	0.0147	0.0622	0.2562	1.2446
3.50 Å	1.6210e-3	6.7964e-3	0.0314	0.1291	0.3473
3.75 Å	5.3231e-4	2.8462e-3	0.0144	0.0589	0.1296
4.00 Å	8.6234e-5	1.0210e-3	6.0419e-3	0.0247	0.0501
4.25 Å	-7.1339e-5	2.5184e-4	2.2322e-3	9.5706e-3	0.0189
4.50 Å	-1.0911e-4	-3.2291e-5	6.5740e-4	3.3267e-3	6.5918e-3
4.75 Å	-1.0284e-4	-1.1233e-4	7.7370e-5	9.5218e-4	2.0273e-3
5.00 Å	-8.4207e-5	-1.1608e-4	-9.8006e-5	1.3692e-4	4.5304e-4
5.25 Å	-6.5125e-5	-9.6879e-5	-1.2603e-4	-9.5743e-5	-2.6498e-5
5.50 Å	-4.9217e-5	-7.4764e-5	-1.0921e-4	-1.3207e-4	-1.3242e-4
5.75 Å	-3.6960e-5	-5.5988e-5	-8.4277e-5	-1.1329e-4	-1.2762e-4
6.00 Å	-2.7830e-5	-4.1603e-5	-6.2416e-5	-8.5897e-5	-9.9453e-5
6.25 Å	-2.1110e-5	-3.1019e-5	-4.5765e-5	-6.2617e-5	-7.2658e-5
6.50 Å	-1.6170e-5	-2.3330e-5	-3.3707e-5	-4.5360e-5	-5.2271e-5
6.75 Å	-1.2519e-5	-1.7742e-5	-2.5095e-5	-3.3121e-5	-3.7763e-5
7.00 Å	-9.7969e-6	-1.3652e-5	-1.8925e-5	-2.4506e-5	-2.7576e-5
7.25 Å	-7.7449e-6	-1.0625e-5	-1.4456e-5	-1.8388e-5	-2.0457e-5
7.50 Å	-6.1798e-6	-8.3564e-6	-1.1175e-5	-1.3988e-5	-1.5424e-5
7.75 Å	-4.9742e-6	-6.6350e-6	-8.7358e-6	-1.0786e-5	-1.1815e-5
8.00 Å	-4.0327e-6	-5.3144e-6	-6.9000e-6	-8.4208e-6	-9.1881e-6
8.25 Å	-3.2932e-6	-4.2900e-6	-5.5021e-6	-6.6492e-6	-7.2378e-6
8.50 Å	-2.7066e-6	-3.4889e-6	-4.4258e-6	-5.3029e-6	-5.7645e-6
8.75 Å	-2.2368e-6	-2.8567e-6	-3.5880e-6	-4.2659e-6	-4.6345e-6
9.00 Å	-1.8603e-6	-2.3541e-6	-2.9297e-6	-3.4592e-6	-3.7531e-6
9.25 Å	-1.5556e-6	-1.9516e-6	-2.4082e-6	-2.8254e-6	-3.0605e-6
9.50 Å	-1.3083e-6	-1.6275e-6	-1.9946e-6	-2.3236e-6	-2.5108e-6
9.75 Å	-1.1068e-6	-1.3662e-6	-1.6584e-6	-1.9233e-6	-2.0704e-6
10.00 Å	-9.4123e-7	-1.1541e-6	-1.3908e-6	-1.6010e-6	-1.7177e-6
10.25 Å	-8.0475e-7	-9.7762e-7	-1.1694e-6	-1.3402e-6	-1.4318e-6
10.50 Å	-6.9151e-7	-8.3591e-7	-9.9290e-7	-1.1291e-6	-1.2010e-6
10.75 Å	-5.9742e-7	-7.1732e-7	-8.4649e-7	-9.5711e-7	-1.0139e-6
11.00 Å	-5.1424e-7	-6.1895e-7	-7.2630e-7	-8.1544e-7	-8.6234e-7
11.25 Å	-4.5229e-7	-5.3552e-7	-6.2532e-7	-6.9851e-7	-7.3706e-7
11.50 Å	-3.9419e-7	-4.6691e-7	-5.4183e-7	-6.0187e-7	-6.3354e-7
11.75 Å	-3.4581e-7	-4.0732e-7	-4.7159e-7	-5.2156e-7	-5.4770e-7
12.00 Å	-3.0525e-7	-3.5838e-7	-4.1165e-7	-4.5679e-7	-4.7614e-7

Table A.3 *Ab initio* single point energies (E_h) of the He–cyanoacetylene potential energy surface, calculated at CCSD(T) theory level with aVTZ basis sets.

	θ = 2°	13°	24°	35°	46°	57°
R=2.00 Å	21.6485	2.2182	0.5264	0.2975	0.1270	0.0545
2.25 Å	3.2577	0.9729	0.3758	0.1726	0.0665	0.0263
2.50 Å	0.8965	0.5216	0.2504	0.0948	0.0331	0.0120
2.75 Å	0.5723	0.3506	0.1455	0.0489	0.0156	5.1255e-3
3.00 Å	0.3141	0.1886	0.0742	0.0236	6.9682e-3	2.0003e-3
3.25 Å	0.1336	0.0857	0.0344	0.0106	2.8725e-3	6.5676e-4
3.50 Å	0.0542	0.0361	0.0148	4.4434e-3	1.0435e-3	1.2225e-4
3.75 Å	0.0212	0.0144	5.9594e-3	1.6748e-3	2.8224e-4	-6.3760e-5
4.00 Å	7.9527e-3	5.4153e-3	2.1912e-3	5.2008e-4	-2.8400e-6	-1.0955e-4
4.25 Å	2.7881e-3	1.8687e-3	6.8612e-4	7.9850e-5	-8.9100e-5	-1.0489e-4
4.50 Å	8.5575e-4	5.3612e-4	1.3007e-4	-6.3880e-5	-9.9660e-5	-8.6100e-5
4.75 Å	1.7514e-4	7.2800e-5	-4.9420e-5	-9.4010e-5	-8.5920e-5	-6.6550e-5
5.00 Å	-3.8480e-5	-6.4900e-5	-8.9620e-5	-8.6040e-5	-6.7610e-5	-5.0230e-5
5.25 Å	-8.6840e-5	-8.8950e-5	-8.4090e-5	-6.8920e-5	-5.1330e-5	-3.7680e-5
5.50 Å	-8.2650e-5	-7.8560e-5	-6.7590e-5	-5.2520e-5	-3.8530e-5	-2.8350e-5
5.75 Å	-6.6140e-5	-6.1470e-5	-5.1390e-5	-3.9370e-5	-2.8930e-5	-2.1490e-5
6.00 Å	-4.9910e-5	-4.6120e-5	-3.8320e-5	-2.9470e-5	-2.1860e-5	-1.6440e-5
6.25 Å	-3.7040e-5	-3.4260e-5	-2.8590e-5	-2.2180e-5	-1.6670e-5	-1.2700e-5
6.50 Å	-2.7510e-5	-2.5470e-5	-2.1460e-5	-1.6850e-5	-1.2840e-5	-9.9200e-6
6.75 Å	-2.0590e-5	-1.9170e-5	-1.6270e-5	-1.2930e-5	-1.0000e-5	-7.8200e-6
7.00 Å	-1.5580e-5	-1.4560e-5	-1.2470e-5	-1.0040e-5	-7.8700e-6	-6.2300e-6
7.25 Å	-1.1930e-5	-1.1190e-5	-9.6800e-6	-7.8900e-6	-6.2600e-6	-5.0000e-6
7.50 Å	-9.2500e-6	-8.7200e-6	-7.6000e-6	-6.2600e-6	-5.0200e-6	-4.0500e-6
7.75 Å	-7.2600e-6	-6.8600e-6	-6.0300e-6	-5.0100e-6	-4.0600e-6	-3.3100e-6
8.00 Å	-5.8200e-6	-5.4700e-6	-4.8300e-6	-4.0500e-6	-3.3100e-6	-2.7200e-6
8.25 Å	-4.6000e-6	-4.4000e-6	-3.9100e-6	-3.3000e-6	-2.7200e-6	-2.2500e-6
8.50 Å	-3.8300e-6	-3.5700e-6	-3.1800e-6	-2.7100e-6	-2.2500e-6	-1.8700e-6
8.75 Å	-3.0000e-6	-2.9200e-6	-2.6200e-6	-2.2400e-6	-1.8700e-6	-1.5700e-6
9.00 Å	-2.6300e-6	-2.4100e-6	-2.1600e-6	-1.8600e-6	-1.5700e-6	-1.3200e-6
9.25 Å	-1.9600e-6	-1.9900e-6	-1.8000e-6	-1.5600e-6	-1.3200e-6	-1.1200e-6
9.50 Å	-1.8700e-6	-1.6600e-6	-1.5100e-6	-1.3100e-6	-1.1200e-6	-9.5000e-7
9.75 Å	-1.3100e-6	-1.4000e-6	-1.2700e-6	-1.1100e-6	-9.5000e-7	-8.1000e-7
10.00 Å	-1.3900e-6	-1.1800e-6	-1.0800e-6	-9.5000e-7	-8.1000e-7	-7.0000e-7
10.25 Å	-8.8000e-7	-1.0000e-6	-9.2000e-7	-8.1000e-7	-7.0000e-7	-6.0000e-7
10.50 Å	-1.0500e-6	-8.6000e-7	-7.9000e-7	-6.9000e-7	-6.0000e-7	-5.2000e-7
10.75 Å	-6.0000e-7	-7.3000e-7	-6.8000e-7	-6.0000e-7	-5.2000e-7	-4.5000e-7
11.00 Å	-8.1000e-7	-6.3000e-7	-5.8000e-7	-5.2000e-7	-4.5000e-7	-4.0000e-7
11.25 Å	-4.2000e-7	-5.5000e-7	-5.1000e-7	-4.5000e-7	-4.0000e-7	-3.5000e-7
11.50 Å	-6.3000e-7	-4.8000e-7	-4.4000e-7	-4.0000e-7	-3.5000e-7	-3.1000e-7
11.75 Å	-3.0000e-7	-4.2000e-7	-3.9000e-7	-3.5000e-7	-3.1000e-7	-2.7000e-7
12.00 Å	-5.0000e-7	-3.7000e-7	-3.4000e-7	-3.1000e-7	-2.7000e-7	-2.4000e-7

Table A.3, continued

	$\theta = 68^{\circ}$	79°	90°	101°	112°	123°
R=2.00 Å	0.0265	0.0161	0.0140	0.0184	0.0323	0.0660
2.25 Å	0.0116	6.3142e-3	5.3605e-3	7.6808e-3	0.0150	0.0334
2.50 Å	4.6943e-3	2.2115e-3	1.8017e-3	2.9666e-3	6.6509e-3	0.0161
2.75 Å	1.7052e-3	5.9966e-4	4.3829e-4	9.9284e-4	2.7477e-3	7.3772e-3
3.00 Å	4.8484e-4	2.5200e-5	-3.0720e-5	2.1889e-4	1.0116e-3	3.1812e-3
3.25 Å	3.0860e-5	-1.4215e-4	-1.5679e-4	-5.2460e-5	2.8265e-4	1.2441e-3
3.50 Å	-1.0975e-4	-1.6307e-4	-1.6336e-4	-1.2477e-4	2.7200e-6	3.9697e-4
3.75 Å	-1.3210e-4	-1.3958e-4	-1.3581e-4	-1.2514e-4	-8.6575e-5	5.4480e-5
4.00 Å	-1.1600e-4	-1.0843e-4	-1.0429e-4	-1.0438e-4	-1.0080e-4	-6.5770e-5
4.25 Å	-9.1780e-5	-8.1150e-5	-7.7720e-5	-8.1190e-5	-8.9260e-5	-9.3170e-5
4.50 Å	-6.9650e-5	-6.0020e-5	-5.7440e-5	-6.1410e-5	-7.1760e-5	-8.7350e-5
4.75 Å	-5.2080e-5	-4.4430e-5	-4.2580e-5	-4.6050e-5	-4.5770e-5	-7.1990e-5
5.00 Å	-3.8880e-5	-3.3120e-5	-3.1800e-5	-3.4580e-5	-4.2130e-5	-5.6270e-5
5.25 Å	-2.9190e-5	-2.4940e-5	-2.4000e-5	-2.6130e-5	-3.1930e-5	-4.3030e-5
5.50 Å	-2.2110e-5	-1.8980e-5	-1.8310e-5	-1.9920e-5	-2.4290e-5	-3.2680e-5
5.75 Å	-1.6910e-5	-1.4610e-5	-1.4120e-5	-1.5330e-5	-1.8600e-5	-2.4860e-5
6.00 Å	-1.3080e-5	-1.1360e-5	-1.1000e-5	-1.1920e-5	-1.4380e-5	-1.9030e-5
6.25 Å	-1.0210e-5	-8.9300e-6	-8.7400e-6	-9.3600e-6	-1.1220e-5	-1.4690e-5
6.50 Å	-8.0500e-6	-7.0800e-6	-6.8500e-6	-7.4200e-6	-8.8300e-6	-1.1440e-5
6.75 Å	-6.4100e-6	-5.6700e-6	-5.5300e-6	-5.9300e-6	-7.0100e-6	-9.0000e-6
7.00 Å	-5.1500e-6	-4.5800e-6	-4.4600e-6	-4.7800e-6	-5.6200e-6	-7.1500e-6
7.25 Å	-4.1700e-6	-3.7200e-6	-3.6300e-6	-3.8800e-6	-4.5400e-6	-5.7200e-6
7.50 Å	-3.4000e-6	-3.0500e-6	-2.9800e-6	-3.1800e-6	-3.6900e-6	-4.6200e-6
7.75 Å	-2.7900e-6	-2.5152e-6	-2.4500e-6	-2.6200e-6	-3.0300e-6	-3.7500e-6
8.00 Å	-2.3100e-6	-2.0900e-6	-2.0400e-6	-2.1700e-6	-2.5000e-6	-3.0700e-6
8.25 Å	-1.9200e-6	-1.7400e-6	-1.7000e-6	-1.8100e-6	-2.0700e-6	-2.5300e-6
8.50 Å	-1.6100e-6	-1.4600e-6	-1.4300e-6	-1.5100e-6	-1.7300e-6	-2.1000e-6
8.75 Å	-1.3500e-6	-1.2300e-6	-1.2100e-6	-1.2800e-6	-1.4500e-6	-1.7500e-6
9.00 Å	-1.1400e-6	-1.0500e-6	-1.0300e-6	-1.0800e-6	-1.2300e-6	-1.4700e-6
9.25 Å	-9.7000e-7	-8.9000e-7	-8.7000e-7	-9.2000e-7	-1.0400e-6	-1.2400e-6
9.50 Å	-8.3000e-7	-7.6000e-7	-7.9000e-7	-7.9000e-7	-8.9000e-7	-1.0500e-6
9.75 Å	-7.1000e-7	-6.6000e-7	-6.5000e-7	-6.8000e-7	-7.6000e-7	-9.0000e-7
10.00 Å	-6.2000e-7	-5.7000e-7	-5.6000e-7	-5.8000e-7	-6.5000e-7	-7.7000e-7
10.25 Å	-5.3000e-7	-4.9000e-7	-4.8000e-7	-5.1000e-7	-5.7000e-7	-6.6000e-7
10.50 Å	-4.6000e-7	-4.3000e-7	-4.2000e-7	-4.4000e-7	-4.9000e-7	-5.7000e-7
10.75 Å	-4.0000e-7	-3.7000e-7	-3.7000e-7	-3.9000e-7	-4.3000e-7	-5.0000e-7
11.00 Å	-3.5000e-7	-3.3000e-7	-3.2000e-7	-3.4000e-7	-3.7000e-7	-4.3000e-7
11.25 Å	-3.1000e-7	-2.9000e-7	-2.9000e-7	-3.0000e-7	-3.3000e-7	-3.8000e-7
11.50 Å	-2.7000e-7	-2.6000e-7	-2.5000e-7	-2.6000e-7	-2.9000e-7	-3.3000e-7
11.75 Å	-2.4000e-7	-2.3000e-7	-2.2000e-7	-2.3000e-7	-2.6000e-7	-2.9000e-7
12.00 Å	-2.2000e-7	-2.0000e-7	-2.0000e-7	-2.1000e-7	-2.3000e-7	-2.6000e-7

Table A.3, continued

	θ = 134°	145°	156°	167°	178°
R=2.00 Å	0.1434	0.2836	0.4737	2.3185	31.0756
2.25 Å	0.0770	0.1694	0.3344	1.1682	4.7243
2.50 Å	0.0397	0.0989	0.2483	0.6922	1.6926
2.75 Å	0.0197	0.0557	0.1768	0.5950	2.3347
3.00 Å	9.3454e-3	0.0297	0.1115	0.4388	6.7155
3.25 Å	4.1650e-3	0.0149	0.0624	0.2565	1.2452
3.50 Å	1.6941e-3	6.8995e-3	0.0315	0.1293	0.3477
3.75 Å	5.8083e-4	2.9188e-3	0.0145	0.0590	0.1290
4.00 Å	1.1744e-4	1.0704e-3	6.1096e-3	0.0248	0.0503
4.25 Å	-5.1790e-5	2.8428e-4	2.2791e-3	9.6233e-3	0.0189
4.50 Å	-9.7050e-5	-1.1760e-5	6.8936e-4	3.3613e-3	6.6378e-3
4.75 Å	-9.5490e-5	-9.9900e-5	9.7390e-5	9.7414e-4	2.0529e-3
5.00 Å	-7.9760e-5	-1.0862e-4	-8.6040e-5	1.4980e-4	4.6543e-4
5.25 Å	-6.2440e-5	-9.2670e-5	-1.1947e-4	-8.8790e-5	-1.9130e-5
5.50 Å	-4.7590e-5	-7.2430e-5	-1.0575e-4	-1.3867e-4	-1.2809e-4
5.75 Å	-3.5960e-5	-5.4730e-5	-8.2580e-5	-1.1142e-4	-1.2505e-4
6.00 Å	-2.7190e-5	-4.0990e-5	-6.1660e-5	-8.5140e-5	-9.8090e-5
6.25 Å	-2.0680e-5	-3.0400e-5	-4.5440e-5	-6.2430e-5	-7.2170e-5
6.50 Å	-1.5870e-5	-2.3180e-5	-3.3540e-5	-4.5380e-5	-5.2190e-5
6.75 Å	-1.2300e-5	-1.7560e-5	-2.4970e-5	-3.3140e-5	-3.7840e-5
7.00 Å	-9.6300e-6	-1.3460e-5	-1.8800e-5	-2.4510e-5	-2.7740e-5
7.25 Å	-7.6200e-6	-1.0460e-5	-1.4316e-5	-1.8370e-5	-2.0630e-5
7.50 Å	-6.0700e-6	-8.2100e-6	-1.1030e-5	-1.3940e-5	-1.5550e-5
7.75 Å	-4.8900e-6	-6.5100e-6	-8.5924e-6	-1.0700e-5	-1.1850e-5
8.00 Å	-3.9600e-6	-5.2100e-6	-6.7700e-6	-8.3100e-6	-9.1400e-6
8.25 Å	-3.2300e-6	-4.2100e-6	-5.3900e-6	-6.5200e-6	-7.1300e-6
8.50 Å	-2.6600e-6	-3.4200e-6	-4.3300e-6	-5.1800e-6	-5.6300e-6
8.75 Å	-2.2000e-6	-2.8000e-6	-3.5100e-6	-4.1600e-6	-4.4900e-6
9.00 Å	-1.8300e-6	-2.3200e-6	-2.8700e-6	-3.3700e-6	-3.6200e-6
9.25 Å	-1.5400e-6	-1.9200e-6	-2.3600e-6	-2.7600e-6	-2.9500e-6
9.50 Å	-1.3000e-6	-1.6100e-6	-1.9600e-6	-2.2700e-6	-2.5000e-6
9.75 Å	-1.1000e-6	-1.3500e-6	-1.6400e-6	-1.8800e-6	-1.9800e-6
10.00 Å	-9.4000e-7	-1.1500e-6	-1.3800e-6	-1.5700e-6	-1.6700e-6
10.25 Å	-8.0000e-7	-9.7000e-7	-1.1600e-6	-1.2500e-6	-1.4000e-6
10.50 Å	-6.9000e-7	-8.4000e-7	-9.9000e-7	-1.1200e-6	-1.2900e-6
10.75 Å	-6.0000e-7	-7.1643e-7	-8.4000e-7	-9.5000e-7	-9.1000e-7
11.00 Å	-5.2000e-7	-6.2000e-7	-7.3000e-7	-8.1000e-7	-8.6000e-7
11.25 Å	-4.5000e-7	-5.4000e-7	-6.2000e-7	-7.0000e-7	-7.2000e-7
11.50 Å	-3.9000e-7	-4.7000e-7	-5.4000e-7	-6.0000e-7	-6.3000e-7
11.75 Å	-3.5000e-7	-4.1000e-7	-4.7000e-7	-5.2000e-7	-5.5000e-7
12.00 Å	-3.0000e-7	-3.6000e-7	-4.1000e-7	-4.6000e-7	-4.8000e-7

Appendix B

Table B.1 Rotational energy levels of He–HCCCN in the ground vibrational state (cm^{-1}), for the aVQZ +BF, aVTZ + BF, and aVTZ *ab initio* potential energy surfaces, and the rotational energy levels determined for the aVTZ +BF surface when it is scaled by multiplying it by 1.03 and 1.12. Radial basis sets of 50 tri-diagonal Morse functions and angular basis sets of 50 Legendre polynomials were sufficient for convergence to within 0.0002 cm^{-1} for all calculated rotational energy levels. The eigenvalues and eigenvectors of the Hamiltonian matrix were obtained using 4000 Lanczos iterations.

	He–HCCCN				
J_{KaKc}	aVQZ +BF	aVTZ + BF	aVTZ	1.03×(aVTZ +BF)	1.12×(aVTZ +BF)
0_{00}	-17.0986	-16.8817	-13.9134	-17.6800	-20.1227
1_{01}	-16.8398	-16.6230	-13.6553	-17.4213	-19.8640
1_{11}	-16.6545	-16.4395	-13.4861	-17.2365	-19.6756
1_{10}	-16.5993	-16.3842	-13.4277	-17.1816	-19.6217
2_{02}	-16.3322	-16.1159	-13.1514	-16.9140	-19.3563
2_{12}	-16.1940	-15.9796	-13.0315	-16.7760	-19.2136
2_{11}	-16.0289	-15.8139	-12.8571	-16.6116	-19.0524
3_{03}	-15.5948	-15.3796	-12.4241	-16.1771	-18.6174
3_{13}	-15.5082	-15.2946	-12.3548	-16.0902	-18.5257
2_{21}	-15.4770	-15.2674	-12.3543	-16.0608	-18.4902
2_{20}	-15.4671	-15.2573	-12.3430	-16.0509	-18.4807
3_{12}	-15.1798	-14.9652	-12.0091	-15.7631	-18.2046
3_{22}	-14.7134	-14.5043	-11.5978	-15.2970	-17.7244
3_{21}	-14.6654	-14.4556	-11.5429	-15.2490	-17.6784
3_{31}	-13.6601	-13.4595	-10.6211	-14.2457	-16.6555
3_{30}	-13.6589	-13.4583	-10.6190	-14.2445	-16.6544

Table B.2 Rotational energy levels of He–DCCCN in the ground vibrational state (cm^{-1}), for the aVQZ +BF, aVTZ + BF, and aVTZ *ab initio* potential energy surfaces, and the rotational energy levels determined for the aVTZ +BF surface when it is scaled by multiplying it by 1.03 and 1.12. Radial basis sets of 50 tri-diagonal Morse functions and angular basis sets of 50 Legendre polynomials were sufficient for convergence to within 0.0002 cm^{-1} for all calculated rotational energy levels. The eigenvalues and eigenvectors of the Hamiltonian matrix were obtained using 4000 Lanczos iterations.

	He–DCCCN				
J_{KaKc}	aVQZ +BF	aVTZ + BF	aVTZ	1.03×(aVTZ +BF)	1.12×(aVTZ +BF)
0_{00}	-17.1603	-16.9547	-13.9786	-17.7554	-20.2037
1_{01}	-16.9179	-16.7125	-13.7370	-17.5132	-19.9616
1_{11}	-16.7214	-16.5181	-13.5569	-17.3176	-19.7623
1_{10}	-16.6727	-16.4693	-13.5053	-17.2691	-19.7148
2_{02}	-16.4408	-16.2358	-13.2631	-17.0364	-19.4844
2_{12}	-16.2872	-16.0845	-13.1281	-16.8835	-19.3269
2_{11}	-16.1414	-15.9382	-12.9739	-16.7382	-19.1845
3_{03}	-15.7435	-15.5396	-12.5741	-16.3397	-18.7862
3_{13}	-15.6396	-15.4379	-12.4888	-16.2361	-18.6775
2_{21}	-15.5558	-15.3591	-12.4383	-16.1550	-18.5900
2_{20}	-15.5483	-15.3515	-12.4298	-16.1475	-18.5828
3_{12}	-15.3493	-15.1465	-12.1826	-15.9467	-18.3937
3_{22}	-14.8403	-14.6442	-11.7294	-15.4394	-17.8726
3_{21}	-14.8039	-14.6071	-11.6875	-15.4029	-17.8376
3_{31}	-13.7480	-13.5622	-10.7155	-14.3510	-16.7666
3_{30}	-13.7472	-13.5614	-10.7141	-14.3502	-16.7660

Table B.3 Rotational energy levels of He–HCCC^{15}N in the ground vibrational state (cm^{-1}), for the aVQZ +BF, aVTZ + BF, and aVTZ *ab initio* potential energy surfaces, and the rotational energy levels determined for the aVTZ +BF surface when it is scaled by multiplying it by 1.03 and 1.12. Radial basis sets of 50 tri-diagonal Morse functions and angular basis sets of 50 Legendre polynomials were sufficient for convergence to within 0.0002 cm^{-1} for all calculated rotational energy levels. The eigenvalues and eigenvectors of the Hamiltonian matrix were obtained using 4000 Lanczos iterations.

	He–HCCC^{15}N				
J_{KaKc}	aVQZ +BF	aVTZ + BF	aVTZ	1.03×(aVTZ +BF)	1.12×(aVTZ +BF)
0_{00}	-17.1357	-16.9182	-13.9462	-17.7179	-20.1635
1_{01}	-16.8835	-16.6662	-13.6948	-17.4658	-19.9115
1_{11}	-16.6941	-16.4785	-13.5214	-17.2769	-19.7189
1_{10}	-16.6416	-16.4258	-13.4658	-17.2246	-19.6677
2_{02}	-16.3883	-16.1714	-13.2030	-16.9708	-19.4161
2_{12}	-16.2443	-16.0292	-13.0772	-16.8271	-19.2677
2_{11}	-16.0870	-15.8714	-12.9111	-16.6704	-19.1141
3_{03}	-15.6671	-15.4512	-12.4910	-16.2500	-18.6935
3_{13}	-15.5740	-15.3598	-12.4156	-16.1567	-18.5953
2_{21}	-15.5226	-15.3124	-12.3956	-16.1073	-18.5396
2_{20}	-15.5138	-15.3034	-12.3855	-16.0984	-18.5311
3_{12}	-15.2610	-15.0458	-12.0860	-15.8449	-18.2894
3_{22}	-14.7786	-14.5689	-11.6584	-15.3629	-17.7934
3_{21}	-14.7354	-14.5251	-11.6090	-15.3197	-17.7520
3_{31}	-13.7114	-13.5102	-10.6678	-14.2979	-16.7107
3_{30}	-13.7104	-13.5092	-10.6660	-14.2969	-16.7098